Influence of Cr and Cr+Nb on the interphase precipitation and the mechanical properties of microalloyed steels for the automotive industry

by

Karol Felipe Rodriguez Galeano

Thesis submitted for the Degree of Doctor of Philosophy

Department of Materials Science & Engineering

The University of Sheffield

September 2022

ABSTRACT

Steels for the car industry are engineered to enhance the strength (yield and ultimate), total elongation, and weldability to lighten cars and minimize fuel consumption. This can be achieved by combining ferritic matrixes toughen with nanoprecipitates formed during the austenite-to-ferrite transformation. Samples of two alloys were initially tested, V-Mo and Cr-V-Mo, which were claimed to have exceptional mechanical properties but with no complete information on the processing. At the Department of Materials Science and Engineering of the University of Sheffield, microalloyed steels V-Mo-0.4 and Cr-V-Mo-0.4 were produced to evaluate a large hot-working strain per pass before the isothermal transformation and to observe the prior-austenite grain behaviour. Results showed superior mechanical properties with a microstructure composed of a majority of ferrite. Values of $\sigma_Y \approx 1GPa$, $\sigma_{Ult} \approx 1{,}3\ GPa$ with total elongation of about ~14% were found for steels with no Cr additions, and $\sigma_Y \approx 1GPa$, $\sigma_{Ult} \approx 1{,}3\ GPa$ with total elongation of ~17% for steels with Cr addition.

Another three alloys were manufactured at the University of Sheffield to evaluate lower magnitudes of strain per pass on the same compositions and add a new one (Cr-Nb-V-0.2) because of the well-known effect of Nb on the grain refinement of the final microstructure plus the addition of Cr which showed a higher percentage of ferrite after the isothermal transformation, and better mechanical properties than steel free of Cr. The change in the strain per pass during the hot-rolling produces a drop in the final mechanical properties of about 200 MPa for the yield stress, 300 MPa for the ultimate stress and about 3% in the total elongation. Also, less ferrite volume fraction was found in these last alloys. To clarify that, identification and quantification of the interphase precipitation within the ferrite were performed followed by the calculation of the strength contributions.

It was established that steels with higher strain per pass during the hot-working produce more volume fraction of interphase precipitation, of dislocation density and maximize the solid solution strengthening contribution. Also, the addition of Cr showed higher precipitation of vanadium carbides.

TABLE OF CONTENTS

TABLE OF FIGURES

LIST OF TABLES

ACKNOWLEDGEMENTS

Firstly, I would like to thank God for everything, all the glory and honour are yours forever and ever.

I would like to start by expressing my gratitude to the department of Materials Sciences and Engineering at the University of Sheffield for giving me the opportunity of joining this worldwide recognized department. In addition, the three and a half years of scholarship made it possible to me to study in this top-world faculty.

My sincere gratitude to my supervisor, Professor Mark Rainforth, FREng., for his guidance, support, and help which were crucial for the success of this research. In addition, I express my most sincere gratitude to the Department of Materials Science and Engineering staff, with a special mention to senior research technicians and friends Dean Haylock and Neil Hind for all their help and guidance during the experiments. In addition, I would like to thank the postdoctoral research associate John Nutter for his help with the usage of the TEM, and for being always willing to help me and guide me in every question I had. I also want to thank Dr Lisa Hollands, Tesoro Monaghan, Dr Ian M. Ross, Dr Cheryl Shaw, Dr Le Ma and all other technicians and leaders who helped me with training and equipment operation.

I would like to express my gratitude to the friends who supported me throughout the process, with a special acknowledgment to Leonardo Corredor, Dean Haylock, Luis F. Romano-Acosta, Daniel Olguin, Natalia Hurtado, Alex Roocroft, Francisco Iriarte-Marrero, Eduardo Alvarez, Daniel Jensen, Mozart Quieroz, Bhushan Rakshe, Colm O'Regan, Edisson Martinez, and all the other wonderful people I met during my time in Sheffield. I would like to give a special shoutout to Les Wyzykiewicz, who provided personal assistance and support during the challenging times. I recognize that without his help, this project would not have been possible.

Finally, I would like to give special recognition to my family - the most important pillar in my life. I am grateful for the unwavering support of my beloved girlfriend, Karol (otita), my sister Jennifer, my parents Maria del Carmen and Alcides, my brother Oscar, my aunt Ines, my uncles Manuel, Jorge, and Juan, as well as all my cousins who stood by me throughout the research process. Without their patience, understanding, advice, care, and love, this endeavour would not have been possible.

CHAPTER 1: INTRODUCTION

Dual-phase steels (ferrite + martensite) have a good combination of tensile properties such as continuous yielding, high strength, and good uniform elongation, ideal for reduced-weight automobile designs with better fuel efficiency[1–4]. The mechanical properties of microalloyed steels depend on multiple factors, one of them is the contribution made by precipitation which is determined by the size, density, distribution and morphology of the carbides[5]. Some investigations in this field of metallurgy are focused on maximizing the tensile strength via grain refinement and precipitation hardening[6–9].

Conventional high-strength low-alloy (HSLA) steels are strengthened by the combination of solid solution hardening, grain refinement and precipitation hardening. The grain refinement can be successfully achieved by controlling the rolling parameters of TMCP schedule[10–14]. The rolling at the austenite recrystallization region refines the grain size by successive recrystallization. The austenite grain boundaries provide nucleation sites for $\gamma \rightarrow \alpha$ transformation, meaning that the austenite grain refination makes the final ferrite grain size becomes smaller. The rolling at the austenite non-recrystallization region accumulates internal stress in austenite grains like dislocations, which act as nucleation sites for ferrite and thus producing ferrite grain refinement[15–17].

The interphase precipitation of carbides and carbonitrides during the austenite to ferrite ($\gamma \rightarrow \alpha$) transformation has been successfully applied to strengthen steels with the presence of ferritic phase[18]. These precipitations increase the ferrite strength thanks to their characteristic rowed dispersion which blocks the movements of dislocations. Since then, additions of microalloying carbide-forming elements have been studied aiming to lower the $\gamma \rightarrow \alpha$ transformation temperature to retard the generation of pearlite and large cementites and replace them for fine carbides within ferritic phase[7]. Research works reported the effect of carbide-forming additions on interphase precipitation, precipitate spacing, orientation relationship, volume fraction, etc. and correlate them with the obtained strength gain[7–9,18–22].

In previous studies, the interphase precipitation in steels with Cr additions had been reported[23–25] to have a significant gain in the tensile properties but with no agreement of which is the effect of Cr. More recent studies of steels for the automobile industry by researchers at the University of Sheffield has shown interphase precipitation during the austenite to ferrite transformation in steels. This is an effective way to increase the tensile strength of steels with no excessive cost increase in the manufacturing process[26,27]. In those studies, Gong et al. analysed several microalloyed steels, including one patented by Tata Steel, IJmuiden. Important correlations were made between small additions of microalloying elements (vanadium, titanium, and molybdenum), changes in the temperature of the isothermal heat treatment (at which transformation takes place) and their effect on nanoprecipitation formation, coarsening and spacing. All of these factors contributed in different ways to the tensile properties of steels.

The development of V-Cr and V-Cr-Nb microalloyed steels with an excellent combination of tensile properties (yield strength > 900 MPa, ultimate tensile strength > 1200 MPa, and total elongation ≈ 20%) has been achieved. This combination of properties is due to the significant strengthening contribution of the interphase nanometer-sized precipitation in the ferrite. Dilatometry is a highly dependable technique that provides consistent experimental data by monitoring thermal cycles in steels in real-time [28–30]. This is why it has been utilized to conduct accurate heat treatments and investigate the impact of Cr and Cr+Nb additions on the $\gamma \rightarrow \alpha$ isothermal transformation in V-based

microalloyed steels. The microstructure of the samples and the volume fraction of ferrite was obtained by the point counting method on optical microscopy (OM) images. Further tensile tests were made and their results correlated with the interphase precipitation found via TEM imaging. The contribution of the interphase precipitation to the tensile strength is presented as a function of the analysis made.

CHAPTER 2: LITERATURE REVIEW

2.1. STEEL FOR THE AUTOMOBILE APPLICATIONS

Historically, research on automotive vehicles has focused on improving the efficiency of them and satisfying all the characteristics that novel standards and designs require, such as low emissions, good crashworthiness, high stiffness, and the forming of very complex contours related with modern vehicles [31,32]. The use of light metals such as aluminum has become increasingly popular to reduce the component's weight. The density of aluminum is just a third that of steel, but also its strength and Young's modulus are also about one third that of steel. This is the reason why it is so hard to substitute aluminum in components which historically had been produced with steel, particularly without a large modification in the designs to toughen them [33]. In-response, automotive modular designs have been developed, permitting the usage of different materials to perform securely, comfortability and efficiently in vehicles [34,35]. Besides that, low-carbon steels have always been some of the favourite materials for the automotive industry, bringing benefits such as low cost of production, good attributes for safety parts, great weldability and recyclability, among others [36]. There are different steel families that have been used in the automobile industry, some of them are discussed below.

2.1.1. HIGH STRENGTH LOW ALLOY (HSLA) STEELS

The term High-Strength Low-Alloy (HSLA) steel has never been precisely defined neither its origin or its first historical use. Some correlate the origin of HSLA steels with the development of Nb microalloyed steels, and niobium had an important transition from being little more than a laboratory curiosity to being an important commercially produced ferroalloy convenient for addition to steel in 1965, with the first successful commercial fabrication of ferroniobium by the Companhia Brasileira de Metalurgia e Mineração (CBMM) mine in Araxa, Brazil. After that ferroniobium as a microalloying element was widely available to the steel industry [37,38]. Furthermore, the origin of HSLA steels could be linked to Williams'[39] results in 1900, in which he enhanced the corrosion resistance in steels with copper additions.

An example of a study which used a name close to that of HSLA dates from mid-1930s. Cone [40] refers to steels evolved from carbon-steel base as "low-alloy high-tensile steels". Following this, several studies investigated low alloy additions in combination with multiple heat treatments, and manufacturing processes with the aim to enhance the tensile properties of steels.

An appropriate definition for HSLA might be the one given by Porter and Repas [41], which is "steels having yield strength over 40 ksi (175MPa) with alloying additions designed to provide specific desirable combinations of properties such as strength, toughness, formability, weldability, and atmospheric corrosion resistance". Many other kinds of steels have been included as HSLA steels, some of them are:

2.1.1.1. WEATHERING STEELS:

Steel with a total alloying content of less than 5% designed to give better durability under conditions of atmospheric corrosion. The enhanced corrosion resistance is a result of the addition of alloying elements such as Cu, Cr, Ni, etc. The steels are usually used for roofs, artistic features or heavy structures under relative corrosive environments as transmission towers.

2.1.1.2. CONTROL ROLLED STEELS:

These are steels that have been rolled at temperatures below the recrystallization stop temperature to obtain an austenitic structure with a very high residual strain. After cooling the deformed structure will become a very fine equiaxed ferrite structure.

2.1.1.3. PEARLITE-REDUCED STEELS:

Steels with low carbon content, resulting in little or no pearlite in the microstructure. Their principal hardening and strengthening mechanisms are a very fine-grained ferrite as the main structure, plus some strengthening from precipitation.

2.1.1.4. MICROALLOYED STEELS:

They are steels where producers use very small intentional additions of alloying elements such as boron, titanium, niobium, vanadium, etc. (usually below 0.10% each), to control simultaneously multiple properties, such as grain refinement, precipitation hardening, inclusion shape and size control, very high hardenability and weldability.

Because the main topic of this thesis is related to microalloyed steels, it will be discussed in detail in the following chapters.

In the 1990s, the automotive industry developed and widely used a HSS steel which combined the required properties as a result of micro- alloying additions. They were mainly C-Mn steels strengthened with the addition of a microalloying amount of titanium, vanadium, or niobium known as High-Strength, Low-alloy (HSLA) Steels [42]. While the HSLA steels were developed, it was clear that the martensitic phase is stronger and harder than ferritic based microstructures. To increase the combination of formability and strength of the steel, a combination of phases had to be used, such as ferrite and martensite, leading to the evolution of dual phase (DP) steels which represents the first generation of Advanced High-strength steels (AHSS).

2.1.2. AHSS STEELS

The AHSS family of steels were developed to fulfil a commercial need to optimize the total elongation and the strength. The most relevant for this industry are:

2.1.2.1. DUAL-PHASE (DP) STEEL:

DP steels are usually composed of martensite islands within a ferrite matrix. They exhibit similar values of strength to HSLA steels but with better formability, which has made them suitable for the automobile industry. Some of them exhibit ultimate tensile strength above 1GPa and a total elongation close to 15% [43].

DP steels are obtained by heating the steel into the $(\alpha + \gamma)$ and held, typically at $790^0 C$, for several minutes to allow small regions of austenite to form in the ferrite, and then cooling to ambient temperature quickly to transform these regions of austenite into martensite [44]. The martensite volume fraction determines the mechanical properties, with the DP steels designed according to industrial specifications of elongation and strength.

The mixed microstructure gives DP steels one of their most well-known characteristics, that is to have continuous yielding with no sharp yield point in the engineering stress vs engineering strain curve (Figure 1). In addition, DP steels have relatively low proof strength and a high work hardening rate, making them a very good option for energy-absorption tasks.

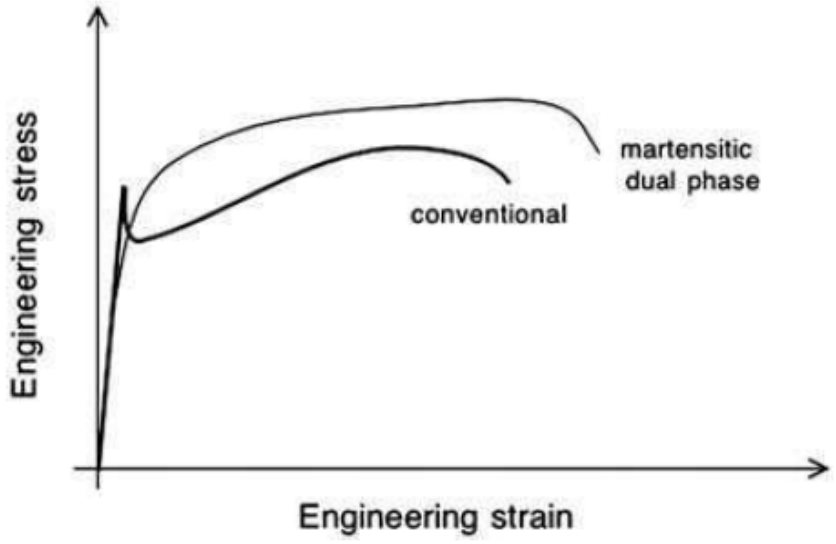

Figure 1. Schematic stress-strain curves comparing the behavior of a conventional automobile steel with that of a dual-phase steel. [44]

2.1.2.2. COMPLEX-PHASE (CP) STEELS:

In addition to ferrite and martensite, these steels contain bainite as the main constituent, and exhibit higher formability than DP steels [45]. The addition of elements such as niobium, titanium and /or vanadium enhances some important properties, i.e., precipitation hardening and creep resistance (Table 1). A strength of 0.8 GPa or more can be achieved, which can be compared to that of TRIP steels, but with lower alloying addition. Their weldability is enhanced at the expense of formability[46].

Alloying element	Role of the alloying element
Niobium	• Promotes precipitation hardening caused by finely dispersed carbides[47]. • Enhances resistance against intergranular corrosion. • Increases creep resistance.
Vanadium	• The main purpose of the addition of vanadium to CP steels is to reduce the grain growth and thus to limit the grain size of austenite. The resulting fine microstructure, also containing vanadium carbides, produces a substantial improvement in hardness and strength. • Vanadium enhances impact and creep resistance.
Titanium	• Addition of titanium results in the formation of titanium carbides (TiC) and titanium nitrides (TiN). Grain refinement of the steel is achieved by the grain growth inhibition effect from the TiC and TiN particles. • Titanium also provides corrosion resistance in oxidizing environments.

Table 1. Effect of main alloying elements added in CP steels. Modified from [48]

The manufacturing of CP steels consists of austenizing above the inter-critical region, and then cooling. Depending on the approach taken, cooling can be slow to room temperature, or soaking in the bainitic region after a rapid cooling and then cooling to room temperature. The alloy is quenched to the isothermal holding in the bainitic region from the austenising temperature. Alloy additions are made to retard the transformation to ferrite and pearlite so that the pearlite region is bypassed. Any change in the processing parameters influences the microstructure of CP steels[49], leading to variations in tensile properties that are reported extensively in the bibliography.

2.1.2.3. PRESS-HARDENED STEEL (PHS):

Widely used for producing structural parts for automobiles, PHS exhibit good weldability and high tensile strength (~1.5GPa), making them very important materials for structural reinforcements and safety anti-intrusion parts (pillars, bumpers, impact beams, door beams, roof rails, etc) since the 1970's [50]. However, a critical characteristic of them is low residual ductility due to the martensitic microstructure (~6%)[51].

Hot press forming (HPF), also is known as die quenching, press hardening or hot stamping, but mainly is a process in which cold-rolled steel blanks are full austenised to a temperature between 900 and 950^0C, then the hot sheet is press formed by water-cooled dies. They cool the blanks down below the martensitic transformation finish temperature $\sim 200^0$C (Figure 2). The required cooling rate commonly is between 40^0C/s and 100^0C/s [52].

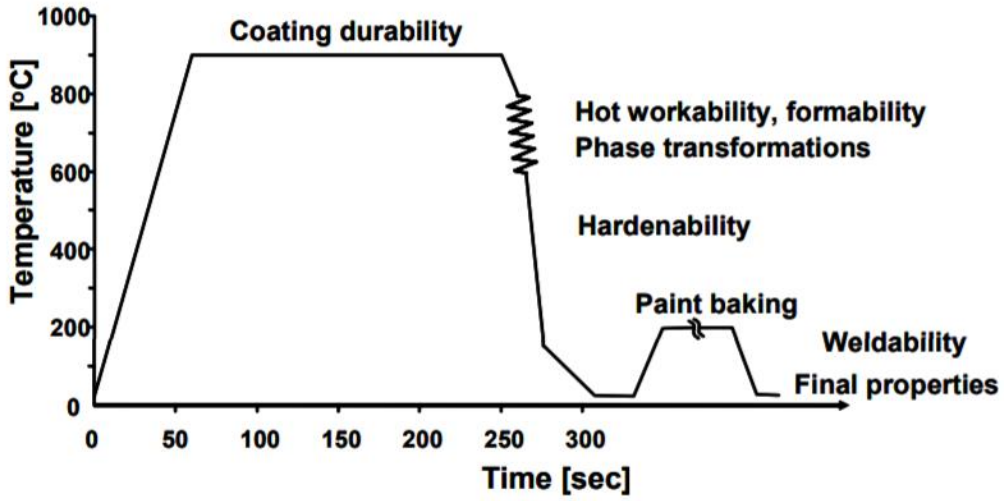

Figure 2. Scheme of the thermal cycle of HPF steel [53].

Because of the weldability limit, the C in these steels generally has a maximum value of 0.2% wt. Additions of other important alloying elements are made, such as Mn, B, Cr and Mo. Their mainly effects on HPF steels are enlisted in Table 2.

Alloying element	Role of the alloying element
Manganese	• Enhances hardening. • Retards most austenite decomposition reactions.
Boron	• Increases hardenability in HPF steels by retarding the heterogeneous nucleation of ferrite at the boundaries of the austenite grain.
Chromium	• Strong hardenability agent. • Suppresses the bainite transformation.
Molybdenum	• Via solute drag mechanism, suppresses the pearlite formation kinetics and also ferrite, increasing the hardenability.

Table 2. Effect of alloying elements on HPF steels [54,55].

2.1.2.4. TRANSFORMATION- INDUCED PLASTICITY (TRIP) STEELS:

TRIP steels have an exceptional combination of high ductility, strength, and impact resistance, due to their multi-phase microstructures composed of martensite (1-5%), retained austenite (7-15%), bainite (30-35%) and ferrite as a maximum constituent (50-55%). The properties result from transformation of retained austenite (RA) to martensite during straining, which is called the TRIP effect [56]. The most common processing route to obtain TRIP steels is by austenising, then a cool to the inter-critical region where the material is deformed to increases the rate of the austenite to ferrite ($\gamma \rightarrow \alpha$) phase transformation, and at the same time to increase the bainite nucleation rate but decreasing its growth rate. The remaining austenite becomes enriched in carbon which stabilizes the austenite. The alloy is then cooled into the bainite region to give transformation of some of the austenite to bainite, which forms in small plates, followed by a final quench to room temperature [57], as is shown in Figure 3.

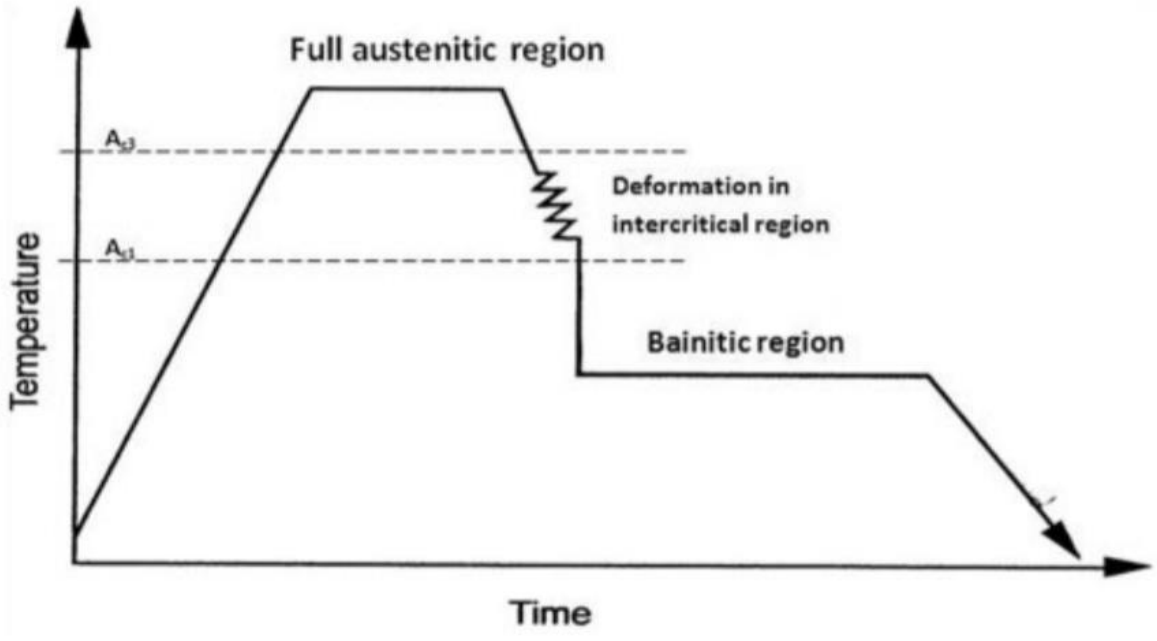

Figure 3.Scheme of the thermal cycle of TRIP steel [48].

The addition of austenite stabilisers is very important for TRIP steels, especially carbon and manganese. A silicon addition is made to suppress carbide formation and thereby keep the carbon free for austenite stabilization. The addition of aluminum is also made to getter nitrogen [58], limiting the free nitrogen and its harmful effect within the steel. Processing TRIP is complicated given the need for the complex heat treatment, making them expensive which limits the possible industrial application of TRIP steels.

2.1.2.5. TWINNING- INDUCED PLASTICITY (TWIP) STEELS:

The TWIP steels microstructure consists mainly of austenite to obtain a greater balance of elongation (50% maximum) and tensile strength (above 1GPa) [59].

Their common composition consists of 15 to 35% wt. Mn or Ni, 1 to 3% wt. of Al and around 1% of Si[60,61]. Other additions are made for different purposes, as they contribute to solid solution strengthening (C, Si, N, Al), to obtain retained austenite at room temperature (C, Mn, N, Al), etc. (Table 3). In general, alloying elements mostly decrease the stacking fault energy (SFE) of the steel, enhancing twinning behavior during deformation, reducing the dislocation density and as a result an improvement of ductility is obtained. For pure twinning, the SFE value should be $20\,\mathrm{mJ}/m^2$ or greater, otherwise a conversion from austenite to martensite occurs (TRIP effect) [62]. Thus, a small addition of Al is very important to increase the SFE, retarding the TRIP effect to produce deformation purely by twinning.

Effect	C	Mn	Si	B	Ti	N	Al
γ-stabiliser	✓	✓				✓	✓
Solid solution	✓		✓			✓	✓
strengthening austenite			✓				✓
ε–martensite refinement							
Hot ductility				✓	✓		

Table 3. Effect of alloying elements on properties of high manganese steels [61].

Unfortunately, even with the superior mechanical performance of TWIP steels, they have limited industrial production and application mainly because of three reasons:

1- Cost ineffectiveness.
2- Poor productivity.
3- Delayed fracture.[63]

This thesis has been focused in microalloyed steels, and so the following sections will focus on the different mechanisms to strengthen these steels.

2.1.2.6. STRENGHTENING MECHANISMS OF MICROALLOYED STEELS

Alloying elements play three main functions in microalloyed (MA) steels, which are: 1) solid solution strengthening, 2) grain refinement, and 3) dispersion strengthening. All three are related to the alloy content, but grain refinement and dispersion strengthening also on thermomechanical processing. Furthermore, microalloying elements are selected to reduce the $\gamma \rightarrow \alpha$ transformation temperature, to obtain a fine-grained product. In general, austenite recrystallisation is retarded by the addition of microalloy elements via particle pinning and/or solute drag of grain boundaries. Table 4 is a reproduction of the table published by Vervynct et al.[14], who summarises the general effect of the alloying elements additions on MA steels.

Element	Wt-%	Influence
C	< 0.25	Strengthener.
Mn	0.5 - 0.2	Delays austenite decomposition during accelerated cooling. Decreases ductile to the brittle transition temperature. Mild solid solution strengthener.
Si	0.1 - 0.5	Deoxidiser in molten steel. Solid solution Strengthener.
Al	< 0.02	Deoxidiser. Limits grain growth as AlN.
Nb	0.02 - 0.06	Very strong ferrite strengthener as Nb(C, N) which at the same time controls the grain size coarsening. Delays $\gamma \rightarrow \alpha$ transformation.
Ti	0 - 0.06	γ Grain size control by TiN formation. Strong ferrite strengthener.
V	0 - 0.1	Strong ferrite strengthener by VN formation.
N	< 0.012	Forms TiN, VN and AlN.
Mo	0 - 0.3	Promotes bainite formation. Ferrite strengthener.
Ni	0 - 0.5	Increases fracture toughness.
Cu	0 - 0.55	Ferrite strengthener. Improves corrosion resistance.
Cr	0 - 1.25	Improves atmospheric corrosion resistance (when Cu is also added).

Table 4. Common alloying elements used in the fabrication of MA steels[14].

2.1.2.7. SOLID SOLUTION

Since it was developed by Pickering et al.[64] Equation 1 has been used to predict the yield strength of low carbon steels. It only considers the effects of solid solution and the grain size hardening. It correlates the ferrite grain size (d) with the weight percentages of the free nitrogen dissolved in ferrite (N_f), manganese and silicon.

$$\sigma_y = 15.4\left(3.5 + 2.1\ \mathrm{Mn\%} + 5.4\ \mathrm{Si\%} + 23\ \mathrm{N_f} + 1.13\ \mathrm{d}^{1/2}\right) \quad \textit{Equation 1}$$

It has been shown that this relationship does not fit with experimental data from tensile testing[11]. Furthermore, the differences between the calculated yield stresses with Equation 1 and the experimental ones in steels with different alloying additions after normalising were similar for them all, attributing the additional strengthening contributions to the precipitation of carbonitrides and remnant dislocations from the different processes [11]. Precipitation strengthening is an important topic of this thesis, which is why it will be extended in the following sections.

Dislocation strengthening ($\Delta\sigma_d$) can be quantified by Equation 2[65], where m, α, μ, b and ρ are the appropriate Taylor factor for poly-crystals, a geometrical factor that depends on the type of dislocation interaction, the shear modulus (80.3 GPa for ferrite) and the measured dislocation density respectively. $m\alpha$ values are determined to be between 0.38 and 0.435[11,66].

$$\Delta\sigma_d[\mathrm{MPa}] = m\alpha\mu b\rho^{1/2} \quad \textit{Equation 2}$$

2.1.2.8. GRAIN REFINEMENT

In the same decade as The Great Lakes Steel Corporation introduced its niobium-treated steels and reactivated the marketing and research on MA steels, Hall[67], Petch[68] and Cottrell[69] gave the first reliable understanding of the parameters that rule the strength of crystalline materials. More specifically, the Hall-Petch equation (Equation 3) correlates the yield stress σ_y with the ferrite grain size *d* of MA steels.

$$\sigma_{YS} = \sigma_0 + K_y d^{-1/2} \quad \textit{Equation 3}$$

In this expression σ_0 is a materials constant, which is the resistance of the lattice of dislocation motion and *K* is the strengthening coefficient, a material specific constant. Also, there are other influencing factors on the yield strength of MA steels such as solid solution strengthening, dislocation strengthening and precipitation strengthening. Figure 4 shows how each of these contributes to the total yield strength of MA steels (hot rolled plates). Furthermore, the most important strength contributor to fine-grain ferrite steels is grain refinement. In austenite, the microalloying elements are responsible for this effect, but to further refine the ferrite grain size other methods also need to be used such as thermomechanical processing and severe plastic deformation. This last one is very

difficult to implement in a continuous production line, therefore advanced thermomechanical processing methods and controlling phase transformation are the most common in the industry.

Due to developments in the cooling systems after hot rolling a range of microstructures can be achieved for a given composition, depending on the properties that the industry needs. Figure 5 shows how the process started by minimizing the austenite grain size followed by a deformation between A_{r3} and A_{e3}, producing a grain-refined microstructure with constituents that depend on the cooling rate. The pan-caking phenomenon increases the grain boundary area and generates deformation bands that bring additional sites for ferrite nucleation, resulting in finer grains[70,71].

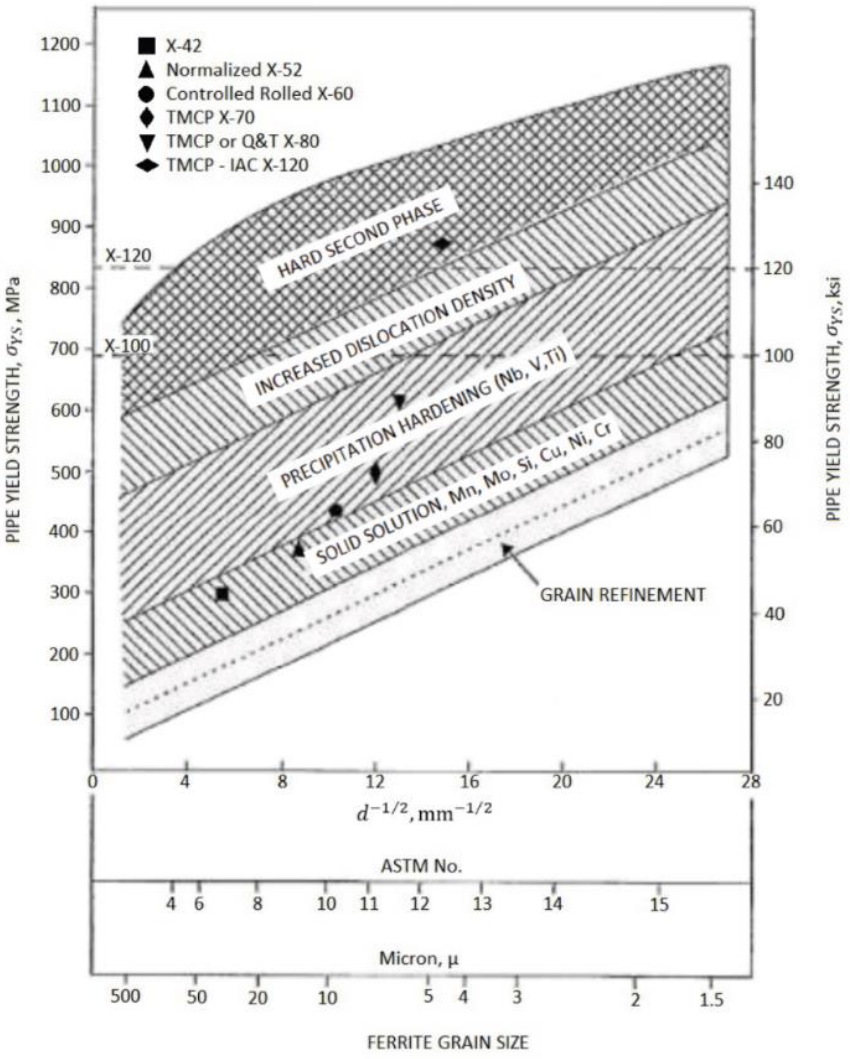

Figure 4. Strengthening components of the yield strength for rot-rolled plate and skelp. Modified from [72].

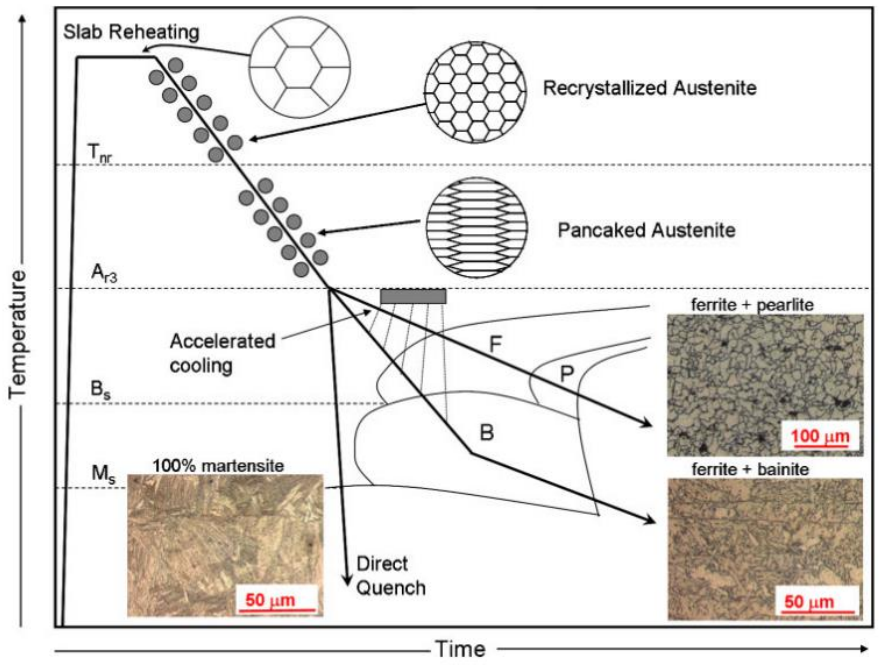

Figure 5. Schematice of the resultant microstructures from thermomechanically controlled processing (TMCP)[14].

2.1.2.9. HEAT TREATMENT SCHEDULE FOR ISOTHERMAL TRANSFORMATION

To obtain a miciroalloyed steel with excellent mechanical properties, it is important to understand the different contributing factors from alloy additions, precipitation strengthening and by grain refinement. Since the 1960's [73,74] the physical metallurgy of hot working has evolved, producing more refined alloys and also developing processes to implement them in industry and satisfying the increasing production demand in high property steel markets (Figure 6).

Thermomechanical treatments aim to maximize the contributions of the different strengthening mechanisms by themselves and/or by mixing them. To create a fine-grain structure, every variable of the thermomechanical processing (soaking temperature, heating and cooling rates, strain and strain rates) must be carefully controlled. Thermomechanical controlled processing (TMCP) is used to obtain fine-grained steels with excellent combination of strength, toughness and weldability[13,75].

Austenite conditioning is used to influence the ferrite grain refinement during the $\gamma \rightarrow \alpha$ transformation [76,77]. Combinations of TMCP with heat treatment processes showed MA steels with ultra-fine grained austenite plus high density of nanosized particles[6]. In the current work the objective was to obtain as fine a grain size as possible, but at the same time to maximise the precipitation potential in order to maximise the mechanical properties. This is a balancing act, with the decisions to be taken shown in the conceptual map of Figure 7.

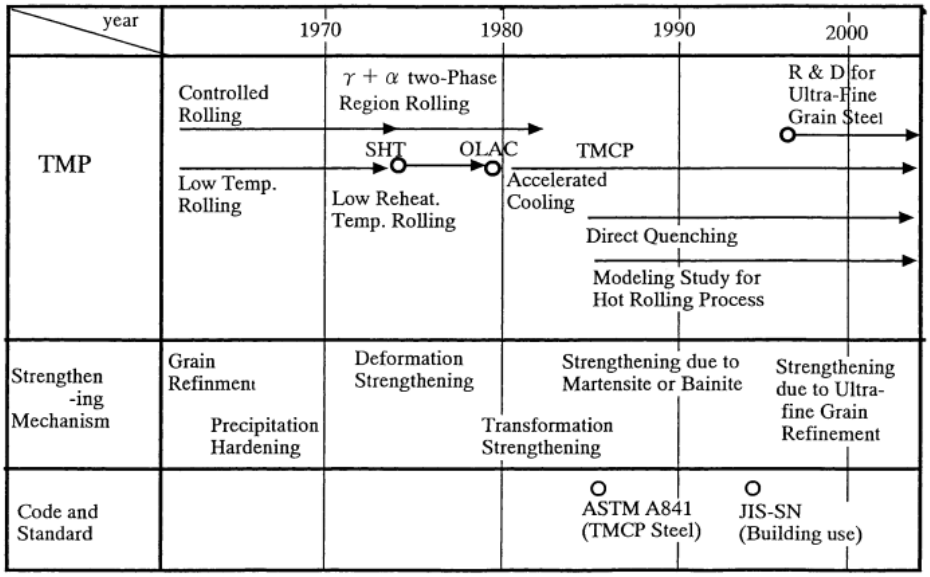

Figure 6. Chronologic development of TMP and strengthening mechanism [13].

Parameters to be controlled by MA additions.

- Conditions for austenite's grain refinement.
  - Austenite's critical temperature to adjust the properties to the desired ones in the final product and also to the available processing equipment:
    - Hot rolling process: The recrystallisation stop temperature.
    - Reheating process: The grain coarsening temperature.
    - Cooling process: The transformation temperature.
- To drop the transformation temperature.
- To produce precipitation hardening of the ferrite [78].

Figure 7. Conceptual map of the first parameters to be controlled for tough MA steels.

2.2.3.1. HOMOGENISATION

The as-cast microstructure in MA steels is typically heterogeneous with a wide range in microstructural scale. Re-austenitizing (homogenisation) helps to reduce the heterogeneities to obtain a uniform distribution of the alloying elements. Heating of the steel is undertaken at a temperature that dissolves the carbides and carbon enriched zones, with sufficient soaking time to allow the diffusion of carbon and other alloying elements to be as uniform as possible. Carbon has a larger diffusion coefficient compared to other alloying elements such as chromium (Figure 8).

Thus, the diffusion of carbon takes a relative short time, varying from a couple of seconds in very fine austenite grains to a few hours in very coarse ones. The diffusivity of elements improves as the temperature increases up to close to the melting point[44], but as temperature increases the austenite grain size grows rapidly. For example Zrnik et al.[77] found that a reheating temperature of 1150^{0}C produces better mechanical properties in microalloyed steels with Nb-Ti additions than a reheating temperature of 1240^{0}C. At this higher temperature, they found that the austenite grain coarsening in the samples was a greater factor than the precipitation strengthening.

The time taken for the steel to attain its temperature in the furnace depends on its thickness. Soaking times recommended for 815^{0}C are listed in Table 5, but a general rule based on practice says that the required time for the steel to heat through is 1 hour per inch of thickness [79].

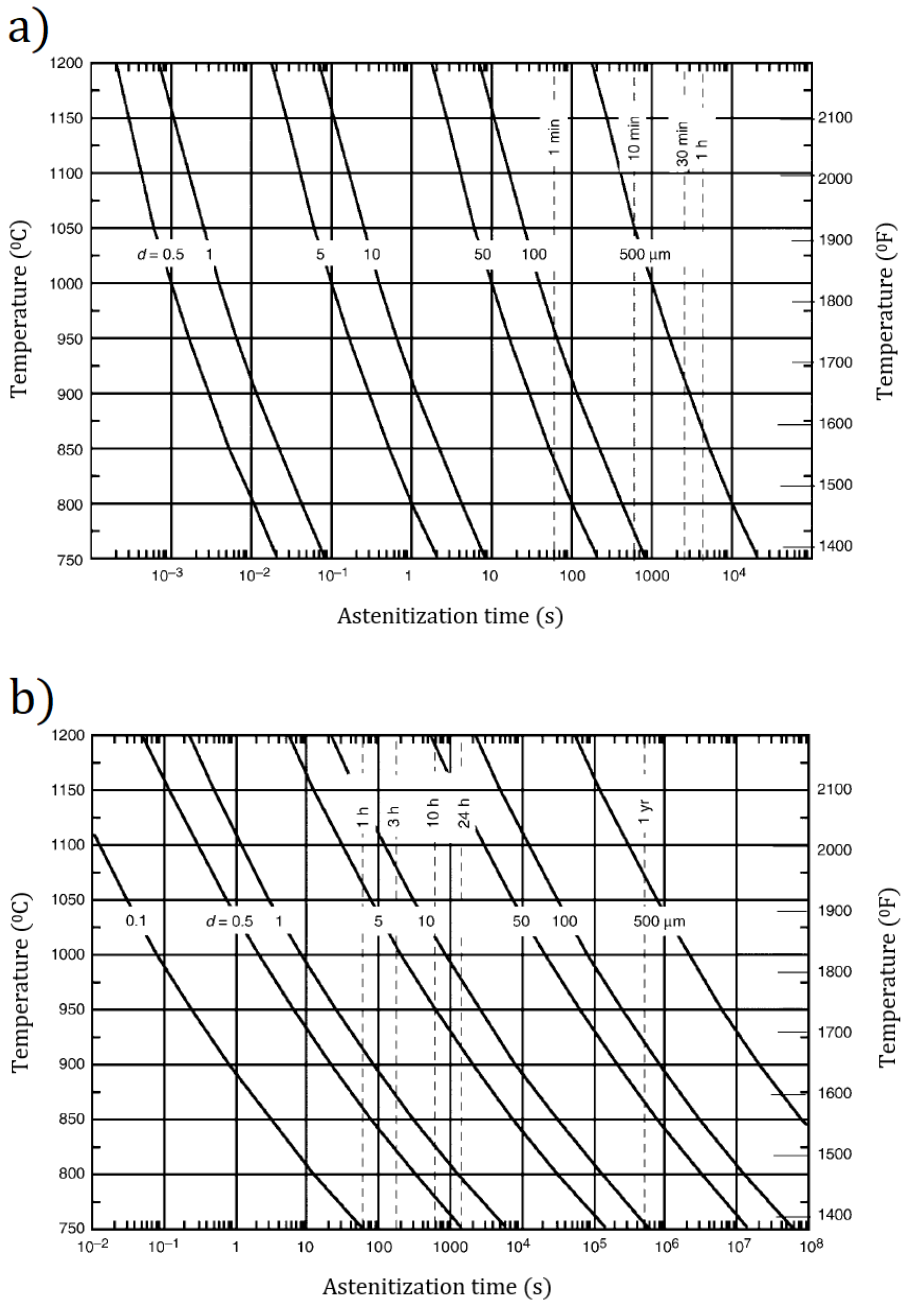

Figure 8. Time required to diffuse d distances in austenite, depending on the temperature for a) Carbon, b) Chromium [79].

Thickness (Inches)	Time of Heating to Required Temperature (h)	Soaking Time (h)
Up to 1/8	0.06 to 0.12	0.12 to 0.25
1/8 to 1/4	0.12 to 0.25	0.12 to 0.25
1/4 to 1/2	0.25 to 0.5	0.25 to 0.5
1/2 to 3/4	0.5 to 0.75	0.25 to 0.5
3/4 to 1	0.75 to 1.25	0.5 to 0.75
1 to 2	1.25 to 1.75	0.5 to 0.75
2 to 3	1.75 to 2.25	0.75 to 1
3 to 4	2.25 to 2.75	1 to 1.25
4 to 5	2.75 to 3.5	1 to 1.25
5 to 8	3.5 to 3.75	1 to 1.5

Table 5. Approximate soaking time for full austenitisation depending on the thickness [80].

2.2.3.2. AUSTENITE GRAIN SIZE CONTROL

Particles restrict austenitic grain growth. For a boundary to move beyond a particle, the grain boundary must expand its superficial area the same as the particle's superficial area (Figure 9). The particle produces a pinning force on boundary motion. This force is the result of the increased energy product of the increased grain boundary area. A relation between the matrix grain radius *R*, assumed as spherical, and the pinning particles volume fraction *f* and radius *r* was derived by Zener[81] in 1948 (Equation 4). After that, more models have been derived including more realistic parameters, that is the case of Gladmand[82,83] (Equation 5) who said that the grain geometry was more like a tetrakaidecahedron instead than a sphere but correlated to an effective grain radius R_0, and including the size advantage of a growing grain over its neighbours (R/R_0).

Second-phase particles coarsen with increasing temperature until they dissolve in the solution, leading to rapid grain growth. This is called secondary recrystallisation because of the similitude of its kinetics with recrystallization[84].

Silicon used to be popular as deoxidizing addition for steels, but this addition does not produce second-phase particles that effectively inhibit the austenite grain growth. Aluminium also is used to deoxidize steels limiting gas evolution by the formation of oxides that float out of liquid steel, creating a quiet or "killed" bath of liquid solution, giving the name *Aluminium-killed steels.* Figure 10 shows the number of austenite grains per square inch (also the ASTM number) of coarse-grained steel deoxidized with silicon and fine-grained aluminium-killed steel. At low austenitising temperatures, aluminium-killed steel does not present a relevant grain growth until a specific temperature at which the austenite grain size increases rapidly. This behavior is consistent with the described secondary recrystallization, and that temperature is the one at which precipitation responsible for the pinning effect dissolves. Conversely, in coarse-grained steel the average grain growths continuously even at relatively low austenitising temperatures.

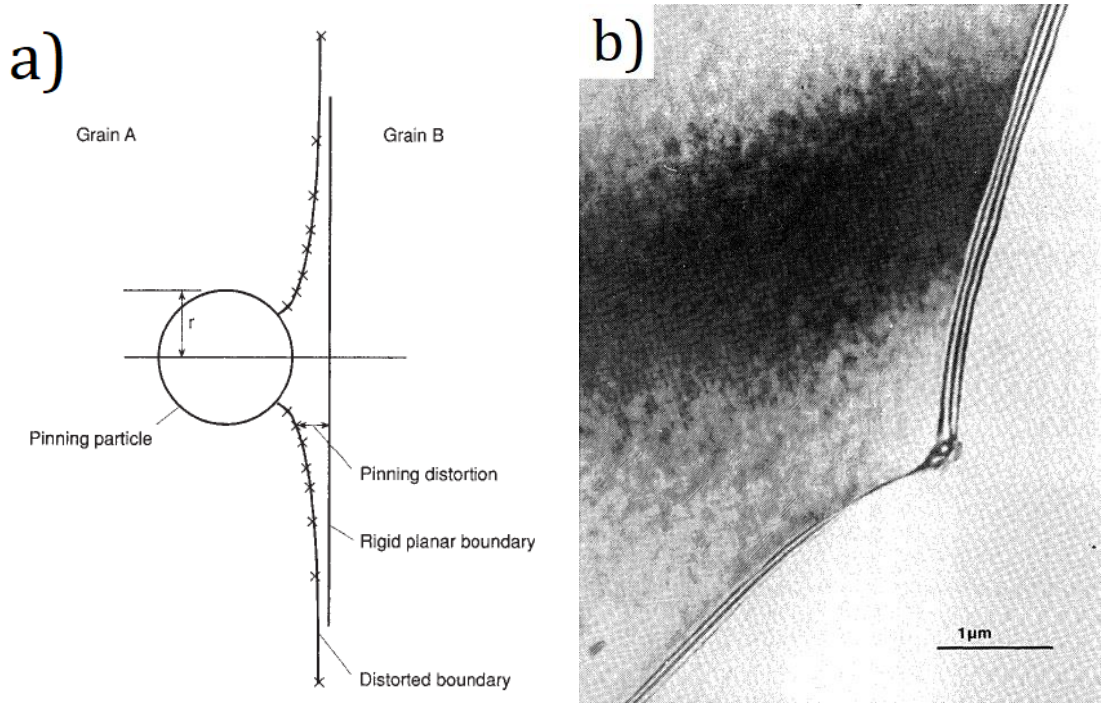

Figure 9. a) Scheme of the grain-boundary pinning produced by a second-phase particle[82], b) Transmission electron microscopy of an alumina particle producing pinning of high-angle grain boundary in aluminium[85]

$$R = \frac{4r}{3f} \qquad \textit{Equation 4}$$

$$R_0 = \left[1 - \frac{4R}{3R_0}\right]\left(\frac{r}{f}\right) \qquad \textit{Equation 5}$$

Some aluminium remains in the solid solution and some more as oxide inclusions. The remaining aluminium in solid solution brings austenite grain size control. Because of its high solubility in austenite, producing aluminium nitride crystal formation (AlN) in austenite. This is described by Equation 6 where $\underline{Al}$ and $\underline{N}$ are the amount of dissolved aluminium and nitrogen in austenite, which are a function of the solubility product [%Al][%N] and temperature as shown in Equation 7[86]. the inverse proportion of the product [%Al][%N] against the reciprocal of the temperature is shown in Figure 11, reflecting the tendency of AlN precipitation at low austenitising temperatures.

$$\underline{Al} + \underline{N} = AlN \qquad \textit{Equation 6}$$

$$\log[\%Al]\,[\%N] = -\frac{7400}{T} + 1.95 \qquad \textit{Equation 7}$$

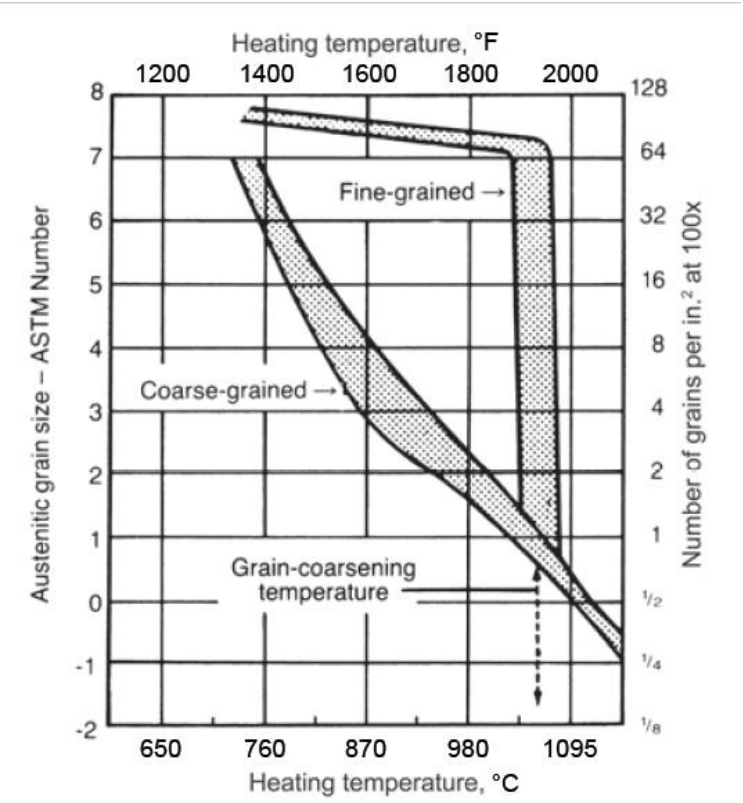

Figure 10. Austenite grain size of fine-grained and coarse-grained steels as a function of austenitising temperature[87].

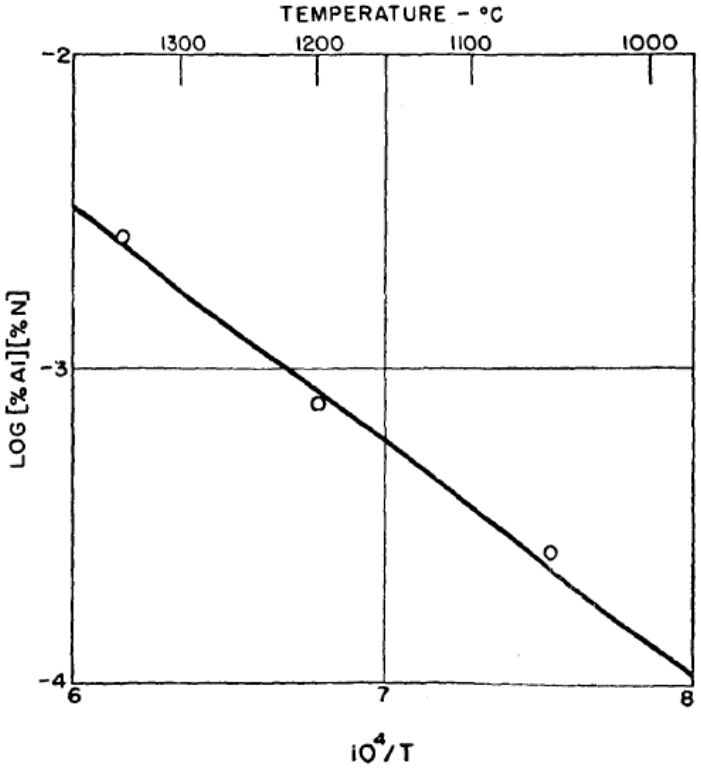

Figure 11. The solubility product of AlN in austenite as a function of the temperature[86].

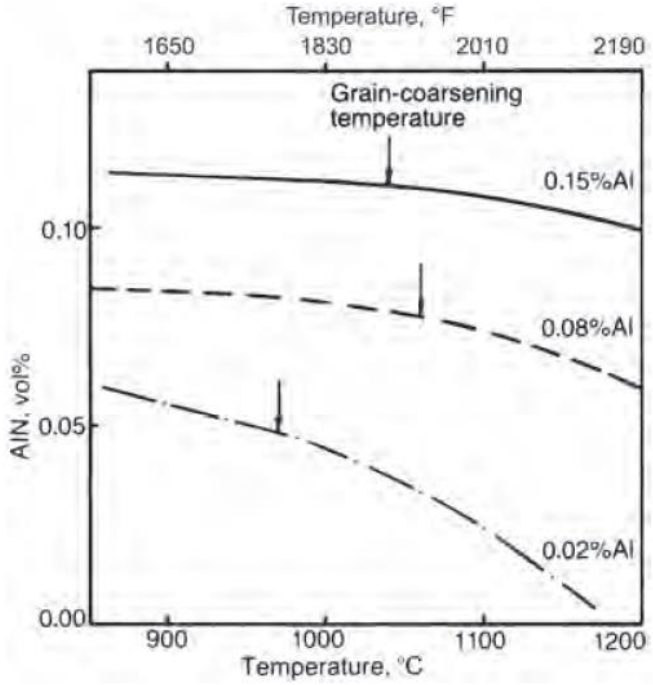

Figure 12. AlN volume fraction in mild steel as q function of temperature[88].

Figure 12 presents the AlN volume fraction in steel containing 0.01% N and 0.15% Al. It is observed that the higher volume fraction of AlN for those three steels corresponds to the steel with 0.15% Al content, but its grain-coarsening temperature is lower than for the addition of 0.08% Al. This is attributed to coarser AlN particles from solidification and hot working rather than the solution of aluminium nitride particles and/or any coarsening effect while the austenitizing treatments.

Using the same principle of aluminium-killed steels, other alloying elements are added to MA steels for austenite grain refinement, such as Nb, V, and Ti. To evaluate the precipitation fraction of a compound (XY_n) for austenite grain size control, an approach based on reactions between substitutional (*X*) and interstitial (*Y*) elements in austenite is given as:

$$\underline{X} + n\underline{Y} = XY_n \qquad \textit{Equation 8}$$

In Equation 8, the underlining terms indicate that the respective element is in solution in austenite. In addition, common substitutional elements in MA steels are V, Nb, Ti, Al, and B, whereas interstitials are carbon and/or nitrogen[89]. To know the solubility product dependence of the temperature for MA steels, the same expression as for aluminium-killed steels can be used but written as Equation 9.

$$\log[\%X]\,[\%Y]^n = \frac{-A}{T} + B \qquad \textit{Equation 9}$$

$\%X$ and $\%Y$ are the wt% of substitutional and interstitial elements dissolved in austenite respectively. *A* and *B* are constants determined experimentally or estimated from free-energy data. *T* is the temperature in Kelvin. Table 6 lists the carbides, nitrides, and carbonitrides and their respective temperature dependence. Figure 13 shows them as a function of temperature in austenite. All decrease with decreasing temperature, meaning that the austenite will become supersaturated with the elements and precipitation occurs. The higher solubilities correspond to V and Nb compounds.

Figure 14 shows how the addition of different elements to a plain carbon suppress the austenitic grain growth[90]. The plain carbon steel (marked as C-Mn in the chart) with no particle dispersions has a continuous increase of its austenite grain size with increasing temperature. The rest of them show suppression of grain growth at relatively low temperatures. Titanium Nitride is a very stable precipitate, no relevant grain coarsening of austenite was observed even at temperatures in a higher range than the typical hot work and forging[91]. on the contrary, other particles such as vanadium carbonitride precipitates derived from high solubility substitutional elements (V) dissolve at low temperatures, showing there the discontinuous grain coarsening.

Figure 15 shows how a group of Nb-containing steels have different temperatures at which the solubility is exceeded. The higher the Nb content, the higher the temperatures at which austenite grain shows discontinuous grain coarsening.

Solubility product	$\log[\%X]\,[\%Y]^n$
$[\%Al][\%N]$	$\frac{-6770}{T} + 1.03$
$[\%B][\%N]$	$\frac{-13970}{T} + 5.24$
$[\%Nb][\%N]$	$\frac{-10150}{T} + 3.79$
$[\%Nb][\%C]^{0.87}$	$\frac{-7020}{T} + 2.81$
$[\%Nb][\%C]^{0.7}[\%N]^{0.2}$	$\frac{-9450}{T} + 4.12$
$[\%Ti][\%N]$	$\frac{-15790}{T} + 5.40$
$[\%Ti][\%C]$	$\frac{-7000}{T} + 2.75$
$[\%V][\%N]$	$\frac{-7700}{T} + 2.86$
$[\%V][\%C]^{0.75}$	$\frac{-6560}{T} + 4.45$

Table 6. Solubility products' temperature dependence for common carbides, nitrides, and carbonitrides in MA steels[89].

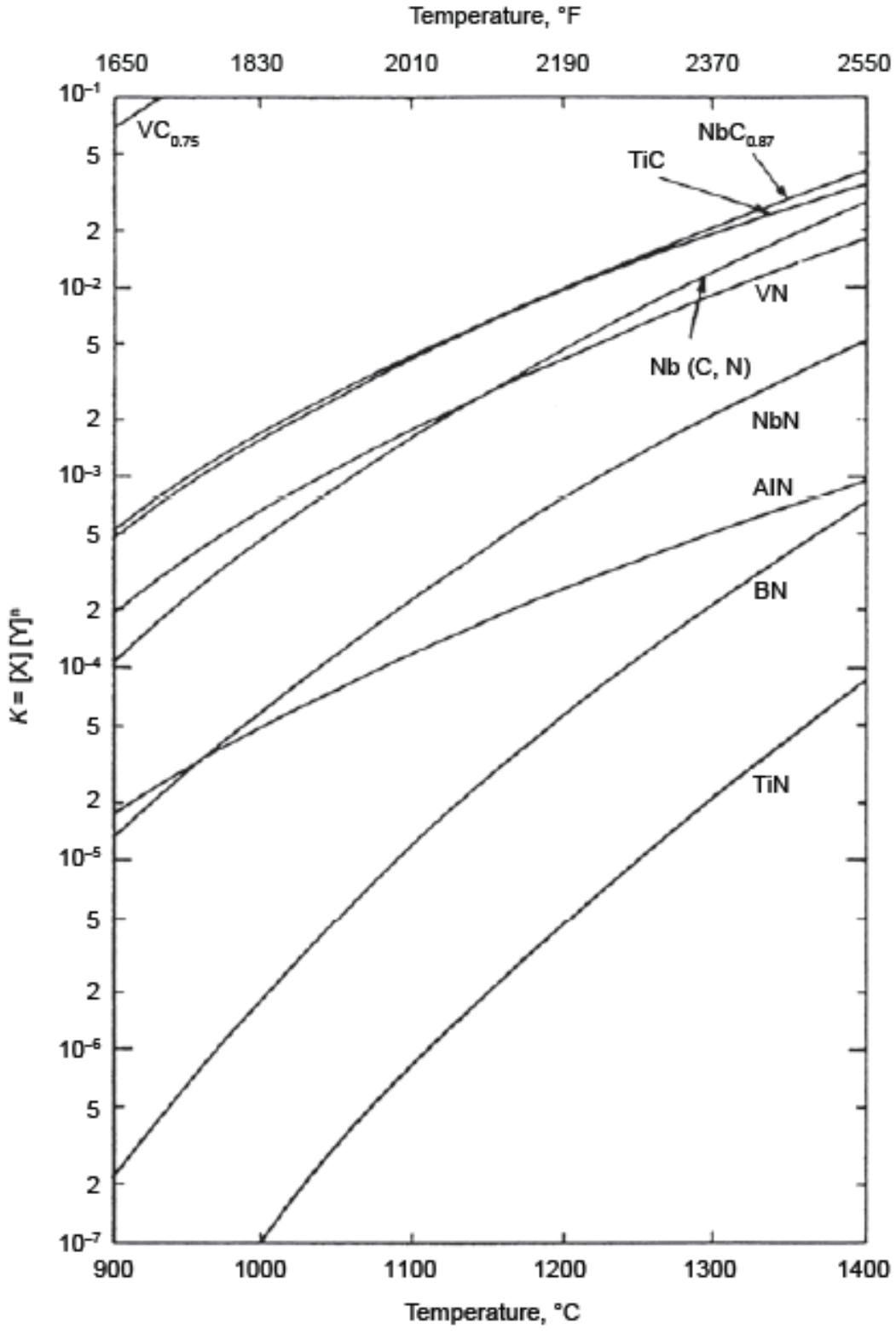

Figure 13. Solubility products as a function of the temperature in austenite[89].

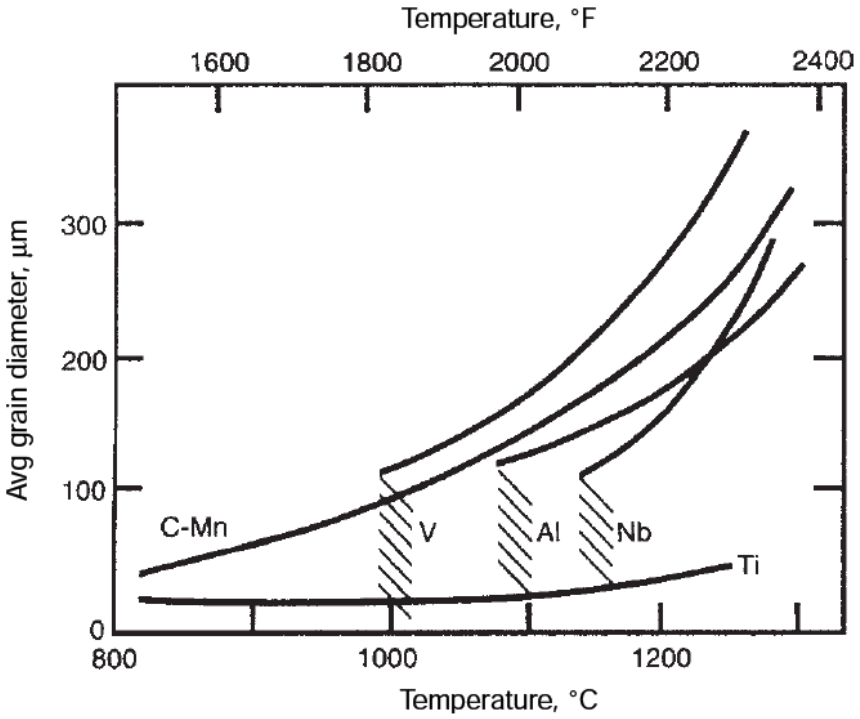

Figure 14. MA steels' austenite grain coarsening depending on the element additions[90].

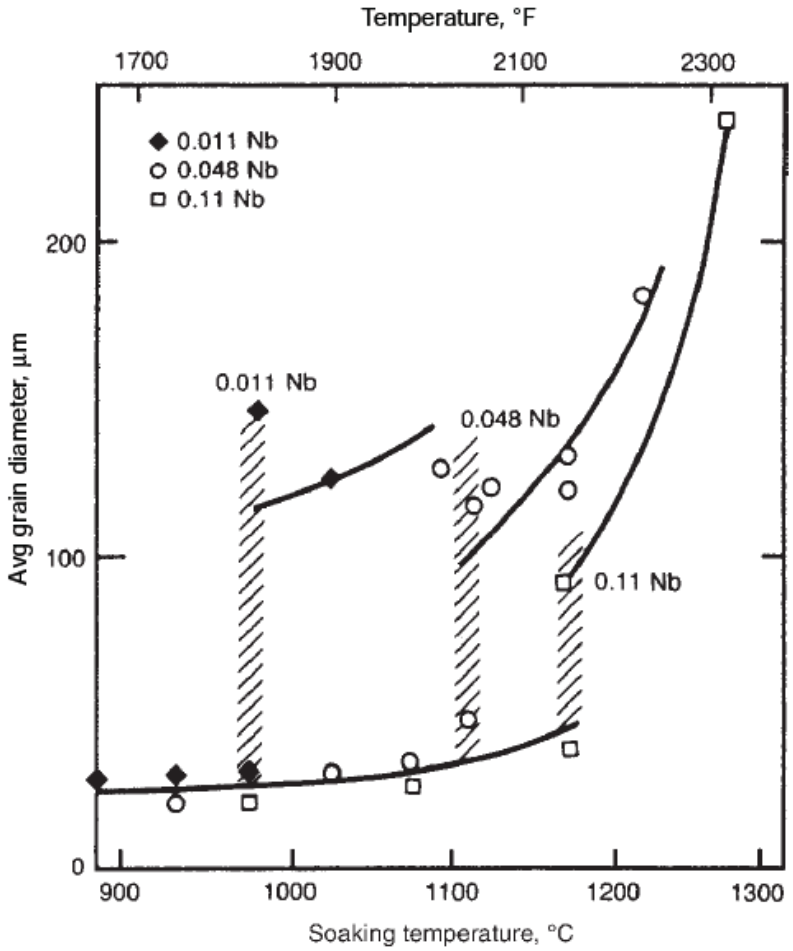

Figure 15. Austenite grain-coarsening in MA steels with different amounts of Nb[92].

2.2.3.2. HOT-ROLLING

The austenite grain size and the potential nucleation sites for transformation to ferrite will determine the properties of the final product. Hot rolling in the austenite field aims to refine the austenite grain size with increasing strain, and also to introduce a high density of nucleation sites for ferrite transformation[93]. All these are introduced by rolling reduction, which eventually reaches a limit value[94].

By hot rolling, the original equiaxed austenitic grains deform and elongate by dislocation motion and multiplication. The remaining strain energy from the dislocation defect structure conduct recrystallization [krauss]. Figure 16 shows a diagram of how the rolling process produces changes in the microstructure. Two main types of recrystallization can occur:

1) Static recrystallization: occurs after passing through the rolls.
2) Dynamic recrystallization: occurs while deformation in the rolls.

The most common types of rolling schedules are:

1) Recrystallization Rolling: the austenite grains are progressively refined to as small as 20μm while they are entirely recrystallised between passes.
2) Controlled rolling: where a considerable reduction occurs under the austenite recrystallisation stop temperature. As a result, pancaked austenite grains have a conditioned structure with a minimized effective spacing of ferrite nucleation sites. In other words, the production of fine-grained MA steels with ferritic microstructures from unrecrystallized austenite is referred as controlled rolling[95].
3) Intercritical rolling: The last passes of the rolling process take place in the $\alpha + \gamma$ phase field. The untransformed austenite receives very large deformation while the ferrite is deformed as it progressively forms, producing fine subgrain size[77].

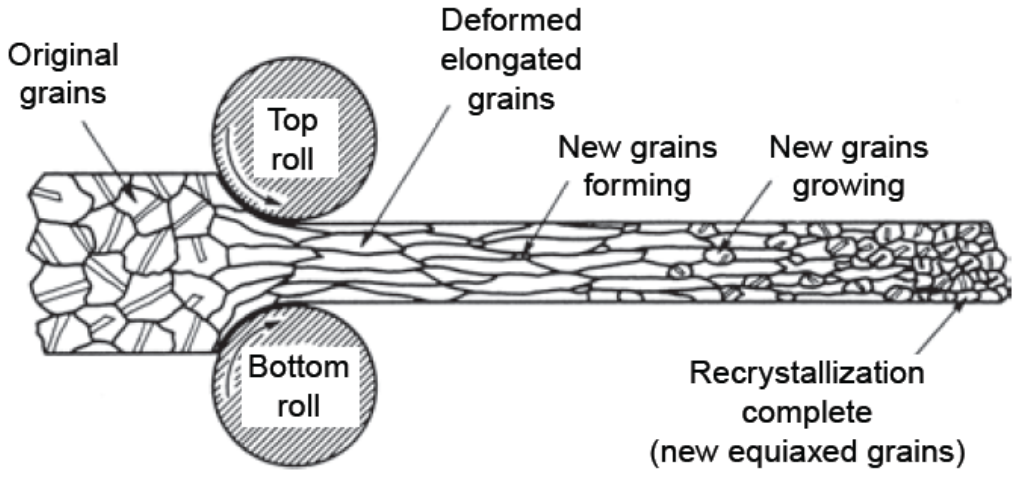

Figure 16. Scheme of austenitic microstructure's changes produced by hot rolling[96].

Controlled rolling aims to produce steels with a fine grain size of polygonal and/or acicular ferrite, and also bainitic structures[97]. It is aimed at promoting the nucleation of ferrite in the austenite grain interior, as well as at the grain boundaries. This contrasts conventional hot-rolled steels where the

ferrite nucleation occurs exclusively at the austenite grain boundaries, producing coarser microstructures[10].

In the absence of recrystallisation during hot rolling, austenite grains deform and elongate by conventional deformation mechanisms[98]. Strain induced precipitation of Nb(C, N) occurs on dislocations and grain boundaries before the recrystallization below T_{RXN}. The precipitates provide Zenner pinning and act as grain growth barriers and as effective nucleation areas for ferrite, resulting in a transformation of very fine ferrite grain size (~2-5µm) [77] with excellent combination of strength-plasticity.

Two main parameters can control precipitation strengthening and improve toughness during the controlling rolling process: the coiling temperature, and the total deformation[99]. Studied by Kozasu et al.[93], the temperature of deformation in MA steels shows the important influence on the final microstructure. If it is above 1000^0C, coarse recrystallized austenite grains are normally developed, resulting in upper bainite and coarse ferrite. In addition, this temperature is too high to produce strain-induced precipitation due to the quick annihilation of dislocations. Deformation performed below the temperature at which recrystallisation stops T_{RXN}, between 1000 and 900^0C transforms into fine ferrite. This is a result of the refined pancaked austenite grains obtained from the rolling which retain the deformation structures such as deformation bands which are potential sites for ferrite nucleation. Finally, the deformation in the $\gamma + \alpha$ region can result in equiaxed ferrite grains plus other structures such as bainite or martensite, when the rolling is just above the A_{r3}.

2.2.3.3. STATIC RECOVERY, RECRYSTALLIZATION AND GRAIN GROWTH

Deformed materials store energy derived from point defects and dislocations. This stored energy can be reduced by recovery and recrystallization.

2.2.3.3.1. RECOVERY

In recovery only partial rearrangement of the dislocations occurs with a minimum effect on the grain boundaries of the deformed structure. Recovery demands much lower driving force than recrystallisation and generally occurs more rapidly[100]. This phenomenon can be observed by transmission electron microscopy and can be seen as a stress relaxation in mechanical tests[101,102].

Figure 17 shows the evolution of the dislocation structures during the recovery process in a deformed material, showing dislocations as "T" and grain boundaries as solid lines. In stage 1, dislocation rearrangement occurs through climb and cross-slip resulting in the formation of "cell-walls" and a cell structure, as shown in Figure 18. In stage 2, further dislocation rearrangement occurs leading to the formation of dislocation cell blocks. In progressing through stage 3 to 4, the dislocation walls have developed into subgrain boundaries ultimately leading to a homogeneous structure of equiaxed ultrafine grains (stage 5)[103,104]. While the substructures change in recovery, the yield stress drops and the work hardening increases.

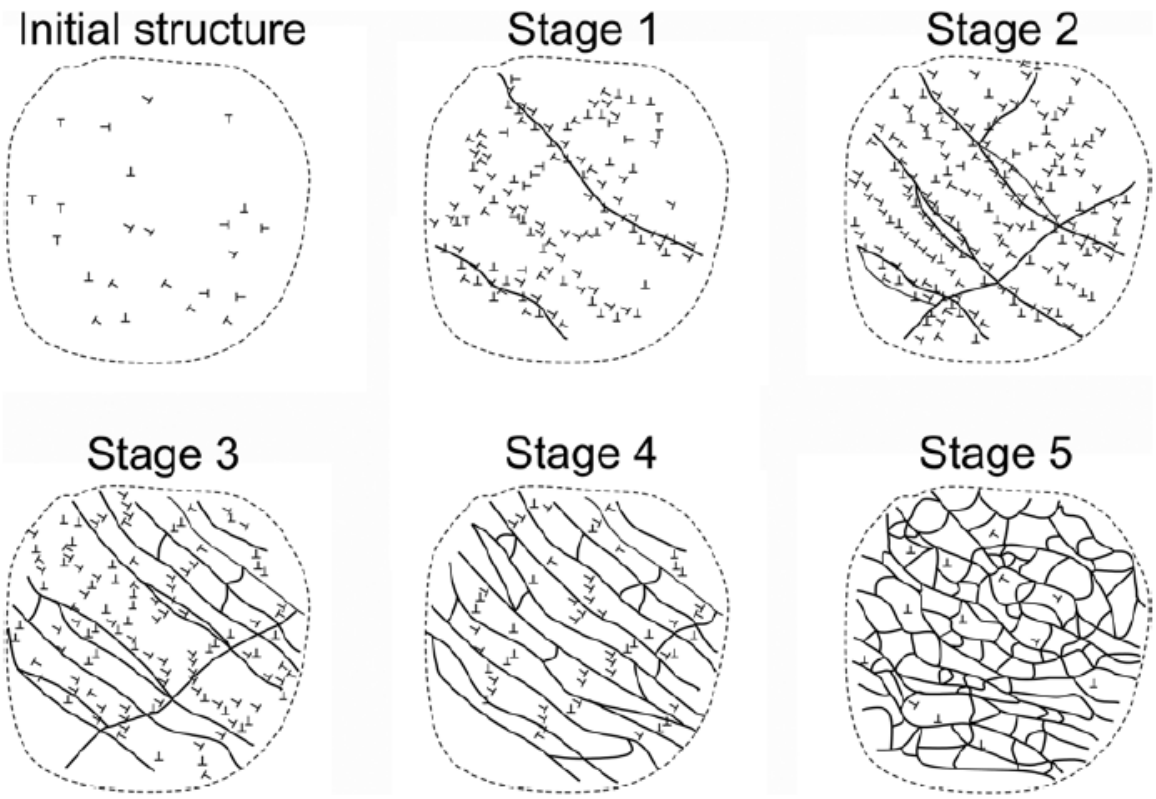

Figure 17. Schematic illustration of how the grain refinement is achieved during recovery[103].

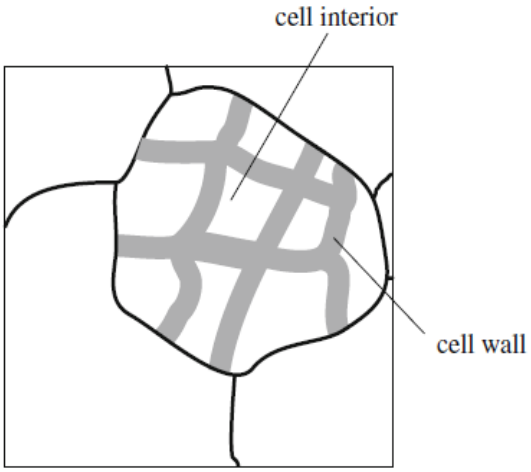

Figure 18. Scheme of a cell-like structure in a grain of a deformed material[105].

2.2.3.3.2. RECRYSTALLIZATION

The recrystallisation process consists of the nucleation and growth of new strain-free grains with a low dislocation density, consuming the deformed and/or recovered microstructure[106,107]. This process can occur during deformation or afterwards, when sufficient driving force, i.e. stored energy is present. In materials with low stacking fault energy dislocation mobility is low and cross-slip is restricted leading to rapid work hardening and dislocation structures that are resistant to recovery. In this case, recrystallisation occurs with very little recovery of dislocation structure[108].

Elongated grains provide closely spaced grain boundaries where ferrite crystals nucleate[98]. There are two distinguishable stages: 1) The nucleation of new grains in the microstructure, and 2) their subsequent growth, which replaces the deformed structure[109]. These stages are controlled by the annealing parameters and how they promote a larger fraction of nuclei or a quicker nucleation rate[110,111].

With high annealing temperature, recrystallisation occurs after deformation when the pre-strain is below the critical value for dynamic recrystallisation and above the critical value for static recrystallisation. The recrystallization temperature was defined as the temperature at which 50% of recrystallisation is achieved in the material at a constant time[14,112,113]. This recrystallisation temperature is inversely proportional to the deformed strain and annealing time[114], correlated by the Arrhenius equation[114].

Mechanical properties and metallography examination can be used to quantify recrystallization, which is dependent on the annealing temperature and the holding time [115]. Figure 19 shows how the true tensile properties of 15R30V steel change with temperature after deformation. The higher the temperature, the lower the true strain of the steel. In steels with low annealing temperature, the true stress drops after the maximum value which is an effect of the dynamic recrystallisation while the sample's deformation[115].

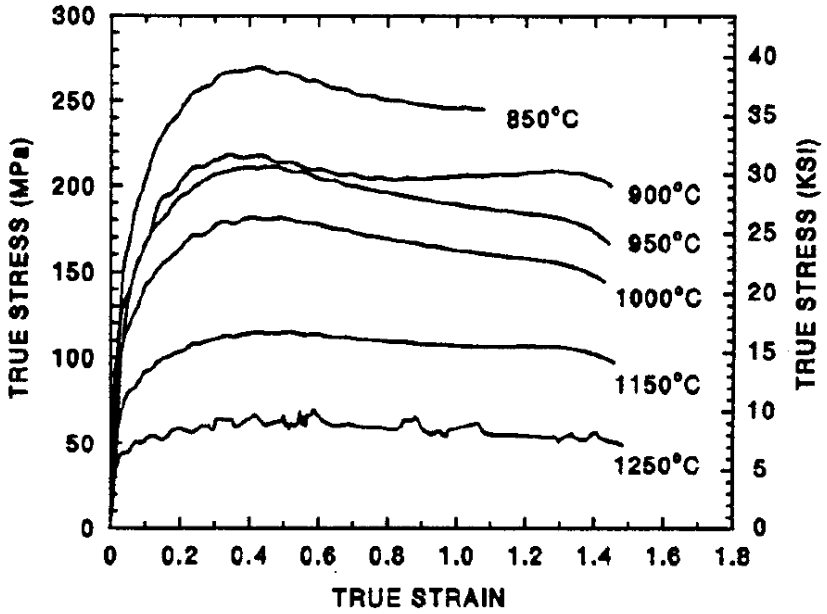

Figure 19. True strain vs true stress curves at various temperatures for a 15R30V steel deformed at 22 s^{-1} [115].

Alloying additions are often made to MA steels to retard recrystallisation through solute drag and precipitate pinning during thermomechanical processing[116]. In MA steels the volume fraction of recrystallisation (X_v) can be calculated with Avrami equation (Equation 10), where $t_{0.5}$ and *n* are the time when recrystallised volume fraction = 50% and the Avrami exponent respectively[117].

$$X_v = 1 - exp\left[(-ln2)\left(\frac{t}{t_{0.5}}\right)^n\right]$$

Equation 10

It was reported that two kinds of driving force act during the recrystallisation: the one for recrystallisation F_R, and the one of pinning from precipitation F_P[118]. If $F_R < F_P$, the recrystallisation will be fully retarded by precipitates, but if $F_R \gg F_P$, recrystallisation could occur, and as a result, the dislocation density reduces and the number of nucleation sites for precipitation decreases too. This interaction between the precipitation kinetics and the recrystallisation kinetics is plotted in the recrystallisation-precipitation-time-temperature (RPTT) curve. Figure 20 illustrates the RPTT for a low-carbon aluminium-killed steel containing 1.3 pct Mn, in which precipitation is thermodynamically impossible over T_0 (which is the precipitates dissolution temperature). Complete recrystallization occurs before precipitation starts with no interaction. Precipitation takes place between P_S^D and P_S curves in the recrystallised austenite. Any such precipitation is preceded by recrystallisation processes defined by the R_s and R_f (the recrystallisation start and finish curves). The recrystallisation stop temperature (T_R) is the intersection of P_S^D and R_s curves. Figure 21 shows how increasing the elements' content in solution increases T_R[119].

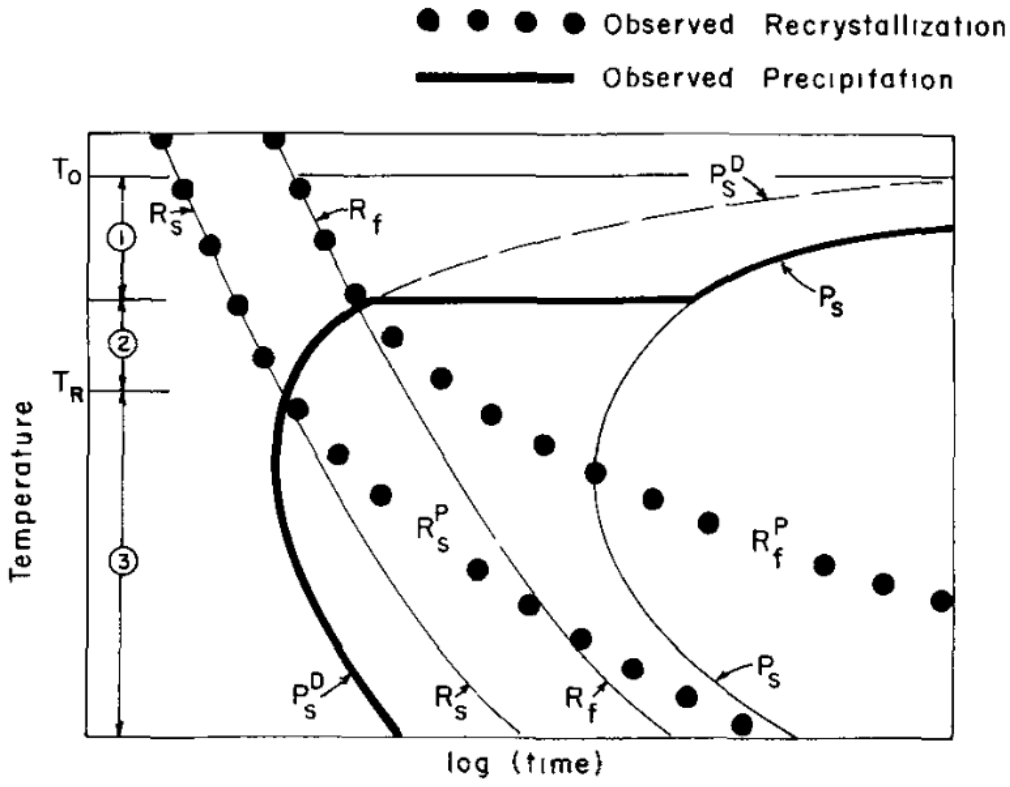

Figure 20. recrystallisation-precipitation-time-temperature (RPTT) curve for a low-carbon aluminium-killed steel containing 1.3 pct Mn[118].

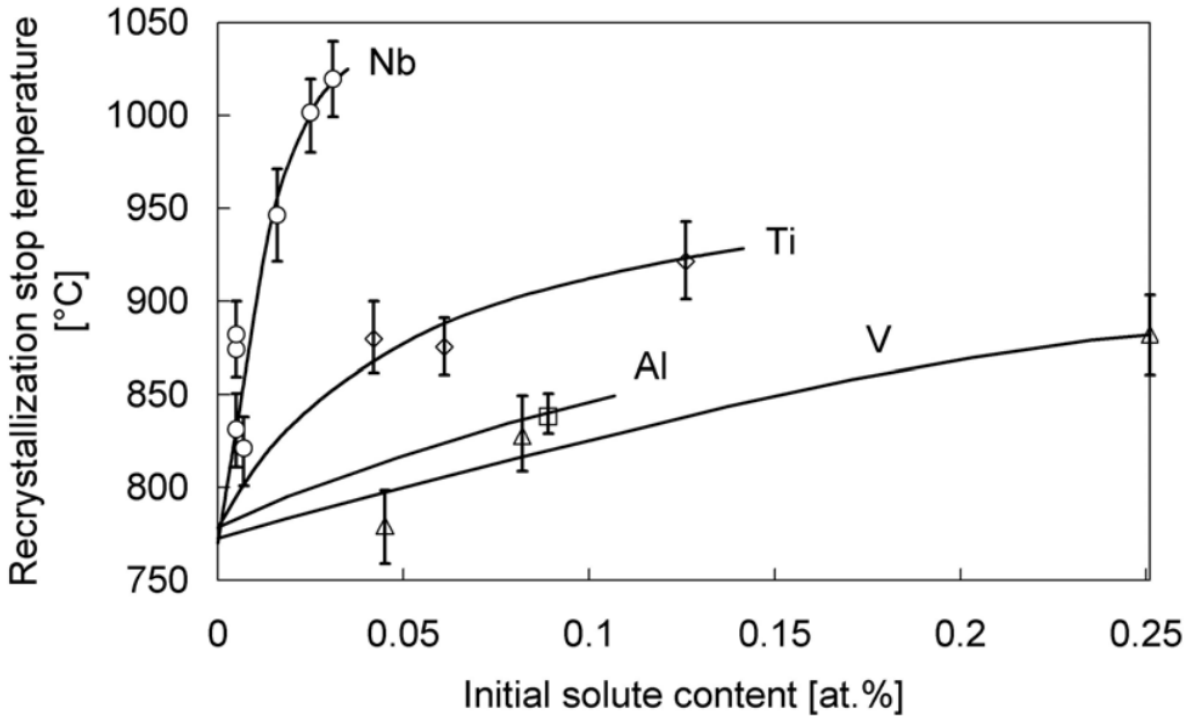

Figure 21. No-recrystallisation temperature as a function of the initial solute content[119].

2.2.3.3.3. GRAIN GROWTH COARSENING

Before thermomechanical processing MA steels need to be reaustenitised at a temperature where the precipitates are dissolved and allow the elements to be taken into solution. Of course, dissolution of the precipitates removes grain boundary pinning resulting in much faster grain growth rates[120,121]. Grain growth usually occurs very fast at temperatures between 1100 and 1200^{0}C and is more sluggish at temperatures below the 1100^{0}C.

Grain growth is a coarsening phenomenon that is not desirable in steels. The main mechanism by which grains grow is from curvature-driven growth[122]. The grain boundaries move towards their curvature centre. Large grains will grow consuming small grains and reduce the grain boundary area per unit volume [123] causing adverse effects on the mechanical properties that it involves.

In general, grains may coarsen by any of these two phenomena: 1) normal primary coarsening, which is observed as a gradual increase in grain size with temperature[124]. 2) Abnormal grain growth, also known as secondary recrystallization, is the grain growth where some selected grains grow to large dimensions consuming other finer grains around them[125]. This last one occurs at high temperatures when normal grain growth is obstructed, and the particle dispersion is unstable[126]. The abnormal grain growth stops when the grains are thermodynamically stable because the driving force for grain growth stabilises the pinning force applied by the particles on the moving grain boundary [127].

Khaki et al.[128] identified the onset of abnormal grain-coarsening for MA steels with 0.04wt% of Nb at 1250^{0}C. Figure 22 shows that the prior-austenite grain size increases slowly from 1000 to 1250^{0}C, but after that, the increase is very rapid. This is attributed to the easy movement of the austenite grain

boundaries after the dissolution of niobium carbides and nitrides, which acts as Zenner pinning barriers.

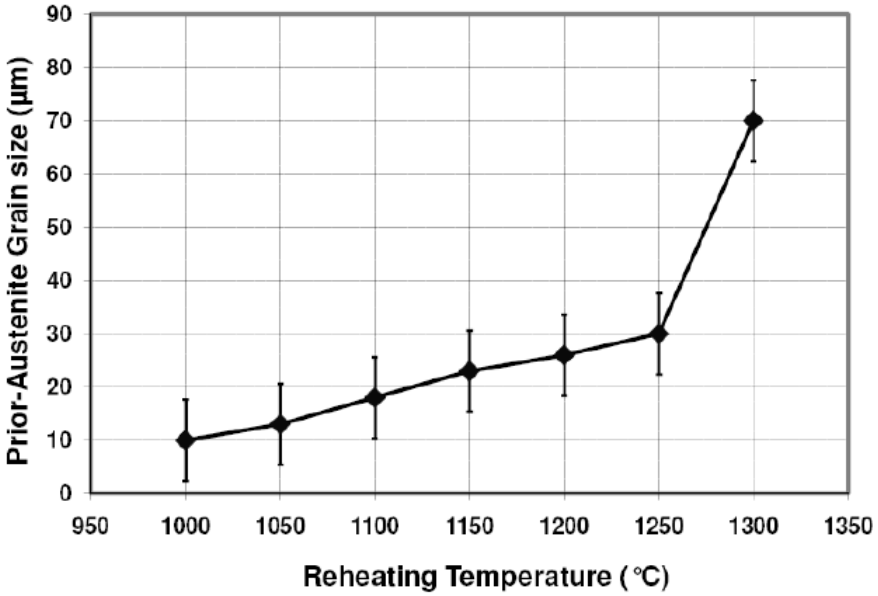

Figure 22. Austenite grain size of MA steel as a function of the reheating temperature[128]*.*

Conditions for abnormal grain growth were presented by Gladman in 1992[129]. The correlation between the pinning force and the driving force is given by Equation 11. r_g is the critical particle size of precipitates along the borders, R_0 is the radius of the matrix grains, f is the volume fraction and Z is the size advantage of the specific grain over that of its neighbours (=R/R_0). The pinning force is given by f and the driving force given by R_0 and Z. Only those grains with a size advantage above this will grow. Eventually the impingement of such grains terminates the growth process.

$$r_g = \frac{R_0 f^{0.5}}{(3 - 4Z)} \qquad \textit{Equation 11}$$

The introduction of an array of less stable particles is capable of inhibiting grain growth even if grains attain a size advantage. Observations indicate that below the required temperature for complete dissolution of precipitates in the steels, grain-coarsening occurs. This means that while the temperature is increasing the particle within the steel grows to a critical radius where grain-growth starts (Equation 12) [125]. Grains with the largest size advantage would expand first, and the other large grains are pinned until more particle coarsening. r_r is the critical size for random particles.

$$r_r = \frac{3R_0 f}{\left(3 - {}^{4}/_{Z}\right)} \qquad \textit{Equation 12}$$

2.1.2.10. DILATOMETRY

Historically the heat treatment performed on steels used to be done in two different stages, firstly the austenisation and quenching to room temperature, and then reheating the alloy in the intercritical region ($\alpha + \gamma$) Figure 23. This is an inefficient practice, which has led to new heat treatments which incorporate both the solution and the precipitation treatments Figure 24. By avoiding the reheating in the middle of the two stages, a significant cost is saved in the industrial production process, especially in large scale production such as the automotive sector [130].

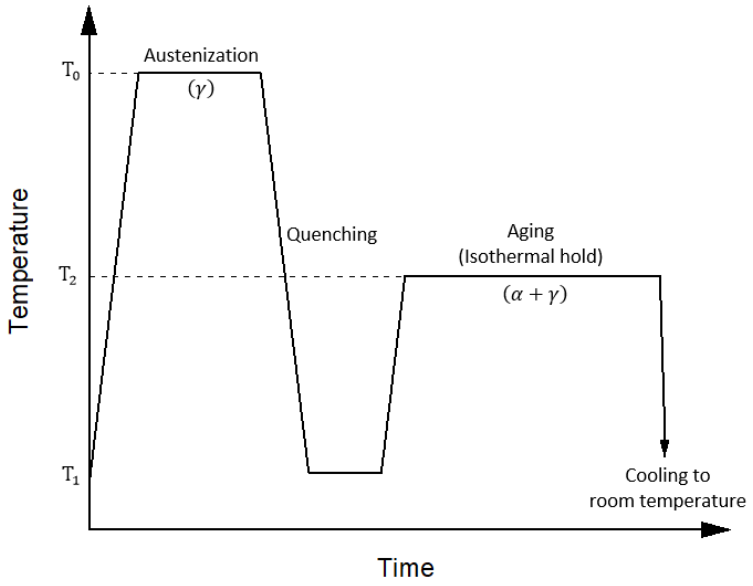

Figure 23. Conventional heat treatment divided in two stages to obtaining precipitation strengthening.

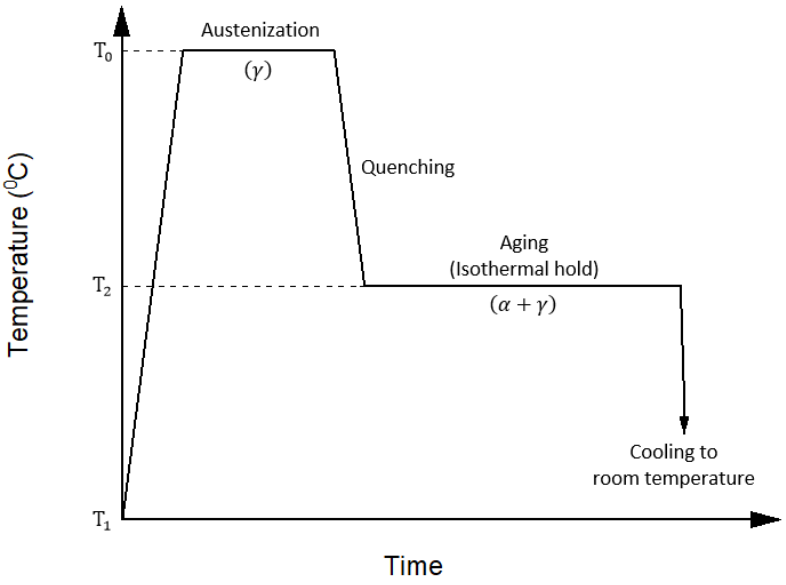

Figure 24. More recent heat treatment for precipitation strengthening with no reheating need.

To study proeutectoid phase transformations, the heat treatment requires particular precision to characterise the individual effects of parameters on properties, one of the more accurate techniques

used to achieve that is dilatometry. The length changes of normalised samples during cooling or heating are recorded. In steel, a shift in the direction and rate of length change vs temperature (contractions and dilatations) allows the temperatures where phase transformations take place to be defined[131].

The complete precipitation heat treatment consists of three principal steps: austenitisation between 1100-1200^{0}C, isothermal transformation below A_{e3} and water or iced brine quenching[132]. Firstly, the alloy must be heated to a temperature at which the alloy is a monophasic solid solution and held there for enough time to dissolve any dissolvable precipitates. That stage is well-known as *austenisation*. The alloy is then *quenched* with the aim of suppressing any precipitate formation resulting in a supersaturated solid solution. Finally, the *isothermal transformation* treatment involves maintaining the alloy at a temperature to get the formation of fine-scale precipitates within a ferritic matrix.

The cooling rate is an important parameter in determining phase transformation in MA steels, and therefore it is important to have accurate control with this technique. A faster cooling rate will lower the transformation temperature, which should give interphase precipitation on a finer scale and also the transformation induced dislocation density will be higher. However, there is a limit at which the $\gamma \rightarrow \alpha$ interface moves too fast to allow interphase precipitation, suppressing precipitation leading to a drop in the strength[133].

During the isothermal transformation ($\gamma \rightarrow \alpha$) the length changes proportionally to the sample's initial length concerning the formation of ferrite. This correlation can be expressed by Equation 13, where $\Delta L/L$ is the length change per unit length, *V* is the ferrite volume fraction, a_α is the lattice parameter of ferrite at the reaction temperature, and $\overline{a_\gamma}$ is the lattice parameter of austenite at the beginning of the reaction[134]. $\Delta L/L$ is relatively proportional to the volume fraction of formed ferrite. Thus, the dilatometric curves display in a direct way the volume fraction of ferrite as a function of time during the isothermal transformation (Figure 25)[23].

$$\frac{\Delta L}{L} = \frac{V\left[2(a_\alpha)^3 - \left(\overline{a_\gamma}\right)^3\right]}{3\left(\overline{a_\gamma}\right)^3} \qquad \textit{Equation 13}$$

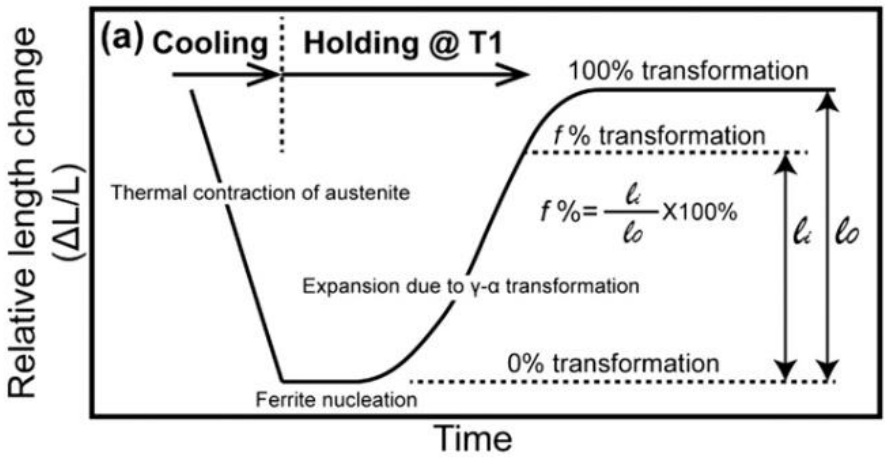

Figure 25. A Schematic dilatometry curve showing the expansion of the steel sample after the ferrite nucleation.

Ferrite (α) forms in in two main shapes, c. Allotriomorphic refers to shapes of crystals dictated by adjacent crystals and not by their own structure. In contrast, idiomorphic ferrite is where the shape is dictated by their own crystal structure with no influence of the surrounding grains[132]. Aaronson[135] complementary to the work of Dube[136], made a classification of the shapes of proeutectoid ferrite in isothermally transformed steels. Figure 26 shows these shapes, starting with a) grain boundary allotriomorph, b) extended into austenite grains, Widmanstätten needles nucleated on grain boundaries (b1) or on already formed precipitates at the grain boundaries (b2), c) Sawtooth Widmanstätten, which is similar to sideplates but with a larger angle, and (d) intergranular. Other structures such as idiomorphs (e) which usually nucleates at inclusions within the grains, but also can be found at the grain boundaries. And lastly, aggregates of ferrite precipitate crystals, massive structures form within the matrix grains. Knowing that the austenite grains form tetrakaidecahedrons [122], all these structures do not form in needle-shape but in large lath-shapes as shown by Kral and Spanos[137] in their reconstructions Figure 27. Which microstructure is found depend on the temperature at which the steels are soaked and the cooling rate (Figure 28).

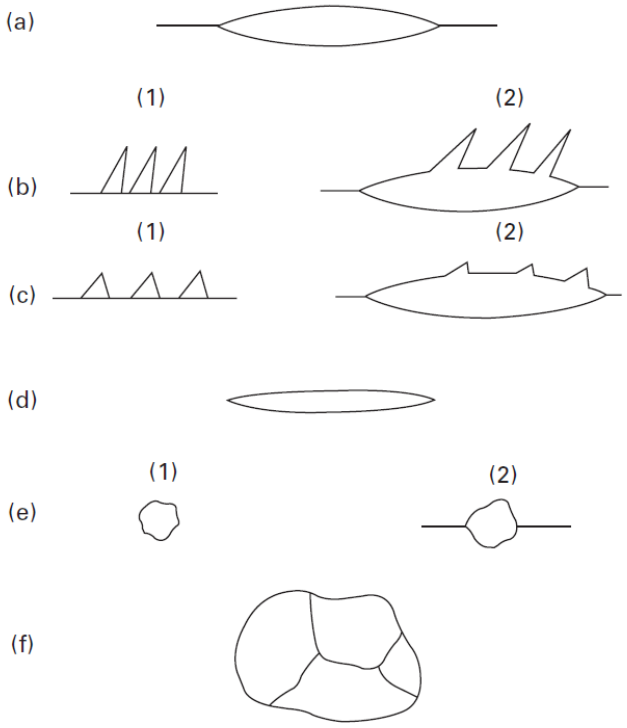

Figure 26. Dube-Aaronson morphological classification system of ferrite. Edited from [135].

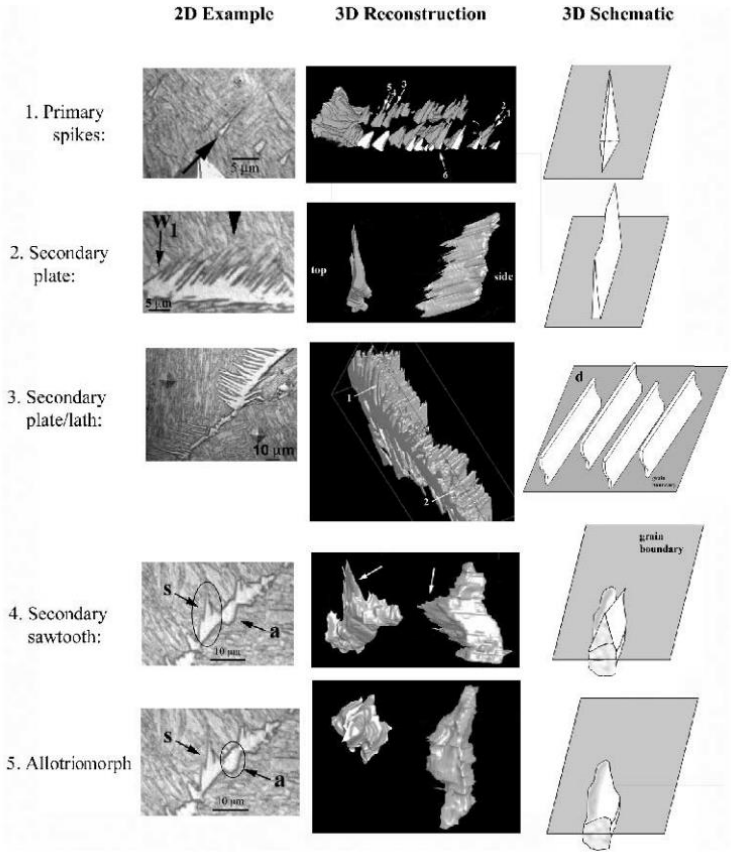

Figure 27. 3D reconstruction of proeutectoid ferrite structures[137].

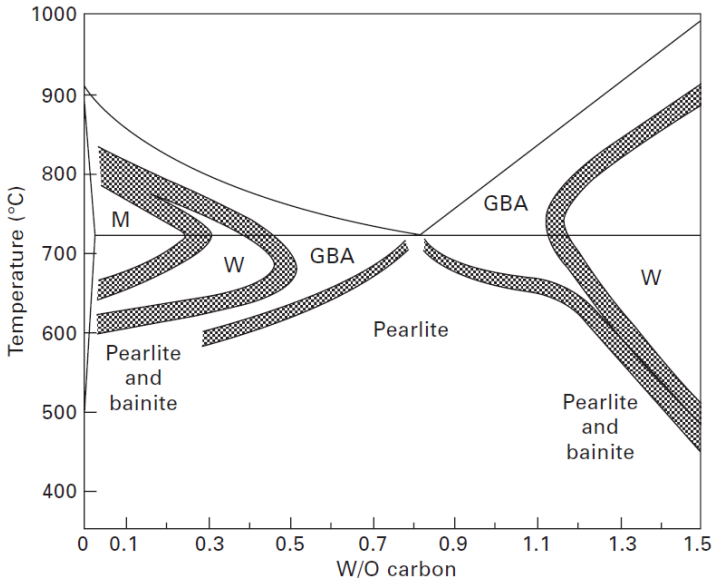

Figure 28. Temperature ranges in which the ferrite morphologies dominate at late reaction times for steel with austenite grain size~250-350μm Edited from [135]*. In this chart, M, W and GBA mean massive, Widmanstätten and grain boundary allotriomorphs respectively.*

2.1.2.11. PRECIPITATION STRENGTHENING

In addition to the solid solution and dislocation ($\Delta\sigma_d$) strengthening, precipitation ($\Delta\sigma_P$) strengthening represents an important component of the total strength of MA steels. To quantify the contribution the Orowan-Ashby model is usually used as it shows reasonable prediction of the observed strength in MA steels[138]. The strength contribution from precipitation hardening, $\Delta\sigma_P$, is given by Equation 14, proposed by Gladman[82]

$$\Delta\sigma_P[\text{MPa}] = 10.8\frac{\sqrt{f}}{d}ln(1630d) \qquad \textit{Equation 14}$$

Where *f* is the volume fraction and *d* is the particle diameter in µm. Clearly, the strength contribution is very important and is a strong function of several parameters such as composition.

For MA steels, the compositions are between 0.05 and 0.2% of carbon, between 0.6 and 1.6% of manganese, and around 0.1% for the other elements. Some of the most common second phases found in HSLA steels are listed in Table 7. These precipitates are a major contribution to the strength with reported yield strength of up to 1200 MPa with reasonable elongations of 5-10 % from interphase precipitation induced by isothermal transformation between 650 and 700^0C [139].

Principal Element (s)	Main Precipitates
Niobium	Nb(C,N), Nb_4C_3
Vanadium	V(C,N), V_4C_3
Niobium + molibdenum	(Nb,Mo)C
Vanadium	VN
Copper + niobium	Cu, Nb(C,N)
Titanium	Ti(C,N), TiC
Aluminum	AlN

Table 7. Common Precipitates in HSLA steels. edited from [140].

Precipitates also form after the $\gamma \rightarrow \alpha$ transformation in ferrite on dislocations and grain boundaries[44,141]. The precipitates' nucleation on dislocations is considered as strain energy relief from the high energy dislocation core[142]. Compared to atoms in the bulk, atoms in the crystal's surface have incomplete bounding, having a higher energy than the rest of the crystal's atoms. This strain energy introduced by a dislocation per unit length of dislocation line have been written as follows:

$$E_{elastic} = const.Gb^2 \qquad \textit{Equation 15}$$

Where the constant "const" can have values between 0.5 and 1.0, *G* is the sear modulus and *b* is the size of Burgers Vector. Gomez-Ramirez and Pound, like Cahn[142,143] agreed that the free energy to produce a nucleus in a system of unstable equilibrium with the matrix (ΔG^*) is not a function of the particles' shape. They also concluded the presence of meta-stable embryos on dislocations, making them great nucleation catalysts. Some further relations have been developed such as the one developed by Russel[144] in which the nucleation rate of carbonitrides of microalloying elements due to

controlled diffusion (J) is a function of the dislocation density (ρ), the lattice parameter of the matrix (a), the diffusivity (D_{MA}) and the concentration (X_{MA}) of the microalloying additions and inversely proportional to the temperature as follows:

$$J \cong \frac{\rho}{a_\gamma^3} D_{MA} X_{MA} \exp\left(-\frac{\Delta G^*}{kT}\right) \quad \text{Equation 16}$$

The kinetics of interfaces depend on the involved lattices structure and their relative orientations. When both crystals have approximately the same lattice parameter and the same structure is called the coherent interface (Figure 29 a)), only the composition changes from one phase to the other. When the precipitate and the matrix have different crystal structure, it is impossible for the entire precipitate to be coherent with the matrix. Completely incoherent interface occurs if there is no lattice matching of the two crystal structures[145].

Nucleation is a mechanism which wind down the energy of the local area, leading to minimum energy configurations. The poor bounding of the incoherent interface means a relatively high energy compared to coherent interface. Thus, incoherent grain boundaries provide excellent conditions for precipitates' nucleation[146]. Semi-coherent interfaces occur when the two crystal structures alloy full coherency, but a disorder in the form of wide spaced interfacial dislocations filling the discrepancy (Figure 29 b)).

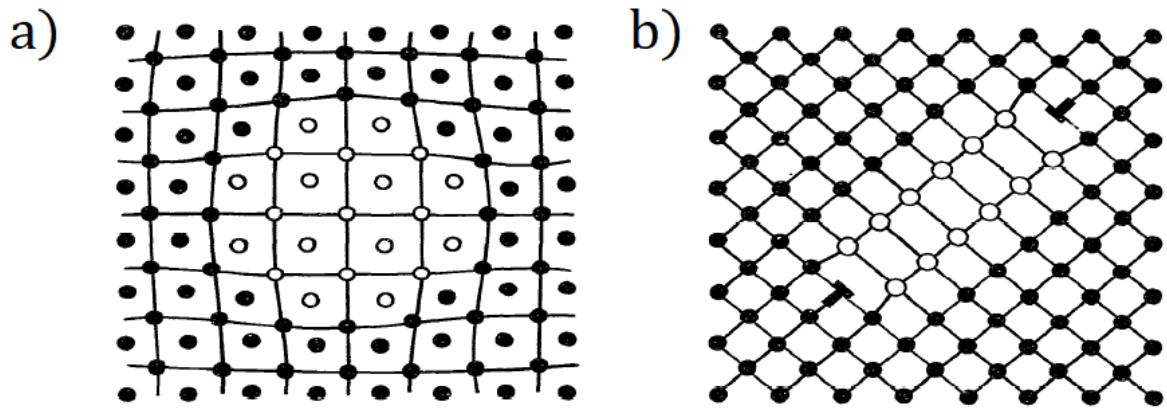

Figure 29. Scheme of interfacial structures of solids nucelation: a) completele coherent interface, b) semi-coherent interface[145].

Precipitates formed in the austenite tend to be coherent or semi-coherent when they are formed, but loose coherence during $\gamma \rightarrow \alpha$ transforamation. Contrarily, precipitates formed in the ferrite have a strong tendency to form coherently or semi-coherently[105].

In MA steels, precipitation is based on the combination of carbon or nitrogen or both with metallic elements. Usually, these are transition metals (V, Nb, Ti), but also other precipitates may form such as AlN which has special importance for MA[147]. During MA steels processing, carbide and nitride precipitation occurs in three stages, leading to the formation of three different kinds of particles:

Type I: Precipitates formed at the liquid/solid interface in δ iron. They are characterized by being very stable, the coarser ones do not influence the austenite recrystallization, but the smallest one can retard it during reheating[148].

Type II: Precipitates formed during hot deformation, while the temperature decreases[149]. These strain-induced precipitates (SIP) mainly contribute to the grain refinement of MA steels and also retard the austenite solution annealing[150]. Dislocations and dislocation sub structures are the preferred nucleation sites for SIP which are not randomly distributed but heterogeneously distributed in a chain like manner[151,152].

Type III: Known as interphase precipitation, they form during the $\gamma \rightarrow \alpha$ phase transformation and are observed as fine rows within the ferrite[153].

Type III precipitates usually are carbides with sizes of few nanometers, they do an important individual contribution on MA steels, in some cases greater than the contribution made by the carbonitride precipitations in austenite or the dislocation hardening[11]. Different types of precipitate can appear within steels, and the most well-known are listed in Table 8. The orientation relationship with the matrix of carbides and carbonitrides depends on whether they nucleated in austenite, which tend to have a random orientation with the ferrite, while the ones nucleated in ferrite adopt any of its three variants of the well-known Baker-Nutting relationship[154]:

- $(0\ 0\ 1)_{MX}$ || $(0\ 0\ 1)_{ferrite}$ and $[1\ 1\ 0]_{MX}$ || $[1\ 0\ 0]_{ferrite}$
- $(1\ 0\ 0)_{MX}$ || $(0\ 0\ 1)_{ferrite}$ and $[0\ 1\ 1]_{MX}$ || $[1\ 0\ 0]_{ferrite}$
- $(0\ 1\ 0)_{MX}$ || $(0\ 0\ 1)_{ferrite}$ and $[1\ 0\ 1]_{MX}$ || $[1\ 0\ 0]_{ferrite}$

Interphase precipitates only maintain a single variant[155]. Figure 30 shows a diagram of diffraction patterns where IP carbides and ferrite have the Baker-Nutting orientation relationship with the electron beam parallel to [0 0 1] ferrite.

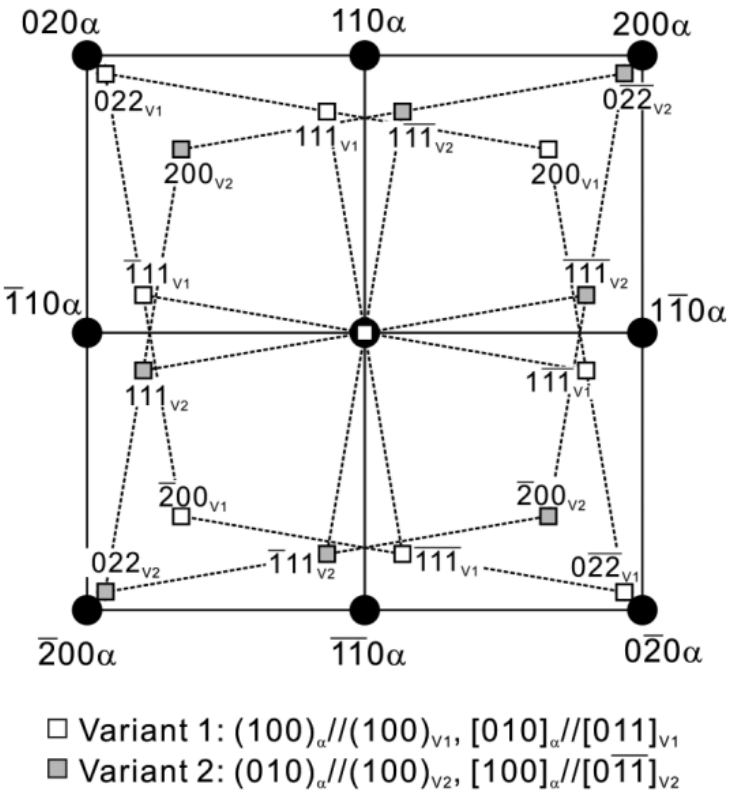

Figure 30. Scheme of the diffraction pattern of precipitated MC and ferrite matrix matching the Baker-Nutting orientation relationship with an incident beam parallel to [0 0 1] of ferrite matrix. Two of the variants are indicated[156].

Type of carbide	Lattice type	Remaks
M_3C	Orthorhombic	A carbide of the cementite (Fe_3C) type. M may be Fe, Mn, Cr, with a little W, Mo, V.
M_7C_3	Hexagonal	Mostly found in Cr alloy steels. Resistant to dissolution at medium temperatures. Hard and abrasion resistant. Found as a product of tempering high-speed steels.
$M_{23}C_6$	Face-centered cubic	Present in high-Cr steels and all high-speed steels. The Cr can be replaced with Fe to yield carbides with W and Mo
M_6C	Face-centered cubic	A W- or Mo-rich carbide. May contain moderate amounts of Cr, V, Co. Present in all high-speed steels. Extremely abrasion resistant.
M_2C	Hexagonal	W- or Mo-rich carbide of the W_2C type. Appears after temper. Can dissolve a considerable amount of Cr.
MC	Face-centered cubic	V-rich carbide. Resist dissolution. Small amount that does dissolve reprecipitates on secondary hardening.

Table 8. General description of alloy carbides types and their characteristics in tool steels [157]

The Table 9 correlates the most common precipitates found in reheated and quenched steels with their coherence with the matrix. The notation M is used where there are two or more different metal elements in the carbides. Fe-X and M-X are carbides and nitrides. M-M are intermetallic precipitates.

There are two principal modes of carbide formation in steels, "*fibrous carbides"* and *"interphase precipitation"*[158]. Interphase precipitation in steels has been important for many years and remains vital for the development of tough and strong hot-rolled steels with upgraded weldability due to reduced carbon content [7].

Precipitate			Matrix	
			bcc	fcc
Fe - X			> 150°C	> 250°C
Fe_2C	hex	ε-carbide	+	
Fe_3C	orh	cementite	+	−
$Fe_{16}N_2$	bct	α"-nitride	++	
Fe_4N	fcc	γ-nitride	+	++
M - X			> 450°C	> 600°C
MC	fcc	V, Nb, Ti	+	−
M_2C	hex	Mo, V	+	
M_7C_3	hex	Cr	−	−
$M_{23}C_6$	fcc	Cr	−	+
M_6C	fcc	Mo, W	−	−
MN	fcc	Cr	+	
MN	hex	Al	−	−
M_2N	hex	Cr	−	
M - M			> 450°C	> 700°C
NiAl	bcc	B_2-phase	++	
Ni_3Al	fcc	γ'-phase		++
Ni_3Ti	hex	η-phase	−	−
$Fe_7(Mo,W)_6$	rh	μ-phase	−	
$Fe_2(Mo,W)$	hex	Laves-phase	−	+
FeCr	tetr	σ-phase	−	−
$Fe_{36}Cr_{12}Mo_{10}$	bcc	χ-phase	−	−
$(Fe, Ni)_{16}Ti_6Si_7$	bcc	G–phase	+	

Table 9. Enlists the common precipitates obtained on reheating a quenched microstructure, their atomic ordering and their matching. incoherent (-), partially coherent (+) and completely coherent (++) [159].

2.2.4.2. INTERPHASE PRECIPITATION IN STEELS

Research into interphase precipitation in steels has a long history. In 1968, Davenport et al., [153] and Gray & Yeo[160] showed for the first time that during the $\gamma \rightarrow \alpha$ transformation, on the austenite/ferrite interface, niobium carbonitrides are formed in uniformly distributed precipitation rows. That phenomenon was called Interphase precipitation. Considered as one of the most important strengthening mechanisms of HSLA steels, interphase precipitation enables development of high-resistance hot-rolled steels with improved weldability[161]. Processing for interphase precipitation aims to avoid the formation of cementite in low carbon iron alloys cooled from austenite, to obtain mainly ferritic microstructures with very fine transition metal carbides, nitrides and/or carbonitrides bands at room temperature [141,153,162]. It is accomplished by the addition of strong carbide-forming elements like vanadium or molybdenum, in quantities less than 0.5% wt.

Figure 31 shows how the transformed ferrite, advancing into the austenite, contains very fine parallel lines of V_4C_3 precipitates in an Fe-0.2C-2V steel. The precipitate bands are parallel and it is clear that they are parallel to the interphase boundary. When nucleation occurs, carbon is removed from a narrow zone of austenite along the boundary, the austenite stability is reduced, and thus the boundary

moves forward across the denuded region to a new site, forming a new nucleation site for interphase precipitation [153]. Davenport and Honeycombe [163] developed a schematic model, corroborating previous observations and showing how the formation of interphase precipitates occurs (Figure 32). They affirm that the interphase precipitation occurs parallel to the moving parts of the $\gamma - \alpha$ boundary. Figure 32 (a) shows the γ/α boundary in a new position for ferrite nucleation with a sharp partition of carbon across it. Ferrite has a carbon concentration C_α while $C_\gamma^{\gamma\alpha}$is the critical value obtained by the adjacent enriched austenite. During the movement of the $\gamma - \alpha$ boundary, it collects solute atoms which drag the boundary, to finally nucleate carbide particles on the ferrite side impoverishing carbon in the adjacent austenite $C_\gamma^{\gamma\rho}$ (Figure 32 (b)). With the decreased carbon concentration in austenite, the phase boundary moves to a new position ahead of the precipitate row. Then, the boundary once more becomes locked by solute atoms, restarting the precipitation process as is shown in Figure 32(c).

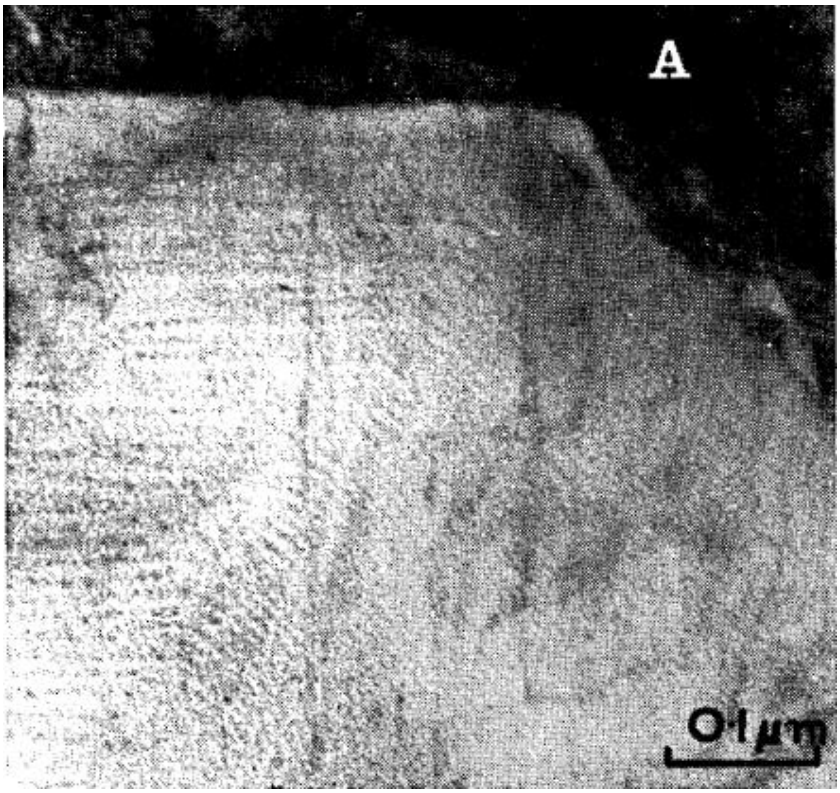

Figure 31. Fe-0.2C-2V steel, partially transformed at 600°C for 10s. it shows precipitate arrows parallel to austenite/ferrite interface. The black region nomenclated as A is martensite formed from austenite on quenching out. [153]

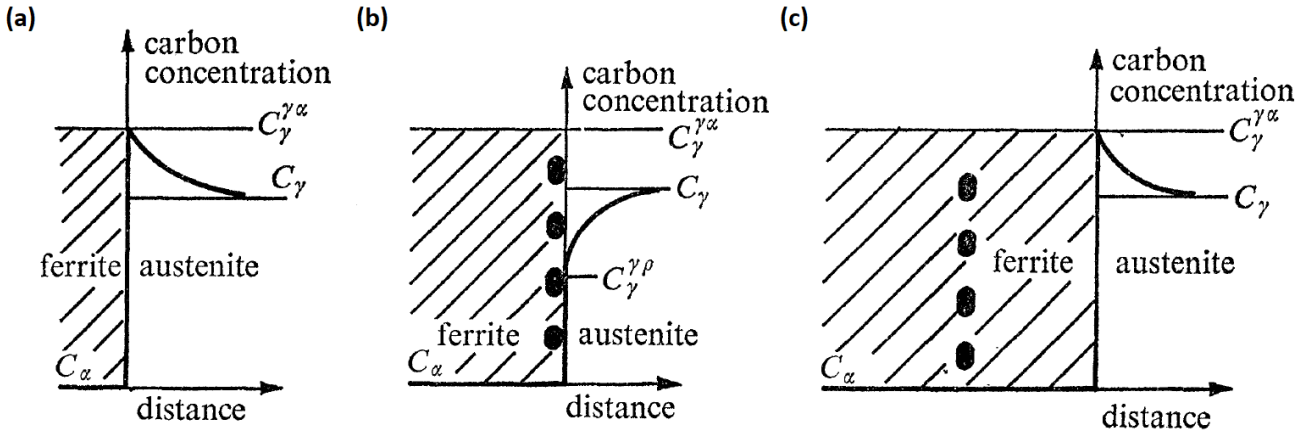

Figure 32. Schematic model of the formation of interphase Precipitation [163].

Commercially, different alloying additions have been investigated, looking to depress the coiling and transformation temperatures which optimize the tensile strength by the minimisation of interphase particles size, row, and inter-particle spacing. Numerous studies demonstrate that the size of the interphase precipitates and also the spacing between rows increased with increasing temperature of transformation, varying between 5 and 500 nm. [22,24,164]. The addition of carbon and other alloying elements change the size of the interphase particles [164]. Thus, studies of different alloying additions and their effect had been done, concluding that for hot rolled steels, a low coiling temperature promotes smaller precipitate size, with finer row and inter-particle spacing, which promotes higher yield strength [165,166]. This also results in an increase in dislocation density, which benefits the precipitates nucleation.

Interphase precipitation is classified according to the morphology that they have. Three identified types have been reported[167]:

(1) Planar interphase precipitates with regular sheet spacing (PIP).
(2) Non-planar interphase precipitates
    (2.1) Curved interphase precipitates with regular sheet spacing (regular CIP).
    (2.2) Curved interphase precipitates with irregular sheet spacing (irregular CIP).

As any other precipitate formed in ferrite, interphase precipitates have always been found to adhere to the Baker-Nutting relationship with the ferritic matrix. This has been used as a practice to identify if the precipitates formed in the ferrite or in other phases.

2.2.4.2.1. PLANAR INTERPHASE PRECIPITATES WITH REGULAR SHEET SPACING (PIP)

Planar interphase precipitates are related to ferrite by the Baker and Nutting orientation relationship and appear as parallel equi-spaced laths, quite similar to a very fine pearlite.

While the ferrite nuclei grow into the adjacent austenite grain, the ferrite exhibits a rational orientation relationship with the austenite partially coherent $(111_\gamma \| 110_\alpha)$, and when the precipitate is related by the same orientation relationship, the precipitate will adopt the same ferrite correlation variant, which allows the precipitate to be cube-cube related with the austenite [168]. The consequent parallelism, in all three phases across the interface/γ/α, of close-packed planes enables

low energy facets to develop interfaces on both α/precipitate and γ/precipitate. It considerably reduces the free energy of activation for critical nucleus formation [169](Figure 33 (a)).

2.2.4.2.2. NON-PLANAR INTERPHASE PRECIPITATES

2.2.4.2.2.1. CURVED INTERPHASE PRECIPITATES WITH REGULAR SHEET SPACING (REGULAR CIP).

Cases where unique three-phase crystallography cannot be possible, the single precipitate variant will be controlled by the development of low energy facets on the precipitate/α interface. The angle between this facet normal and the local $\gamma - \alpha$ interface normal. The orientation variant of the precipitate with respect to the ferrite minimizes the angle between the low energy facet plane and the $\gamma - \alpha$ interface, reducing the free energy of activation for critical nucleus formation[163,170,171].

Ricks and Howel [172] applied an energy balance model to the migration of interphase faces and concluded that a minimum precipitate spacing is required for the bowing mechanism to occur (the transformation interface bow between pinning precipitates before finally breaking away from them[24]). On the boundary, if the precipitate spacing is less than that value, the boundary must migrate by a 'quasiledge' mechanism, whereby steps of ledges are required to laterally traverse the boundary for forwarding migration to occur, in the same manner as that described for low-energy inherently immobile boundaries [172]. This, produces a curved banded arrays of precipitates, or even a probability precipitates with no clear interphase origin.

2.2.4.2.2.2. CURVED INTERPHASE PRECIPITATES WITH IRREGULAR SHEET SPACING (IRREGULAR CIP).

For an interface containing unequally spaced precipitates, bowing and ledge mechanisms could work simultaneously. For ledges that were re-pinned by further precipitation, a camber formed in a boundary between widely spaced precipitates. These ledges would then allow the unbowed section of the interface to migrate [172] (Figure 34).

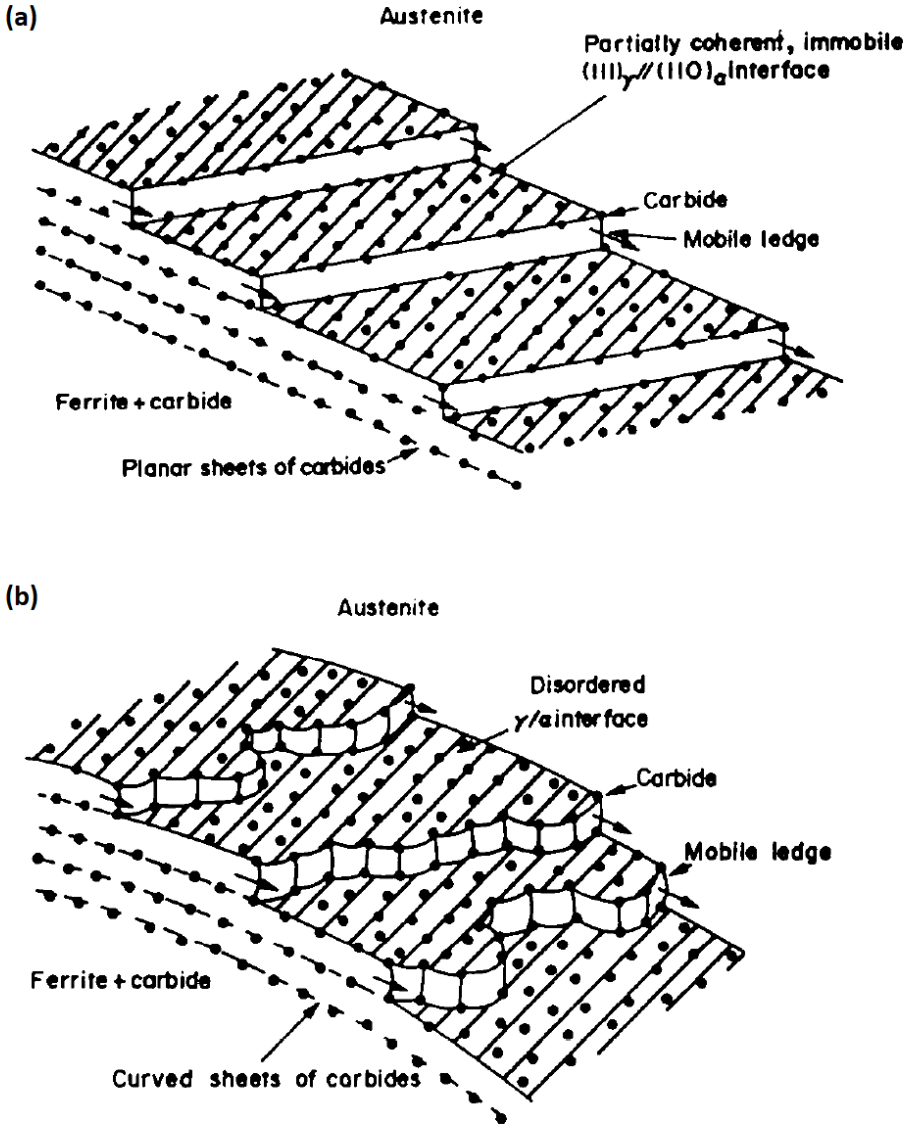

Figure 33. Schematic diagrams illustrating in 3D the migration of $\gamma - \alpha$ boundaries. (a) Partially coherent $111_\gamma \| 110_\alpha$ interface forming planar sheets of precipitates. (b) disordered boundary (immobilized by copious precipitation) forming curved sheets of precipitates [171].

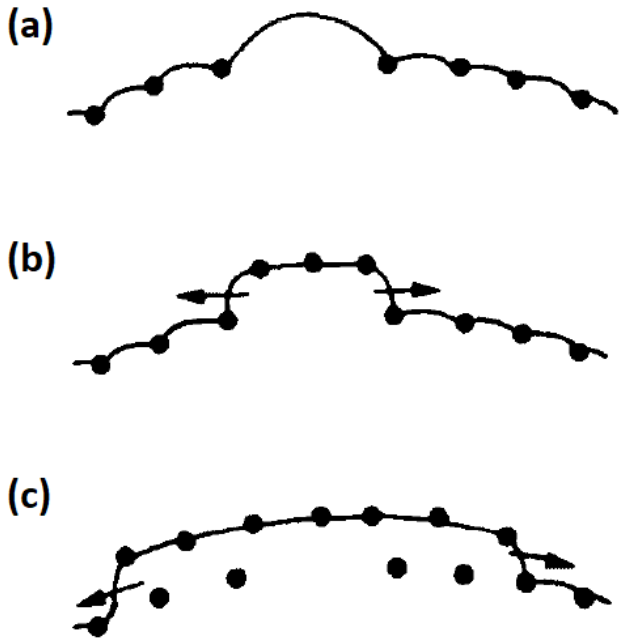

Figure 34. Scheme of a mobile interphase pinned by precipitation (a) acting as a source of ledges. (b) bulge repined by subsequent precipitation. (c) the end of the bulge being forced to move sideways [172].

The interphase precipitation has a strong tendency to be PIP at low isothermal transformations. While the isothermal temperature rises, the morphology tends to be firstly PIP, then regular CIP and afterwards irregular CIP with much larger sheet spacings[18]. The average IP sheet spacing is dependent on the isothermal transformation temperature, both decreasing simultaneously. At the same temperature, the IP sheet spacing has minor variations between grains[18]. This trend is consistent for different compositions like Fe-C-V steels[161], Fe-C-Ti steels[173], Fe-C-Nb steels[174] and Nb-microalloyed steels[9]. Also, the average inter-carbide spacing increases with isothermal transformation temperature[18]. This has been summarized by Sakuma and Honeycombe in the scheme shown in Figure 35. With the lower transformation temperature, finer and denser carbides on the sheet planes are achieved because of:

- The nucleation rate increases due to the improved driving force.
- The diffusion rate reduces, retarding the carbide growth.
- Enhancement of the carbon fraction at the interface, increasing the saturation and contributing to the higher nucleation rate of carbides[18].

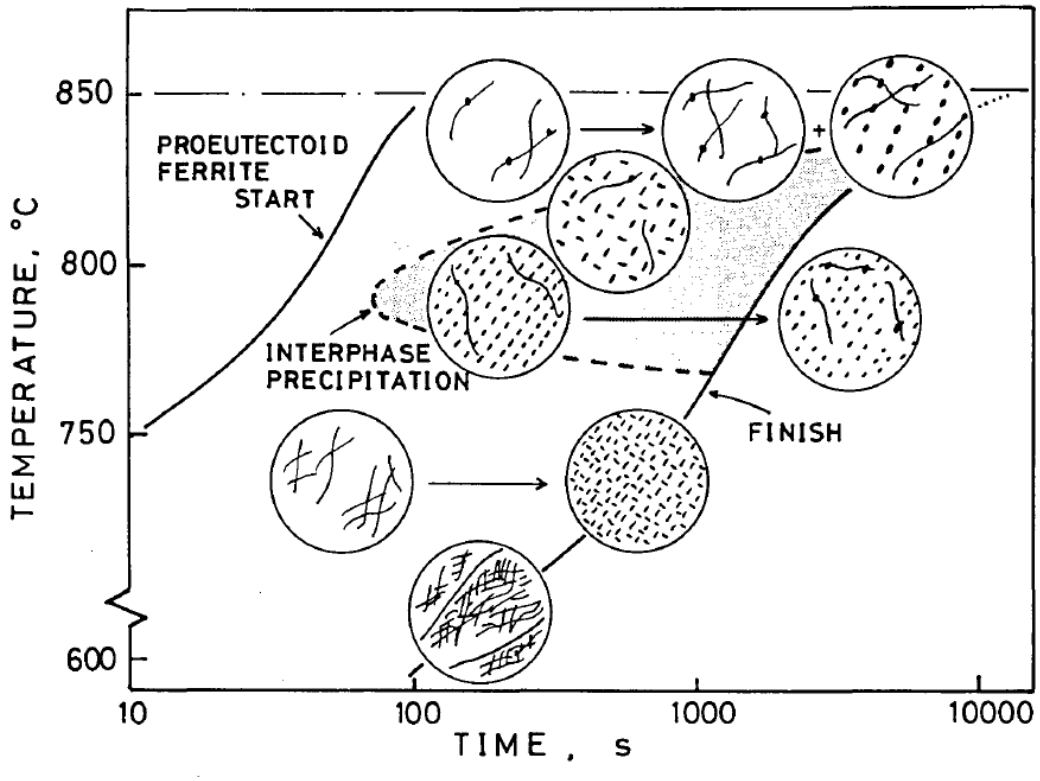

Figure 35. Microstructures and interphase precipitation formed by isothermal transformation for proeutectoid ferrite reaction[174].

2.2.4.2.3. EFFECT OF CHEMICAL COMPOSITION ON INTERPHASE PRECIPITATION

The formation of interface precipitates can be controlled by the diffusion of precipitate forming elements along the interface, and by the driving force for precipitation nucleation. Most alloying additions increase the relative thermodynamic stability of the austenite (excluding Co, and Al), retarding the transformation of the austenite into ferrite[19].

During direct transformation of austenite, the alloying elements influence the type of carbide morphology in two ways:

1) By altering the kinetics of the basic γ/α reaction.
2) By changing the structure and composition of the carbide phase[158].

The major role of microalloying additions can be for several reasons: 1) The diffusivity ahead and along the boundary. 2) The mobility of the γ/α boundary. 3) The free energy of the boundary. 4) The relation between the precipitate-matrix interface with the precipitate structure.

Equation 1 The nucleation rate is a function of the number of nucleation sites per unit volume (N), the temperature of the system (T), the activation energy for the transfer of atoms across (Q^*) the interface, the free energy change per unit volume of nuclei (ΔG_v), the activation energy for nucleation (G^*), the interfacial energy per unit area (σ), and the Planck and the Boltzmann constants (h and k respectively) and the formula was written as:

$$I = N\frac{kT}{h}exp\left\{\frac{-(G^*+Q^*)}{kT}\right\}$$ *Equation 17*

$$G^* = \frac{16\pi}{3}\frac{\sigma^3}{\Delta G v^2}$$ *Equation 18*

This equation gives a direct indicator of the sequence of nucleation rates for various carbides, identifying which precipitations nucleate first and which alloying elements substitute others to produce late-formation products[26].

Table 10 summarizes the effect of individual additions of elements to the microalloyed steels and their effect on interphase precipitation. Table 11 lists the most common interphase precipitates found in microalloyed steels.

In addition to composition, there is a relationship between the precipitation hardening effect, the precipitation size, the nucleation mechanisms and even the accumulated dislocations from processing, leading to a possible drop of it if those are not known and controlled[193]. It has been shown that variations in the thermomechanical processing schedule, especially with variants in coiling temperature, produce big changes in the precipitation within the ferrite which reflects directly on the mechanical properties of the final product[181].

Strong carbide-forming elements such as V and Ti are prone to form MC precipitates due to their enhanced diffusivity at higher coiling temperatures. However, the precipitation hardening does not increment linearly because the second phase particles become coarser at high coiling temperatures181. Cr is also known for being a strong carbide former, especially of M_3C, M_7C_3, and $M_{23}C_6$ carbides, dependent on bulk Cr content[194–198]. For low alloy Cr-Mo-V steel with about 1 wt% Cr, the existence of metastable $M_{23}C_6$ carbide has been reported[198–200], especially at relatively low temperatures and as a transition phase which transforms in other precipitates after longer annealing times[196,201]. Chromium is also known for increasing the stability of austenite to ferrite (restrains ferrite transformation)[202] in low carbon steels, facilitating the bainite transformation[203,204]. The addition of Cr reduces the Bs and Ms temperatures, leading to a separation of the bainite C-curve and an expansion of the bainite formation range[205,206]. Combined Cr+Al additions give improved ductility in a bainite+ferrite product at the expense of the high tensile strength obtained in bainitic low-carbon steels[204].

Interphase precipitation has been noted in steels microalloyed with different carbonitride-forming elements like Nb[38,133,207,208], Ti[7,11,23], and V[189,190,209,210]. No reports of interphase precipitation with Cr as the main element for interphase precipitation have been done yet. Cr additions have been reported as a solubility improver of other microalloying elements such as Ti[23,211], and Nb[211–213], and also as a reducer of precipitate sizes[214,215].

Element	Effect on the interphase precipitation
V	Vanadium is well-known to produce interphase precipitates in microalloyed steels[44,141,164]. It causes an accelerated reaction with stepped growth of ferrite with interphase precipitation of vanadium carbides[161]. These carbides tend to form at lower temperatures compared to other precipitations such as NbC due to their high solubility in austenite[175]. This means that the vanadium carbides play a relevant role in precipitation strengthening of the studied alloys, while Nb is much more effective in grain refinement. The addition of V to Ti-Mo-bearing steels produces three main effects: 1. Refines the microstructure and precipitates to a finer scale. 2. Increases the volume fraction of precipitation[176]. 3. The higher stability of complex precipitates compared to (Ti,Mo)C, which means that they maintain very fine nano-sizes during coiling process[177]. V-microalloyed steels produce larger precipitate radius than Ti-Microalloyed steels[26].
Ni	Slows down the transformation and increases the formation of fibrous vanadium carbide.
Mn	Slows down the transformation and increases the formation of fibrous vanadium carbide.
Cr	Cr additions slow down the $\gamma \rightarrow \alpha$ transformation and increase the formation of fibrous vanadium carbide. In MA steels it has been reported that Cr additions reduce the starting temperature of the austenite to ferrite phase transformation[178]. The slower growth rate of ferrite brings about much denser carbides on the sheet planes, decreasing the intercarbide spacing[23]. Also, Cr additions improve the hot ductility of Nb-MA steels and increases the fraction of ferrite high-angle grains[178].
Ti	Ti-microalloyed steels present smaller row spacing than MA alloyed steels with other additions such as V[26]. Increases the fraction of fibrous carbide by the usage of other alloying elements which slow down the reaction. Strengthen the steel by the formation of titanium carbide during the $\gamma \rightarrow \alpha$ transformation[21]. The interphase precipitation of Ti-MA steels contributes more than 300 MPa to the overall yield strength[7].
Mo	Addition of Mo in MA steels reduces the ferrite grain size, the IP size, the IP row spacing, and increases the precipitate number density[7,19,26,156,179,180]. Mo addition suppresses the annihilation of dislocations at relatively high temperatures, resulting in heightened nucleation sites for precipitation[180]. Also, the Mo atomic ratio increases in MC particle with increase in the coiling temperature, benefiting the subsequent precipitation[181]. Steels with Mo additions require more alloying elements to form Mo_2C and M_6C. Mo_2C IP progresses in a rod-like of a needle morphology changing to fibrous carbides[182]. M_6C forms at higher transformation temperatures[158].

	Its effect on the phase transformation is greater in V-MA steels than in Ti-MA steels[26].
Si	Accelerates the kinetics of the γ/α reaction at high transformation temperatures increasing the rates of nucleation and also the growth of ferrite[183].
Al	Accelerates the kinetics of the γ/α reaction at high transformation temperatures increasing the rates of nucleation and also the growth of ferrite[183].
B	B additions to MA steels results in formation of $Fe_{23}(B, C)_6$ and BN. The first one is a preferential site for the nucleation of intragranular ferrite, and the second preferentially forms at the gran boundary, decreasing the amount of grain boundary ferrites and thus improving the steel's ductility[184,185].
Co	Increases the rate of nucleation[183].
Nb	In microalloyed steels, apart from the important contribution that Nb does on the grain refinement strengthening, interphase precipitation of NbC provides a much higher contribution to yield strength than the strength contribution from precipitation on dislocations[133].

Table 10. Table of common micro-alloying elements added to microalloyed steels and their effect on interphase precipitation.

Interphase Precipitation	**Lattice parameter [nm]**	**Orientation relationship with respect to the ferrite matrix**	**Reference**
TiC	0.432	$(1\ 0\ 0)_{MX} \parallel (1\ 0\ 0)_{ferrite}$ and $[0\ 1\ 1]_{MX} \parallel [0\ 0\ 1]_{ferrite}$	Peng et al[186].
(Ti, Mo)C	0.433	$(0\ 0\ 1)_{MX} \parallel (0\ 0\ 1)_{ferrite}$ and $[1\ 0\ 0]_{MX} \parallel [1\ 0\ 0]_{ferrite}$	Chen et al. and Yokota et al.[5,179].
(Ti,Nb)C	0.438>MX>0.427		Bu et al[8].
$(Ti, Mo)_2C$		$(0\ 0\ 1)_{MX} \parallel (0\ 0\ 1)_{ferrite}$ and $[1\ 1\ 0]_{MX} \parallel [0\ 0\ 1]_{ferrite}$	Iza-Mendia et al[187].
VC	0.4165	$(0\ 0\ 1)_{MX} \parallel (0\ 0\ 1)_{ferrite}$ and $[1\ 0\ 0]_{MX} \parallel [1\ 1\ 0]_{ferrite}$	Chong et al[188]., Miyamoto et al[189].
V_4C_3	0.404	$(0\ 0\ 1)_{MX} \parallel (0\ 0\ 1)_{ferrite}$ and $<0\ 1\ 0>_{MX} \parallel <0\ 1\ 1>_{ferrite}$	Chong et al[188]., Baker[190].
V(C, N)		$(0\ 0\ 1)_{MX} \parallel (0\ 0\ 1)_{ferrite}$ and $[1\ 1\ 0]_{MX} \parallel [1\ 0\ 0]_{ferrite}$	Honeycombe[158]
(V,Mo)C		$(1\ 0\ 0)_{MX} \parallel (1\ 0\ 0)_{ferrite}$ and $[1\ 0\ 0]_{MX} \parallel [1\ 0\ 0]_{ferrite}$	Gong et al[26].
$(V,Mo)_4C_3$		$(1\ 0\ 0)_{MX} \parallel (1\ 0\ 0)_{ferrite}$ and $[1\ 1\ 0]_{MX} \parallel [0\ 0\ 1]_{ferrite}$	Gong et al[26].
AlN	$a = 0.3111$ $c = 0.4978$	$(0\ \bar{1}\ 1\ 0)_{MX} \parallel (0\ 1\ \bar{1})_{ferrite}$ $(\bar{1}\ \bar{1}\ 2\ 0)_{MX} \parallel (2\ 0\ 0)_{ferrite}$ and $[0\ 0\ 0\ 1]_{MX} \parallel [0\ 1\ 1]_{ferrite}$	Iza-Mendia et al[187].

NbC	0.4471	$(1\ 0\ 0)_{MX} \parallel (1\ 0\ 0)_{ferrite}$ and $[0\ 1\ 1]_{MX} \parallel [0\ 1\ 0]_{ferrite}$	Nartowski et al[191]. Brito and Kestenbach[192].
$Cr_{23}C_6$	0.1064	$\{1\ 1\ 1\}_{MX} \parallel \{1\ 1\ 0\}_{\alpha}$ and $<1\ 1\ 0> \parallel <1\ 1\ 1>_{\alpha}$	Westgren[25]. Campbell and Honeycombe[24]

Table 11. Table of common interphase precipitations found in microalloyed steels.

In this research, a V-Mo microalloyed steel was designed to evaluate the separate effect of Cr on the interphase precipitation and its effect on the tensile properties. The experimental steps are based on a previous study at the University of Sheffield[130]. A detailed characterization after each manufacturing process was undertaken on the first samples to evaluate each step of the structure refinement, and also of the interphase precipitation formed within the ferrite after the isothermal transformation. A new alloy was proposed to evaluate the effect of a different manufacturing process, finding a route to control an important parameter which influences the final product properties, the prior austenite grain size. To study and advance this topic, researchers in general perform the experiments:

- Dilatometry: Measuring the dilatation the time when the transformation ends during the ageing is known. It is known that low transformation kinetics produces larger precipitation volume fractions, which determines the strength of the steel.
- Optical Microscopy: combined with standard preparation and etching, images of the grain boundaries and also microstructure revelation can be achieved. It is well known that the grain size of steels is inversely proportional to the tensile strength. Further, austenitic grain size shows what is the effect of the alloying additions before the isothermal transformation, and grain refinement by the ferrite and bainite nucleation. A first correlation between general parameters and mechanical properties can be done, added to other experiments to obtain information about the alloy.
- Carbon extraction replicas: this experiment allows precipitate size and composition to be measured.
- Thin foil TEM samples: thin foil samples are used to confirm data of precipitate size, and also to examine the precipitate distribution and orientation relationship.
- Transmission electron microscopy (TEM): it is mandatory to carry out TEM to identify the interphase precipitation of the aged samples.

CHAPTER 3: EXPERIMENTAL PROCEDURE

3.1. MATERIALS

3.1.1. MICROALLOYED STEELS RECEIVED FROM TATA STEEL, IJMUIDEN.

This project started with the base-line steel composition of 0.1%C-1.5%Mn-0.2%Si-0.2%V-0.5Mo, supplied by Tata Steel, Ijmuiden. This first issue to address was the effect of small (0.5%) Cr additions, which have had confusing results in the past, with some research suggesting that Cr is beneficial, while other research suggests it is detrimental. This was probably because these studies did not take into account the effect of Cr on the time-temperature-precipitation behaviour. To investigate the effect of Cr on the microstructure and properties of the steels, two compositions were manufactured with only two differences: firstly, there was the intended addition of 0.5% Cr to one steel, with the other having identical composition but no Cr. Secondly, there was a slight increase in the aluminium amount, but this was at trace levels and was probably unintentional. The exact chemical compositions are shown in Table 12. A vacuum induction melted split cast was made of 30kg, with the Cr addition made to one half of this casts. Ingots were cast with dimensions 620mm × 105mm × 35mm. Then they were homogenized for two hours at 1250^0C followed by a hot forging process of several passes to reduce the thickness to 8mm. Then, samples for dilatometry were machined to a size of 120mm × 12mm × 5mm to control temperature with a thermocouple. Because of the lack of information about the number of hot-rolling passes and the strain per pass, these materials were named as 0.0.

The normalization process was performed at 1250^0C for 30 min in a furnace with a controlled atmosphere (argon), followed by water quenching for a further heat treatment. To guarantee the temperature control, the treatment was performed using a dilatometer. First, samples were re-austenitised at 1200^0C for 3min, followed by fast cooling, at a rate of 10^0C/s, to the respective transformation temperature (600^0C, 625^0C and 650^0C). These temperatures were held for 90 min, followed by water quenching.

Materials	C	Mn	Si	Al	V	Mo	Cr	N
V-Mo-0.0	0.1	1.6	0.2	0.02	0.2	0.5	-	0.13
Cr-V-Mo-0.0	0.1	1.6	0.2	0.045	0.2	0.5	0.5	0.13

Table 12. Chemical composition of the steels.

Special attention was placed on controlling the temperature. The dilatometer works as a second order system, so the damping factor was changed to ~1.0 by the modification of several parameters to control the austenitisation temperature with no oscillation over it, but also without retarding the time to reach the steady value as shown in Figure 36. This is because such high temperatures give rapid austenite grain coarsening which would result in a significant drop in the tensile strength of the steel.

At the same time, this process should be as quick as it can be possible because the longer the time the alloy is fully austenitic (800^{0}C in most steels), the more significant the grain growth becomes [216]. However, the more rapid the heating, the more likely temperature over-runs will occur. As is shown in Figure 37, after the austenitisation, the samples were cooled quickly at 10^{0}C/s, to be held at a constant transformation temperature (T_{Ag}).

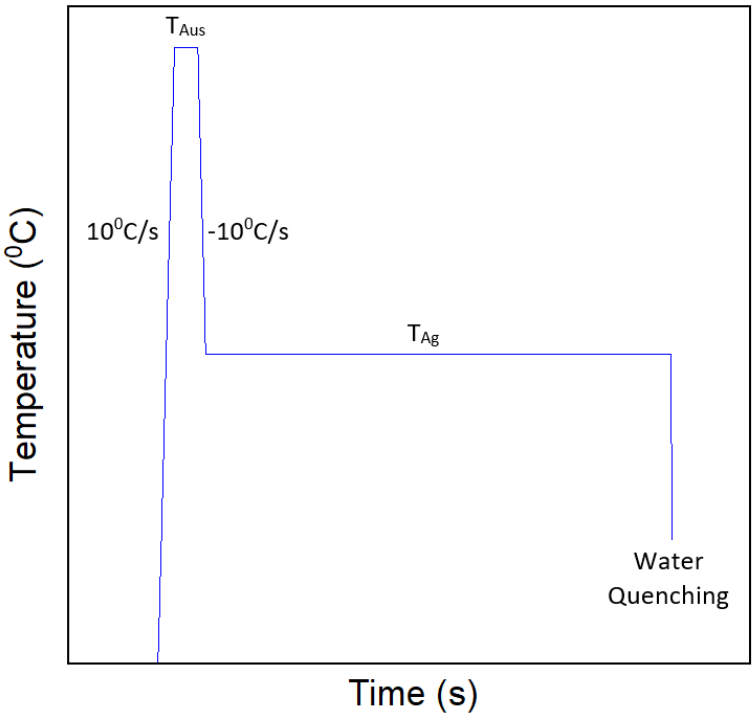

Figure 36. Scheme of the thermal history for processing of samples MA with Al and Cr (V-Mo-0.0 and Cr-V-Mo-0.0).

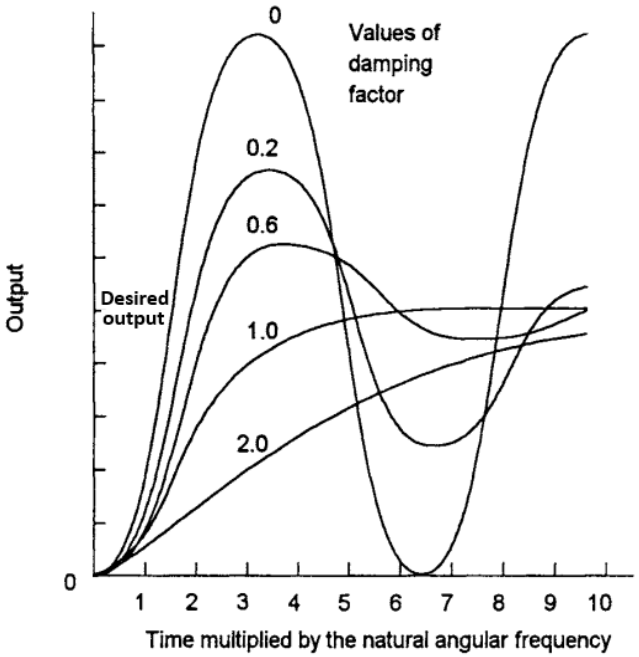

Figure 37. second order system response with a unit step input. While the damping increases, the system output change from a continuous oscillation with a damping factor of 0 to a damped-out output with a damping factor of 1. Further damping increments retard the output, leading to longer times for reaching the steady state value[Modified from 217].

3.1.2. STEELS PRODUCED AT THE UNIVERSITY OF SHEFFIELD

Greater control over composition variations and thermomechanical process treatment was required. Therefore, there was a drive to produce the steels in-house, rather than relying on Tata Steel. The first step was to reproduce steel V-Mo-0.0 and Cr-V-Mo-0.0 in-house. These steels were denoted V-Mo-0.4 as the equivalent of V-Mo-0.0, and Cr-V-Mo-0.4 as the equivalent of Cr-V-Mo-0.0. Another two alloys were produced to study the effect of changes in the hot-rolling parameters on the interphase precipitation, plus another one with Cr+Nb addition. Their compositions are listed in Table 13. The steels were cast following vacuum induction melting in a Consarc small-scale VIM in the Quarrell lab of the University of Sheffield, with help of the Dr. Yunus Azakli. Ingots of 80mm × 80mm × 90mm were produced, which were then cut in blocks of 80mm x 80mm x 40mm and homogenised for two hours at 1300^0C and then water quenched. The following thermomechanical treatment was selected, based on the studies of Kostryzhev et al.[218] and Pereloma et al.[219] in order to maximise the precipitation on transformation. Samples were heated to 1050^0C (accounting for the temperature drop while the steel is moved from the furnace and rolled). After that, alloys V-Mo-0.4 and Cr-V-Mo-0.4 had 4 hot-rolling passes using a Fenn 2 high reversing rolling mill, with a strain of 0.4 in each, to reduce the thickness to ~18% of the initial thickness, with the final deformation at $\sim 975^0$C. The samples were then air cooled. Alloys V-Mo-0.2, Cr-Nb-V-0.2 and Cr-V-Mo-0.2 were hot-rolled at the University of Warwick using the same temperatures for the hot-rolling reduction. These last alloys were rolled according to the equipment limitation of load during the rolling, allowing a reduction of 5.8 mm. The ingots were reduced in 6 passes as is shown in Table 14, with an average strain per pass of 0.22 at the University of Warwick.

Two main samples were cut from the as-rolled block with extensive cooling to minimise any thermal effect that the cutting could have on the microstructure. Figure 38 shows how the block was divided; squared samples from the centre of the block were obtained (12 x 12 x 7.7 mm) to evaluate the effect of reheating on austenite grain size. Each sample was heated for 30min in a furnace with a controlled argon atmosphere from 950 to 1300^0C and then water quenched. Next, the samples were cut in half, mounted in bakelite and prepared for metallographic analysis to observe the microstructure in the rolling direction.

Materials	C	Mn	Si	Al	V	Mo	Cr	N	Nb
V-Mo-0.4	0.12	1.11	0.23	<0.01	0.2	0.47	0.01	<0.003	-
Cr-V-Mo-0.4	0.1	1.3	0.22	<0.01	0.2	0.47	0.51	<0.003	-
V-Mo-0.2	0.13	1.56	0.19	<0.005	0.21	0.5	0.51	-	-
Cr-Nb-V-0.2	0.13	1.42	0.25	0.016	0.21	0.51	0.48	-	0.03
Cr-V-Mo-0.2	0.12	1.41	0.21	<0.005	0.2	0.48	-	-	-

Table 13. Chemical composition of the steels.

Pass	Initial thickness [mm]	Final thickness [mm]	Reduction per pass [%]
1st	40	34.2	14.5
2nd	34.2	28.4	17
3rd	28.4	22.6	20.4
4th	22.6	16.8	25.7
5th	16.8	11	34.5

Table 14. Hot-rolling initial and final thickness per pass for steels V-Mo-0.2, Cr-Nb-V-0.2 and Cr-V-Mo-0.2.

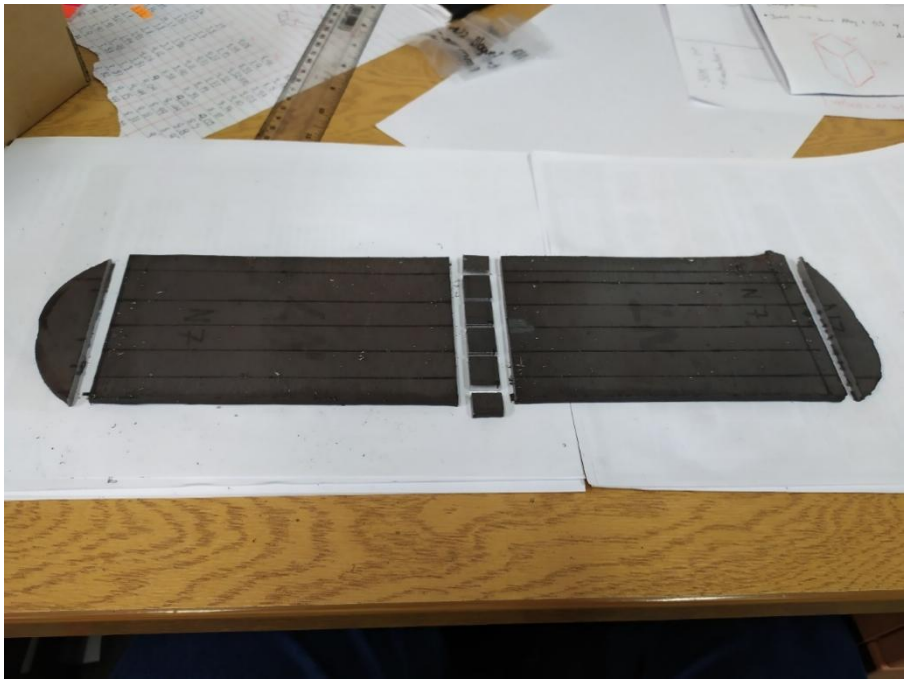

Figure 38. Sectioning of the hot-rolled plate.

Dilatometry samples of steels made at the University of Sheffield were cut longer than the ones provided by TATA Steel (150mm × 15mm × 7mm), getting closer to the ideal samples for dilatometry according to the specifications of the used machine. The rest of the process for them was the same as steels V-Mo-0.0 and Cr-V-Mo-0.0.

3.2. Dilatometry

Historically, to analyse the effect of the alloying elements additions on the kinetics of the phase transformation of steels, dilatation curves had been used by metallurgists. In this study, a Dilotronic dilatometer at the University of Sheffield was used. To verify that the temperature registered by the dilatometer is accurate and reliable, the thermocouples were first tested first in a thermocouple

calibration equipment: ISOTHECH Pegasus 1200. Obtaining dilatometer curves proved much more difficult than expected. The equipment is not easy to control, because its heating mechanism is by induction, and the parameters listed below have to be considered:

1. The heating by induction depends on the mass and the geometry of the sample. To control the target temperature, the heating rates, and the cooling rates as well, the mass of the sample and the area to transfer heat are fundamental parameters. Firstly, a 12 x 12 x 150mm sample of X80 steel was used to analyze the effect of the 14 parameters on the heat treatment. Thereby, the best parameters were found, but this is for a large sample. Then, using the same parameters on sample V-Mo-0.0, which had a smaller size, resulted in burning the sample. Thus, new samples needed to be produced with the same geometry as the ones provided by Tata Steel, using other microalloyed steels. To do that, special pins to hold the sample into the coils were required and the calibration process had to be repeated.

2. The induction heating depends on the material resistivity [220]. After all calibration practices mentioned above, very cautious experiments were done, to have a meticulous observation of temperature fluctuations as a function of the parameters used (Figure 39).

3. Six parameters have to be inputted for the heat P.I.D., and also for the quench P.I.D. to control the temperature of the sample:
    - Power low
    - Scanning time
    - Power high
    - Proportional
    - Integral
    - Derivative

    In addition, the other seven parameters have to be loaded to make the machine response as quick as it is desired by the user, to produce drops in the temperature, and also in the cooling system activation to underdamp or overdamp the temperature control. Those parameters are:

    - Watchdog time to P.I.D. control
    - Watchdog temperature at P.I.D. control
    - Power off when the temperature is over the set point
    - Power on when the temperature is under set point
    - Quench off temperature end of the cycle
    - Air quench on temperature over the set point
    - Air quench off temperature under set point

    Each parameter influences the temperature to control. Further, the induction heating process is very sensitive to the magnetic field strength of the material. In low-carbon steels, alloying additions, impurities, texture, and grain size influence the electrical resistance that the material produces. Heat-treated microalloyed steels require less power to heat for two main reasons: first, the alloying additions acts as impurities affecting negatively the magnetic flux through the material; second, the coarser the grain size is, the less core and hysteresis losses [221]. This produces an oscillating temperature during the process due to the sensitization of the heating plus the cooling controls (Figure 40 (a)). Even more, during the heat treatment the grain size change, and also the interphase precipitations form, producing delayed instability

of the temperature (Figure 40 (b)). To avoid that, multiple experiments with variations in almost all the parameters mentioned above were performed, analysing the effect of each of them on the resulting temperature of the sample to obtain the most stable temperature which did not oscillate thought the whole treatment time.

4. The equipment does not control the temperature when the demanded power is less than 6%, a condition which depends on the material. It was observed from several experiments, that the equipment stabilizes the temperature by an equilibrium between the heating power and cooling demand. However, when that equilibrium is obtained with an input heat power under 6%, the temperature oscillates or there is a late increase in the temperature, with the machine control disabled. Such fluctuations and late temperature rise are shown in Figure 39. To correct this, it was found that the mass of the sample must be increased. Therefore, shrouds made from the as-rolled plates of the same steel were manufactured into which the samples were placed which increased the mass and thereby increase the heating power to exceed 6%. Figure 41 shows a curve of the isothermal transformation of a steel Cr-V-Mo-0.0 at 660^0Cwith the mentioned conditions with a fluctuation of only $\pm 1^0$C. Also, it was observed that while the $\gamma \rightarrow \alpha$ transformation occurred, the heating power to hold the isothermal temperature decreased. While that, the cooling power increased until it reached the maximum programmed and after that a late growth in temperature appeared. On the other hand, late oscillation took place when the minimum set cooling power was too high, forcing the machine to activate the upper and lower temperature limits at which the cooling system turned off and turned on.

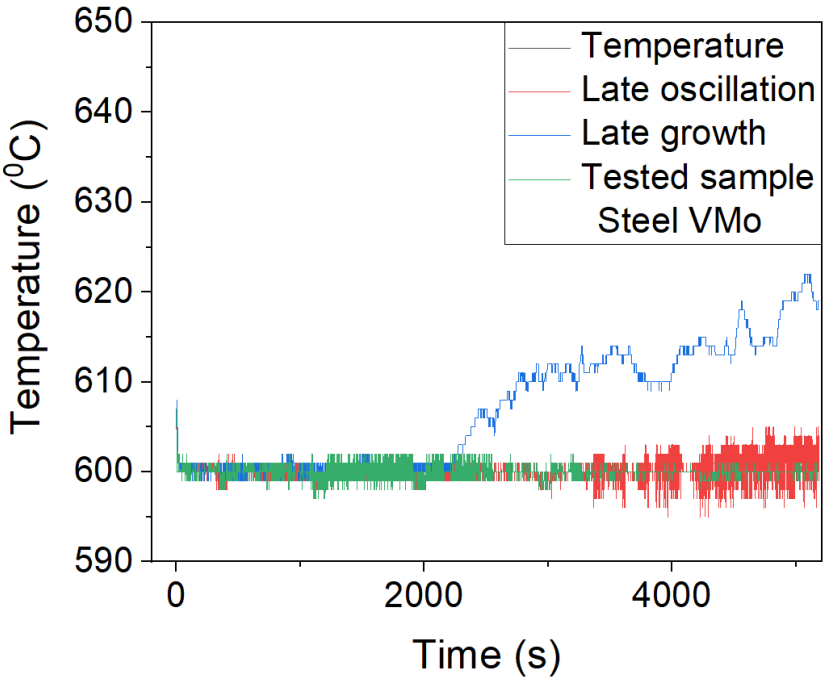

Figure 39. A Curve showing the delayed temperature growth, and also delayed temperature oscillation of microalloyed steels under induction heating. The green colour shows the temperature measured in a sample V-Mo-0.0 which had a maximum difference of $+1^0C$ and -2^0C during the aging programmed at 600^0C.

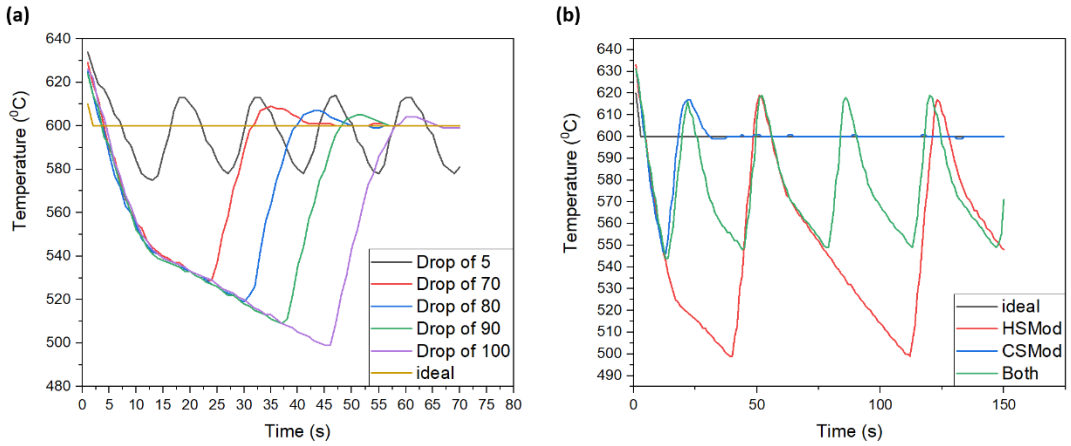

Figure 40. (a) Curves showing that the sample initially undercools by a considerable amount, followed by a rise in temperature which then overshoots the set temperature before eventually reaching the desired temperature. It has a very important effect by changing the power of the cooling system. When it is too low, it produces temperature oscillation in long period holdings. (b) A curve showing the variation on the sample temperature due to changes (reduction) only on the scanning time of the heating P.I.D. system (HSMod), quench P.I.D. system (CSMod), and them both simultaneously.

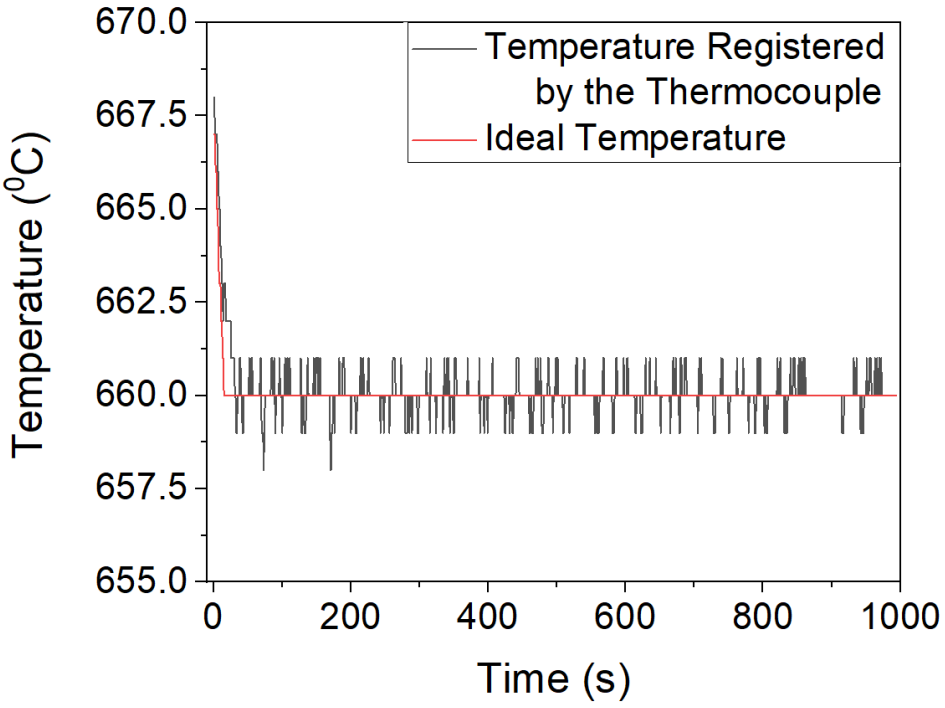

Figure 41. A curve contrasting the programmed temperature in the dilatometer against the real temperature registered in a sample of steel Cr-V-Mo-0.0.

3.3. OPTICAL AND SCANNING ELECTRON MICROSCOPY

Figure 42 shows the samples for optical metallography that were cut and mounted in bakelite. The innermost face of the samples 3 and 4 shown in the Figure 43 was facing the outside of the mounted sample. The microstructure was observed on the rolling direction (RD).

The samples were polished with silicon carbide papers under running water starting with grade 80 and ending with grade 1200 and followed by a polish with diamond cloths with based diamond suspension lubricants of 6 and 1 µm. The polished samples were cleaned with isopropanol to avoid oxidation. The polished samples then were etched. Several etchings and procedures were performed and described in the following section. Immediately after the etching, the samples were cleaned with teepol and then placed in an ultrasonic bath immersed in isopropanol for 2 minutes, and then they were stored in a desiccator to perform the optical and/or SEM analysis.

Optical microscopy was carried out on a Nikon Industrial microscope ECLIPSE LV150. Scanning electron microscopy and EDS were performed on the FEI Inspect F50 scanning electron microscope operating between 5kV and 20Kv equipped with an Oxford instruments EDS detector.

The outer 1mm from the border of the sample was ignored to avoid the decarburized zone and deeper carbon-enriched zone produced during the heat treatment, Figure 44. Moreover, in all the samples for mechanical testing, this affected zone was removed as well.

Figure 42 Samples mounted in conductive bakelite used for optical microscopy, SEM and TEM carbon extraction replicas.

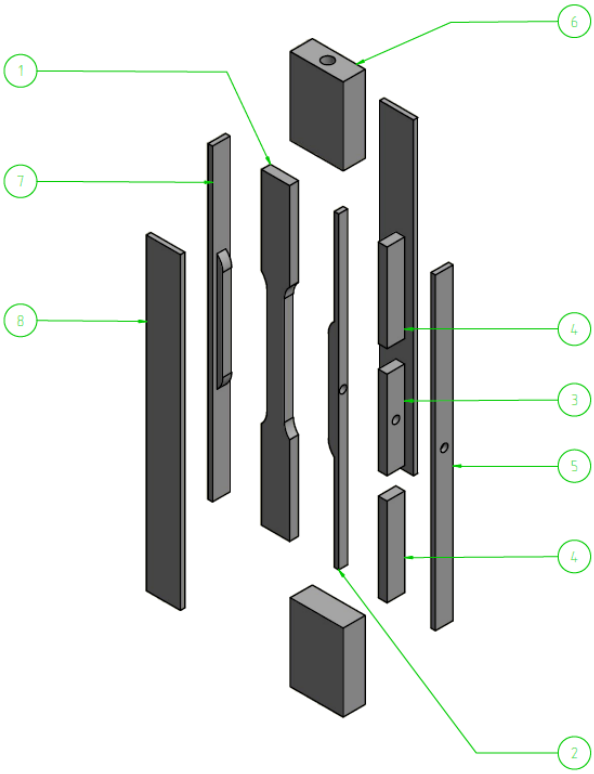

Parts List		
ITEM	QTY	DESCRIPTION
1	1	SAMPLE FOR TENSILE TEST
2	1	REMOVED VOLUME - MECHANIZED
3	1	CENTRAL SAMPLE FOR OPTICAL MICROSCOPY
4	2	SAMPLES FOR OPTICAL MICROSCOPY
6	2	REMOVED VOLUME - MECHANIZED
5	1	REMOVED PART - DECARBURIZED
7	1	REMOVED PART - DECARBURIZED
8	2	REMOVED PART - DECARBURIZED

Figure 43. scheme of the division of a sample after the dilatometry to obtain samples for metallography and tensile evaluation.

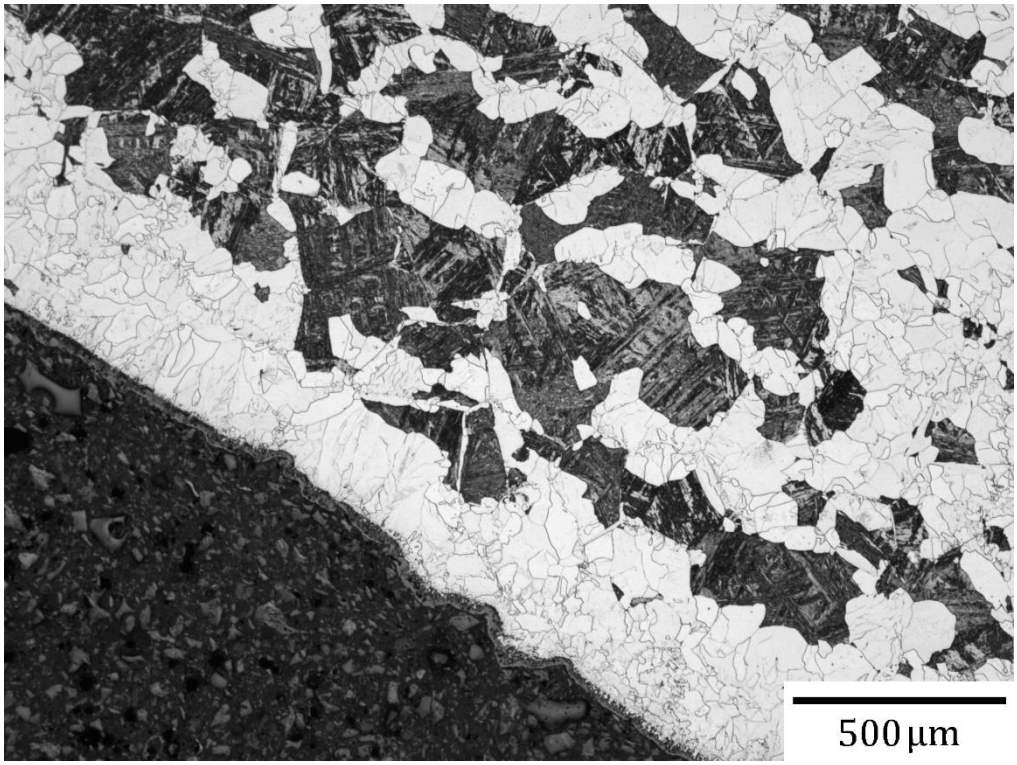

Figure 44 Optical microscopy of the sample V-Mo-0.0 aged at 650^{0}C showing the border of the sample used for dilatometry. From the border, it shows a layer of almost pure ferrite followed by a large amount of martensite.

3.4. ETCHING

Once the dilatometry tests were finished, samples were prepared using standard techniques for metallographic examination as described before. The effect of etching depend on the steel composition and heat treatment [222]. Etching reagents made from saturated aqueous picric acid with additions of wetting agents and some drops of hydrochloric acid (HCl) gave very good grain-boundaries delineation on medium- and high-carbon steels [223–225]. It is different for low-carbon alloy steels, which are very difficult to etch with picric acid or any other reagent [226]. The whole procedure to reveal the prior-austenite grain boundaries of the studied steels is described in the Annex 1.

3.4. TENSILE SPECIMENS

The tensile properties of the steels V-Mo-0.0, Cr-V-Mo-0.0 were obtained from samples following the ASTM standard [227]. Previous researchers at the University of Sheffield had cut the samples with a gauge section of 3 x 2.5 x 12.5 mm, obtaining very stable results [228].

Figure 45 a) shows a tensile sample with gauge section of 3 X 12.5 X 2.5 mm made of a steel Cr-V-Mo-0.4 with a solution annealing at 1150^0C and isothermally transformed at 660^0C, pointing out where the microstructures of the tensile sample were taken. Figure 45 b) shows a much coarser microstructure than the one showed in Figure 45 c). It is because of the distribution of the cooling nozzles in the dilatometer used for the heat treatment. During the isothermal transformation they are always active, splashing out a mist of air and water, cooling more the zones where this mist strikes than the zones facing the heating rings. When the thermocouple was placed in the middle zone of a heating disk, a constant microstructure was observed for a length of approximately 15 mm.

Tensile samples of alloys V-Mo-0.4, Cr-V-Mo-0.4, V-Mo-0.2 and Cr-Nb-V-0.2 were manufactured to guarantee that all the structure of the testing sample is homogeneous with no changes in grain size or volume fraction of the phases, and also following the recommended dimensional relationship suggested by the Great Britain and ASTM E8M standard $L_0/\sqrt{A_0} = 5$, which means a gauge section of 2 x 2.4 x 11 mm. Samples were polished with griding paper number 1000 to remove the affected area of the electrical discharge machining (EDM). The tensile tests were performed at room temperature, and at a constant cross-head speed of 0.6mm/min on the machine Zwick/Roell Z050 A 712493 in the Thermomechanical Processing Laboratory of the University of Sheffield (Figure 46).

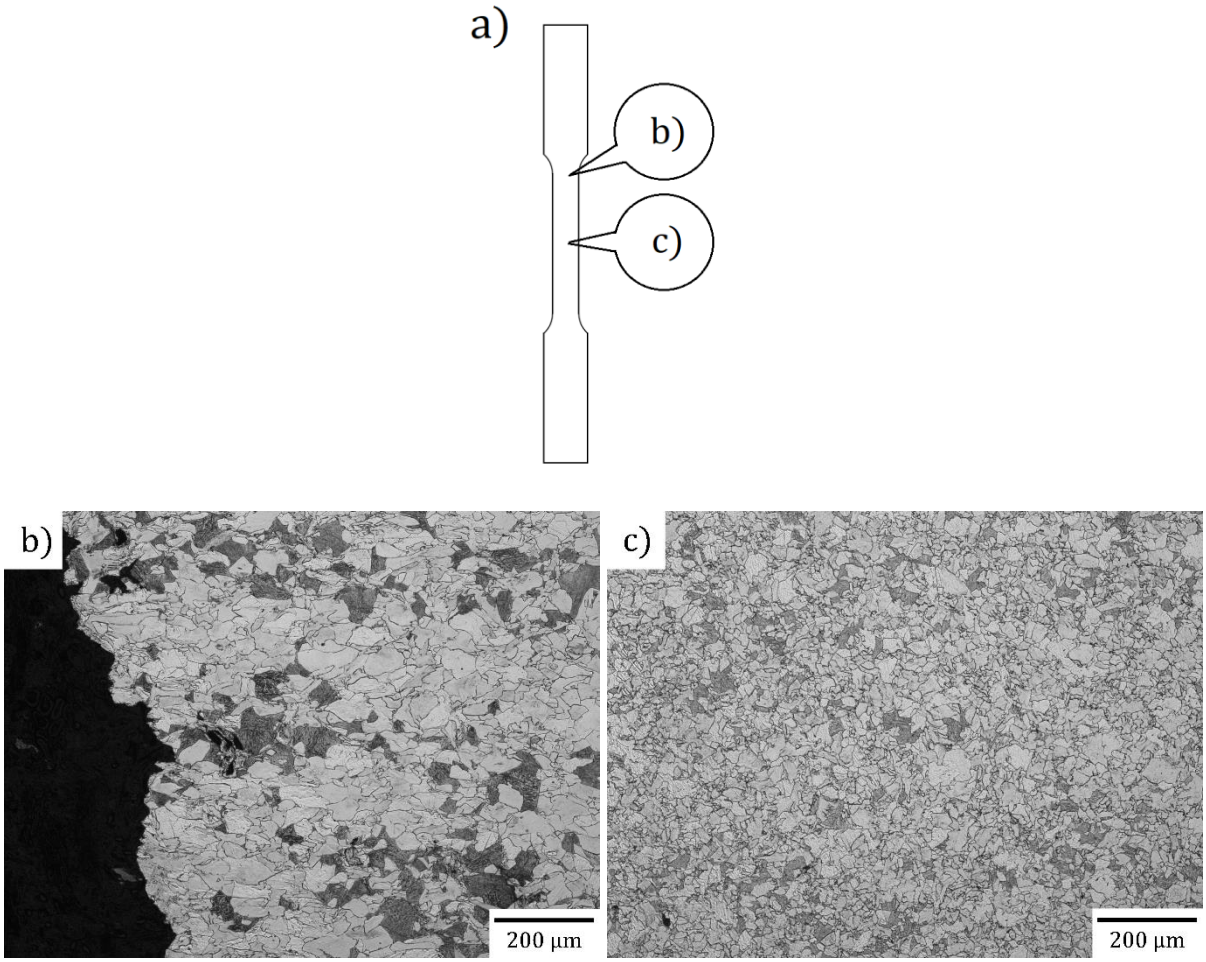

Figure 45. a) places where the microstructures had been taken. b) structure far from the center of the tensile sample. c) structure in the center of the tensile sample, which agrees with the thermocouple used to control the temperature during the dilatometry process.

Figure 46. Machine Zwick/Roell Z050 A 712493 used for the tensile tests at the University of Sheffield.

3.5. TRANSMISION ELECTRON MICROSCOPY

3.5.1. TEM CARBON EXTRACTION REPLICAS

Carbon extraction replicas of the samples were prepared to extract and then analyse the precipitates within the ferrite. After the samples were prepared using standard techniques for optical microscopy a very light etch was performed by running nital 2% with a pipette for around 4 seconds over the surface of the samples. Then a very thin film of amorphous carbon (~7nm) was deposited on the sample with a Quorum Q150T ES plus coater. The approximated thickness of the carbon deposition is provided by the same machine, which has a detector which displays the approximated thickness of the carbon deposition. Scratching with a steel blade, the carbon replicas were divided into ~2mm square grids, with the scratches facilitating the underlying surface's etching as is shown in Figure 47. The second etching consisted of immersion of the samples in 10% nital solution until very small bubbles form on the surface The sample was then placed very gently in isopropanol, where the replicas detach from the samples through the surface tension and float off, later picking up them with 400 mesh copper grids for TEM analysis.

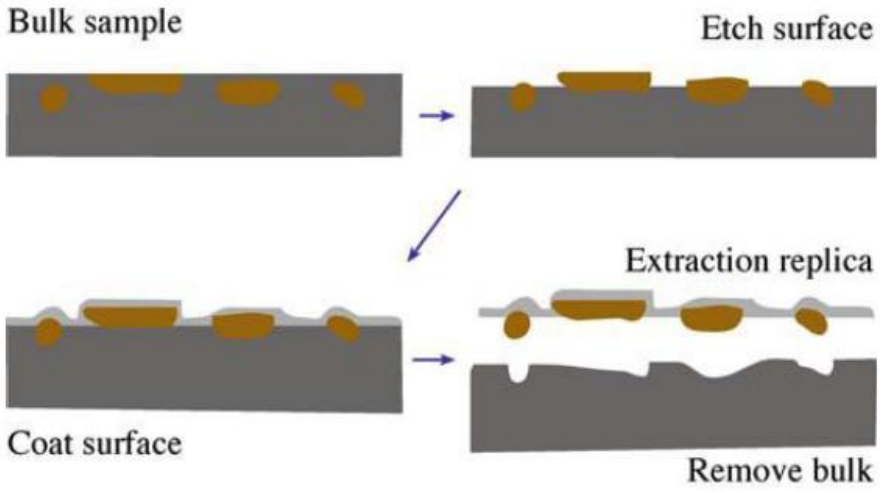

Figure 47. Scheme of the process of the carbon extraction replica [229].

3.5.2. TEM THIN FOILS

Samples for TEM thin foils were cut from the surface of the samples analyzed to obtain the microstructures within 5mm from the hole where the thermocouples were placed to control the temperature. Samples were polished to a final thickness below 0.1mm, ending with grinding paper grade 1200. All the polishing was performed under running water except for the last grade, which was performed with isopropanol to prevent oxidation. 3mm diameter disks were punched, and then further grounded to a thickness around 90µm. The final thinning of the samples was performed via electropolishing using the Metalthin twin jet electropolisher. The electropolishing conditions were

controlled at ~27mA with a jet sensitivity of 8, a temperature of -40^{0}C using an electrolyte solution of 60% methanol, 35%butoxyethanol and 5% perchloric acid.

Both extraction replicas and TEM thin foil samples were examined on a JEOL JEM F200 operating at 200 kV.

3.6. GRAIN SIZE MEASUREMENTS

To measure the mean grain size of the samples, the linear intercept method specified in the standard ASTM E-112 was performed. Optical micrographs were taken at 200x magnification, in which the microstructure and the grain size can be easily recognizable. A series of horizontal lines were drawn, guaranteeing that the minimum distance between them was greater than the largest grain within the image. Measurements of the intercepts between the horizontal lines and the grain boundaries were taken with the software Image J, gauging between 525 and 915 grains from several images of each steel, having special care with the scale and ignoring zones of martensite. The accuracy of the measurements between 0 and 5 µm is just partial because there are regions with very small grains that cannot be measured properly due to resolution limit of optical microscopy. The same procedure had been done with the images etched with picral before the pre-heating and dilatometric studies.

3.7. FERRITE VOLUME FRACTION

Image J software using areal analysis was used to measure the ferrite volume fraction. Figure 48 a) is an optical micrograph of the sample Cr-V-Mo-0.0-K06. In Figure 48 b) shows how the software recognizes the black pixels, including the grain boundaries and the dark areas produced by the pitting corrosion. To remove artefacts (such as pitting), the image was edited (Figure 48 c)) and then measured again with the software. The results from this analysis are presented in Table 15. The difference in the ferrite VF between the edited and the non-edited micrographs is between 13 and 22%, which is much higher than the greater divergence between the edited samples and the point counting (2.35%).

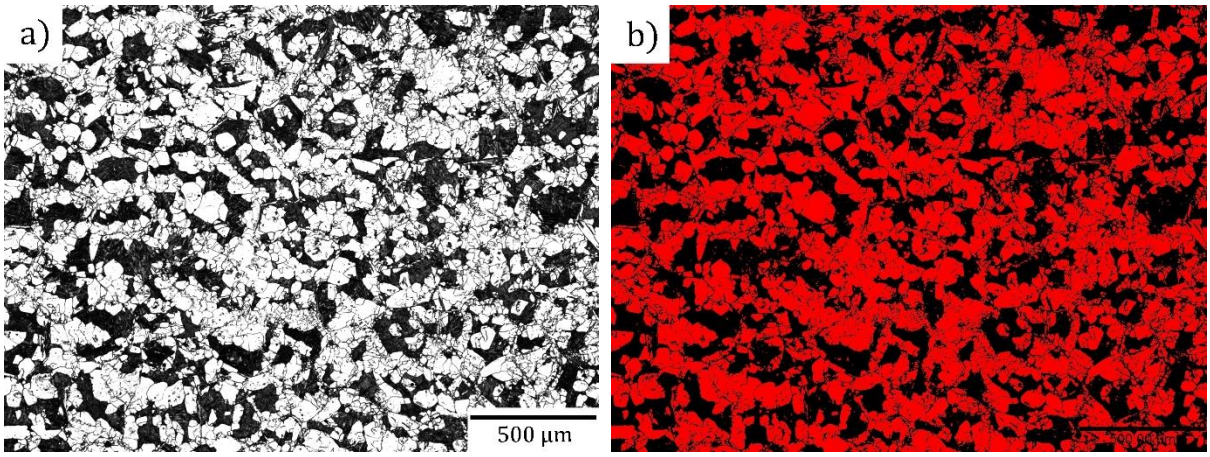

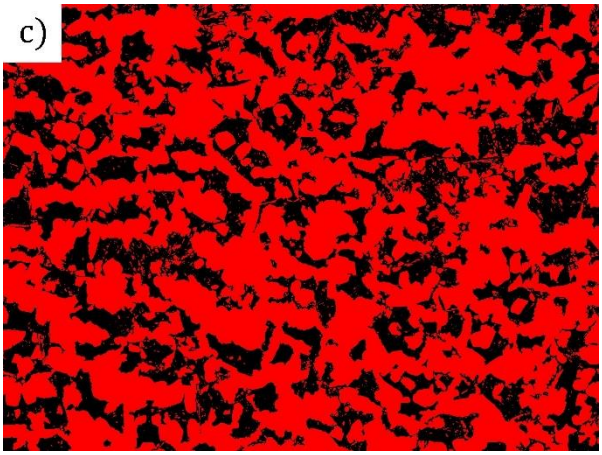

Figure 48. Micrograph of the sample Cr-V-Mo-0.0 a) as it was taken b) as the software image J record the pixels of the clearest areas of the as taken micrograph. c) as the software image J record the clearest pixels of the edited micrograph.

According to Higginson and Sellars [230], to measure the volume fraction by point counting between 400 and 500 points are required. A matrix of points of spacing 95µm was created within each micrograph and divided into 9 square traverses, each of 48 points, for a total of 432 points per micrograph.

Sample	Ferrite VF measured on as taken micrograph	Ferrite VF measured on the edited micrograph	Ferrite VF obtained via point counting
Cr-V-Mo-0.0 – 660^{0}C T_{Ag}	53.03%	74.1%	74.2%
Cr-V-Mo-0.0 – 625^{0}C T_{Ag}	58.4%	72.0%	69.7%
Cr-V-Mo-0.0 – 600^{0}C T_{Ag}	55.69%	75.9%	76.5%

Table 15. Ferrite volume fraction measured via Image J software with micrographs a) as taken, b) edited to increase the contrast and to erase grain

3.8. PRECIPITATES SIZES AND DISTRIBUTION

For precipitate size and distribution analysis, TEM images taken from the carbon extraction replicas were used. Several images from random areas within the samples were taken and manually filtered for further analysis with the software ImageJ function “Analyze particles” (Figure 49). The software registers the particles’ projections in square nanometres, so these areas were analysed assuming that the majority of them were spheres, and the particles diameter were obtained from them. From each sample, at least 10,000 particles were measured. The detailed calculation process is shown in section 4.6.

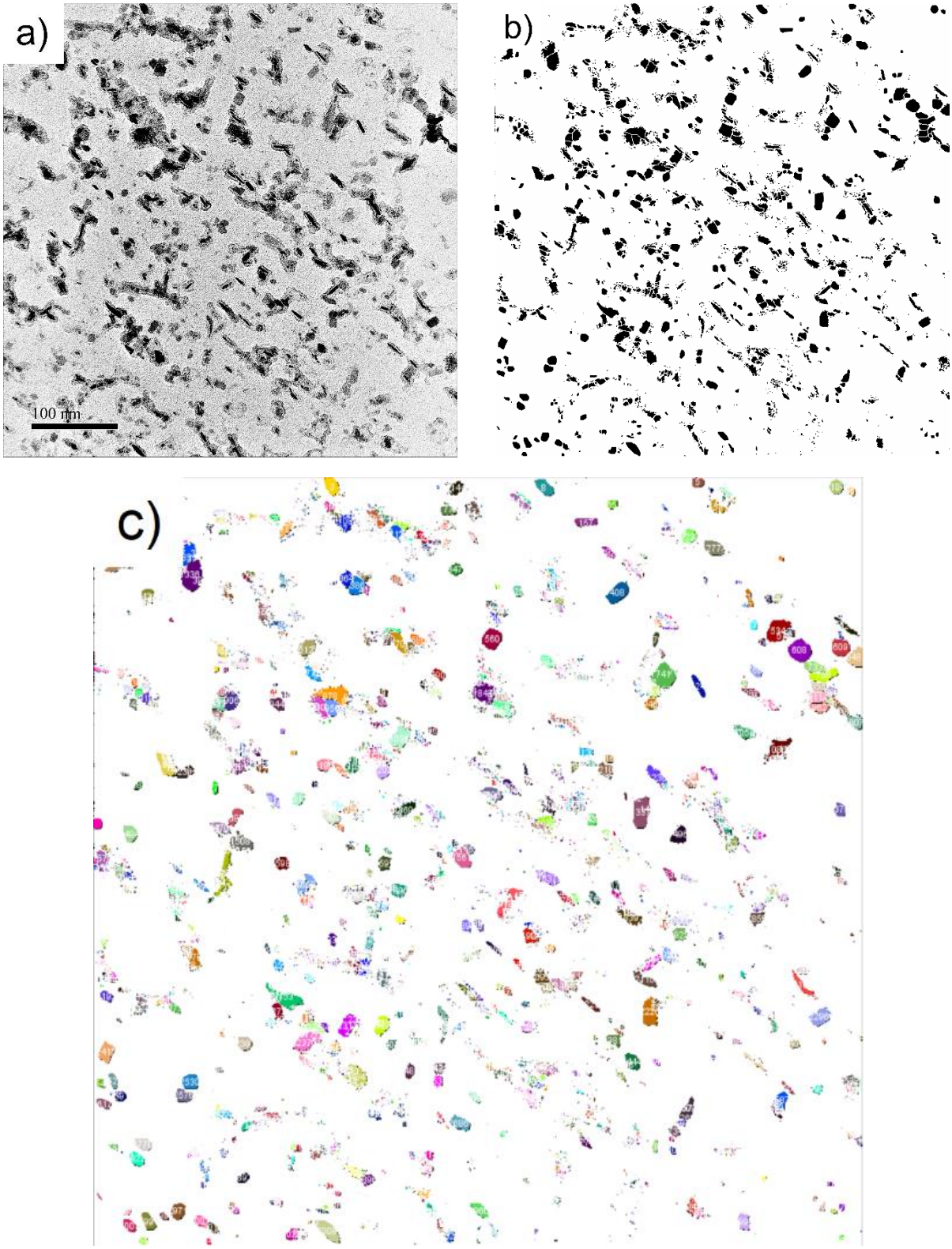

Figure 49. Interphase precipitation analysis with the software ImageJ. a) TEM micrograph of a carbon replica extraction from a sample of steel Cr-V-Mo-0.4 austenitized at 900^{0}C and isothermally transformed at 660^{0}C, b) micrograph filtered to minimize error during the particle area calculation, c) result of the "Analyse particles" function of the software ImageJ.

CHAPTER 4: RESULTS

4.1. DILATOMETRY

4.1.1. TRANSFORMATION TIMES

From Figure 50 to Figure 56 show the dilatation charts of the studied steels. From Table 16 to Table 22 summarize the transformation times. Steels V-Mo-0.0 and Cr-V-Mo-0.0 were austenitized at 1250^0C and isothermally transformed at 600, 625, and 650^0C. The dilatometry charts are shown in Figure 50 and Figure 51. For temperatures around 650^0C, the addition of Cr very slightly reduces the rate of transformation. The transformation at 625^0C was faster for the steel with no Cr addition, but again the value increased with isothermal transformation at 600^0C. The transformation time for steel Cr-V-Mo-0.0 reduces with the isothermal transformation temperature decrease.

Dilatometry tests for steels V-Mo-0.4 and Cr-V-Mo-0.4 were designed to evaluate different austenitization temperatures to maximize the $\gamma \rightarrow \alpha$ transformation. After observation of steels V-Mo-0.0 and Cr-V-Mo-0.0, steels V-Mo-0.4 and Cr-V-Mo-0.4 were designed to reevaluate the chemical compositions of alloys V-Mo-0.0 and Cr-V-Mo-0.0, while avoiding the over-heating in the austenitization, and also observing the changes caused by the hot-work rate. Figure 52 and Figure 53 present the dilatometry charts of steels V-Mo-0.4 and Cr-V-Mo-0.4 respectively at different austenitization temperatures. The transformation time was still faster in V-Mo-0.4 for austenitization at 1150^0C. In steel Cr-V-Mo-0.4 the transformation rate reduces with temperature, so the faster transformation was obtained at the lowest austenitization temperature.

From Figure 54 and Figure 55, it is clear that a reduction in transformation kinetics produces a smaller strain rate. From steels Cr-V-Mo-0.4 and Cr-V-Mo-0.2 we can conclude that the Cr addition accelerates the transformation kinetics of microalloyed steels. This same conclusion also can be done for microalloyed steels with Cr+Nb additions from Figure 56. Complementary with the microstructure analysis, it is not possible to base conclusions on steels V-Mo-0.0 and Cr-V-Mo-0.0 because the process was not fully controlled leading to other phenomena occurring, such as massive grain growth, which clearly affect the kinetics of the $\gamma \rightarrow \alpha$ transformation.

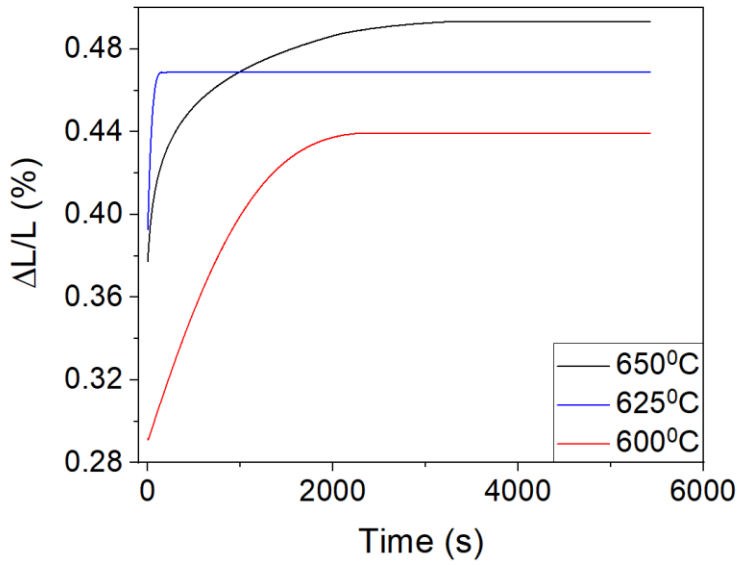

Figure 50. Dilatation curves of V-Mo-0.0 Steel samples with solution annealing over 1250⁰C and all isothermally treated at 600⁰C, 625⁰C, and 650⁰C.

Isothermal Transformation [⁰C]	***Time [s]***
600	~2250
625	~250
650	~3320

Table 16. Transformation times for steel V-Mo-0.0 with solution annealing over 1250⁰C and isothermally transformed at 600⁰C, 625⁰C, and 650⁰C.

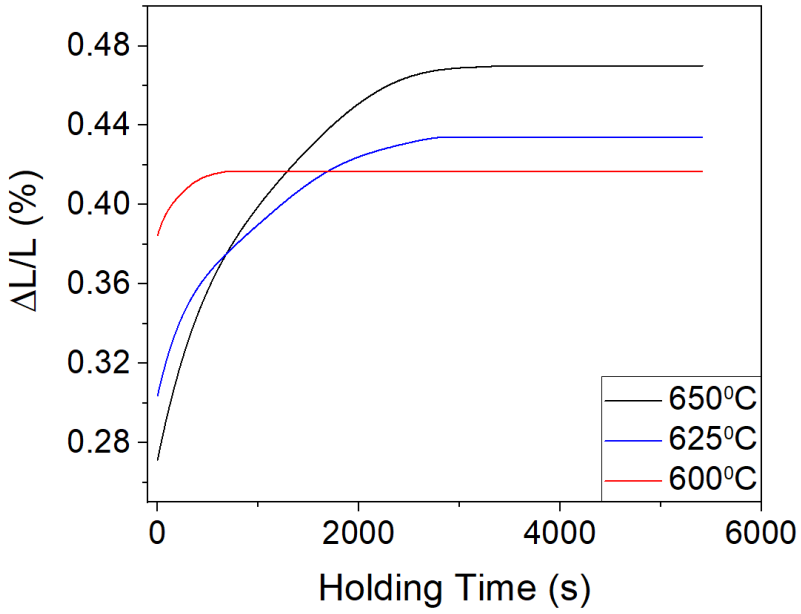

Figure 51. Dilatation curves of Cr-V-Mo-0.0 Steel samples with solution annealing over 1250⁰C and all isothermally treated at 600⁰C, 625⁰C, and 650⁰C.

Isothermal Transformation [⁰C]	***Time [s]***
600	~700
625	~2830
650	~3540

Table 17. Transformation times for steel Cr-V-Mo-0.0 with solution annealing over 1250⁰C and isothermally transformed at 600⁰C, 625⁰C, and 650⁰C.

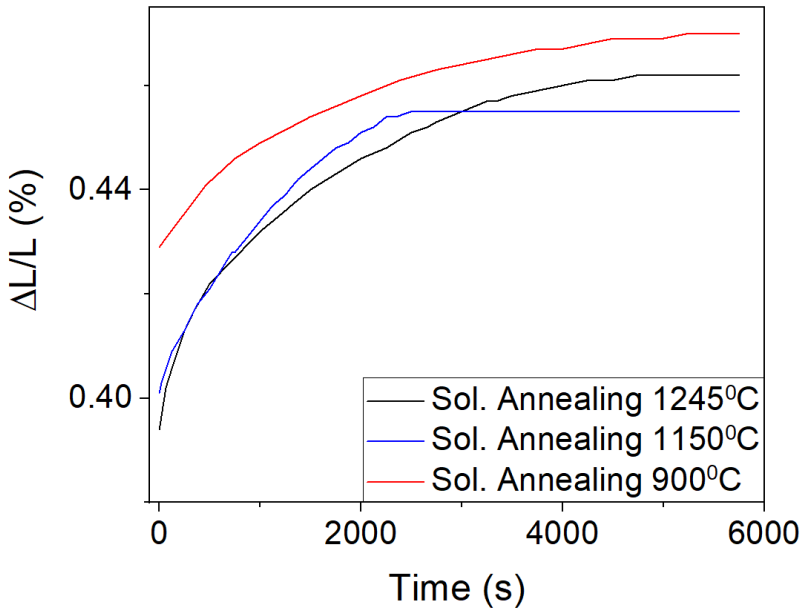

Figure 52. Dilatation curves of V-Mo-0.4 Steel samples with solution annealing at 900⁰C, 1150⁰C, 1245⁰C, and all isothermally treated at 650⁰C.

Austenitization [⁰C]	***Time [s]***
900	~5300
1150	~2625
1245	~4730

Table 18. Transformation times for steel V-Mo-0.4 with solution annealing at 900⁰C, 1150⁰C, 1245⁰C, and all isothermally treated at 650⁰C.

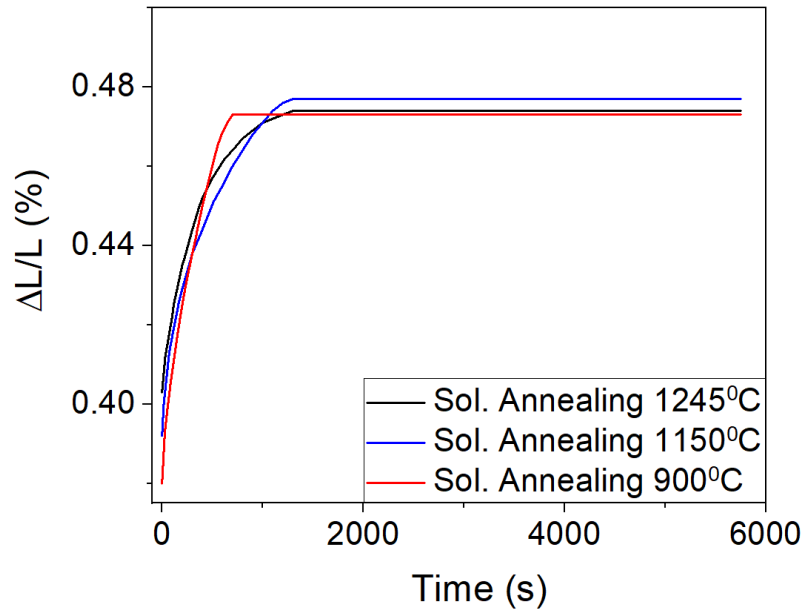

Figure 53. Dilatation curves of Cr-V-Mo-0.4 Steel samples with solution annealing at 900⁰C, 1150⁰C, 1245⁰C, and all isothermally treated at 660⁰C.

Austenitization [⁰C]	***Time [s]***
900	~750
1150	~1300
1245	~1400

Table 19. Transformation times for steel Cr-V-Mo-0.4 with solution annealing at 900⁰C, 1150⁰C, 1245⁰C, and all isothermally treated at 660⁰C.

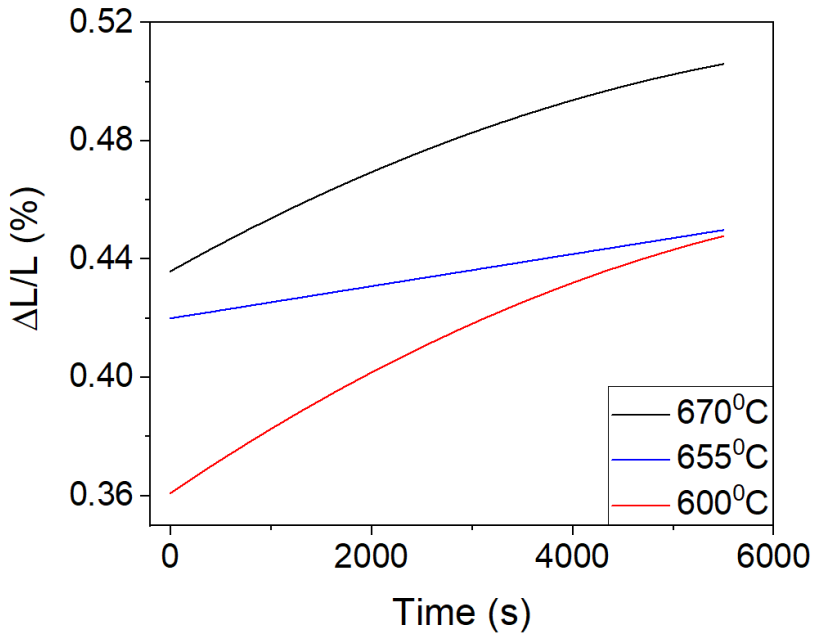

Figure 54. Dilatation curves of V-Mo-0.2 Steel samples with solution annealing at 1100^{0}C and all isothermally treated at 600^{0}C, 655^{0}C, and 670^{0}C.

Isothermal Transformation [^{0}C]	***Time [s]***
600	>5400
655	>5400
670	>5400

Table 20. Transformation times for steel V-Mo-0.2 with solution annealing at 1100^{0}C and isothermally transformed at 600^{0}C, 655^{0}C, and 670^{0}C

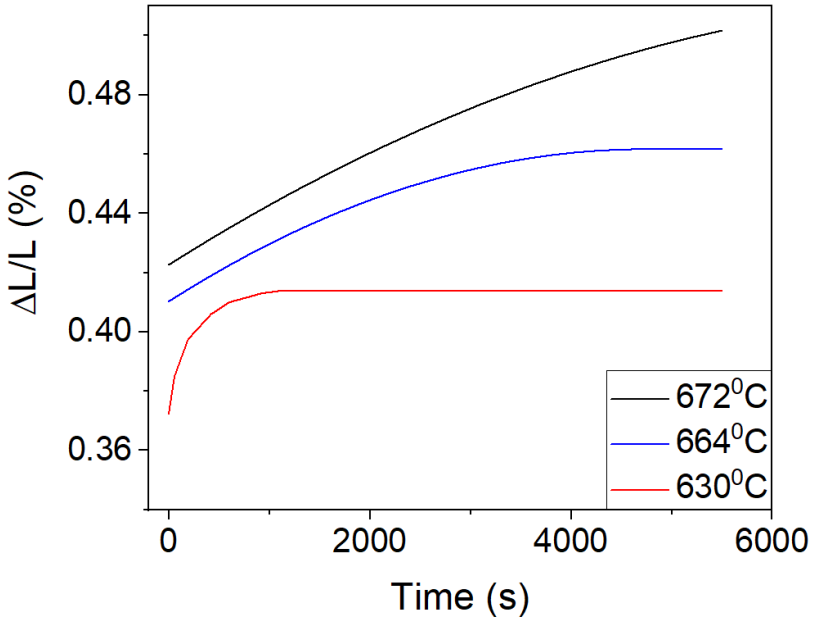

Figure 55. Dilatation curves of Cr-V-Mo-0.2 Steel samples with solution annealing at 1245^{0}C and all isothermally treated at 630^{0}C, 664^{0}C, and 672^{0}C.

Isothermal Transformation [^{0}C]	***Time [s]***
630	~1100
664	~4650
672	>5400

Table 21. Transformation times for steel Cr-V-Mo-0.2 with solution annealing at 1245^{0}C and isothermally transformed at 630^{0}C, 664^{0}C, and 672^{0}C.

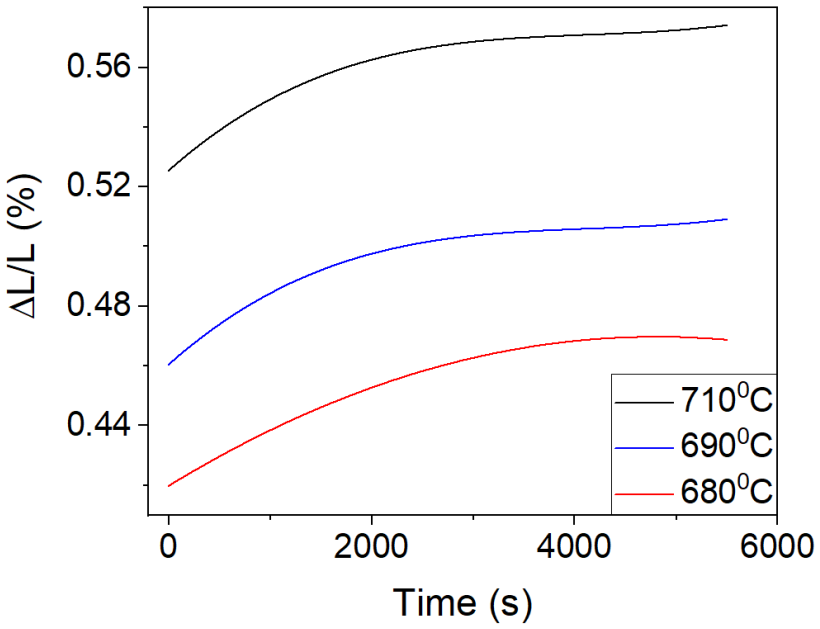

Figure 56. Dilatation curves of Cr-Nb-V-0.2 Steel samples with solution annealing at 1145⁰C and all isothermally treated at 680⁰C, 690⁰C, and 710⁰C.

Isothermal Transformation [⁰C]	***Time [s]***
680	~4580
690	>5400
710	>5400

Table 22. Transformation times for steel Cr-Nb-V-0.2 with solution annealing at 1145⁰C and isothermally transformed at 680⁰C, 690⁰C, and 710⁰C.

4.1.2. PRIOR AUSTENITE GRAIN SIZE

Figure 57 a) and b) show the prior austenite grain size of samples of steels Cr-V-Mo-0.0, before and after the dilatometry experiments. Figure 58 gives the dilatometer time vs temperature chart of an Cr-V-Mo-0.0 sample during austenitization. It shows that a very stable temperature is achieved at the expense of the response time of the machine. However, a short overshoot in temperature above the set temperature of 1200⁰C was recorded at the start of the heating cycle. The registration system of the dilatometer only records temperature once per second, but during the heating, there are some points where the temperature rises more than 50 degrees in a second. To be sure that the temperature was controlled with high accuracy, for each following test the thermocouple was first tested in a thermocouple tester PEGASUS 1200.

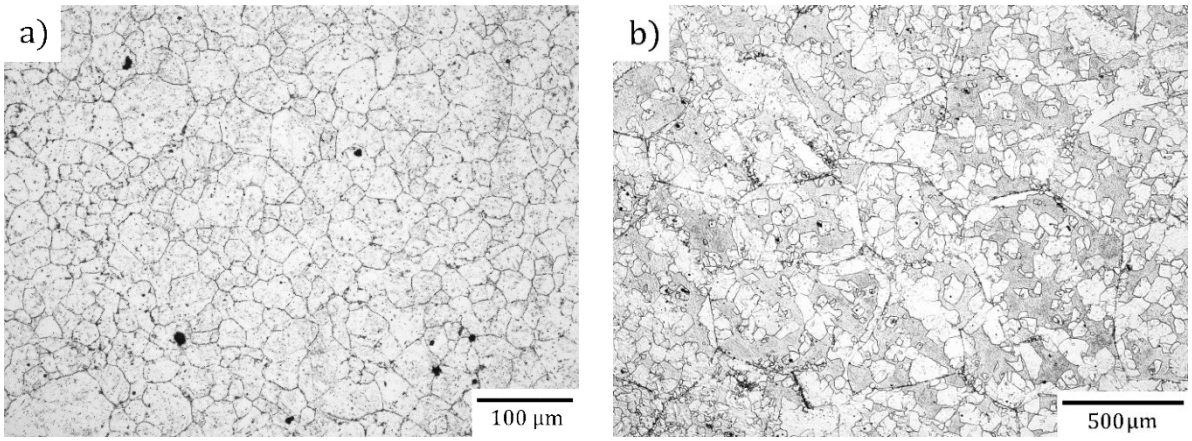

Figure 57. a) Micrograph of a sample of steel Cr-V-Mo-0.0 just before the dilatometry, b) micrograph of a sample of steel Cr-V-Mo-0.0 after the dilatometry treatment with soaking at 625⁰C. Both samples were etched with picral, showing the austenite grain size.

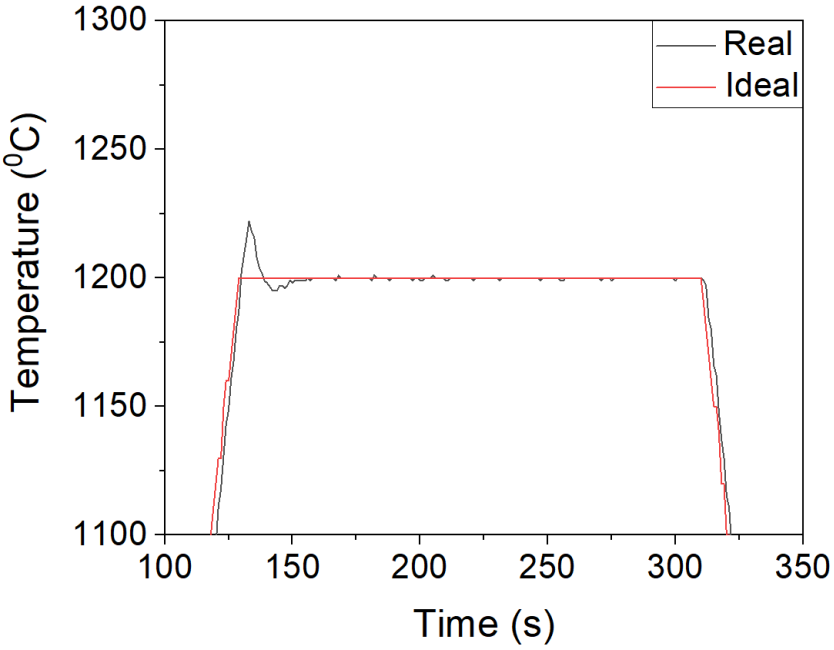

Figure 58. Graph showing the temperature excess at the start of heating in a dilatometry testing of the samples.

As described in the Experimental Procedure section, two new steels V-Mo-0.4 and Cr-V-Mo-0.4 were produced and then homogenized and then hot-rolled. The as-rolled austenite grain sizes of these steels are shown in Figure 59 showing that steel Cr-V-Mo-0.4 has a slightly finer austenite grain size after hot rolling compared to steel V-Mo-0.4.

The process of etching is complicated in MA steels because of variations in chemical composition, heat treatments and other not well-identified factors which affect the chemical etching effect[222]. This was addressed by the procedure described in the paper "A new approach to etching low-carbon microalloyed steels to reveal prior austenite grain boundaries and the dual-phase microstructure", an appendix in this thesis. Samples from the centre of the as-rolled plates were used to evaluate the prior-austenite grains size as a function of solution treatment temperature. Figure 60 to Figure 64 show the prior-austenite grains in steels V-Mo-0.4, Cr-V-Mo-0.4, V-Mo-0.2, Cr-V-Mo-0.2 and Cr-Nb-V-0.2. After each figure, there is a table showing the measured values.

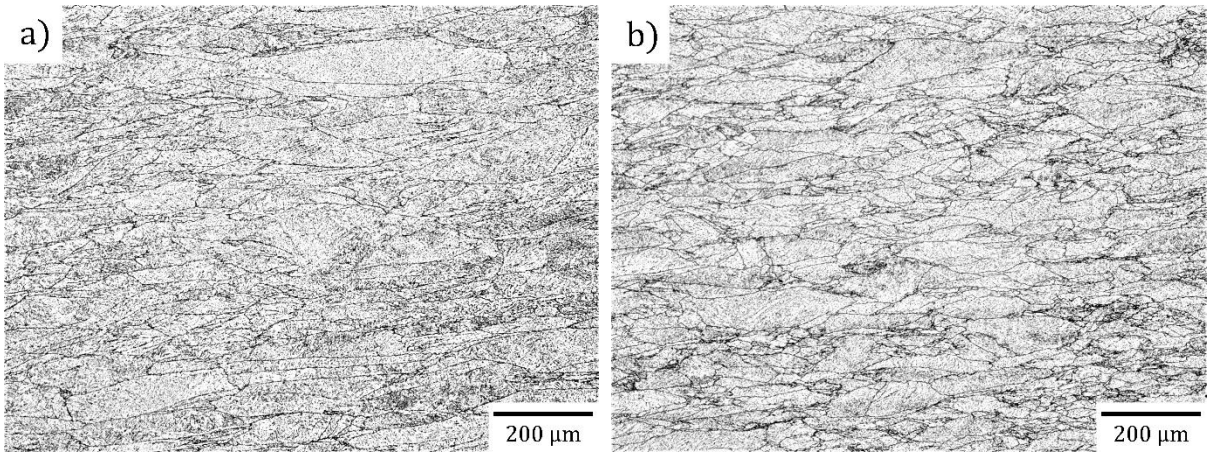

Figure 59. As-rolled MA steels, a) V-Mo-0.4, b) Cr-V-Mo-0.4, etched with picral solution to show the prior austenite grain sizes.

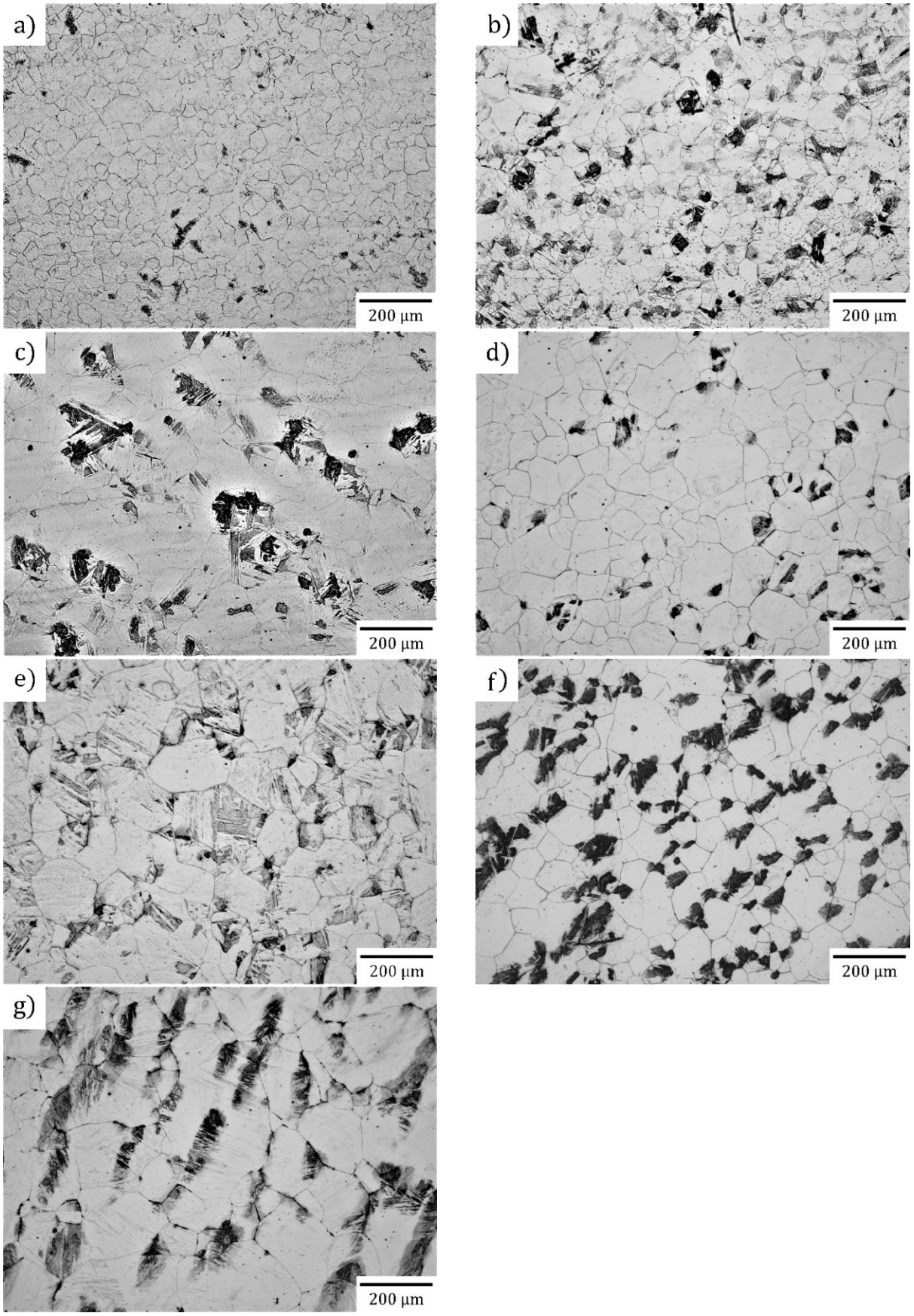

Figure 60. Prior austenite of: a) steel V-Mo-0.4 recovered at 1000^{0}C, b) steel V-Mo-0.4 recovered at 1050^{0}C, c) steel V-Mo-0.4 recovered at 1100^{0}C, d) steel V-Mo-0.4 recovered at 1150^{0}C, e) steel V-Mo-0.4 recovered at 1200^{0}C, f) steel V-Mo-0.4 recovered at 1250^{0}C, g) steel V-Mo-0.4 recovered at 1300^{0}C.

Solution Annealing Temperature (C)	Prior Austenite Grain Size (µm)	Standard Error
1000	30	0.9
1050	44	1.5
1100	56	2
1150	57	1.4
1200	63.1	1.7
1250	65.2	1.9
1300	110.5	2.9

Table 23 . Prior austenite grain size of alloy V-Mo-0.4.

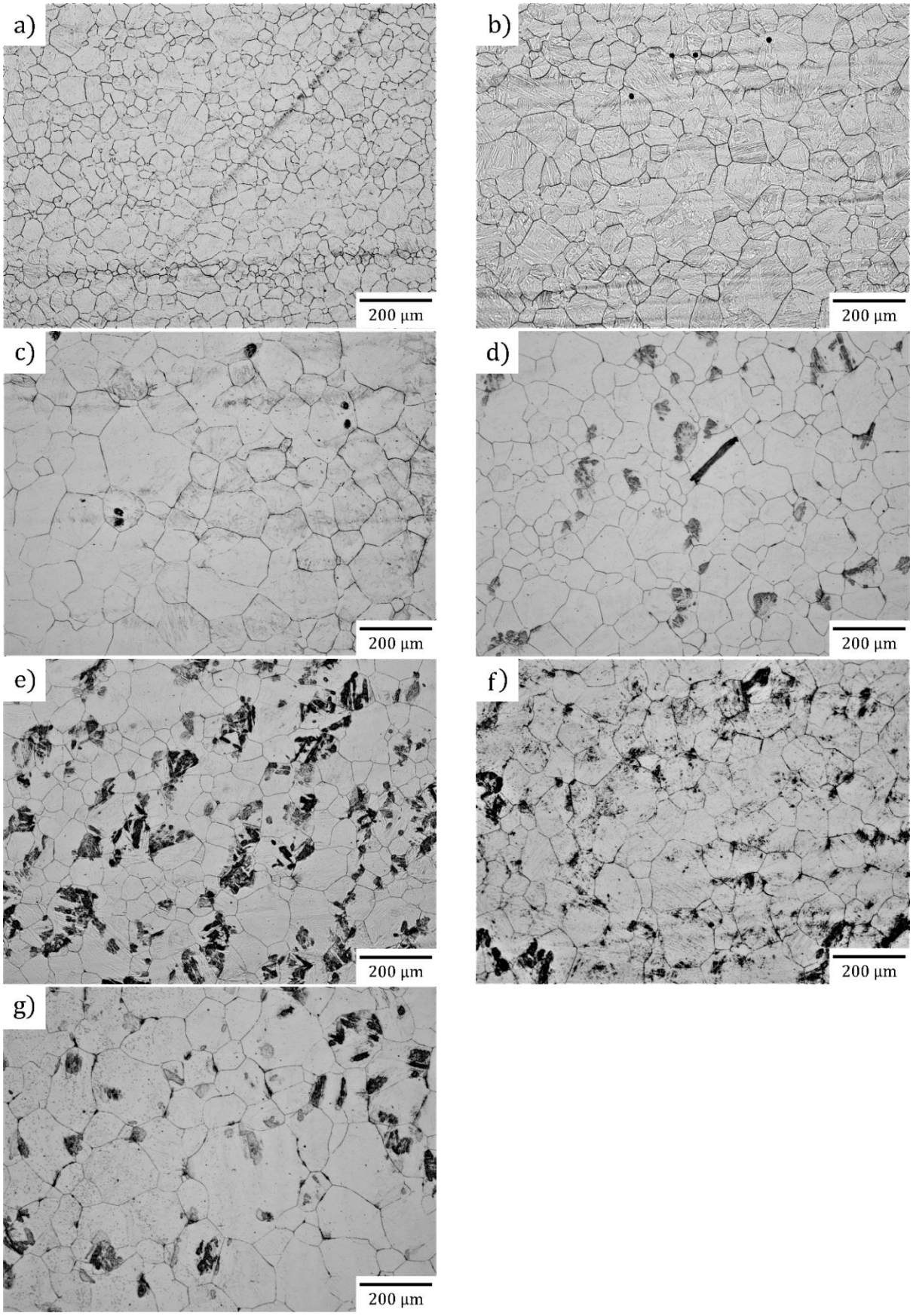

Figure 61. Prior austenite of: a) Steel Cr-V-Mo-0.4 recovered at 1000^{0}C, b) Steel Cr-V-Mo-0.4 recovered at 1050^{0}C, c) Steel Cr-V-Mo-0.4 recovered at 1100^{0}C, d) Steel Cr-V-Mo-0.4 recovered at 1150^{0}C, e) Steel Cr-V-Mo-0.4 recovered at 1200^{0}C, f) Steel Cr-V-Mo-0.4 recovered at 1250^{0}C. g) Steel Cr-V-Mo-0.4 recovered at 1300^{0}C.

Solution Annealing Temperature (C)	Prior Austenite Grain Size (µm)	Standard Error
1000	32	0.7
1050	47	1
1100	54	1.7
1150	52	1.4
1200	51	1.5
1250	58.4	1.6
1300	85.9	2.6

Table 24. Prior austenite grain size of alloy Cr-V-Mo-0.4.

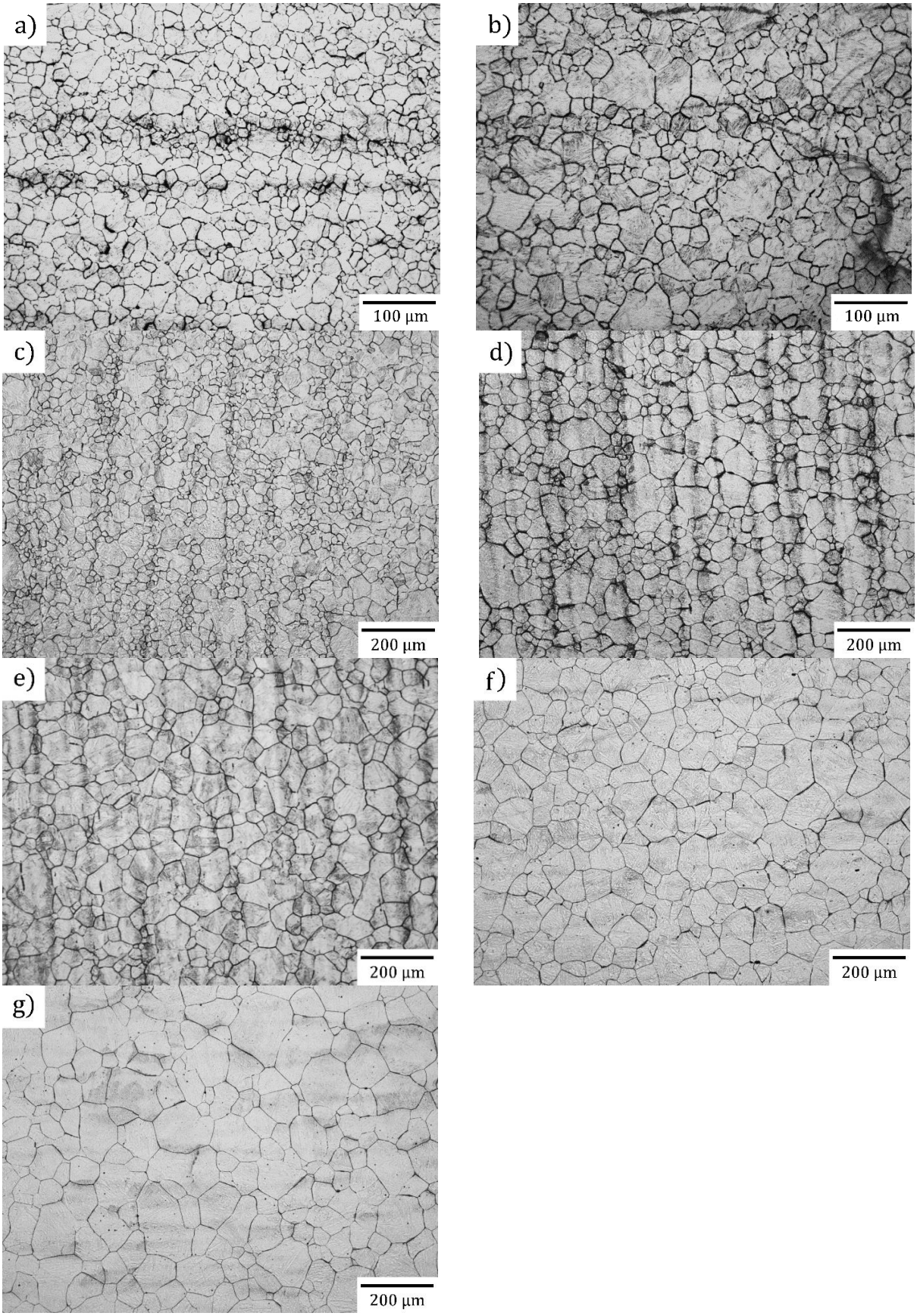

Figure 62. Austenite grain size of alloy V-Mo-0.2 treated at solution annealing temperature of: a) 1000^{0}C, b) 1050^{0}C, c) 1100^{0}C, d) 1150^{0}C, e) 1200^{0}C, f) 1250^{0}C, g) 1300^{0}C.

Solution Annealing Temperature (C)	Prior Austenite Grain Size (µm)	Standard Error
1000	10.9	0.2
1050	14.4	0.4
1100	16.2	0.4
1150	29.5	0.6
1200	31	0.6
1250	42	1.0
1300	52.2	1.4

Table 25. Prior austenite grain size of alloy V-Mo-0.2.

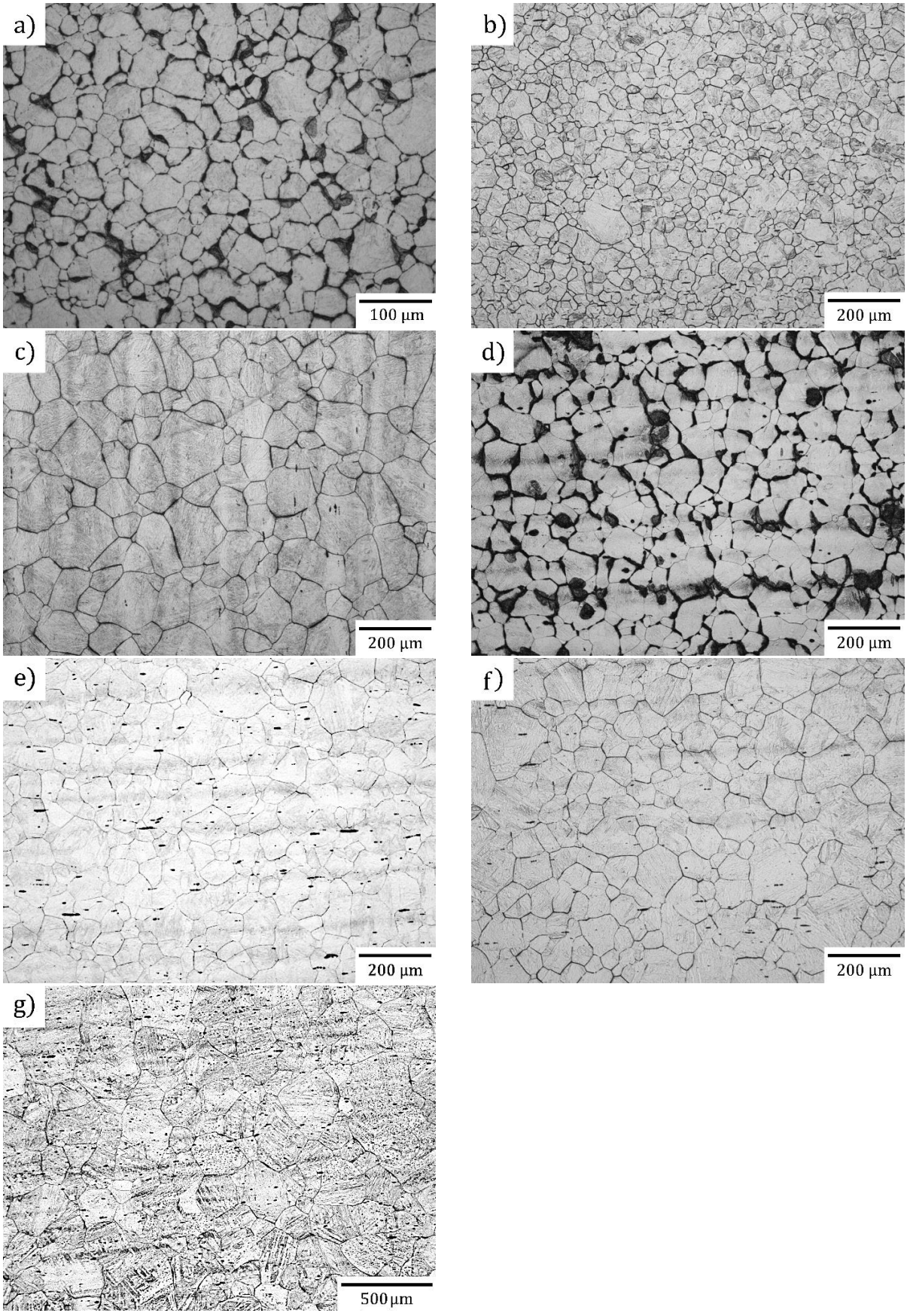

Figure 63. Austenite grain size of alloy Cr-V-Mo-0.2 treated at solution annealing temperature of: a) 1000^{0}C, b) 1050^{0}C, c) 1100^{0}C, d) 1150^{0}C, e) 1200^{0}C, f) 1250^{0}C, g) 1300^{0}C.

Solution Annealing Temperature (C)	Prior Austenite Grain Size (µm)	Standard Error
1000	20.2	0.5
1050	23.4	0.5
1100	45.3	1.4
1150	41.7	1.1
1200	38.4	0.8
1250	41.3	1.1
1300	97.1	3.5

Table 26. Prior austenite grain size of alloy Cr-V-Mo-0.2.

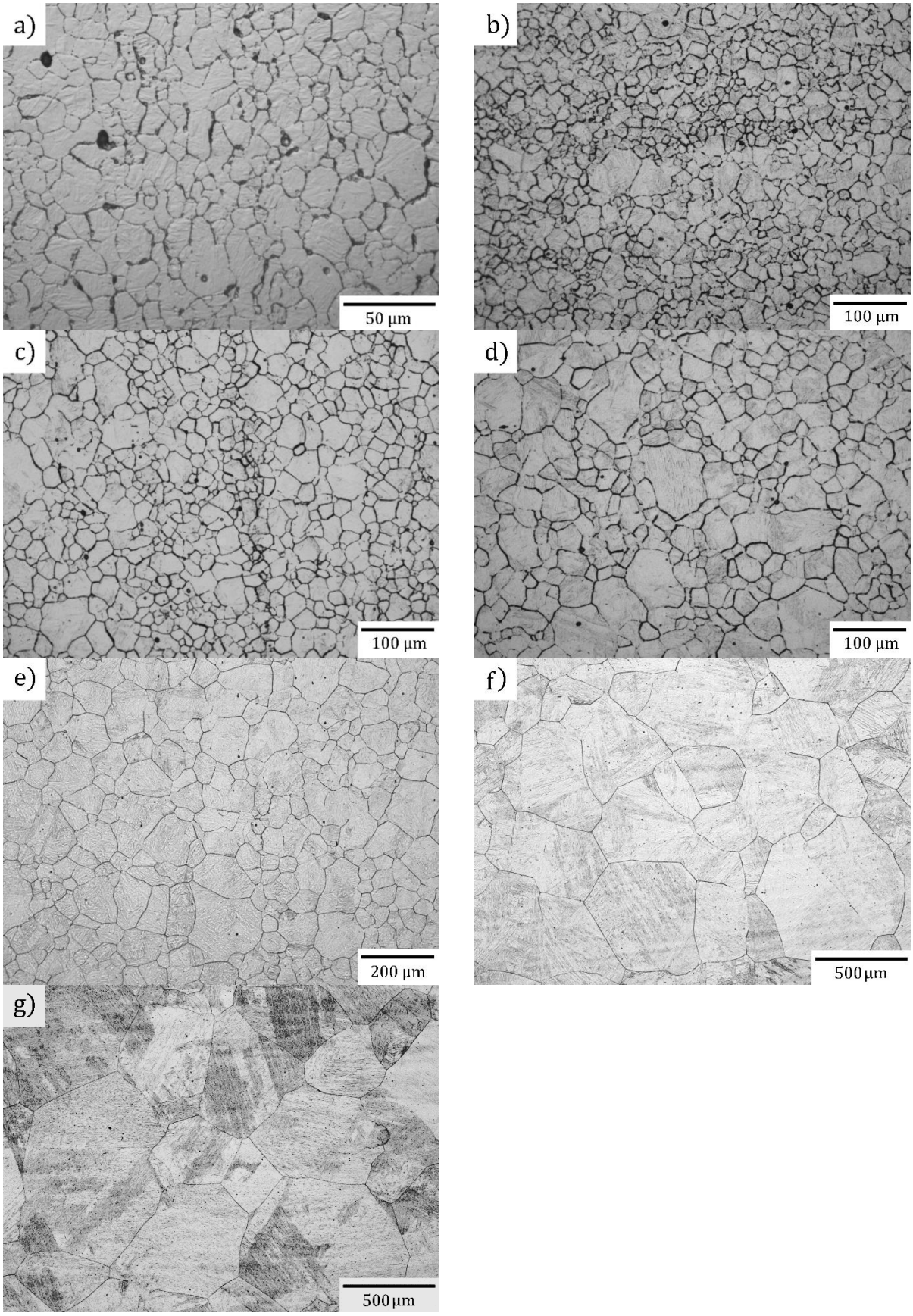

Figure 64. Austenite grain size of alloy Cr-Nb-V-0.2 treated at solution annealing temperature of: a) 1000^{0}C, b) 1050^{0}C, c) 1100^{0}C, d) 1150^{0}C, e) 1200^{0}C, f) 1250^{0}C, g) 1300^{0}C.

Solution Annealing Temperature (C)	Prior Austenite Grain Size (µm)	Standard Error
1000	6.7	0.2
1050	9.3	0.2
1100	13.6	0.3
1150	16.3	0.4
1200	43	1.0
1250	171	8.1
1300	199.8	13.4

Table 27. Prior austenite grain size of alloy Cr-Nb-V-0.2.

Figure 65 shows that microalloyed steels with and without Cr present fully recovered prior-austenitic grains at 1000 ^{0}C, growing reasonably quickly up to 1100 ^{0}C. Grain growth was relatively constant for around 150 ^{0}C and then shows a much more rapid rate of grain growth between 1250 and 1300 ^{0}C. In steels with a higher reduction per pass at the rolling process (V-Mo-0.4 and Cr-V-Mo-0.4), only a very slight grain size reduction observed in the steel with Cr addition. The steels with less reduction per pass at the rolling process show a smaller average prior-austenite grain size for the same total elongation. Also, steels with no Cr addition have a smaller average prior austenitic grain size. Steel with Nb+Cr addition shows a very fine prior-austenite grain sizes and a lower grain coarsening temperature, of around 1200^{0}C.

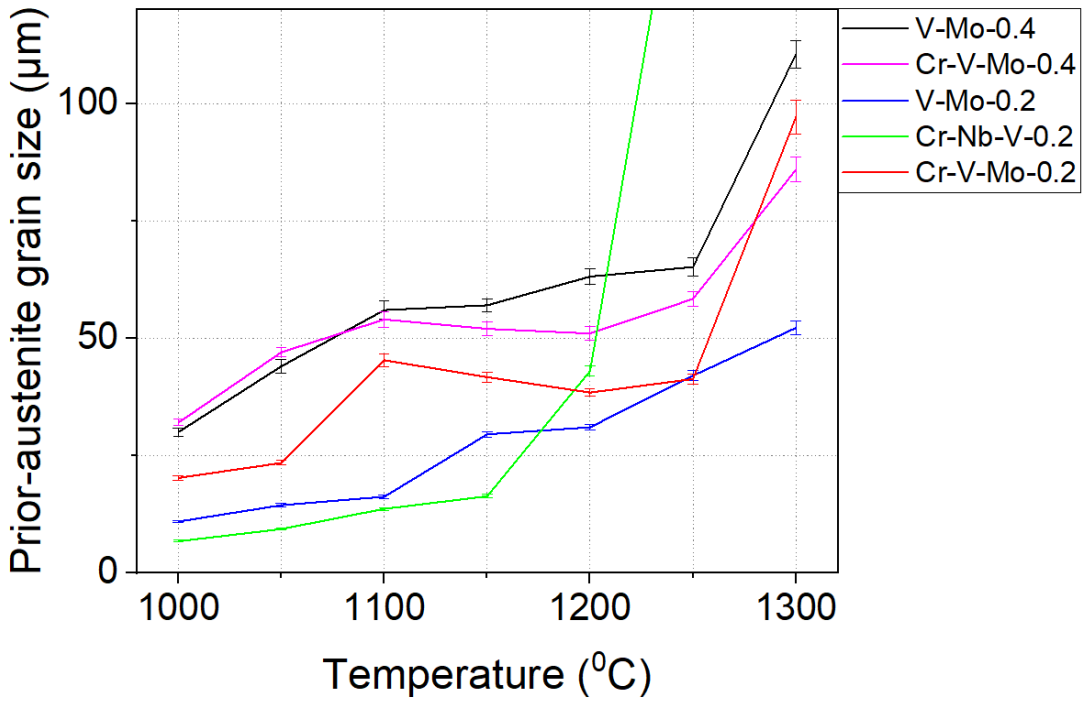

Figure 65. Prior austenite-grain size of the steels V-Mo-0.4, Cr-V-Mo-0.4, V-Mo-0.2, Cr-V-Mo-0.2 and Cr-Nb-V-0.2 as a function of the temperature.

4.2. MICROSTRUCTURE EVOLUTION

Figure 66 – Figure 72 show the microstructure of steels V-Mo-0.0 and Cr-V-Mo-0.0 isothermally transformed at different temperatures. In alloy V-Mo-0.0, the transformation at 600^{0}C mainly produces bainite with some Widmanstätten (α_w), acicular (α_a)and idiomorphic (α_i)ferrite. Micrographs of steel V-Mo-0.0 aged at 600^{0}C after more prolonged etching are shown in Figure 66 c). This shows Widmanstätten (α_w) ferrite forming at the prior austenite grain boundaries, allowing clear identification of the prior austenite boundaries. Regions of idiomorphic ferrite obscured the prior austenite boundary location.

As the transformation temperature was increased, polygonal ferrite replaced the Widmastätten and acicular ferrite grains, reflecting a difference in growth kinetics. Figure 67 and Figure 68 c) show secondary Widmanstätten laths 'degenerating' as Zackay and Aaronson[231] described before, reducing the inter-lath distance, adopting the polygonal shape, indicating lower misfit with the inclusions where these ferrite grains nucleated[44].

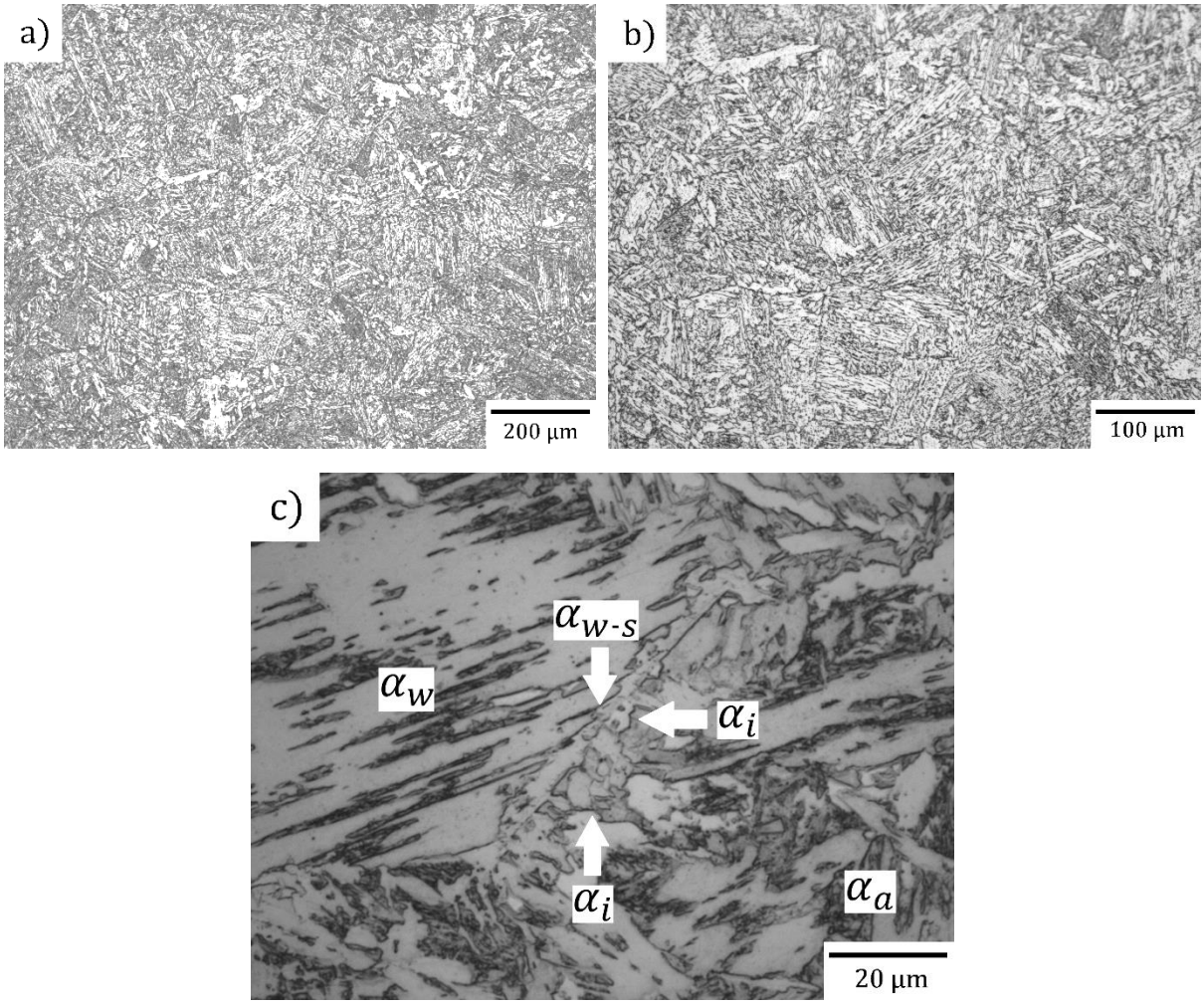

Figure 66. Optical micrographs of steel V-Mo-0.0 Isothermally transformed at 600^{0}C at: a) 50X b) 100X. c) 500X with more nital-etching time.

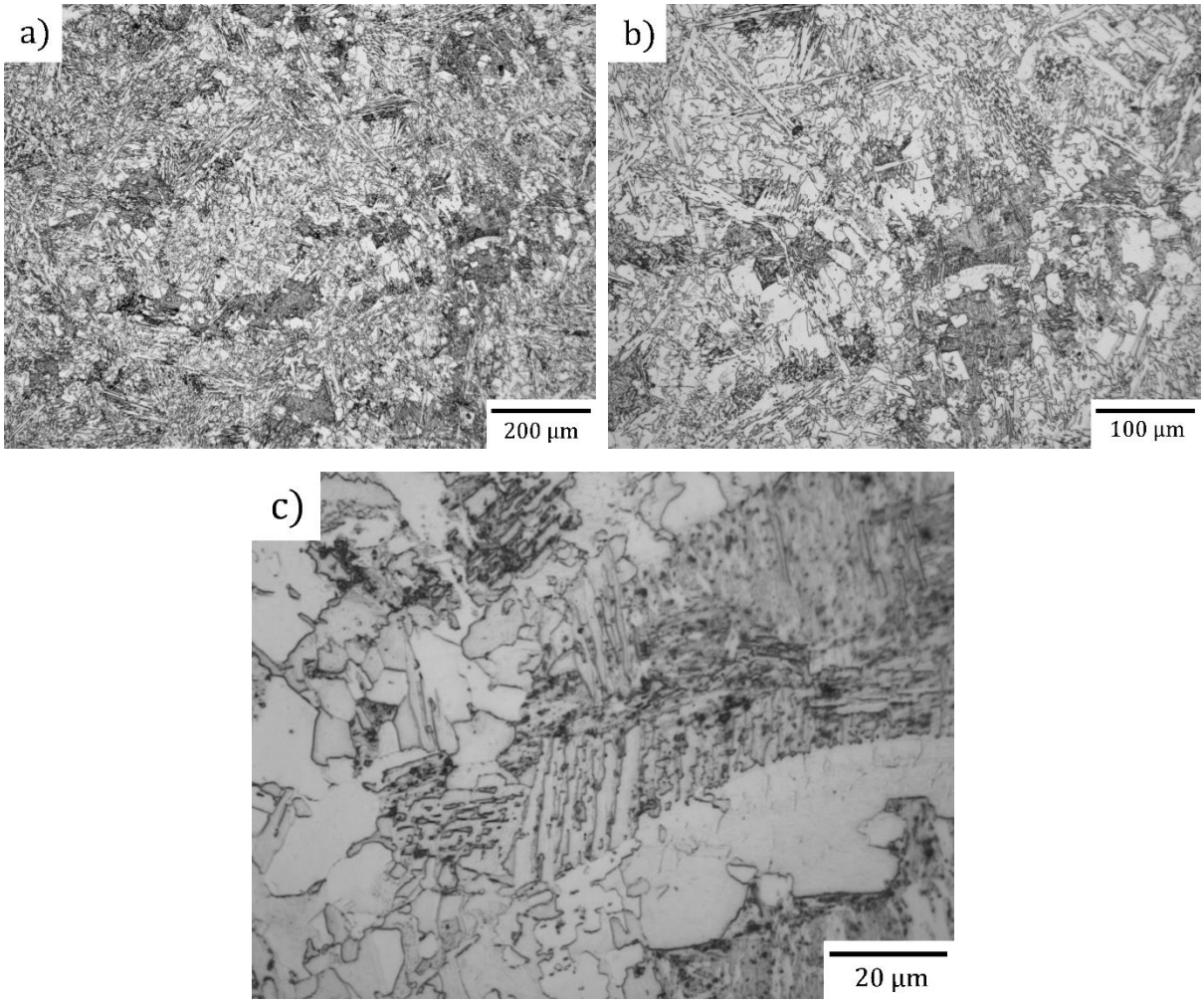

Figure 67. V-Mo-0.0 steel Isothermally transformed at 625^{0}C, a) 50X b) 100X. c) 500X.

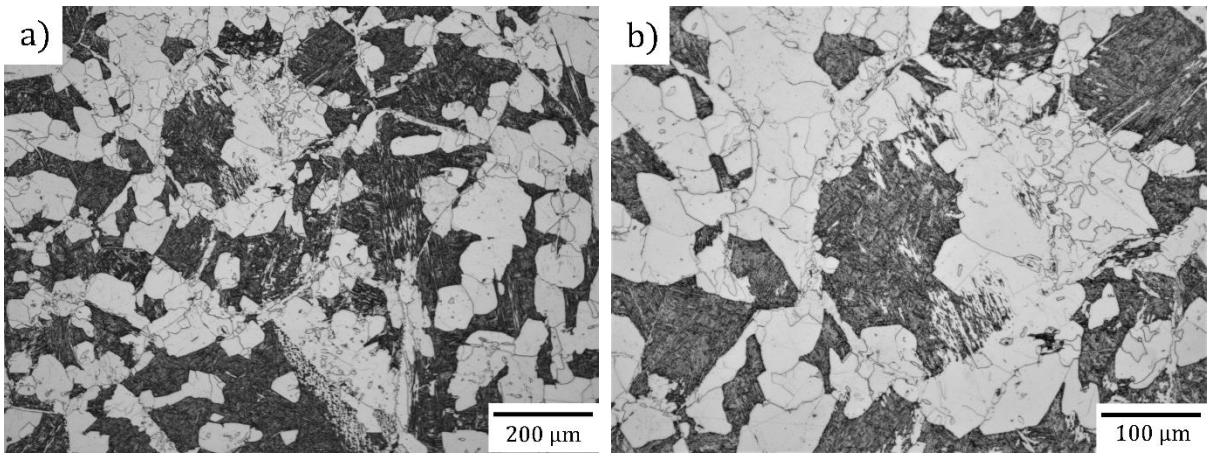

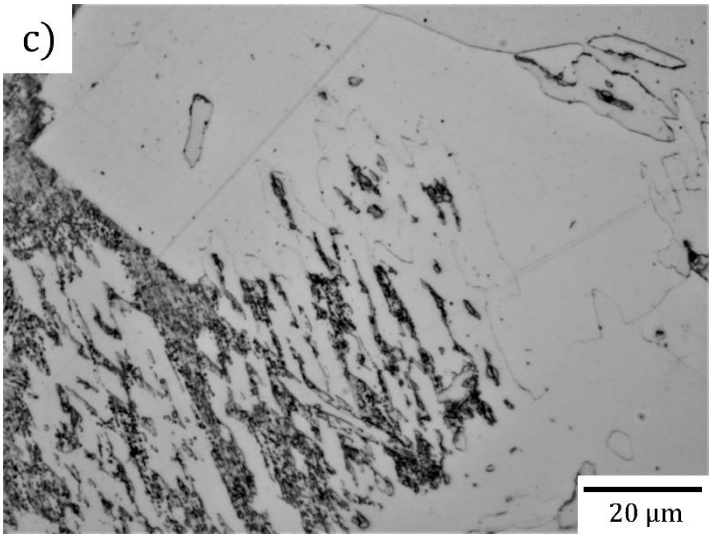

Figure 68. V-Mo-0.0 steel Isothermally transformed at 650^{0}C, a) 50X b) 100X. c) 500X.

Figure 69 shows the microstructure of steel Cr-V-Mo-0.0 with interrupted transformation at 650^{0}C. In low carbon steels, the $\gamma \rightarrow \alpha$ transformation nucleates and grows as 'saturated site nucleation'[232]. In Figure 69 a) very fine Widmanstätten ferrite grains are observed at the borders of the prior austenite grains. Moreover, very coarse prior austenite grain sizes are observed and very little evidence of inter-granular nucleation (Figure 69 b)). The coarse prior austenite grain size means that during the heat treatment of the dilatometry tests, the austenitisation temperature went over the grain coarsening temperature, reducing strain induced precipitation and the Widmanstätten start temperature is a function of austenite grain size Krahe et al. [233]. As shown by comparing from Figure 66 to Figure 72, it is clear that the addition of Cr gives polygonal ferrite at temperatures at which Widmanstätten ferrite was observed without Cr.

The subsequent series of experiments aimed to achieve the smallest grain size possible. This required maximizing the nucleation sites of ferrite, which in turn necessitated minimizing the size of the prior-austenite grains.

Micrographs of Cr-V-Mo-0.0 steels transformed at different temperatures are presented in Figure 70 – Figure 72. The microstructure comprises ferrite with martensite. It is clear that the ferrite grain size reduces as the transformation temperature is reduced. In addition, the ferrite volume fraction increases, but that is discussed in the following sections. Deeper etched micrographs are shown in Figure 73 showing secondary grain boundaries, these appear to be low-angle sub-boundaries which were not generated by polygonization, because if they had been the $\alpha - \alpha$ low angle boundary would have very low energy, minimizing the deflection[234,235]. More recent studies by Yokomizo et al.[236] reconstruct Widmanstätten and allotriomorph ferrite which nucleate radially from precipitates, and generate semi-parallel sub-borders while they coarsened from the same Widmanstätten branch. But if they degenerate and an allotriomorphic grain is close or nucleates in any other direction, ferrite grains will appear within others.

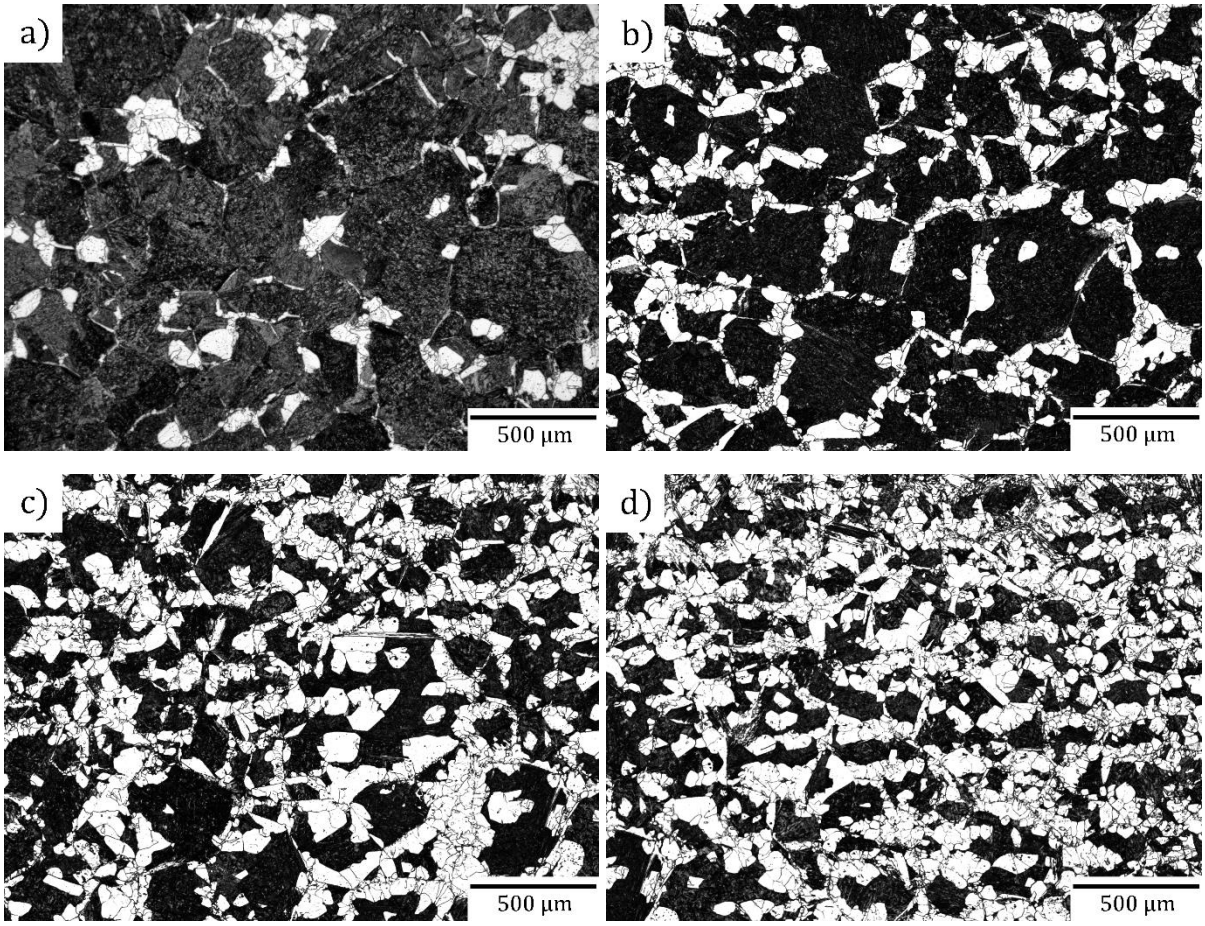

Figure 69. Optical microscopy of samples of steel Cr-V-Mo-0.0 with an interrupted process of $\gamma \rightarrow \alpha$ transformation at 650^{0}C after a) 5s b) 10s c) 180s d) 5400s. It shows the austenite grains boundaries as favourite places to start the ferrite transformation.

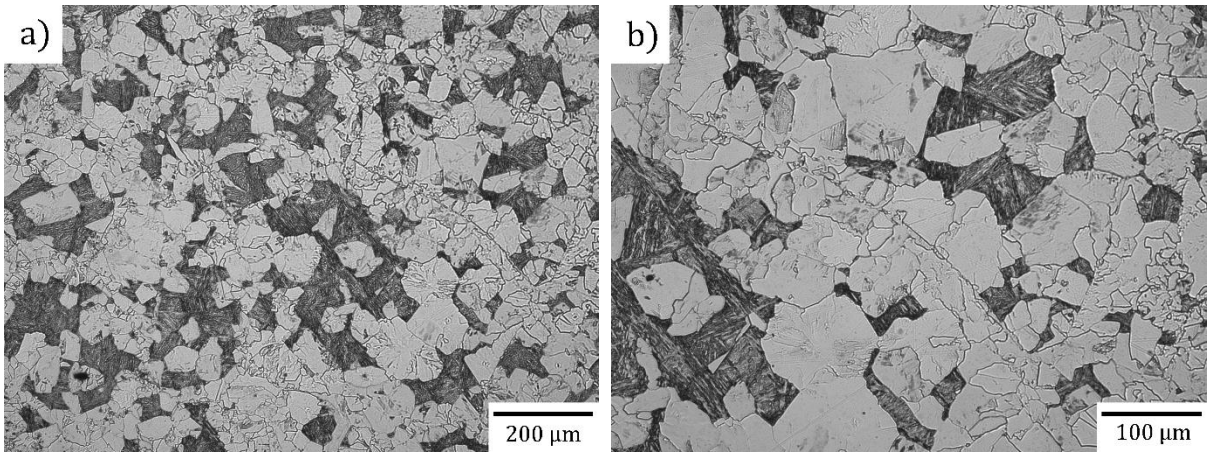

Figure 70. Optical micrograph of steel Cr-V-Mo-0.0 isothermally transformed at 600^{0}C at a) 100X b) 200X.

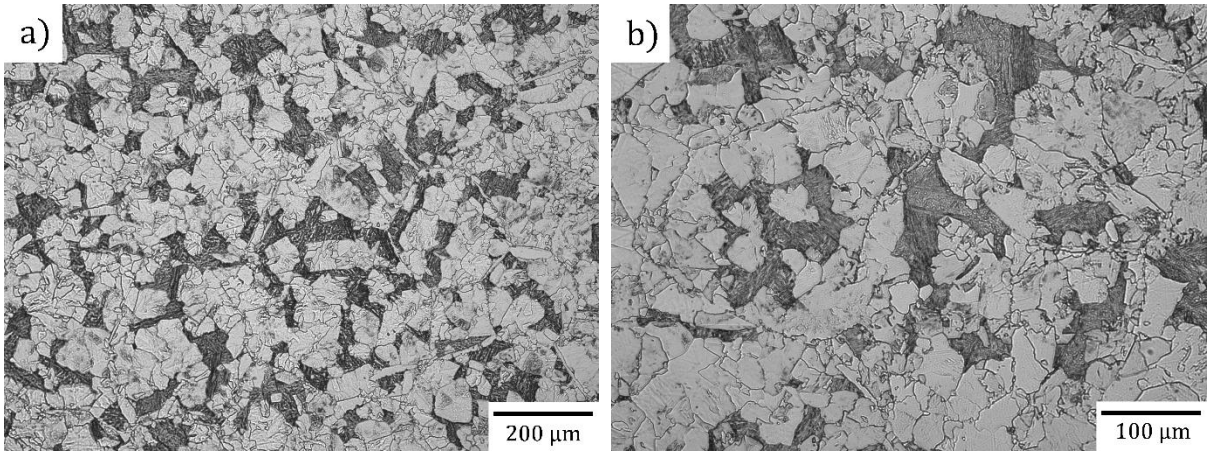

Figure 71. Optical micrograph of steel Cr-V-Mo-0.0 isothermally transformed at 625^{0}C at a) 100X b) 200X.

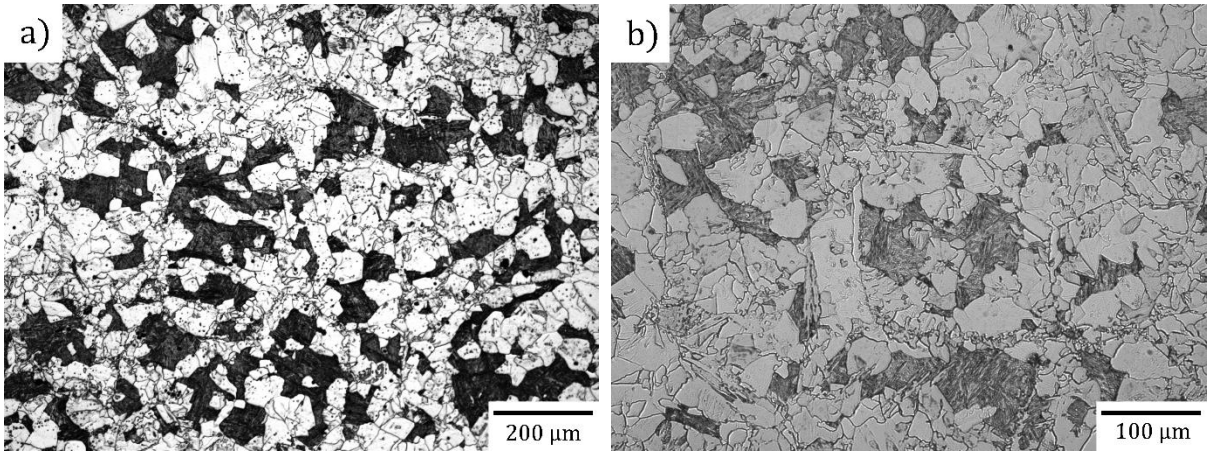

Figure 72. Optical micrograph of steel Cr-V-Mo-0.0 isothermally transformed at 650^{0}C at a) 100X b) 200X.

Figure 74 shows a deeply etched micrograph of sample Cr-V-Mo-0.0 aged at 650^{0}C, where some very fine grains can be distinguished, much finer than the surrounding ferrite grains. As shown in Figure 74 b), the smaller grains, < 3µm, are located within larger ferrite grains. Some of these very small grains have an elongated shape, while some are triangular and hemisphecal which corresponds to primary side plates, primary sawtooth Widmanstätten and idiomorphic ferrite respectively. Because of the long transformation time, they can be considered as second grain boundary allotriomorphs depending on where they are and the shape.

At this point of the research, a shroud of the same microalloyed steel was made to increase the mass of the dilatometer specimens, and at the same time, to make the treatment much more stable to:

1) Make sure that the temperature does not exceed the threshold at which significant grain growth takes place.
2) Avoid the cooling mix of water and air to striking the sample directly and produce cold points around the thermocouple.

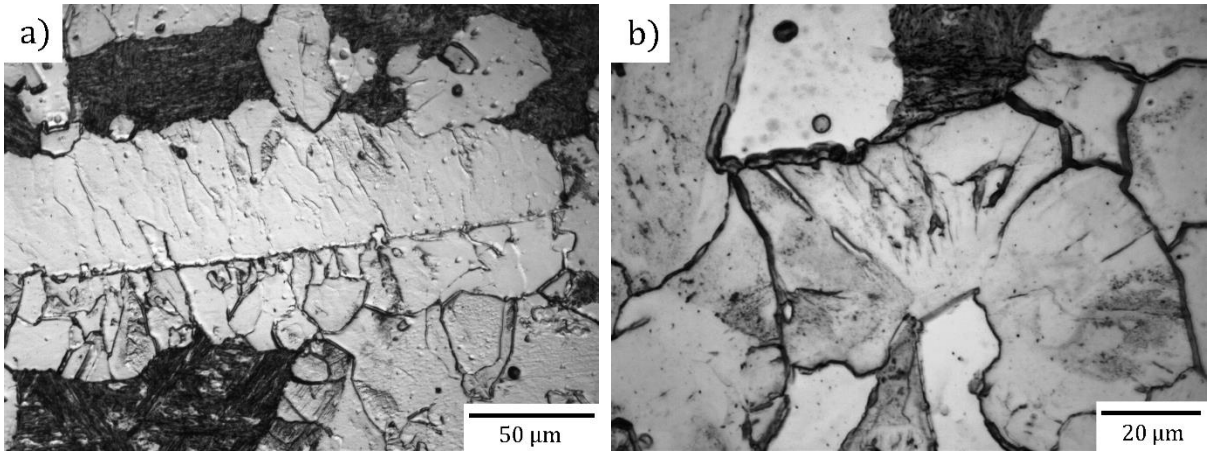

Figure 73. Micrographs of samples Cr-V-Mo-0.0 isothermally transformed at 625^{0}C with a deeper etching which reveals sub-grain boundaries.

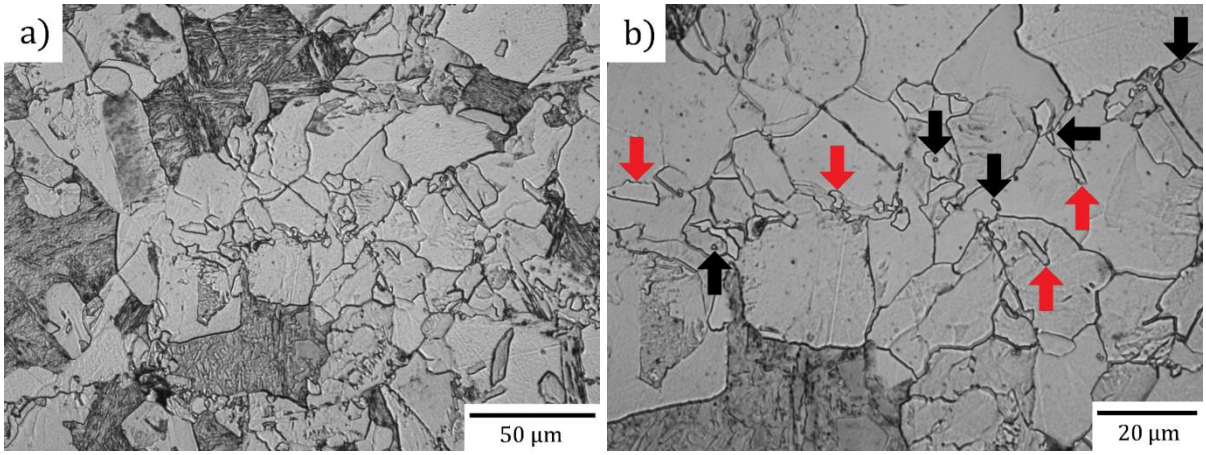

Figure 74. Small grains observed in samples of steels Cr-V-Mo-0.0.

Figure 75 shows the microstructures of the V-Mo-0.4 alloy autenitized and heat-treated at different temperatures. These images show structures comprising a combination of ferrite and some pockets of martensite and others of bainite. Ferrite grains are in their majority allotriomorphic, but some sawtooth Widmanstätten is still present. At all the evaluated temperatures, very small polygonal ferrite grains are observed too.

Steels Cr-V-Mo-0.4, V-Mo-0.2, Cr-V-Mo-0.2 and Cr-Nb-V-0.2 presented no clear microstructural difference from the structures described before. The structures of them are shown in Figure 76 - Figure 79, showing only the temperature at which the maximum ferrite volume fraction of ferrite was reached in each steel, and a few values over and below that. All steels except the one with Nb+Cr addition (alloy Cr-Nb-V-0.2) present a similar description of the microstructure but at different temperatures.

In the case of alloy Cr-Nb-V-0.2, the microstructure below 675^{0}C is bainite. This is because of the retardation in the kinetics of the transformation by the addition of Cr+Nb, the temperature to reach the $\gamma \rightarrow \alpha$ transformation is much higher than steels with only the addition of Cr or no additions of Cr+Nb.

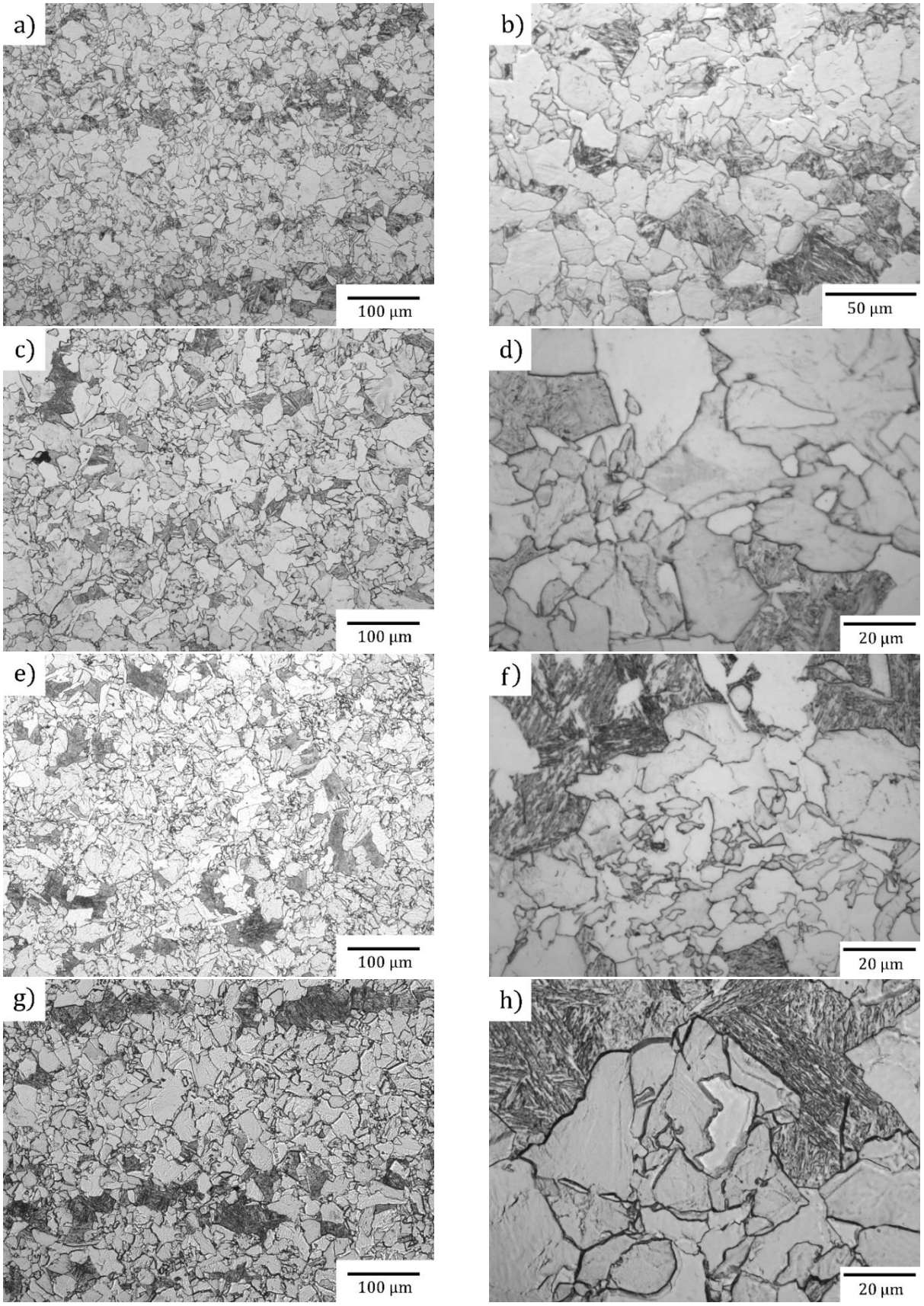
a)
100 µm
b)
50 µm
c)
100 µm
d)
20 µm
e)
100 µm
f)
20 µm
g)
100 µm
h)
20 µm

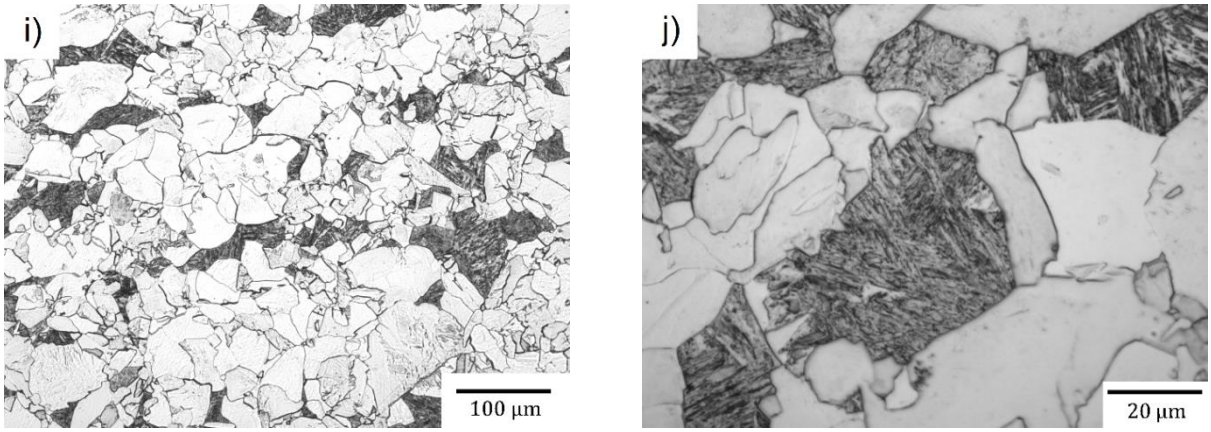

Figure 75 .Structures of steel V-Mo-0.4 heat treated: a) and b) solution annealing at 900^{0}C and isothermally transformed at 650^{0}C, c) and d) solution annealing at 1150^{0}C and isothermally transformed at 650^{0}C, e) and f) solution annealing at 1250^{0}C and isothermally transformed at 650^{0}C, g) and h) solution annealing at 1150^{0}C and isothermally transformed at 660^{0}C, i) and j) solution annealing at 1250^{0}C and isothermally transformed at 660^{0}C.

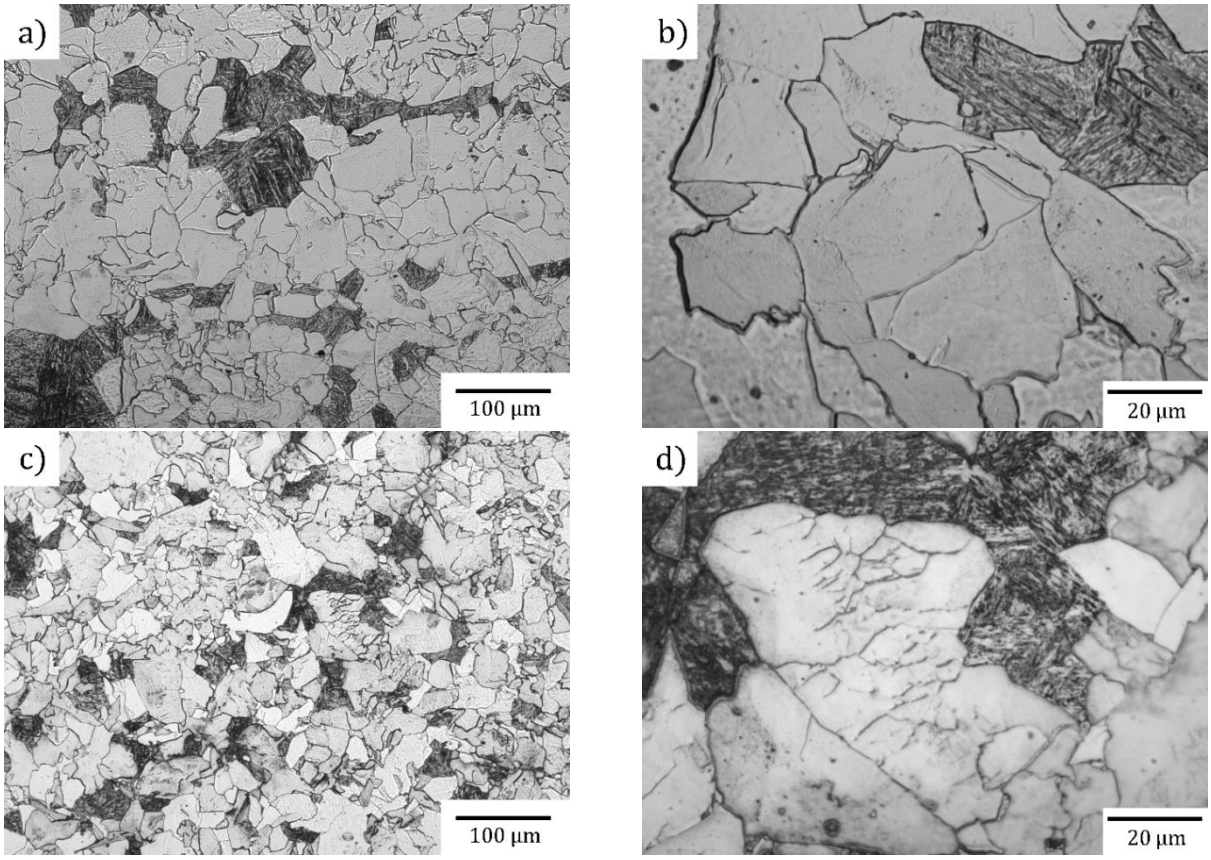

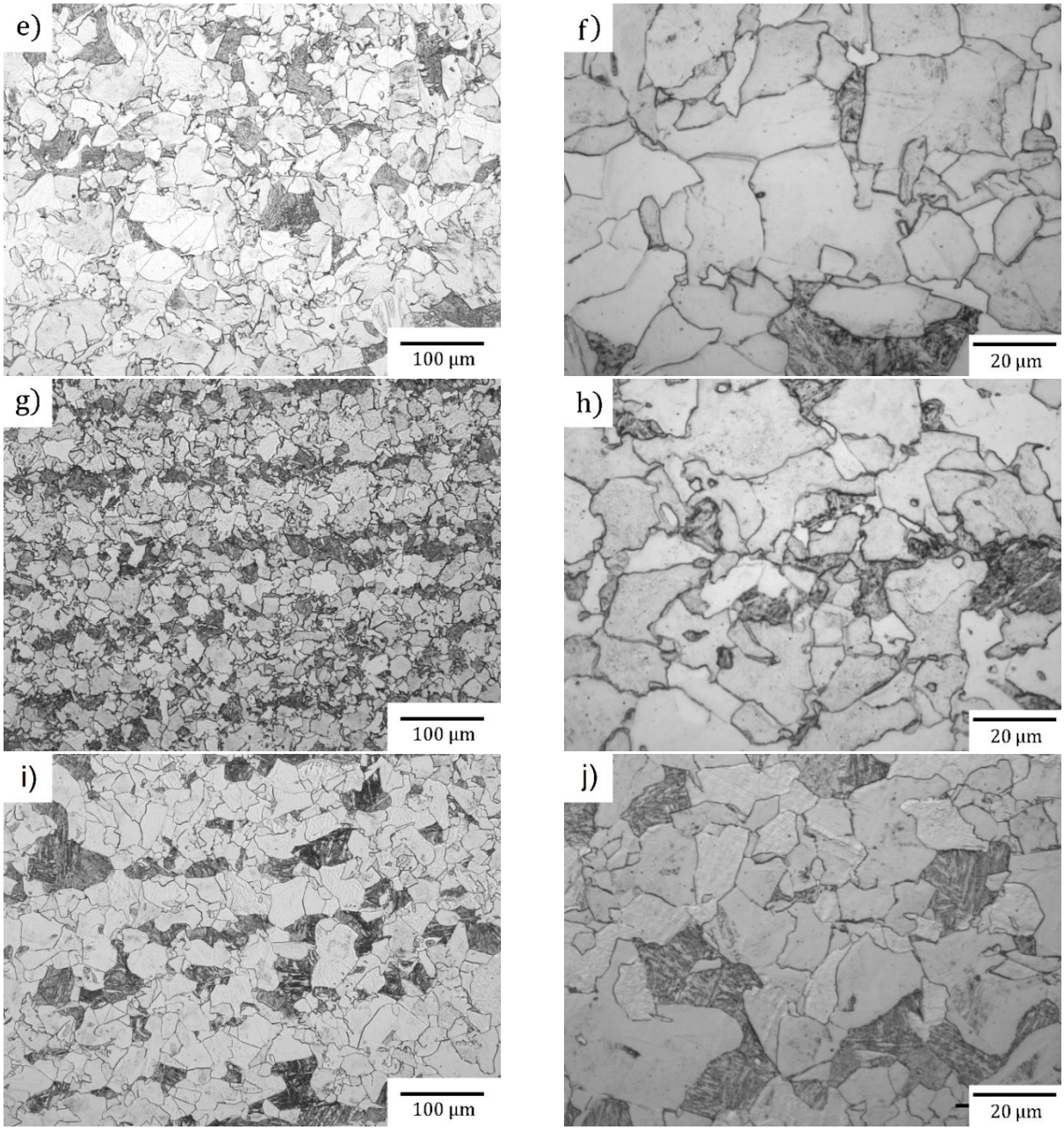

Figure 76. Structures of steel Cr-V-Mo-0.4 heat treated: a) and b) solution annealing at 900^{0}C and isothermally transformed at 660^{0}C, c) and d) solution annealing at 1150^{0}C and isothermally transformed at 660^{0}C, e) and f) solution annealing at 1250^{0}C and isothermally transformed at 660^{0}C, g) and h) solution annealing at 900^{0}C and isothermally transformed at 680^{0}C, i) and j) solution annealing at 1150^{0}C and isothermally transformed at 680^{0}C.

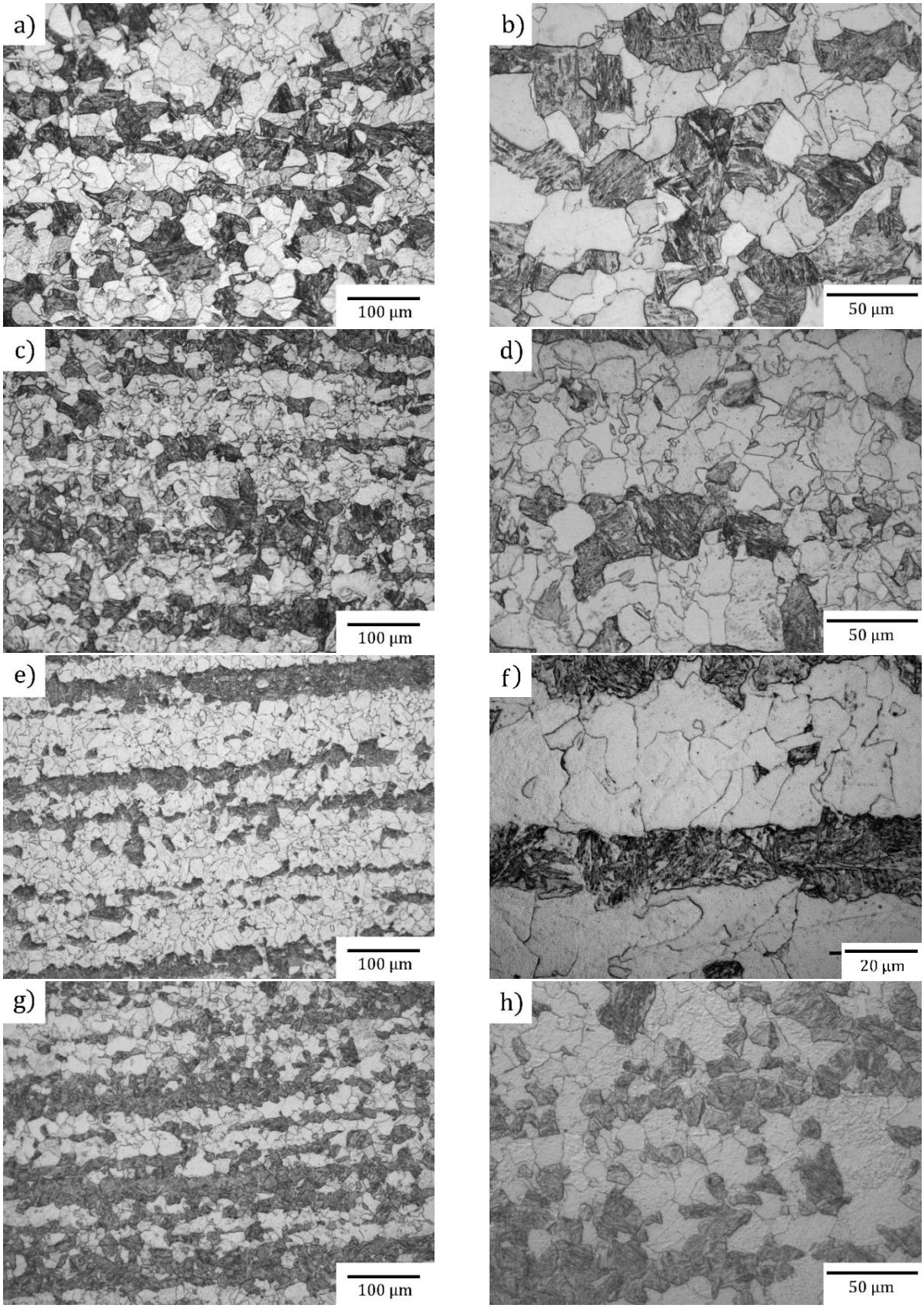

Figure 77. Structures of steel V-Mo-0.2 heat treated: a) and b) solution annealing at 1250^{0}C and isothermally transformed at 600^{0}C, c) and d) solution annealing at 1250^{0}C and isothermally transformed at 630^{0}C, e) and f) solution annealing at 1250^{0}C and isothermally transformed at 655^{0}C, g) and h) solution annealing at 1250^{0}C and isothermally transformed at 670^{0}C.

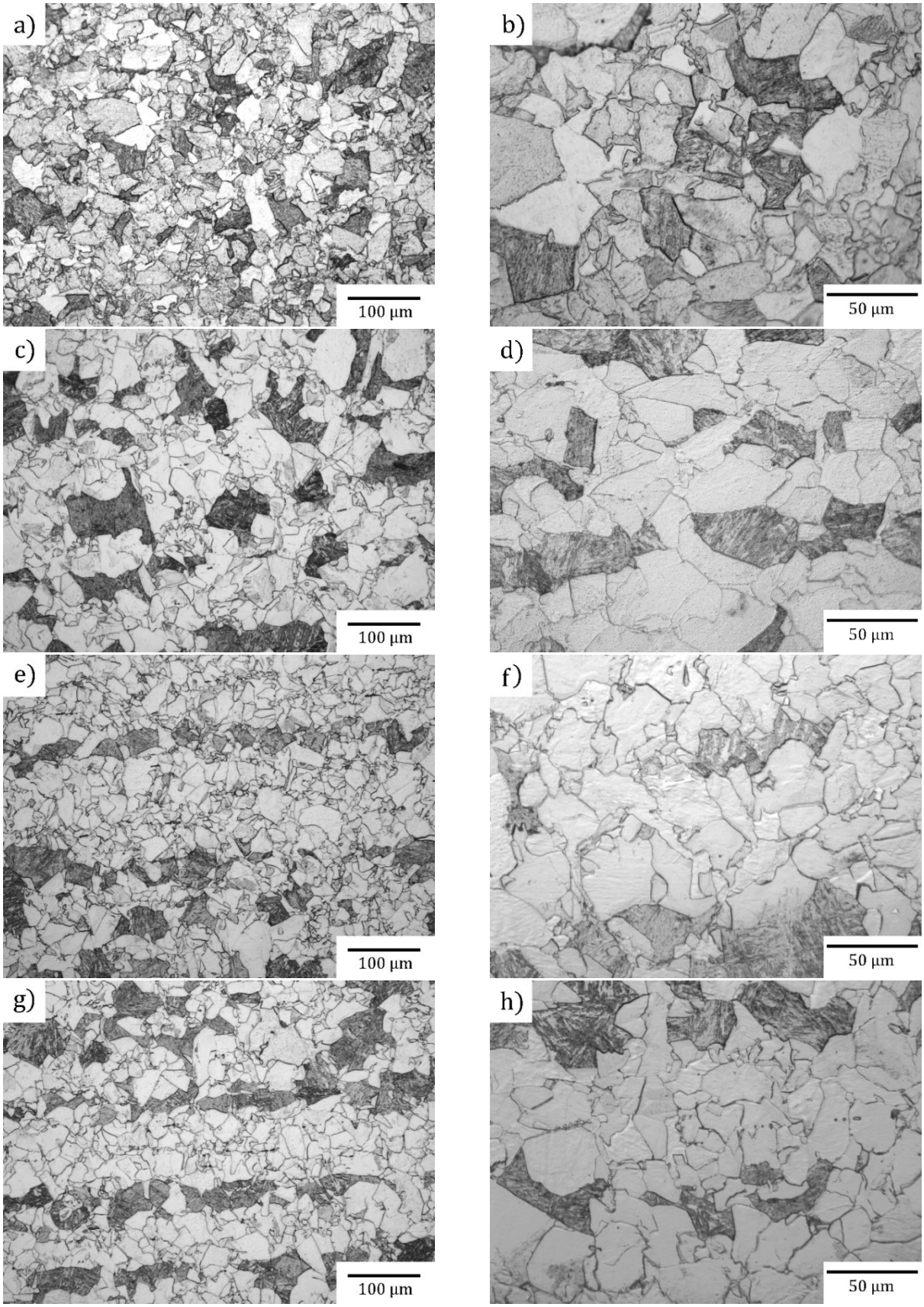

Figure 78. Structures of steel Cr-V-Mo-0.2 heat treated: a) and b) solution annealing at 1250^{0}C and isothermally transformed at 635^{0}C, c) and d) solution annealing at 1250^{0}C and isothermally transformed at 653^{0}C, e) and f) solution annealing at 1250^{0}C and isothermally transformed at 664^{0}C, g) and h) solution annealing at 1250^{0}C and isothermally transformed at 672^{0}C.

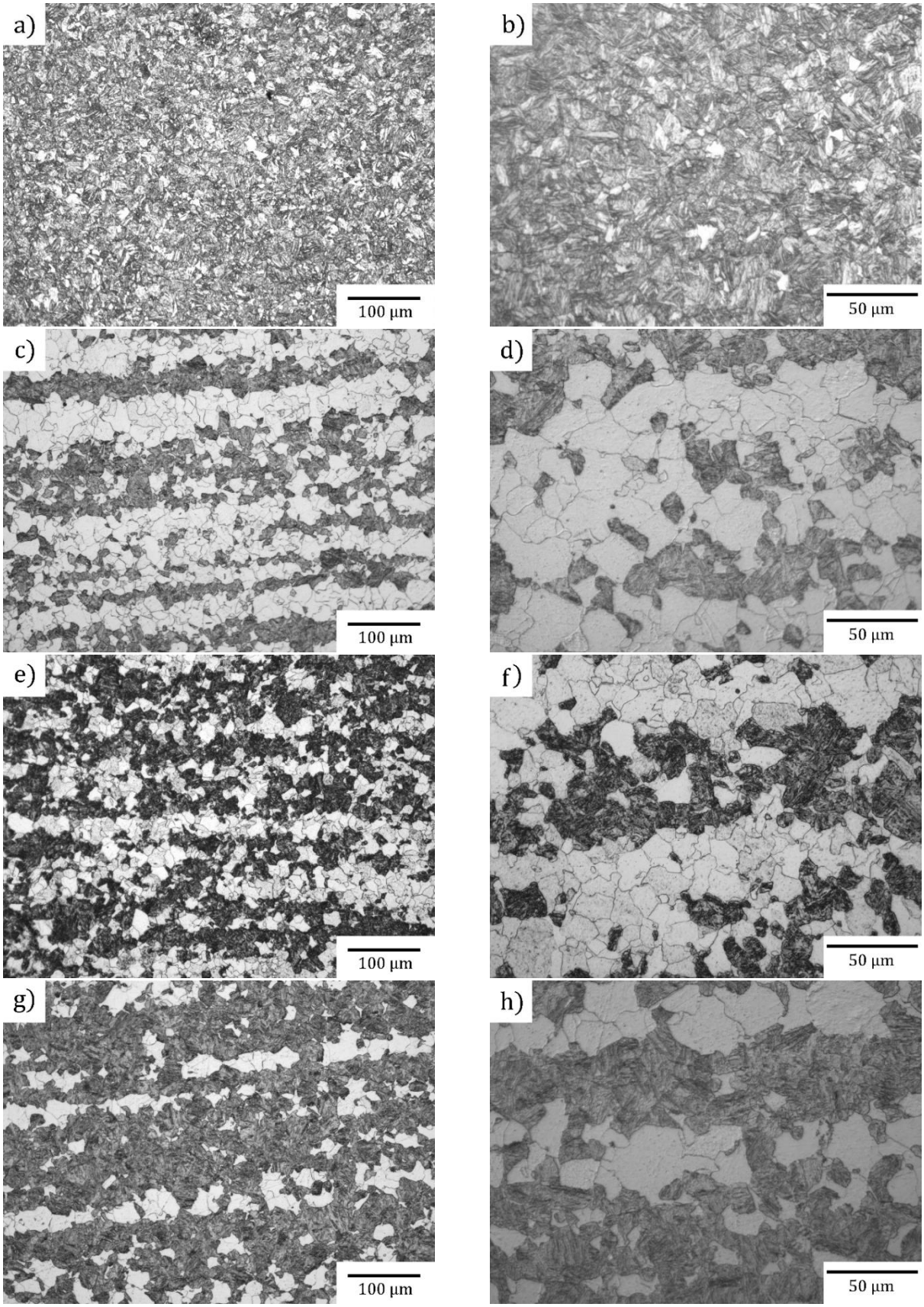

Figure 79. Structures of steel Cr-Nb-V-0.2 heat treated: a) and b) solution annealing at 1250^{0}C and isothermally transformed at 665^{0}C, c) and d) solution annealing at 1250^{0}C and isothermally transformed at 700^{0}C, e) and f) solution annealing at 1250^{0}C and isothermally transformed at 710^{0}C, g) and h) solution annealing at 1250^{0}C and isothermally transformed at 725^{0}C.

Microstructural banding is much clearer in steels Cr-Nb-V-Mo-0.2 than in any other of the studied alloys. The banded condition is not evident with small amounts of transformation but develops gradually as the transformation progresses. This is a very common phenomenon in hot rolled low alloy steels[237–242]. This is produced by the "pancaked" solute-rich regions produced by the hot-rolling[237]. They are the result of the rejection of alloying elements with partition radios <1 such as Mn, Si, P, Al, etc during solidification from the first formed δ ferrite dendrites, concentrating solutes in interdendritic regions[240,242,243].

Some studies reported that yield and tensile strength are little affected by the banding phenomena when it is taken along the rolling direction[241,244]. There are other researches that report important improvements in steels with refined band spacing achieved by changes in the thermal cycle[241,245]. These processes usually are accompanied by other phenomena like microstructure refinement, or changes in the precipitation kinetics, making it difficult to conclude that the tensile improvement is just because of the band spacing refinement. On the contrary, lower values of elongation are obtained in specimens from heavily banded regions[244]. Banding, especially in transverse samples, decreased the notch toughness, particularly the energy required for ductile fracture (shelf energy), and increased the anisotropy[241,244].

Several procedures have been discovered to reduce the banding effect. It was found that by reducing the austenitization temperature, the band spacing is reduced too. Thompson & Howell[246] reported that as the cooling rate decreases, the intensity of microstructural banding also reduces, the reason why it is recommended to perform experiments with higher cooling rates after the reaustenitization at medium temperatures (around 1150^0C) to avoid the microstructural banding in this alloy and observe if the tensile properties change. Also, it would be of interest to perform thermal cycling as an efficient way to reduce the band spacing toward increasing the work hardening capacity of DP steels[245].

Banded structures produce anisotropy of tensile properties, obtaining the maximum properties from longitudinal samples matching the rolling direction[244]. In this investigation, all the tests were conducted with this condition, but it is desirable to produce bigger samples to evaluate the contrast between longitudinal and transverse tensile specimens**.**

4.3. FERRITE VOLUMETRIC FRACTION

To understand the microstructural evolution of the microalloyed steels with Cr and Cr+Nb additions, the ferrite volume fraction after isothermal transformation was measured in all the alloys studied in this thesis. From Figure 80 to Figure 85 the measured ferrite volume fraction for steels Cr-V-Mo-0.0, V-Mo-0.4, Cr-V-Mo-0.4, V-Mo-0.2, Cr-V-Mo-0.2 and Cr-Nb-V-0.2 are presented, and their values are summarized in Table 28. From Figure 80 and Figure 82, it is observed that the total ferrite volume fraction in microalloyed steels with Cr additions is reduced in steels which exceed the abnormal prior-austenite grain coarsening temperature during austenitization. The volume fraction of ferrite remains almost constant for isothermal transformations from 600^0C to 650^0C. Figure 84 shows that this behaviour changes in microalloyed steels with Cr additions when the austenitization temperature is below the prior-austenite grain coarsening temperature, revealing a peak of maximum transformation of around 90% at $\sim 665^0$C. Moreover, for an austenitization of 1250^0C and an isothermal transformation of 665^0C, a higher hot-working strain rate produces an increase of $\sim$5% in the final ferrite volume fraction.

The peak ferrite fraction is 10^0C lower for alloys with no Cr present compared to steels with the addition of Cr. The fraction ferrite values are similar for steels with and without Cr additions for the steels with 0.4 strain per pass during hot working. The final ferrite fraction of steel with lower strain in hot work (Figure 83) is around 15% lower than the one with 0.4 strain.

Figure 85 shows the results for the steel with Nb+Cr addition. The peak of ferrite transformation is observed at a higher temperature (~700^0C) with a value of 60%.

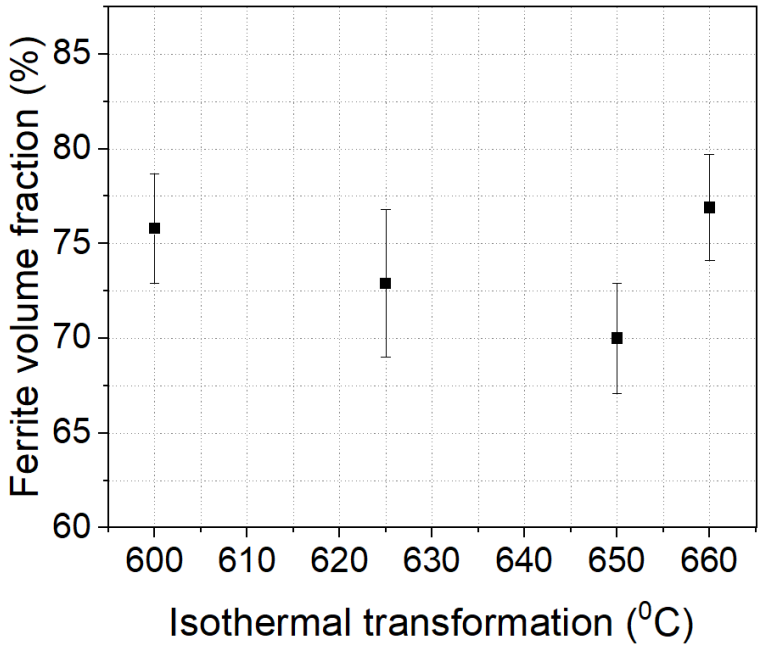

Figure 80. Ferrite volume fraction measured and plotted as a function of the isothermal transformation temperature on steel Cr-V-Mo-0.0.

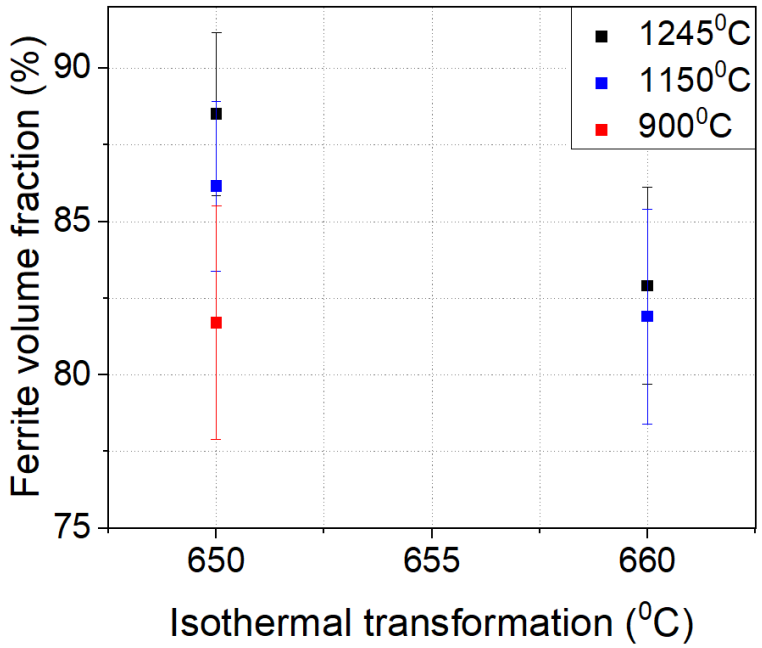

Figure 81. Ferrite volume fraction measured and plotted as a function of the isothermal transformation temperature on steel V-Mo-0.4.

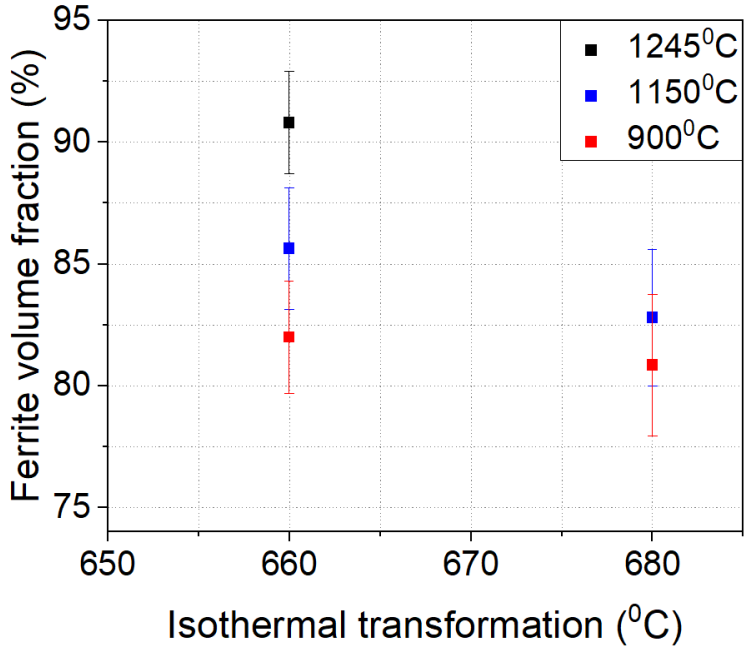

Figure 82. Ferrite volume fraction measured and plotted as a function of the isothermal transformation temperature on steel Cr-V-Mo-0.4.

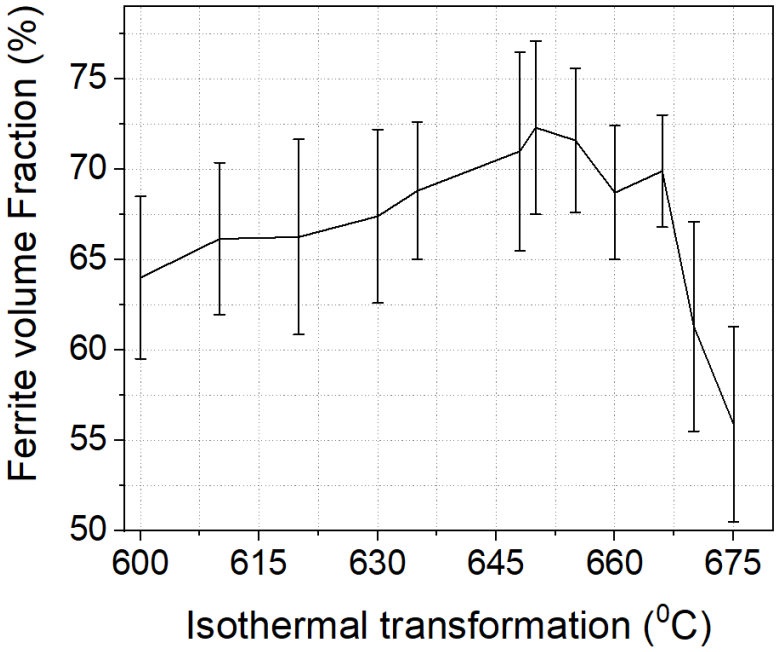

Figure 83. Ferrite volume fraction measured and plotted as a function of the isothermal transformation temperature on steel V-Mo-0.2.

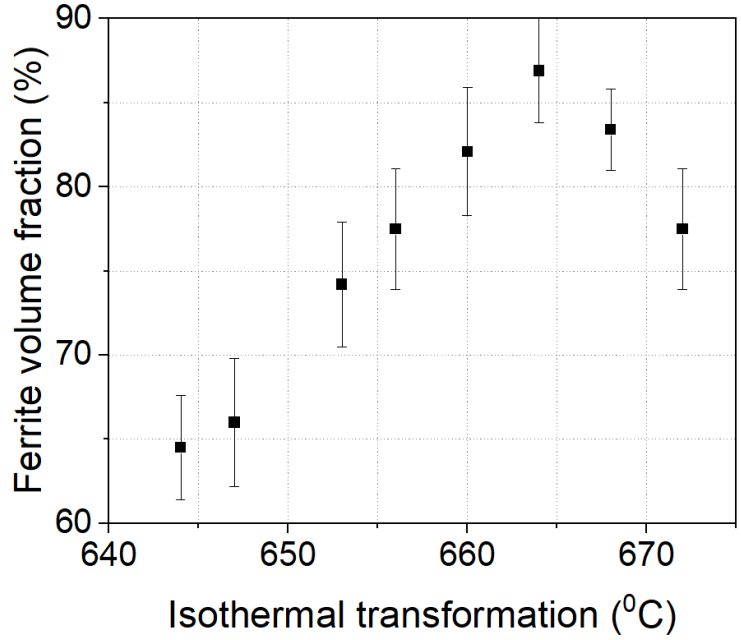

Figure 84. Ferrite volume fraction measured and plotted as a function of the isothermal transformation temperature on steel Cr-V-Mo-0.2.

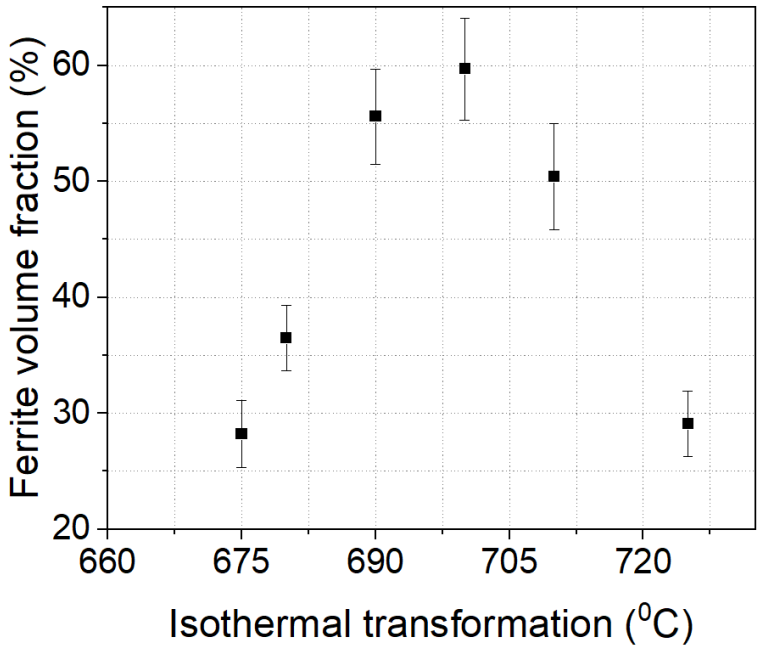

Figure 85. Ferrite volume fraction measured and plotted as a function of the isothermal transformation temperature on steel Cr-Nb-V-0.2.

Austenitization [^{0}C]	Isothermal Transformation [^{0}C]	Ferrite Volume Fraction											
		Cr-V-Mo-0.0	S.D.	V-Mo-0.4	S.D.	Cr-V-Mo-0.4	S.D.	V-Mo-0.2	S.D.	Cr-V-Mo-0.2	S.D.	Cr-Nb-V-0.2	S.D.
900	650	-	-	81.7	3.8	-	-	-	-	-	-	-	-
900	660	-	-	-	-	82	2.3	-	-	-	-	-	-
900	680	-	-	-	-	80.9	2.9	-	-	-	-	-	-
1150	650	-	-	86.2	2.8	-	-	-	-	-	-	-	-
1150	660	-	-	81.9	3.5	85.6	2.5	-	-	-	-	-	-
1150	680	-	-	-	-	82.8	2.8	-	-	-	-	-	-
1245	650	-	-	88.5	2.7	-	-	-	-	-	-	-	-
1245	660	-	-	82.9	3.2	90.8	2.1	-	-	-	-	-	-
1250	600	-	-	-	-	-	-	64	4.5	-	-	-	-
1250	610	-	-	-	-	-	-	66.2	4.2	-	-	-	-
1250	630	-	-	-	-	-	-	66.4	4.6	-	-	-	-
1250	640	-	-	-	-	-	-	-	-	-	-	24.6	2.1
1250	644	-	-	-	-	-	-	-	-	64.5	3.1	-	-
1250	647	-	-	-	-	-	-	-	-	66.0	3.8	-	-
1250	650	-	-	-	-	-	-	67.3	5.5	-	-	-	-
1250	653	-	-	-	-	-	-	-	-	74.2	3.7	-	-
1250	655	-	-	-	-	-	-	69.6	4.0	77.5	3.6	-	-

1250	660	-	-	-	-	-	-	68.7	3.9	82.1	3.8	-	-
1250	664	-	-	-	-	-	-	-	-	86.9	3.1	-	-
1250	666	-	-	-	-	-	-	67.9	3.1	-	-	-	-
1250	668	-	-	-	-	-	-	-	-	83.4	2.4	-	-
1250	670	-	-	-	-	-	-	61.3	3.3	-	-	-	-
1250	672	-	-	-	-	-	-	-	-	77.5	3.6	-	-
1250	675	-	-	-	-	-	-	55.9	4.8	-	-	28.2	2.9
1250	680	-	-	-	-	-	-	-	-	-	-	36.5	2.8
1250	690	-	-	-	-	-	-	-	-	-	-	55.6	4.1
1250	700	-	-	-	-	-	-	-	-	-	-	59.7	4.4
1250	710	-	-	-	-	-	-	-	-	-	-	50.4	4.6
1250	725	-	-	-	-	-	-	-	-	-	-	29.1	2.8
Over 1250	600	75.8	2.9	-	-	-	-	-	-	-	-	-	-
Over 1250	625	72.9	3.9	-	-	-	-	-	-	-	-	-	-
Over 1250	650	70	2.9	-	-	-	-	-	-	-	-	-	-
Over 1250	660	76.9	2.8	-	-	-	-	-	-	-	-	-	-

Table 28. Measured values of the ferrite volume fraction for different temperatures of isothermal transformation.

4.4. FERRITE GRAIN SIZE

Grain size measurements were performed on alloys which present polygonal ferrite colonies. All the measurements were taken from optical microscope images, and the results of the average values obtained are shown in Figure 86 and Figure 87. Figure 86 shows that the ferrite grain size increases with the austenitization temperature. In Figure 87 it is observed that the ferrite isothermally transformed from austenite in the microalloyed steels with Cr and Nb+Cr additions have no clear change from the ones with no additions of these elements. A difference is registered in the steel in which the samples exceed the prior-austenite coarsening temperature. They present a much higher grain size average and the standard deviation is also much higher. Data from these charts are compiled in Table 29.

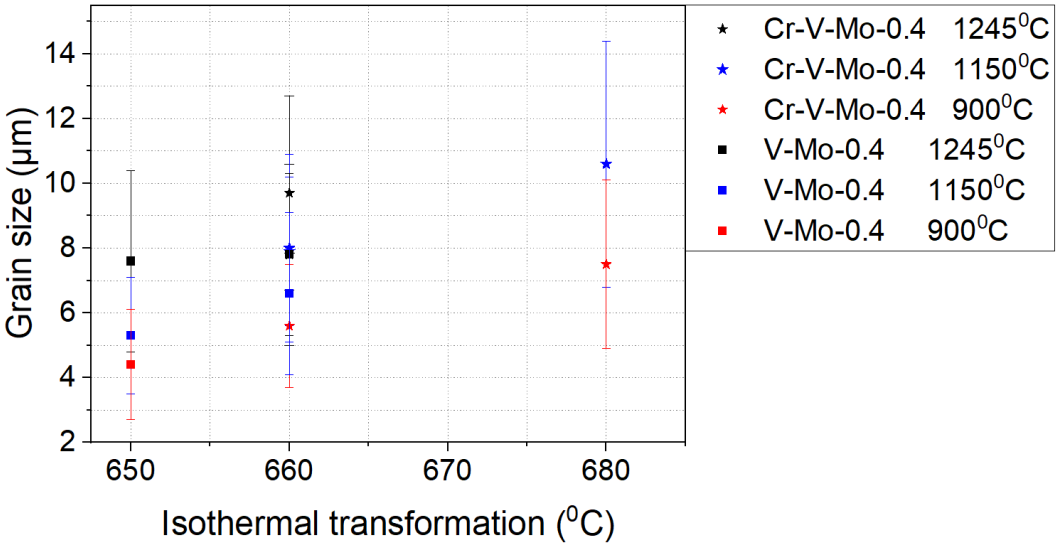

Figure 86. Ferrite grain size as a function of the austenitization temperature + the isothermal transformation in microalloyed steels.

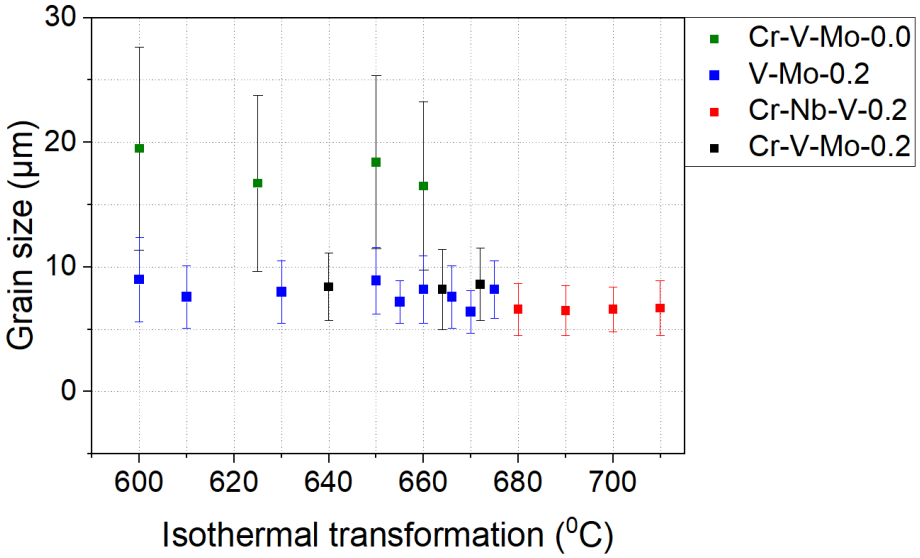

Figure 87. Ferrite grain size as a function of the isothermal transformation temperature in microalloyed steels.

Austenitization [^{0}C]	Isothermal Transformation [^{0}C]	Ferrite Grain Size											
		Cr-V-Mo-0.0	S.D.	V-Mo-0.4	S.D.	Cr-V-Mo-0.4	S.D.	V-Mo-0.2	S.D.	Cr-V-Mo-0.2	S.D.	Cr-Nb-V-0.2	S.D.
900	650	-	-	4.4	1.7	-	-	-	-	-	-	-	-
900	660	-	-	-	-	5.6	1.9	-	-	-	-	-	-
900	680	-	-	-	-	7.5	2.6	-	-	-	-	-	-
1150	650	-	-	5.3	1.8	-	-	-	-	-	-	-	-
1150	660	-	-	6.6	2.5	7.9	2.3	-	-	-	-	-	-
1150	680	-	-	-	-	10.6	3.8	-	-	-	-	-	-
1245	650	-	-	7.6	2.8	-	-	-	-	-	-	-	-
1245	660	-	-	7.8	2.5	9.7	3	-	-	-	-	-	-
1250	600	-	-	-	-	-	-	9	3.4	-	-	-	-
1250	610	-	-	-	-	-	-	7.6	2.5	-	-	-	-
1250	630	-	-	-	-	-	-	8	2.5	-	-	-	-
1250	640	-	-	-	-	-	-	-	-	8.4	2.7	-	-
1250	650	-	-	-	-	-	-	8.9	2.7	-	-	-	-
1250	655	-	-	-	-	-	-	7.2	1.7	-	-	-	-
1250	660	-	-	-	-	-	-	8.2	2.7	-	-	-	-
1250	664	-	-	-	-	-	-	-	-	8.2	3.2	-	-
1250	666	-	-	-	-	-	-	7.6	2.5	-	-	-	-

Austenitization [^{0}C]	Isothermal Transformation [^{0}C]	Ferrite Grain Size											
		Cr-V-Mo-0.0	S.D.	V-Mo-0.4	S.D.	Cr-V-Mo-0.4	S.D.	V-Mo-0.2	S.D.	Cr-V-Mo-0.2	S.D.	Cr-Nb-V-0.2	S.D.
1250	670	-	-	-	-	-	-	6.4	1.7	-	-	-	-
1250	672	-	-	-	-	-	-	-	-	8.6	2.9	-	-
1250	675	-	-	-	-	-	-	8.2	2.3	-	-	-	-
1250	680	-	-	-	-	-	-	-	-	-	-	6.6	2.1
1250	690	-	-	-	-	-	-	-	-	-	-	6.5	2
1250	700	-	-	-	-	-	-	-	-	-	-	6.6	1.8
1250	710	-	-	-	-	-	-	-	-	-	-	6.7	2.2
Over 1250	600	19.5	6.8	-	-	-	-	-	-	-	-	-	-
Over 1250	625	16.7	7.0	-	-	-	-	-	-	-	-	-	-
Over 1250	650	18.4	7.1	-	-	-	-	-	-	-	-	-	-
Over 1250	660	16.5	8.2	-	-	-	-	-	-	-	-	-	-

Table 29 . ferrite grain size of microalloyed steels.

4.5. TENSILE PROPERTIES

Tensile tests were performed on the seven plates of steel to relate the mechanical properties to the microstructure and the interphase precipitation. The results of the tensile tests are shown in Figure 88 - Figure 101. For each alloy three tensile curves are shown: the sample in which the maximum ferrite volume fraction was obtained, one at a higher and one at a lower transformation temperature than this. For each treatment, three to five tensile samples were tested. The average tensile properties are given graphically and in a tabular form.

4.5.1. STEEL V-MO-0.0

Figure 88, Figure 89, and Table 30 show that the tensile properties of steel V-Mo-0.0, which increase from an isothermal transformation of 600^0C to 625^0C. Transformation at 650^0C resulted in a substantial increase in the total elongation at the expense of a small reduction in the UTS, while the yield strength fell by almost 100 MPa.

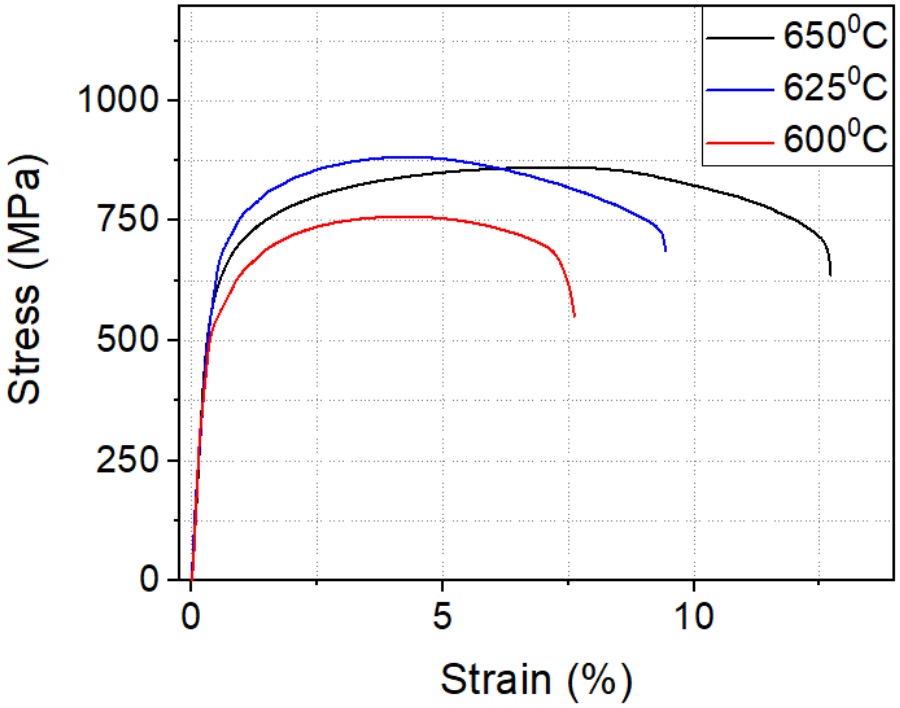

Figure 88. Engineering stress-strain curve of V-Mo-0.0 steel isothermally transformed at 600^0C, 625^0C, and 650^0C.

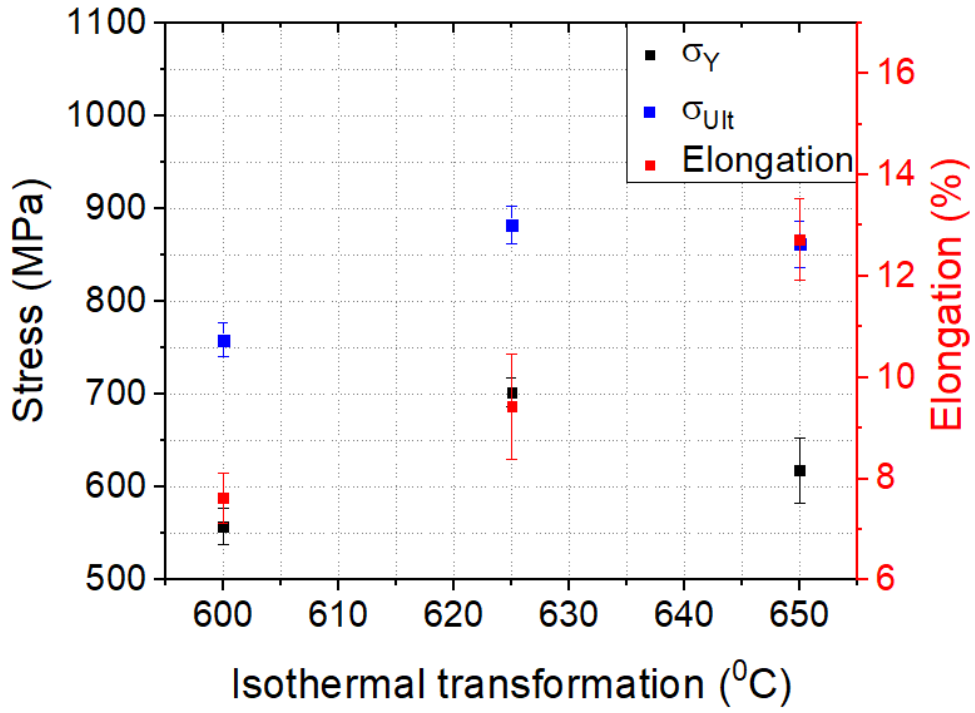

Figure 89. The mechanical properties of the steel V-Mo-0.0 as a function of the transformation temperature.

Isothermal transformation (^{0}C)	Yield stress (MPa)	YS Standard Deviation	Ultimate tensile stress (MPa)	UTS Standard Deviation	Elongation (%)	Elongation Standard Deviation
600	557.8	20.12	758.5	18.5	7.6	0.5
625	702.2	15.35	882.7	20.4	9.4	1.1
650	618.4	35.2	861.3	25.2	12.7	0.8

Table 30. The tensile properties of steels V-Mo-0.0 plotted in Figure 89

4.5.2. STEEL CR-V-MO-0.0

In alloy Cr-V-Mo-0.0, the Cr addition produces an increase in all of the TS, UTS and elongation for increases in isothermal transformations from 600^{0}C to 650^{0}C, Figure 90, Figure 91 and Table 31.

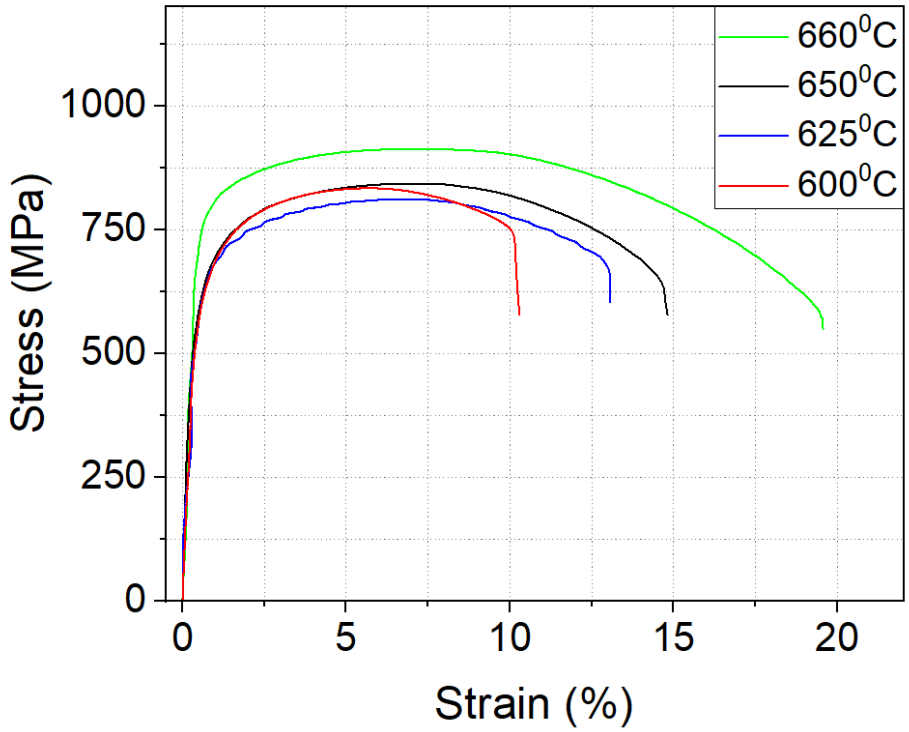

Figure 90. Engineering stress-strain curve of Cr-V-Mo-0.0 steel isothermally transformed at 600⁰C, 625⁰C, 650⁰C and 660⁰C.

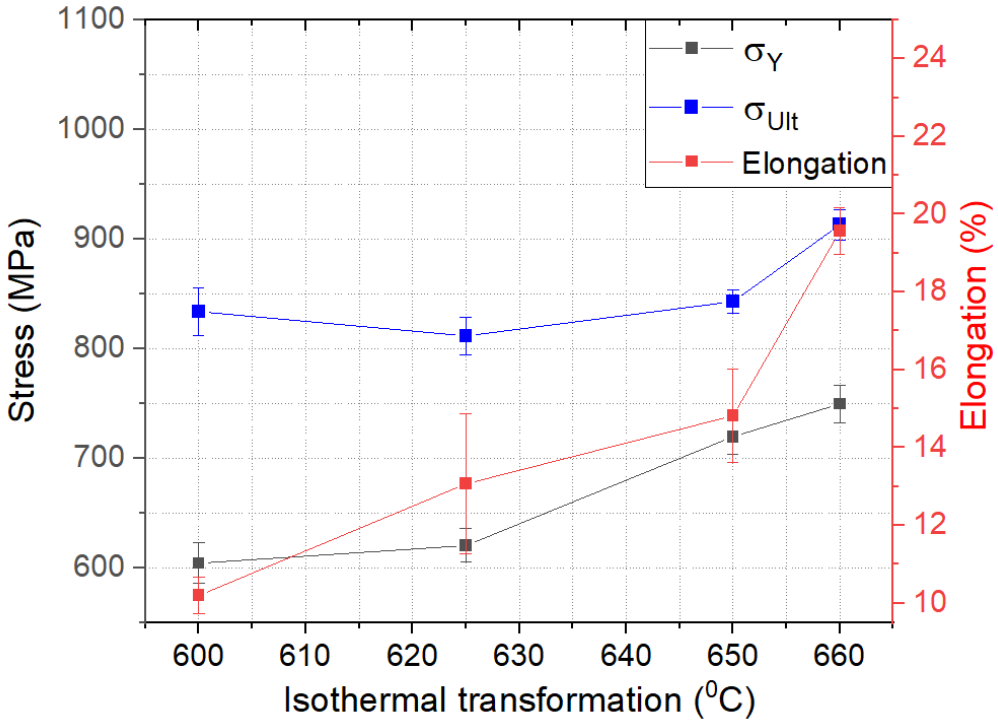

Figure 91. The mechanical properties of the steel Cr-V-Mo-0.0 as a function of the transformation temperature.

Isothermal transformation (^{0}C)	Yield stress (MPa)	YS Standard Deviation	Ultimate tensile stress (MPa)	UTS Standard Deviation	Elongation (%)	Elongation Standard Deviation
600	604.2	18.5	833.7	21.8	10.2	0.5
625	620.4	15.4	811.6	17.3	13.1	1.8
650	719.7	16	842.9	10.3	14.8	1.2
660	749.6	17.2	912.9	14.2	19.6	0.6

Table 31. The tensile properties of steels Cr-V-Mo-0.0 plotted in Figure 91.

4.5.3. STEEL V-MO-0.4 AND STEEL CR-V-MO-0.4

In the following results the elongation of the steels cannot be compared directly to alloys V-Mo-0.0 and Cr-V-Mo-0.0 because of the change in the relationship $L_0/\sqrt{A_0}$ for the tensile samples to be tested. If this relationship increases, the elongation after the UTS is proportionally lower because the longest initial gauge length is much bigger than the necking, represented by the last part of the chart. Results of the tensile properties of steels V-Mo-0.4 and Cr-V-Mo-0.4 presented are at the isothermal transformation temperature at which the maximum ferrite volume fraction was obtained. Changes in the austenitization temperature were evaluated for these two alloys. Figure 92, Figure 93 and Table 32 present the results of steel V-Mo-0.4 isothermally transformed at 650^{0}C. In this alloy, the increase of the YS and the UTS are clear from austenitization at 900^{0}C to austenitizations at 1150^{0}C and 1250^{0}C. The total elongation shows a slight reduction.

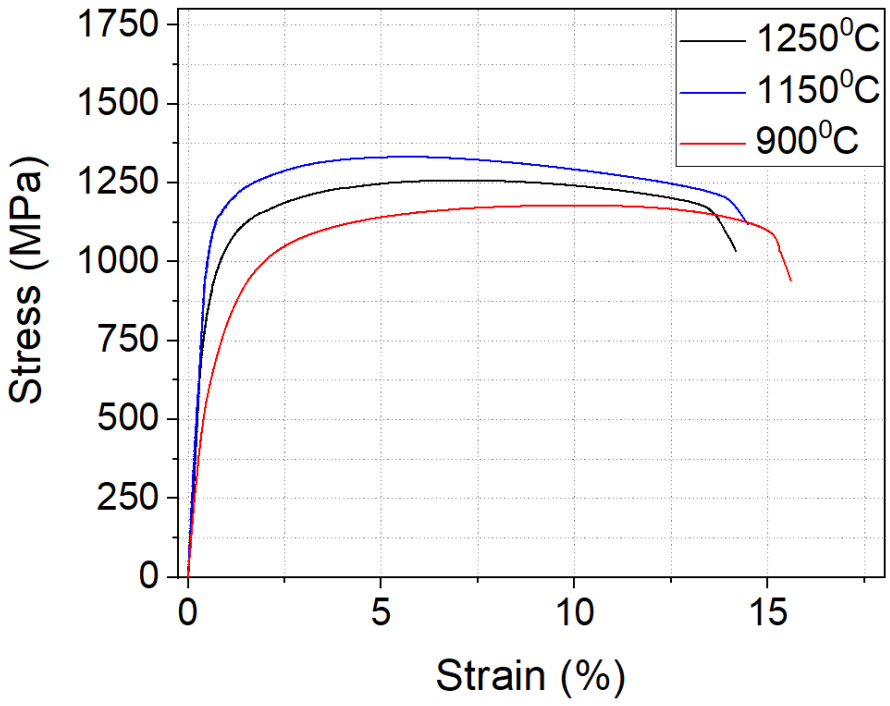

Figure 92. Engineering stress-strain curve of V-Mo-0.4 steel treated at different solution annealing temperatures, and all isothermally transformed at 650^{0}C.

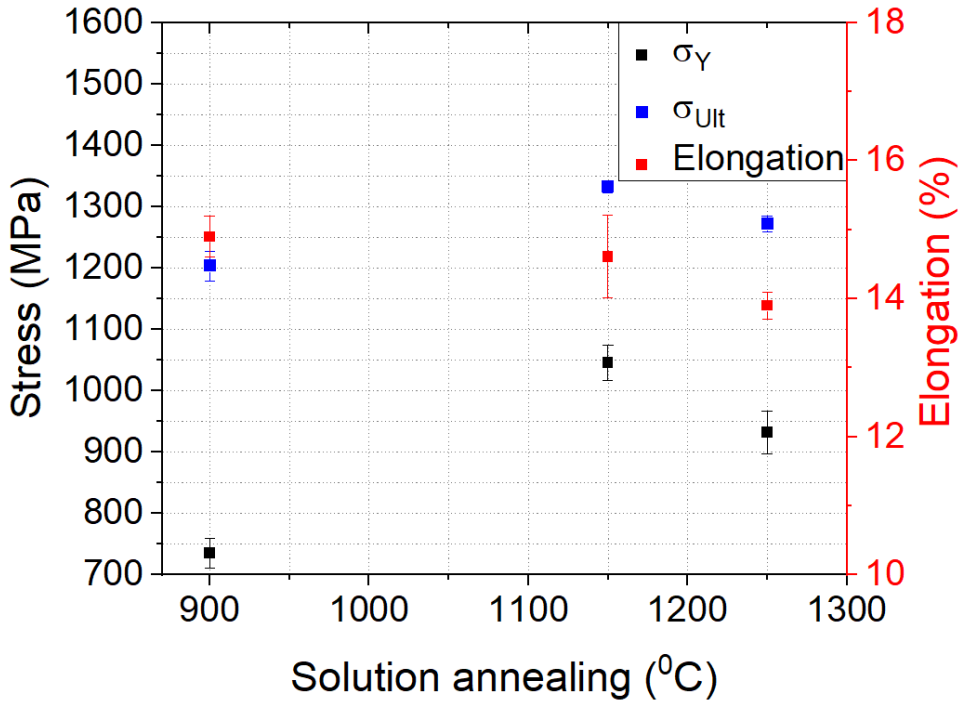

Figure 93. The mechanical properties of the steel V-Mo-0.4 as a function of the solution annealing at a constant isothermal transformation temperature of 650^{0}C.

Solution annealing (^{0}C)	Yield stress (MPa)	YS Standard Deviation	Ultimate tensile stress (MPa)	UTS Standard Deviation	Elongation (%)	Elongation Standard Deviation
900	735.1	24.8	1203.7	24.4	14.9	0.3
1150	1045.7	29	1332.2	9.5	14.61	0.6
1245	931	35.2	1271.9	13.3	13.9	0.2

Table 32. The tensile properties of steels V-Mo-0.4 plotted in Figure 93.

The steel Cr-V-Mo-0.4 isothermally transformed at 660^{0}C presented a good combination of tensile properties, with a YS of over 900 MPa, UTS over 1200 MPa and total elongations over 15%. For this alloy, the maximum elongation was registered in the samples with austenitization of 1150^{0}C, but the maximum YS and UTS correspond to the samples austenitized at 1250^{0}C.

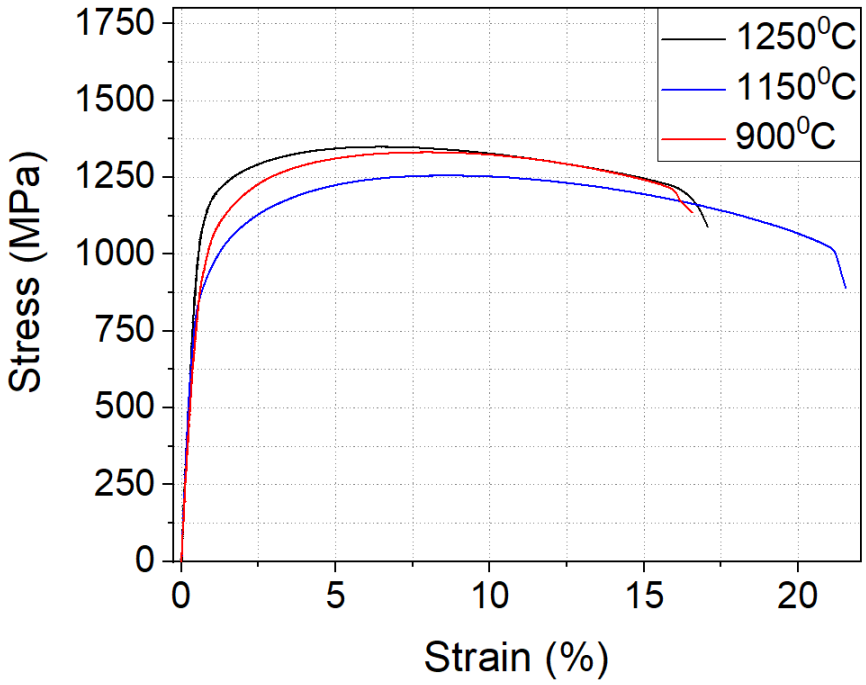

Figure 94. Engineering stress-strain curve of Cr-V-Mo-0.4 steel treated at different solution annealing temperatures, and all isothermally transformed at 660⁰C.

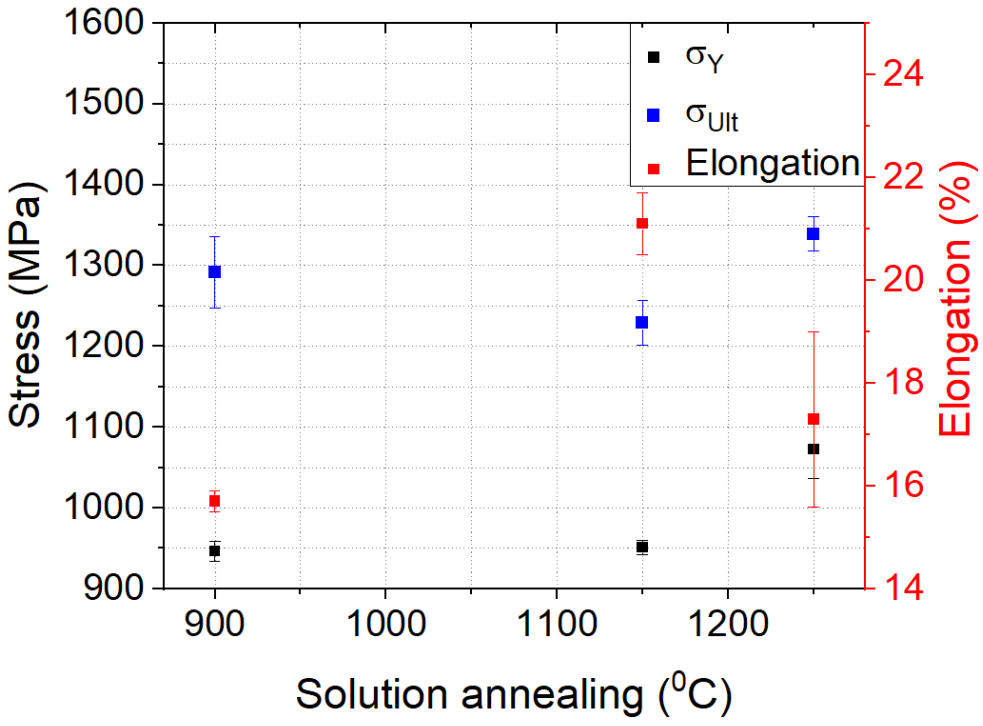

Figure 95. The mechanical properties of the steel Cr-V-Mo-0.4 as a function of the solution annealing at a constant isothermal transformation temperature of 660⁰C.

Solution annealing (^{0}C)	Yield stress (MPa)	YS Standard Deviation	Ultimate tensile stress (MPa)	UTS Standard Deviation	Elongation (%)	Elongation Standard Deviation
900	946.6	12.5	1292	44	15.7	0.2
1150	951	8.9	1228.9	27.4	21.1	0.6
1245	1072.8	36.5	1338.9	21.1	17.3	1.7

Table 33. The tensile properties of steels Cr-V-Mo-0.4 plotted in Figure 95.

4.5.4. STEEL V-MO-0.2 AND CR-V-MO-0.2

The tensile samples for alloys V-Mo-0.2, Cr-Nb-V-0.2 and Cr-V-Mo-0.2 had the same geometry as those V-Mo-0.4 and Cr-V-Mo-0.4, and so the results can be compared directly. The reduction of the strain per pass while rolling produces a reduction in all the tensile properties of microalloyed steels. Figure 96, Figure 97 and Table 34 summarize the properties of alloy V-Mo-0.2. The maximum tensile properties were reached in the sample isothermally transformed at 655^{0}C which corresponds to the sample with the maximum ferrite volume fraction for that steel. For the alloy Cr-V-Mo-0.2 (with Cr addition), the maximum measured properties were obtained from the samples isothermally transformed at 664^{0}C as is shown in Figure 98, Figure 99 and Table 35. This isothermal transformation temperature corresponds to the maximum ferrite volume fraction for that steel. It is clear the Cr addition increases all the tensile properties, especially the elongation.

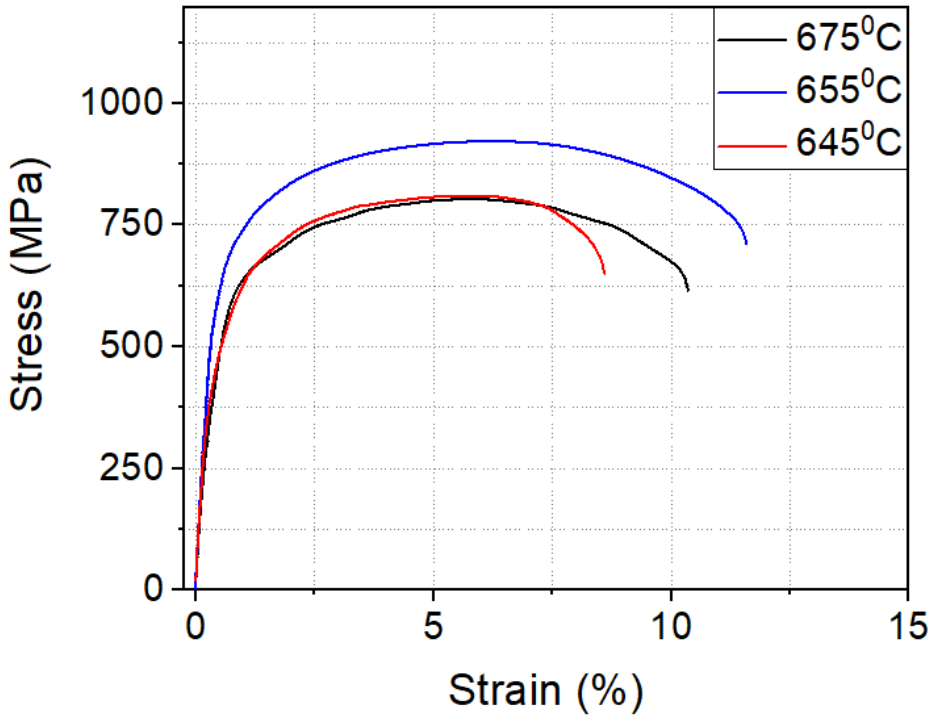

Figure 96. Engineering stress-strain curve of V-Mo-0.2 steel isothermally transformed at 645^{0}C, 655^{0}C, and 675^{0}C.

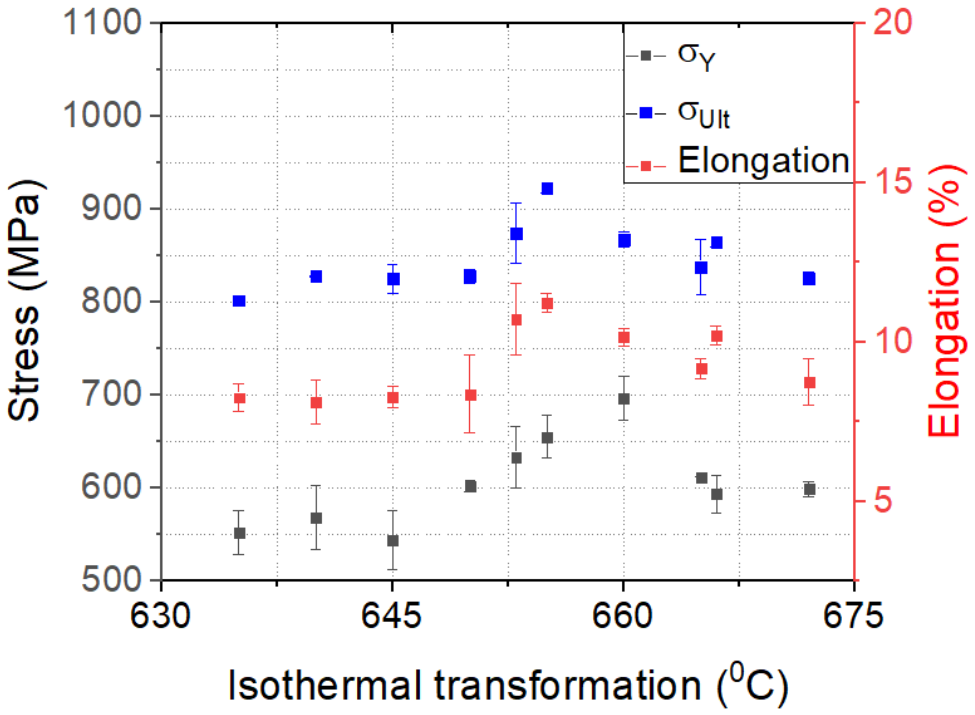

Figure 97. The mechanical properties of the steel V-Mo-0.2 as a function of the transformation temperature after an austenitization temperature of 1240⁰C.

Isothermal transformation (⁰C)	Yield stress (MPa)	YS Standard Deviation	Ultimate tensile stress (MPa)	UTS Standard Deviation	Elongation (%)	Elongation Standard Deviation
600	542.2	12.9	802.5	10.6	10	0.8
610	716.1	5.6	1041.3	35.9	16.4	1.5
635	552.5	23.5	801.8	1.9	8.3	0.5
645	544.2	31.6	825.2	15.2	8.3	0.3
650	601.8	6	827.6	7.6	8.4	1.3
653	633.4	32.8	873.7	32.2	10.7	1.1
655	655.0	22.8	922.5	5.3	11.2	0.3
660	696.6	23.2	867.3	7.6	10.2	0.3
666	594.1	20.2	864.6	5.2	10.2	0.3
672	599.3	8.1	825.7	6.8	8.7	0.7

Table 34. The tensile properties of steels V-Mo-0.2 plotted in Figure 97.

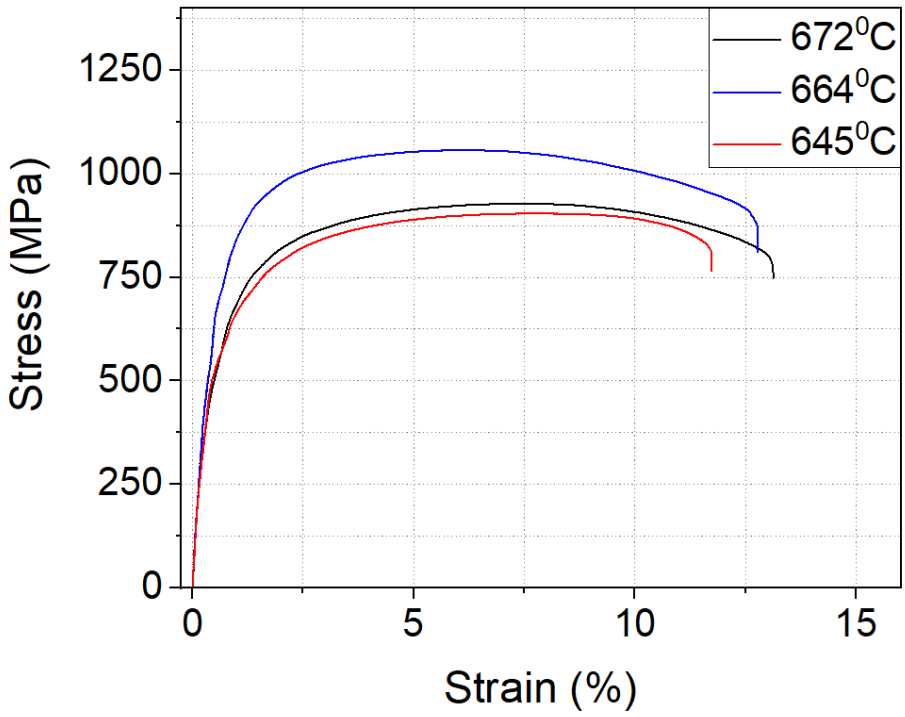

Figure 98. Engineering stress-strain curve of Cr-V-Mo-0.2 steel isothermally transformed at 645⁰C, 665⁰C, and 675⁰C.

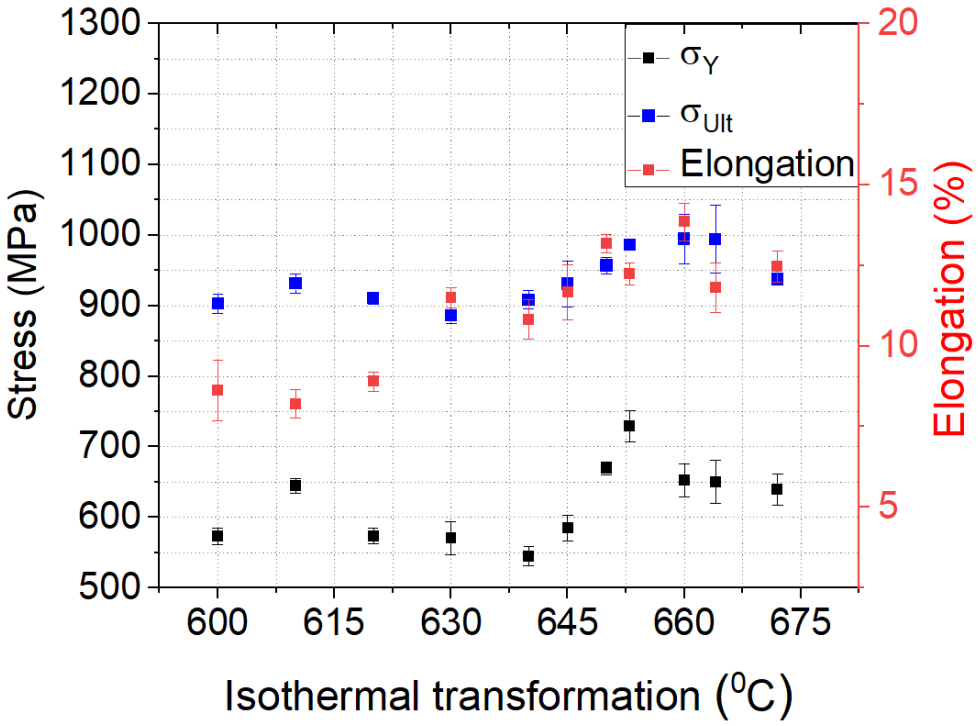

Figure 99. The mechanical properties of the steel Cr-V-Mo-0.2 as a function of the transformation temperature.

Isothermal transformation (^{0}C)	Yield stress (MPa)	YS Standard Deviation	Ultimate tensile stress (MPa)	UTS Standard Deviation	Elongation (%)	Elongation Standard Deviation
600	573.4	11.6	903.3	13.9	8.6	0.9
610	644.8	10.5	931.4	14	8.2	0.4
620	573.6	11.3	910.4	7.8	8.9	0.3
630	570.5	23.4	885.9	11.5	11.5	0.3
640	544.9	13.4	908.6	13.2	10.8	0.6
645	585	18.1	930.8	32	11.7	0.9
650	669.2	8.8	957.1	11.9	13.2	0.3
655	729.1	21.4	985.8	4.7	12.2	0.4
660	652.5	23.7	994.5	35.1	13.9	0.6
666	650.5	30.9	994.2	48	11.8	0.8
670	561.5	16.1	915.1	5.7	9.9	0.4
675	639.5	22.5	938.5	7.1	12.6	0.6

Table 35. The tensile properties of steels Cr-V-Mo-0.2 plotted in Figure 99.

4.5.5. STEEL CR-NB-V-0.2

Results for steel Cr-Nb-V-0.2 are presented in Figure 100, Figure 101 and summarized in Table 36. It is clear that the Nb+Cr additions retards the transformation kinetics and gives a $\gamma \rightarrow \alpha$ transformation temperature that is higher than the steels with no addition of Nb. From Figure 101 it is observed that in the temperature range from 675^{0}C to ~700^{0}C, the elongation increases while YS reduces and the UTS stays the same. Then, at 710^{0}C, the total elongation increases again, finally falling sharply at 725^{0}C. At the same time, YS and UTS remain relatively constant for 710^{0}C and then increases, as expected from the reduction in the total ferrite content. The isothermal transformation at 650^{0}C showed very high YS and UTS with a relatively low reduction in the elongation, which is related to its upper bainite structure.

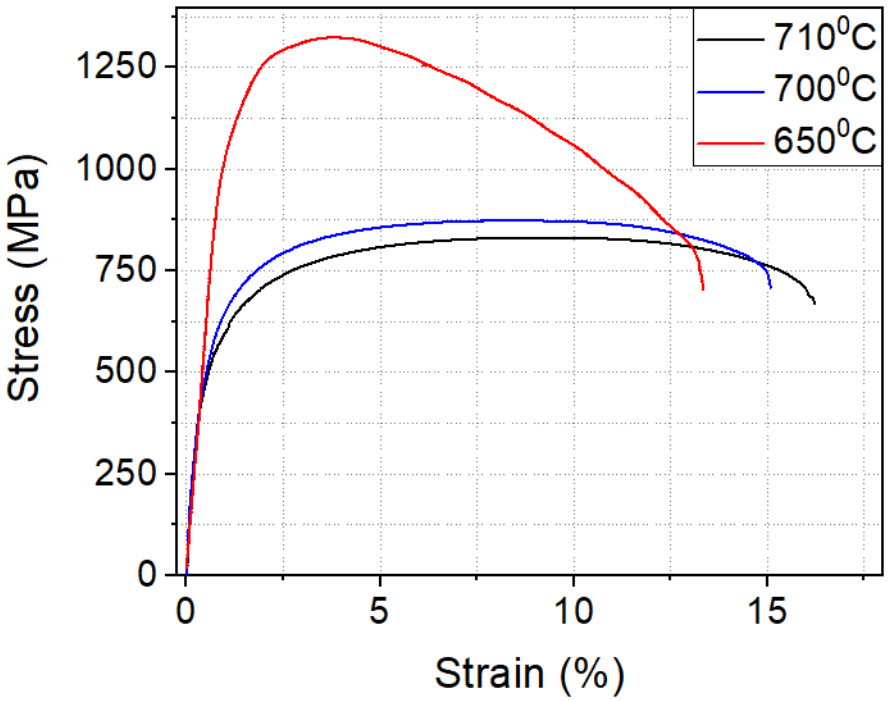

Figure 100. Engineering stress-strain curve of Cr-Nb-V-0.2 steel isothermally transformed at 650⁰C, 700⁰C, and 710⁰C.

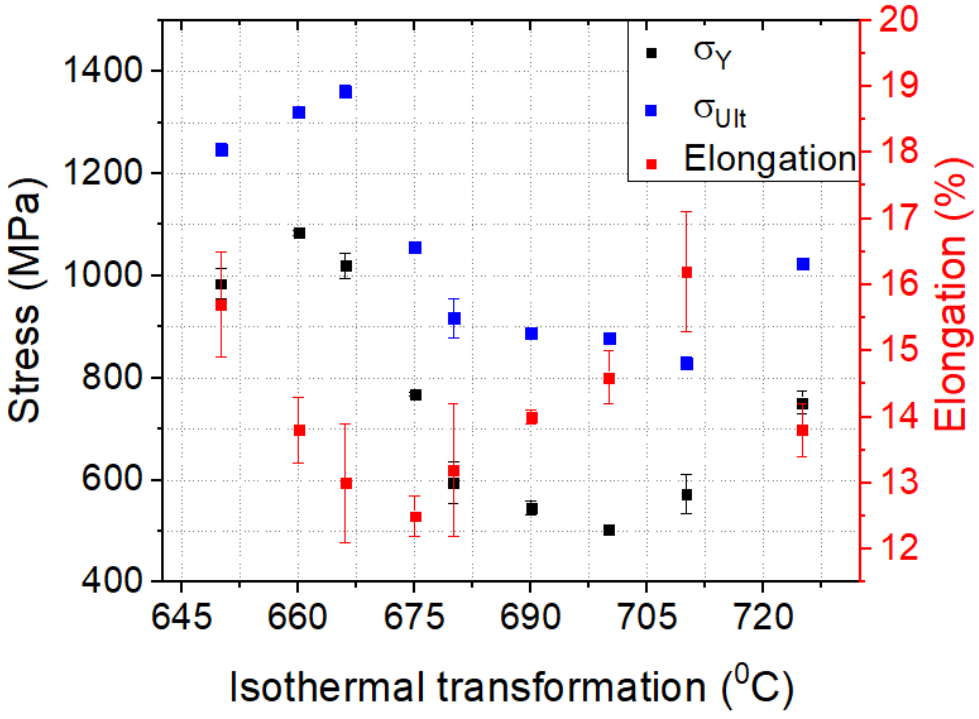

Figure 101. The mechanical properties of the steel Cr-Nb-V-0.2 as a function of the transformation temperature.

Isothermal transformation (^{0}C)	Yield stress (MPa)	YS Standard Deviation	Ultimate tensile stress (MPa)	UTS Standard Deviation	Elongation (%)	Elongation Standard Deviation
650	984.3	29.7	1247.3	10.9	15.7	0.8
660	1084.2	4.7	1320.9	4.6	13.8	0.5
666	1019.3	25.5	1359.95	12.8	13	0.9
675	768.12	3.5	1055.85	4.2	12.5	0.3
680	594.3	40.4	917.4	38	13.2	1
690	545.7	14.4	888.9	4.5	14	0.4
700	502.9	9.1	877.8	4.1	14.6	0.4
710	572.3	38.3	827.7	12.3	16.2	0.9
725	751.9	22.2	1023.7	1.2	13.8	0.4

Table 36. The tensile properties of steels Cr-Nb-V-0.2 plotted in Figure 101.

Table 37 and Table 38 show that the elastic + uniform plastic strain (uniform strain) for alloys treated with the same conditions is greater in the alloys with Cr additions. Also, V-Mo microalloyed steels with higher deformation-per-pass during the hot-rolling exhibit greater values of uniform strain. The greater gain in the uniform strain of Cr-V-Mo alloys was registered in samples with reaustenitization temperature of 1150^{0}C, being this the treatment with lower yield and ultimate strength.

Lastly, the results from alloy Cr-Nb-V-Mo-0.2 show that in the bainitic structures, the gain in ultimate strength is at the expense of the elongation. Comparing samples isothermally transformed at 650^{o}C with the ones isothermally transformed at 700 and 710^{o}C, the proportions between stress and strain are not conserved. While the yield and ultimate stress are reduced between 30 and 50%, the uniform elongation increases ∼230%.

It is recommended to carry on more experiments of tensile samples which show no big difference in the uniform plastic strain, but a clear difference in the non-homogeneous strain (necking strain), especially on the lowest values of this last. A possible reason for this is that the necking and further fracture during the tensile tests took place close to the pins used to measure the elongation with the camera record. In this thesis, the most conservative results are presented, so with more samples treated with all the precautions mentioned, a greater final elongation is expected.

Material	Isothermal transformation temperature [^{0}C]	Total Strain [%]	Elastic + Uniform plastic strain [%]	Non-uniform plastic strain [%]
V-Mo-0.0	600	7.6	4.2	3.4
	625	9.4	4.3	5.1
	650	12.7	7.1	5.6
Cr-V-Mo-0.0	600	10.2	5.7	4.5
	625	13.1	6.8	6.3
	650	14.8	7.1	7.7
	660	19.6	7.4	12.2
V-Mo-0.2	645	8.3	5.7	2.6
	655	11.2	6.2	5
	672	8.7	5.8	2.9
Cr-V-Mo-0.2	645	11.7	7.8	3.9
	664	11.8	6.1	5.7
	672	12.6	7.5	5.1
Cr-Nb-V-Mo-0.2	650	15.7	3.8	11.9
	700	14.6	8.5	6.1
	710	16.2	9.3	6.9

Table 37. Uniform and non-uniform strains of microalloyed steels, their relationship with chemistry, isothermal transformation temperature, and strain per pass during the hot-rolling.

Material	Reaustenitization temperature [^{0}C]	Total Strain [%]	Elastic + Uniform plastic strain [%]	Non-uniform plastic strain [%]
V-Mo-0.4	900	14.9	9.9	4.9
	1150	14.6	5.7	8.9
	1250	13.9	7.1	6.8
Cr-V-Mo-0.4	900	15.7	7.9	7.7
	1150	21.1	8.6	12.5
	1245	17.3	6.5	10.8

Table 38. Uniform and non-uniform strains of microalloyed steels, their relationship with chemistry, isothermal transformation temperature, and strain per pass during the hot-rolling.

Optical micrographs of the fracture surface from the tensile test on a steel Cr-V-Mo-0.0 sample are shown in Figure 102 (parallel to the loading plane). The main fracture is through the ferrite grains, with very small portions through martensite where they fracture almost perpendicular to the load and produces regions of cleavage. Figure 103 gives SEM micrograph of the same crack but in plain view. Figure 103 a) shows that the major fracture mechanism is micro-void coalescence, with a few zones of cleavage as shown in Figure 103 b); these are probably associated with martensite. EDS analysis was performed on the small sphere-shaped "grains" observed in Figure 103 c), results are shown in Figure 104 which suggests these are MnS.

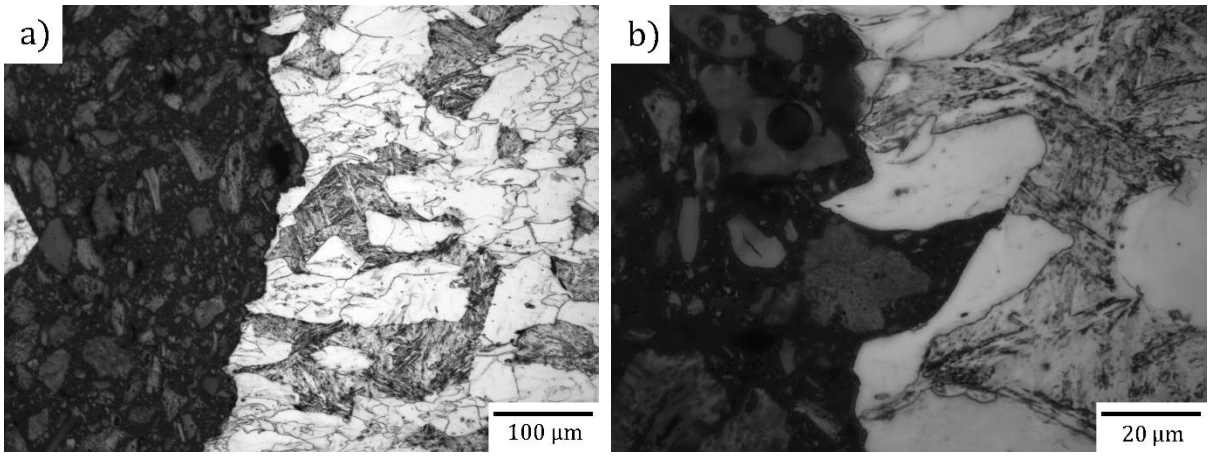

Figure 102. Longitudinal micrograph of the fracture generated by tensile test on a steel Cr-V-Mo-0.0 aged at 650^{0}C.

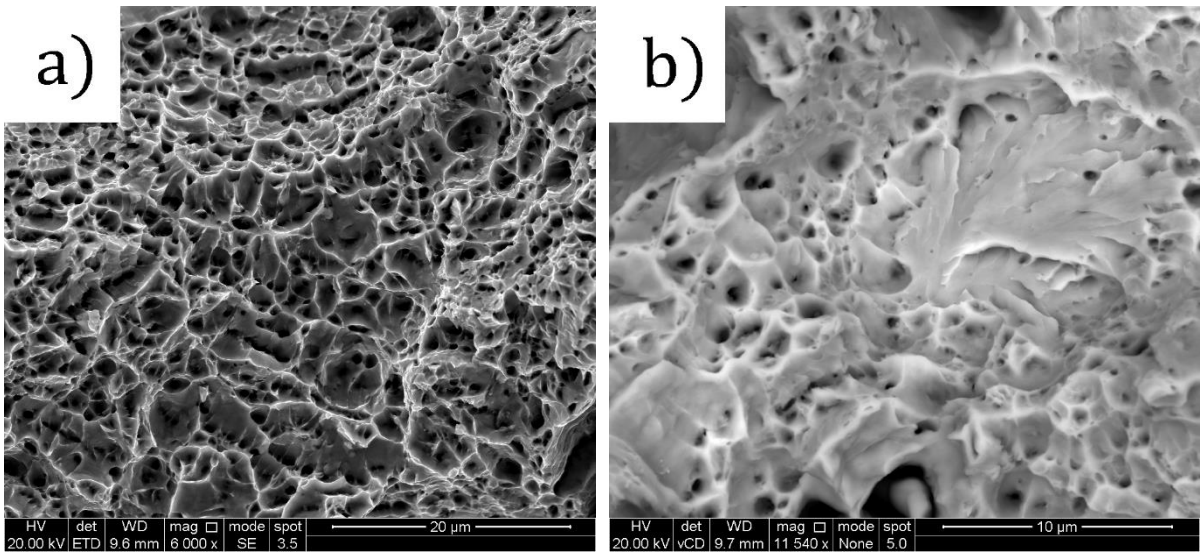

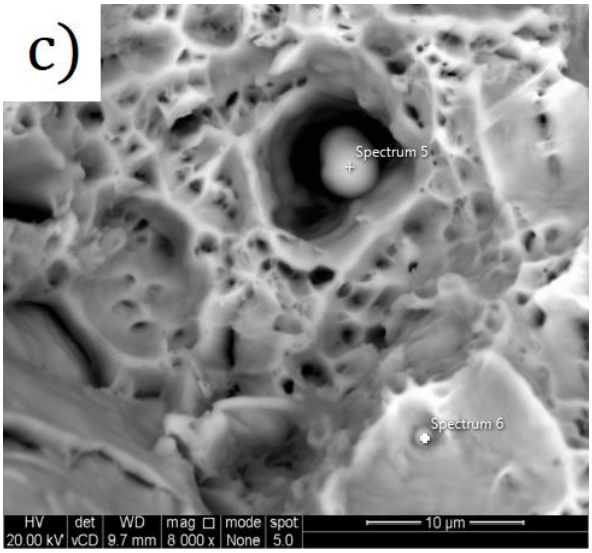

Figure 103. SEM micrographs of the fracture surface generated by tensile test on steels Cr-V-Mo-0.0 aged at 650^{0}C.

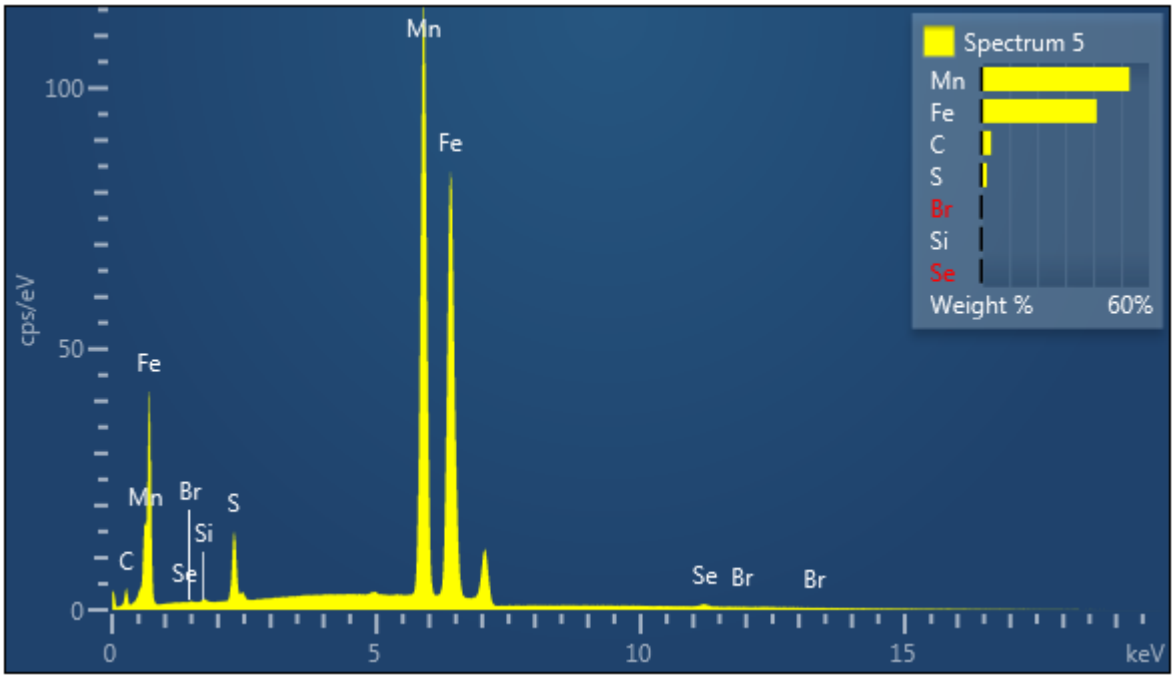

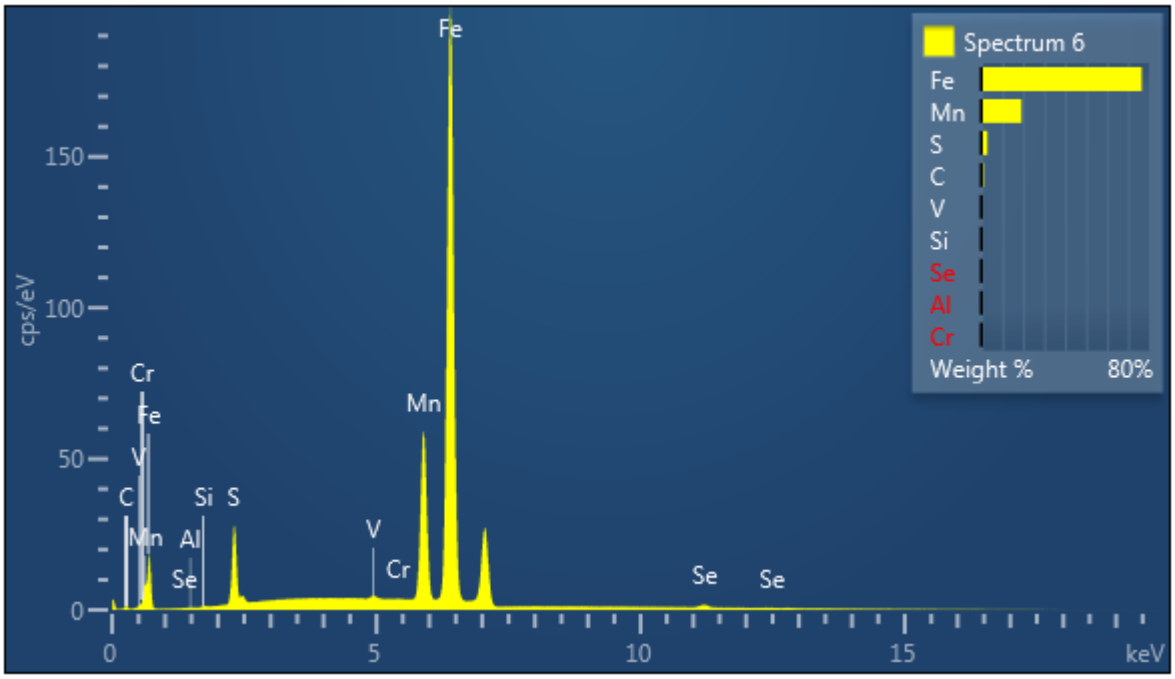

Figure 104. Results of the EDS zones pointed on Figure 103 c).

4.6. CARBON EXTRACTION REPLICAS

In the analysis of the carbon extraction replicas it is assumed that:

1) The sectioned particles by the polishing had been removed by a sufficiently deep first etching (Figure 105a)).

2) They do not contain particles released by the first or the second etch, or pieces of the material (Figure 105 b)).

These two conditions guarantee that images correspond to the true particle diameters. Figure 106 to Figure 111 show micrographs of the extraction carbon replicas obtained from samples Cr-V-Mo-0.0, V-Mo-0.4, Cr-V-Mo-0.4, V-Mo-0.2, Cr-V-Mo-0.2, and Cr-Nb-V-0.2.

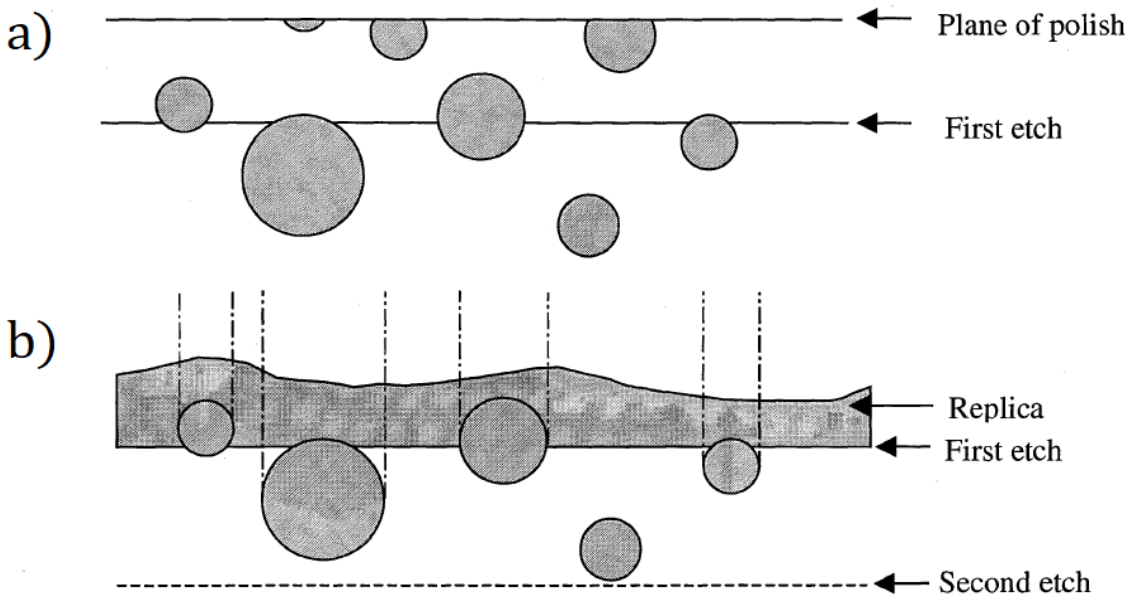

Figure 105. Ideal extraction carbon replica preparation and extraction [230].

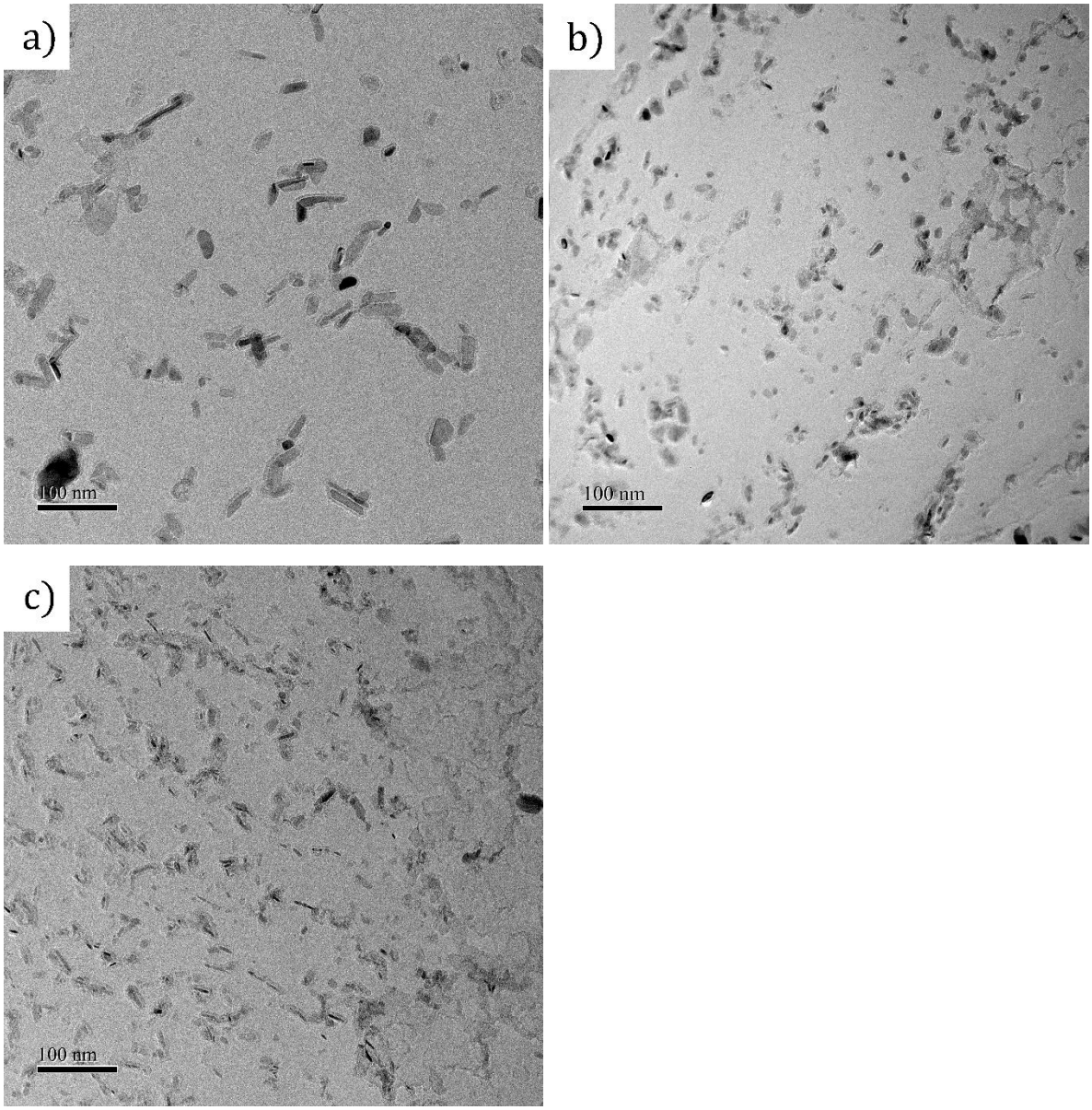

Figure 106. TEM micrographs of the extraction carbon replicas of alloy Cr-V-Mo-0.0 isothermally transformed at a) 625^{0}C, b) 650^{0}C, c) 660^{0}C.

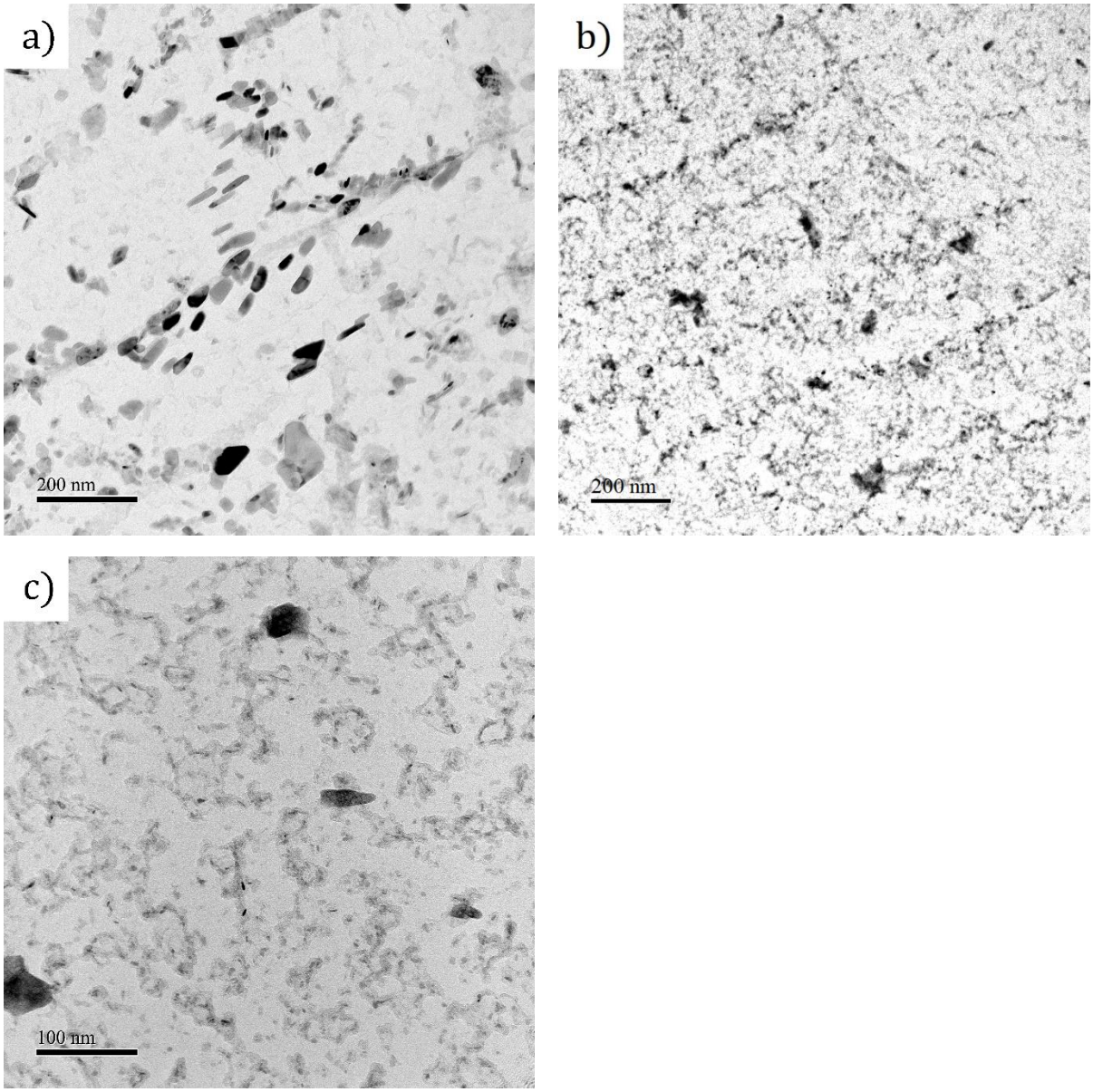

Figure 107. TEM micrographs of the extraction carbon replicas of alloy V-Mo-0.4 all isothermally transformed at 650^{0}C but with different austenitization temperatures: a) 900^{0}C, b) 1150^{0}C, c) 1245^{0}C.

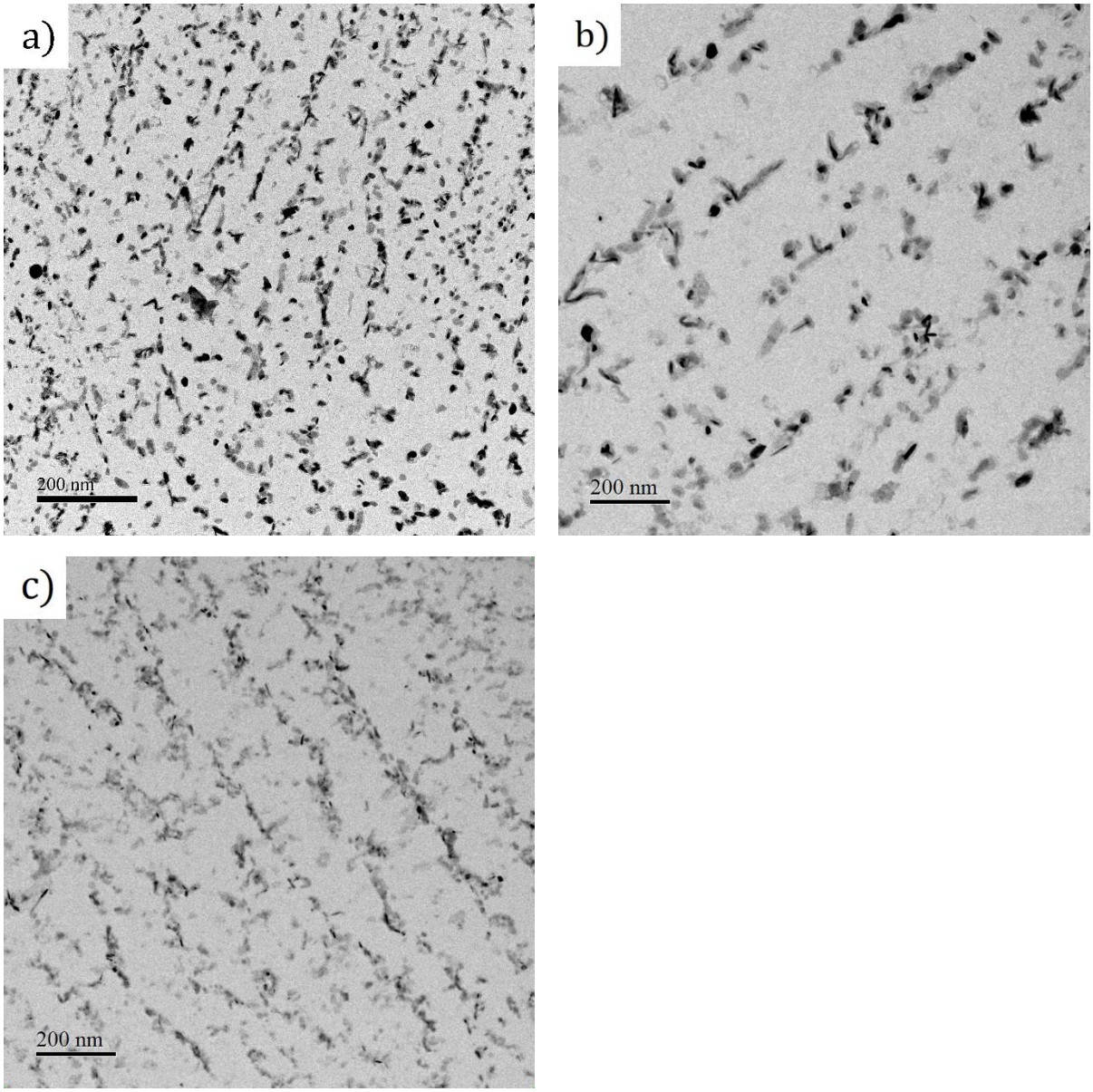

Figure 108. TEM micrographs of the extraction carbon replicas of alloy Cr-V-Mo-0.4 all isothermally transformed at 650^{0}C but with different austenitization temperatures: a) 900^{0}C, b) 1150^{0}C, c) 1245^{0}C.

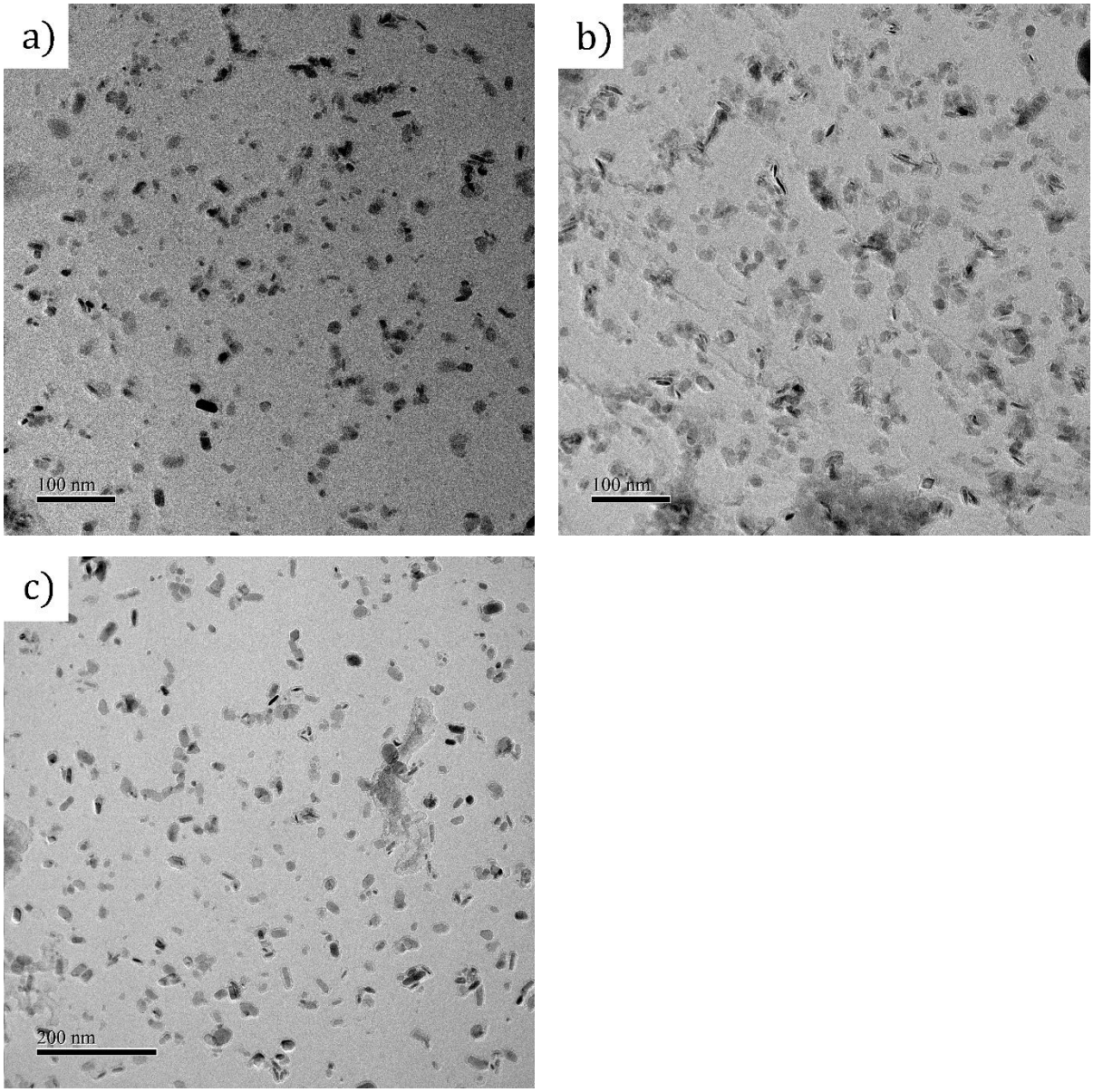

Figure 109. TEM micrographs of the extraction carbon replicas of alloy V-Mo-0.2 isothermally transformed at a) 600^{0}C, b) 655^{0}C, c) 670^{0}C.

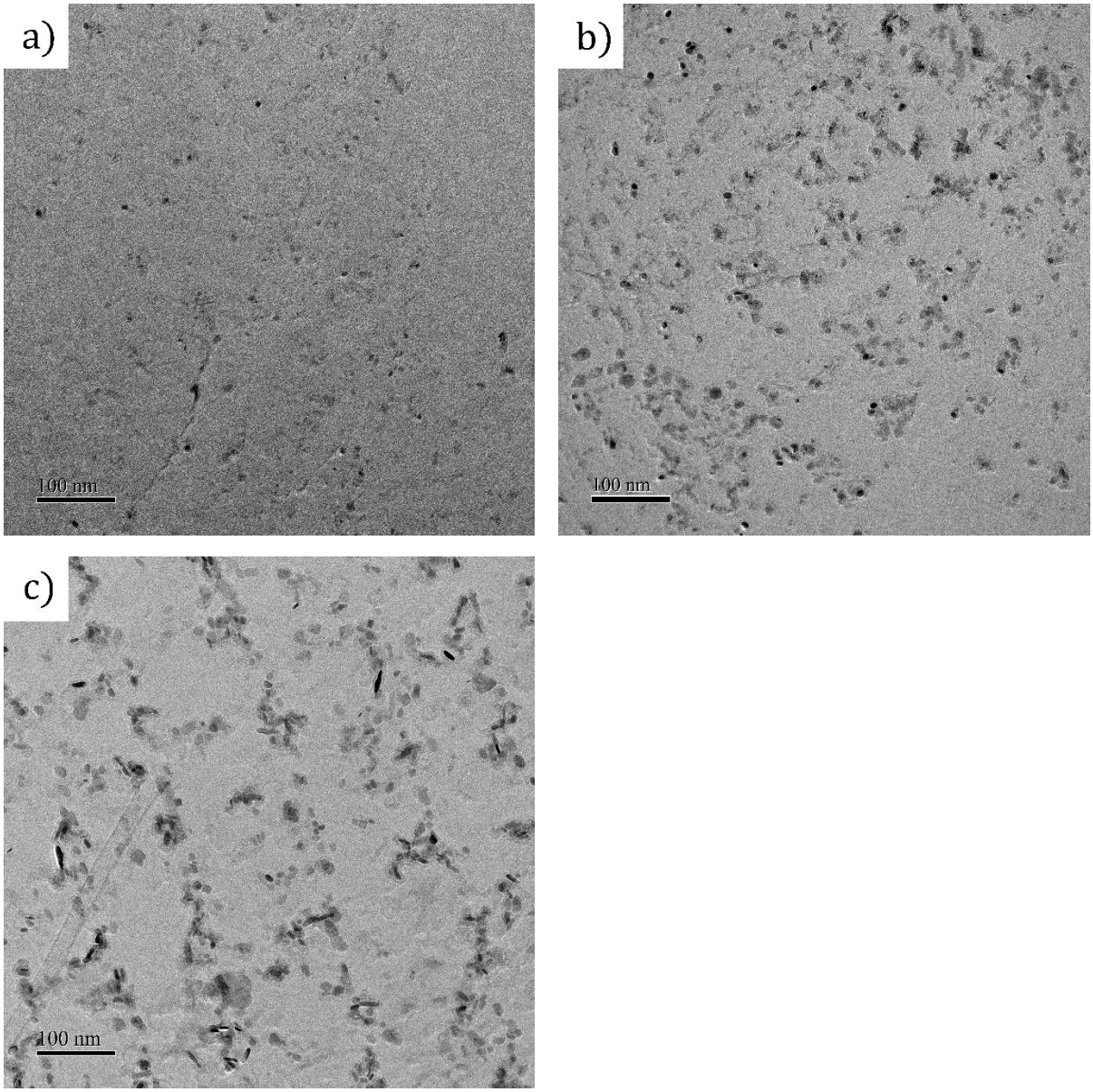

Figure 110. TEM micrographs of the extraction carbon replicas of alloy Cr-V-Mo-0.2 isothermally transformed at a) 640^{0}C, b) 664^{0}C, c) 672^{0}C.

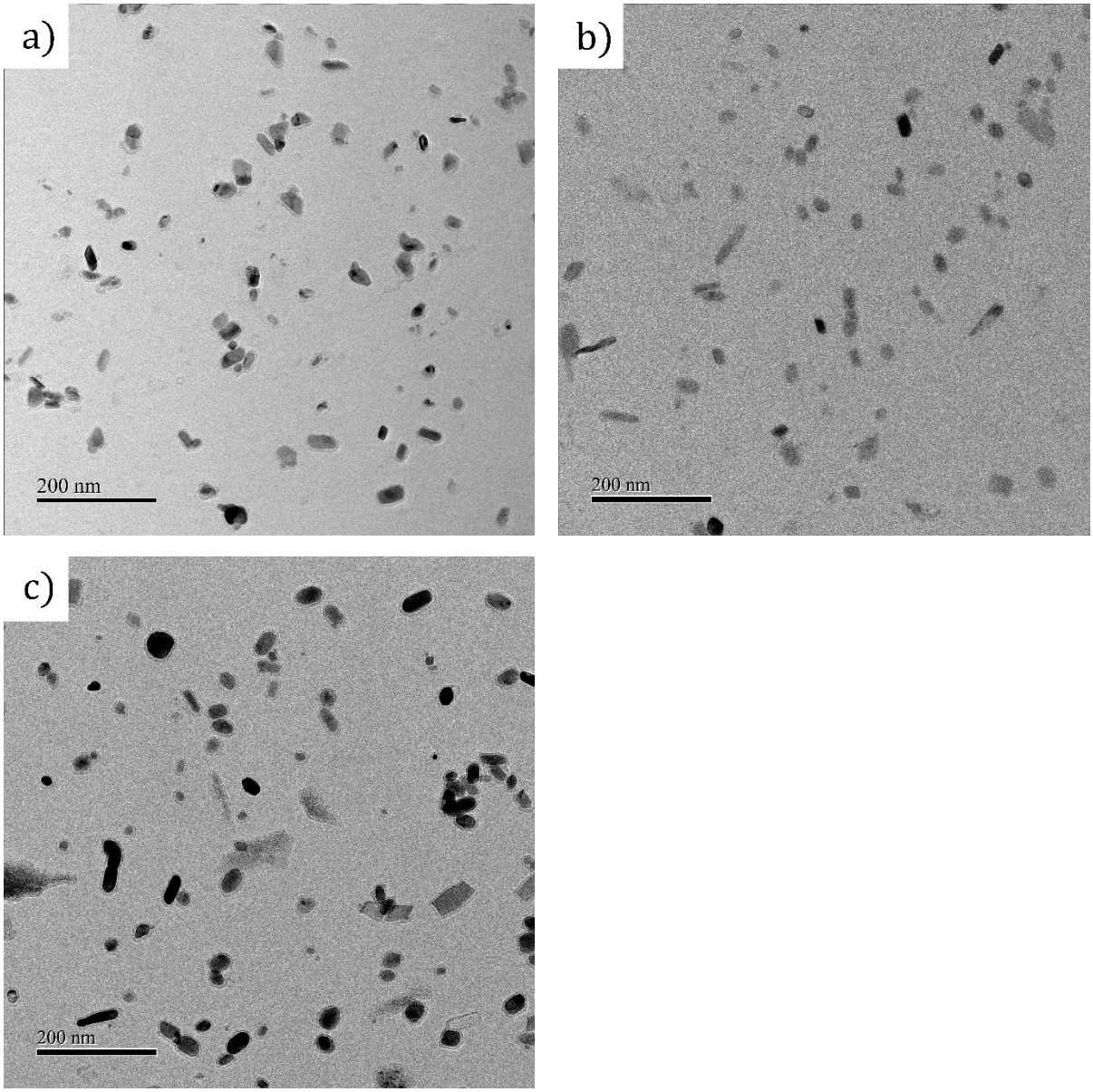

Figure 111. TEM micrographs of the extraction carbon replicas of alloy Cr-Nb-V-0.2 isothermally transformed at a) 680^{0}C, b) 690^{0}C, c) 710^{0}C.

Using the software ImageJ, automatic measurements of the areas projected by the particles were taken. Figure 112 shows an example of a carbon replica picture of steel Cr-V-Mo-0.0 isothermally transformed at 625^{0}C in which the contrast was increased, and thus, a delineation of particles or separation of the ones which joins while the contrast enhancement was performed for a further area counting with the software ImageJ was performed for each image. The software registers the areas of the particles, then, equivalent diameters are calculated assuming that all the areas where circles projected from spheres. For each particle diameter, an approximated volume was calculated as all of them were spheres. Because of the error generated by the contrast enhancement, particles with diameters below 2nm were discarded, such as the noise in the right-hand side of Figure 112 b).

The measured numbers per unit area obtained by the software were multiplied to obtain the number of particles of every group *j* per square millimetre ($N_{A(j)}$). The values were corrected by Equation 19 to obtain the numbers per cubic millimetre volume $N_{V(j)}$ of each group *j* with size interval Δ [230]. This assumption was taken after considering that the average thickness of the carbon replicas registered

by the detector of the coater was 6.5 nm, reducing the interposition of particles. Thus, the approximated volume fraction of that group of particles PVF_j with Equation 20.

$$N_{V(j)} = \frac{N_{A(j)}}{\left(j - \frac{1}{2}\right)\Delta}$$

Equation 19

$$PVF_j = N_{V(j)} \cdot \overline{vol}_j$$

Equation 20

$\overline{vol}_j$ corresponds to the average volume of the particles in the group *j*.

The standard error of the volume fraction corresponds to the number per unit volume $N_{V(j)}$ times the standard error of the particle' volume in each group, divided by the evaluated volume. Results of the interphase precipitates volume fraction into the ferrite in steels Cr-V-Mo-0.0, V-Mo-0.4, Cr-V-Mo-0.4, V-Mo-0.2, Cr-V-Mo-0.2 and Cr-Nb-V-0.2 are presented in Table 39 and plotted in Figure 113. Also, the fraction of interphase precipitates in those steels is shown in Figure 116 and the values are summarized in Table 41. The compositions of these particles are analysed in the next section with the diffraction patterns obtained from thin foils.

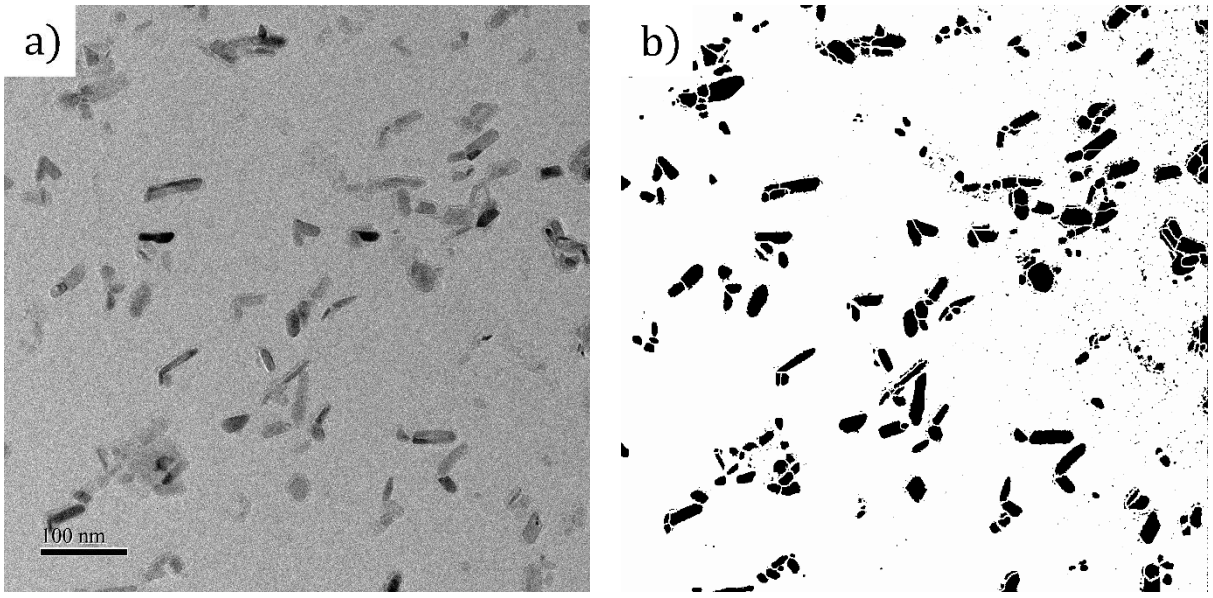

Figure 112. a) TEM image of a carbon extraction replica of alloy Cr-V-Mo-0.0 isothermally transformed at 625^{0}C. b) same image filtered and corrected with the software ImageJ to use the particle counter.

Figure 113 shows that the volume fraction of the interphase precipitation increases with the addition of Cr. Comparing Figure 113 b) with d), and c) with e) it is clear that the higher deformation per pass during rolling increases the interphase precipitation in microalloyed steels with and without Cr additions. From the same figures it is observed that with Cr in the steel the higher the austenitization temperature the higher volume fraction of interphase precipitates. This is because more microalloying elements dissolve in the austenite[247]. The previous conclusions cannot be drawn for Cr-V-Mo-0.0 because the hot-rolling schedule is unknown. Furthermore, the extent of precipitation is less in Cr-V-Mo-0.0 than the other alloys with Cr additions.

The temperature at which each alloy reaches the maximum ferrite volume fraction coincides with a higher volume fraction of precipitates smaller than Ø20 nm within the ferrite. Both lower and higher isothermal transformations produce a distribution with a high-volume fraction of small particles and a relatively low concentration of particles over Ø10 nm in steels with no Cr. In steels with Cr addition, the distribution of interphase precipitates at high isothermal transformation is very similar to the one obtained for austenitization at 1150^0C, in which the maximum volume fraction of precipitates corresponds to particles with diameters between 4 and 10 nm. A Nb+Cr addition (Figure 113 f)) and (Figure 116 f)) increases the fraction of particles with diameters between 10 and 20 nm for the maximum transformation temperature. Importantly, the volume fraction of interphase precipitation is much lower with Nb present than the microalloyed steels with only Cr additions or with no addition of Cr. Also, it is observed that at higher isothermal transformations the proportion of larger interphase precipitation (Ø>10 nm) increases.

Figure 114, Figure 115, and Table 40 present the interphase precipitate size within experimental error for carbon extraction replica samples. No clear trend of the average diameter of the interphase precipitation with the addition of Cr is observed. Furthermore, it is shown that the average diameter of the interphase precipitate mainly increases with the reaustenitization temperature in the alloy with Cr additions, but in the case of the steel with no Cr it reduces after 1150^0C. The fraction of small interphase precipitates in alloys with no Cr additions increases with higher austenitization temperatures (Figure 116). The relative fraction of small interphase precipitation in microalloyed steels with Cr additions is larger in low austenitization temperatures, but the total volume fraction is larger in austenitization of 1250^0C.

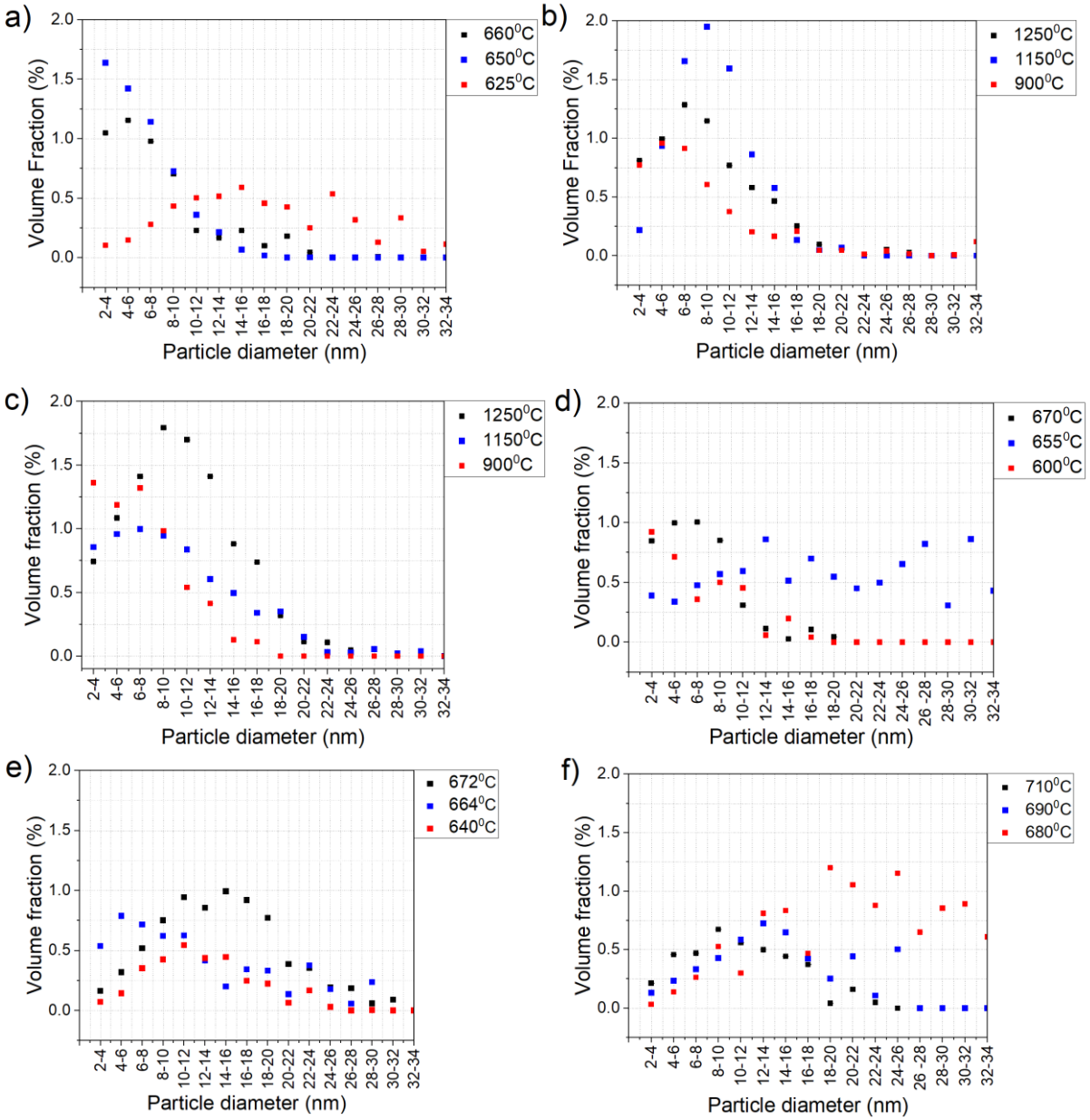

Figure 113. Volume Fraction of the interphase precipitation within the ferrite of steels a) Cr-V-Mo-0.0 austenitization over 1250^{0}C and different isothermal transformations b) V-Mo-0.4 different austenitization temperatures and all isothermally transformed at 650^{0}C, c) Cr-V-Mo-0.4 different austenitization temperatures and all isothermally transformed at 660^{0}C, d) V-Mo-0.2 austenitization below 1250^{0}C and different isothermal transformations, e) Cr-V-Mo-0.2 austenitization below 1250^{0}C and different isothermal transformations, and f) Cr-Nb-V-0.2 austenitization below 1250^{0}C and different isothermal transformations.

Alloy	Cr-V-Mo-0.0						V-Mo-0.4					
Reaustenitization [^{0}C]	<1200		<1200		<1200		900		1150		1250	
Isothermal Transformation [^{0}C]	625		650		660		650		650		650	
	Volume Fraction [%]	S.D.	Volume Fraction [%]	S.D.	Volume Fraction [%]	S.D.	Volume Fraction [%]	S.D.	Volume Fraction [%]	S.D.	Volume Fraction [%]	S.D.
2 to 4 [nm]	0.104	5.3E-4	1.636	9.2E-3	1.048	6.6E-3	0.773	2.5E-3	0.219	1.5E-3	0.810	4.7E-3
4 to 6 [nm]	0.148	4.1E-4	1.421	4.7E-3	1.155	3.9E-3	0.958	1.3E-3	0.936	2.9E-3	0.993	3.3E-3
6 to 8 [nm]	0.279	5.2E-4	1.142	2.8E-3	0.977	2.5E-3	0.914	1.2E-3	1.657	4.0E-3	1.285	3.2E-3
8 to 10 [nm]	0.433	6.5E-4	0.725	1.4E-3	0.703	1.3E-3	0.606	1.2E-3	1.950	3.6E-3	1.148	2.2E-3
10 to 12 [nm]	0.503	5.3E-4	0.361	5.7E-4	0.228	3.9E-4	0.376	9.4E-4	1.593	2.5E-3	0.768	1.2E-3
12 to 14 [nm]	0.515	4.6E-4	0.215	2.5E-4	0.168	1.9E-4	0.205	1.3E-3	0.863	1.2E-3	0.580	7.9E-4
14 to 16 [nm]	0.591	3.6E-4	0.068	7.6E-5	0.228	2.6E-4	0.165	5.9E-4	0.577	7.3E-4	0.465	5.3E-4
16 to 18 [nm]	0.456	2.2E-4	0.018	1.9E-5	0.101	9.1E-5	0.209	7.2E-4	0.134	1.1E-4	0.253	2.6E-4
18 to 20 [nm]	0.425	1.8E-4	0	0	0.181	5.0E-5	0.046	5.2E-4	0.048	3.2E-5	0.097	9.4E-5

20 to 22 [nm]	0.251	2.8E-4	0.003	0	0.044	1.6E-5	0.046	3.4E-4	0.067	0	0.071	5.2E-5
22 to 24 [nm]	0.537	1.4E-4	0	0	0	0	0.013	4.1E-4	0	0	0.014	1.1E-5
24 to 26 [nm]	0.318	2.1E-5	0	0	0	0	0.041	4.3E-4	0	0	0.054	0
26 to 28 [nm]	0.130	0	0	0	6.6E-3	0	0.018	5.3E-4	0	0	0.027	1.1E-5
28 to 30 [nm]	0.333	8.1E-6	0	0	0	0	0	1.8E-4	0	0	0	0
30 to 32 [nm]	0.051	0	0	0	0	0	0.007	4.2E-4	0	0	0	0

Alloy	Cr-V-Mo-0.4						V-Mo-0.2					
Reaustenitization [^{0}C]	900		1150		1250		1250		1250		1250	
Isothermal Transformation [^{0}C]	660		660		660		600		655		670	
	Volume Fraction [%]	S.D.	Volume Fraction [%]	S.D.	Volume Fraction [%]	S.D.	Volume Fraction [%]	S.D.	Volume Fraction [%]	S.D.	Volume Fraction [%]	S.D.
2 to 4 [nm]	1.362	6.5E-3	0.856	8.7E-3	0.743	4.6E-3	0.922	5.8E-3	0.391	2.5E-3	0.848	5.6E-3
4 to 6 [nm]	1.188	3.4E-3	0.959	5.5E-3	1.085	3.7E-3	0.713	2.7E-3	0.337	1.3E-3	0.996	3.8E-3
6 to 8 [nm]	1.321	2.7E-3	0.996	4.1E-3	1.410	3.4E-3	0.358	8.7E-4	0.475	1.2E-3	1.004	2.7E-3
8 to 10 [nm]	0.985	1.5E-3	0.945	3.0E-3	1.793	3.3E-3	0.50	9.2E-4	0.567	1.2E-3	0.850	1.8E-3
10 to 12 [nm]	0.540	5.7E-4	0.836	2.2E-3	1.699	2.7E-3	0.454	7.7E-4	0.594	9.4E-4	0.308	5.6E-4
12 to 14 [nm]	0.413	4.3E-4	0.606	1.3E-3	1.412	1.9E-3	0.059	7.9E-5	0.859	1.3E-3	0.114	1.7E-4
14 to 16 [nm]	0.128	1.1E-4	0.500	9.7E-4	0.882	1.1E-3	0.197	2.7E-5	0.514	5.9E-4	0.028	2.6E-5
16 to 18 [nm]	0.114	7.1E-5	0.340	5.7E-4	0.739	7.6E-4	0.041	0	0.699	7.2E-4	0.105	0
18 to 20 [nm]	0	0	0.350	4.8E-4	0.317	3.0E-4	0	0	0.546	5.2E-4	0.043	5.8E-7

20 to 22 [nm]	0	0	0.151	2.3E-4	0.114	9.3E-5	0	0	0.449	3.4E-4	0	0
22 to 24 [nm]	0	0	0.031	4.1E-5	0.108	6.4E-5	0	0	0.500	4.1E-4	0	0
24 to 26 [nm]	0	0	0.030	3.4E-5	0.049	2.6E-5	0	0	0.653	4.3E-4	0	0
26 to 28 [nm]	0	0	0.056	0	0	0	0	0	0.821	5.3E-4	0	0
28 to 30 [nm]	0	0	0.021	1.3E-5	0.003	1.6E-6	0	0	0.308	1.8E-4	0	0
30 to 32 [nm]	0	0	0.040	0	0	0	0	0	0.863	4.2E-4	0	0

Alloy	Cr-V-Mo-0.2						Cr-Nb-V-0.2					
Reaustenitization [^{0}C]	1250		1250		1250		1150		1150		1150	
Isothermal Transformation [^{0}C]	640		664		672		680		690		710	
	Volume Fraction [%]	S.D.	Volume Fraction [%]	S.D.	Volume Fraction [%]	S.D.	Volume Fraction [%]	S.D.	Volume Fraction [%]	S.D.	Volume Fraction [%]	S.D.
2 to 4 [nm]	0.072	7.5E-4	0.537	5.8E-3	0.164	9.6E-4	0.033	6.2E-5	0.133	1.1E-3	0.214	1.5E-3
4 to 6 [nm]	0.144	7.9E-4	0.789	4.8E-3	0.320	9.0E-4	0.140	6.9E-5	0.235	1.1E-3	0.457	1.7E-3
6 to 8 [nm]	0.353	1.5E-3	0.718	3.0E-3	0.519	1.1E-3	0.264	2.0E-4	0.334	1.0E-3	0.470	1.2E-3
8 to 10 [nm]	0.425	1.3E-3	0.622	1.9E-3	0.751	1.2E-3	0.527	3.4E-4	0.429	1.1E-3	0.672	1.3E-3
10 to 12 [nm]	0.545	1.5E-3	0.624	1.6E-3	0.944	1.2E-3	0.300	1.7E-4	0.585	1.2E-3	0.5441	8.4E-4
12 to 14 [nm]	0.436	9.3E-4	0.419	8.6E-4	0.856	9.1E-4	0.811	3.3E-4	0.726	1.3E-3	0.500	6.0E-4
14 to 16 [nm]	0.446	8.8E-4	0.202	4.0E-4	0.994	9.2E-4	0.834	2.8E-4	0.648	1.0E-3	0.444	4.7E-4
16 to 18 [nm]	0.249	4.1E-4	0.343	5.1E-4	0.920	7.6E-4	0.468	1.5E-4	0.423	5.3E-4	0.374	3.4E-4
18 to 20 [nm]	0.224	3.0E-4	0.332	6.3E-4	0.772	5.6E-4	1.200	4.0E-4	0.251	2.8E-4	0.042	4.5E-5

20 to 22 [nm]	0.065	8.4E-5	0.136	1.7E-4	0.388	2.6E-4	1.053	2.8E-4	0.441	3.3E-4	0.161	0
22 to 24 [nm]	0.169	2.9E-5	0.375	3.2E-4	0.354	2.2E-4	1.053	2.3E-4	0.107	9.5E-5	0.049	0
24 to 26 [nm]	0.030	4.1E-5	0.180	1.7E-4	0.192	1.2E-4	0.880	2.7E-4	0.503	2.2E-4	0	0
26 to 28 [nm]	0	0	0.057	5.9E-5	0.185	4.0E-5	1.153	1.4E-4	0	0	0	0
28 to 30 [nm]	0.004	0	0.237	0	0.060	8.3E-7	0.649	1.4E-4	0	0	0	0
30 to 32 [nm]	0	0	0	0	0.091	0	0.854	1.2E-4	0	0	0	0

Table 39. Data of the interphase precipitates volume fraction of the studied microalloyed steels.

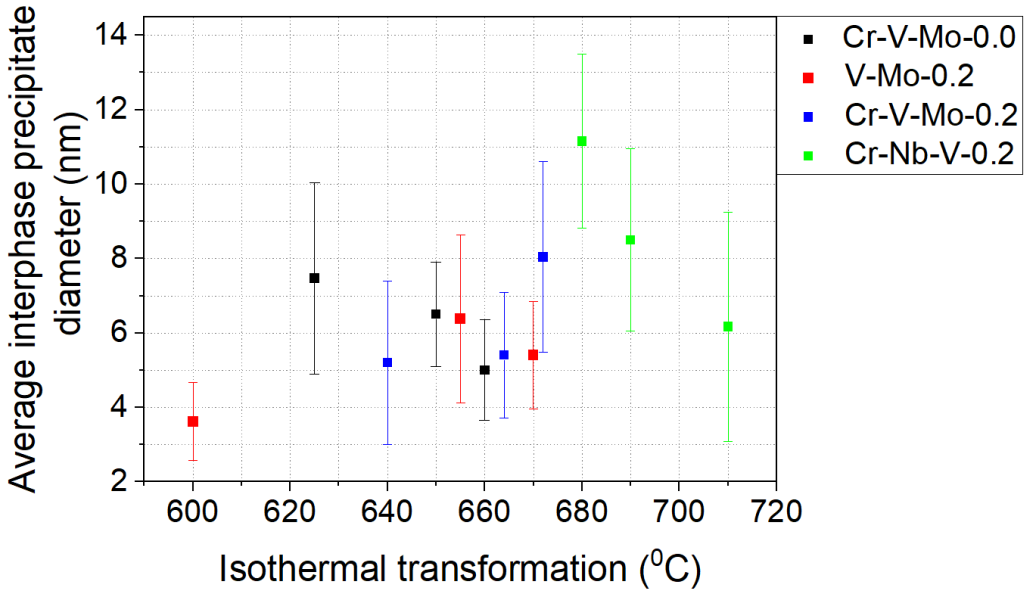

Figure 114. Average diameter of the interphase precipitates in the different alloys at different isothermal transformation temperatures for 90 min.

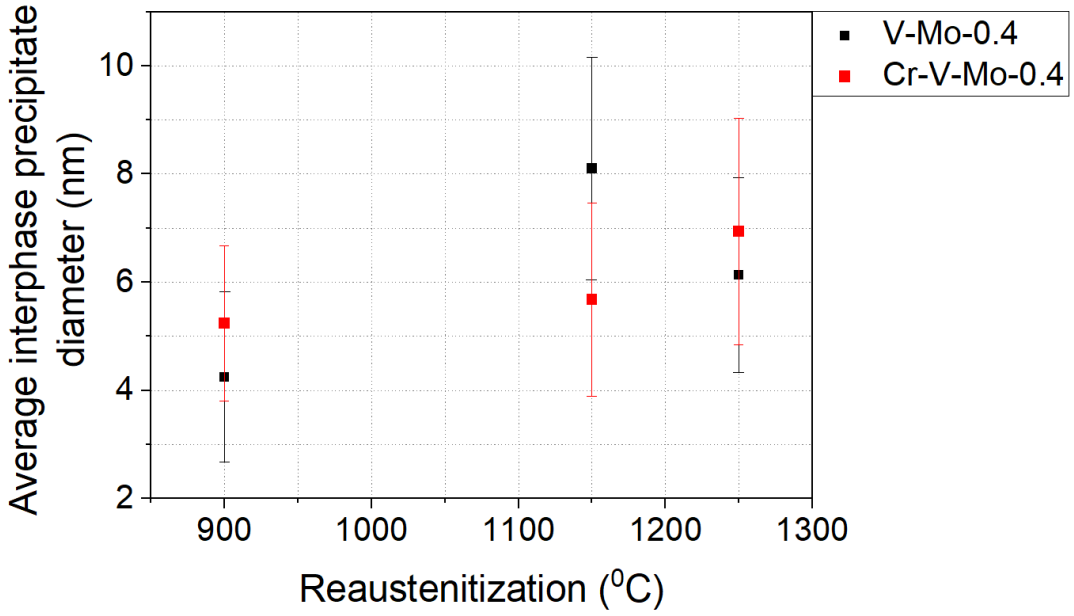

Figure 115. Average diameter of the interphase precipitates in the different alloys at different reaustenitization temperatures before isothermal transformations at 650^{0}C (steel V-Mo-0.4) and 660^{0}C (steel Cr-V-Mo-0.4) for 90 min.

Steel	Reaustenitization temperature [^{0}C]	Isothermal transformation temperature [^{0}C]	Average diameter of precipitation [nm]	S.D.
Cr-V-Mo-0.0	>1200^{0}C	625	7.47	5.2
	>1200^{0}C	650	5	2.7
	>1200^{0}C	660	6.5	2.8
V-Mo-0.4	900	650	4.3	3.1
	1150	650	8.1	4.1
	1250	650	6.1	3.6
Cr-V-Mo-0.4	900	660	5.5	2.9
	1150	660	5.7	4.6
	1250	660	6.7	4.2
V-Mo-0.2	1250	600	3.6	2.1
	1250	655	6.4	4.5
	1250	670	5.4	2.9
Cr-V-Mo-0.2	1250	640	5.2	4.4
	1250	664	5.4	3.4
	1250	672	8.0	5.1
Cr-Nb-V-0.2	1190	680	11.2	5.7
	1190	690	8.5	4.9
	1190	710	6.2	4.3

Table 40. Data of the average diameter measured from the carbon extraction replicas of microalloyed steels.

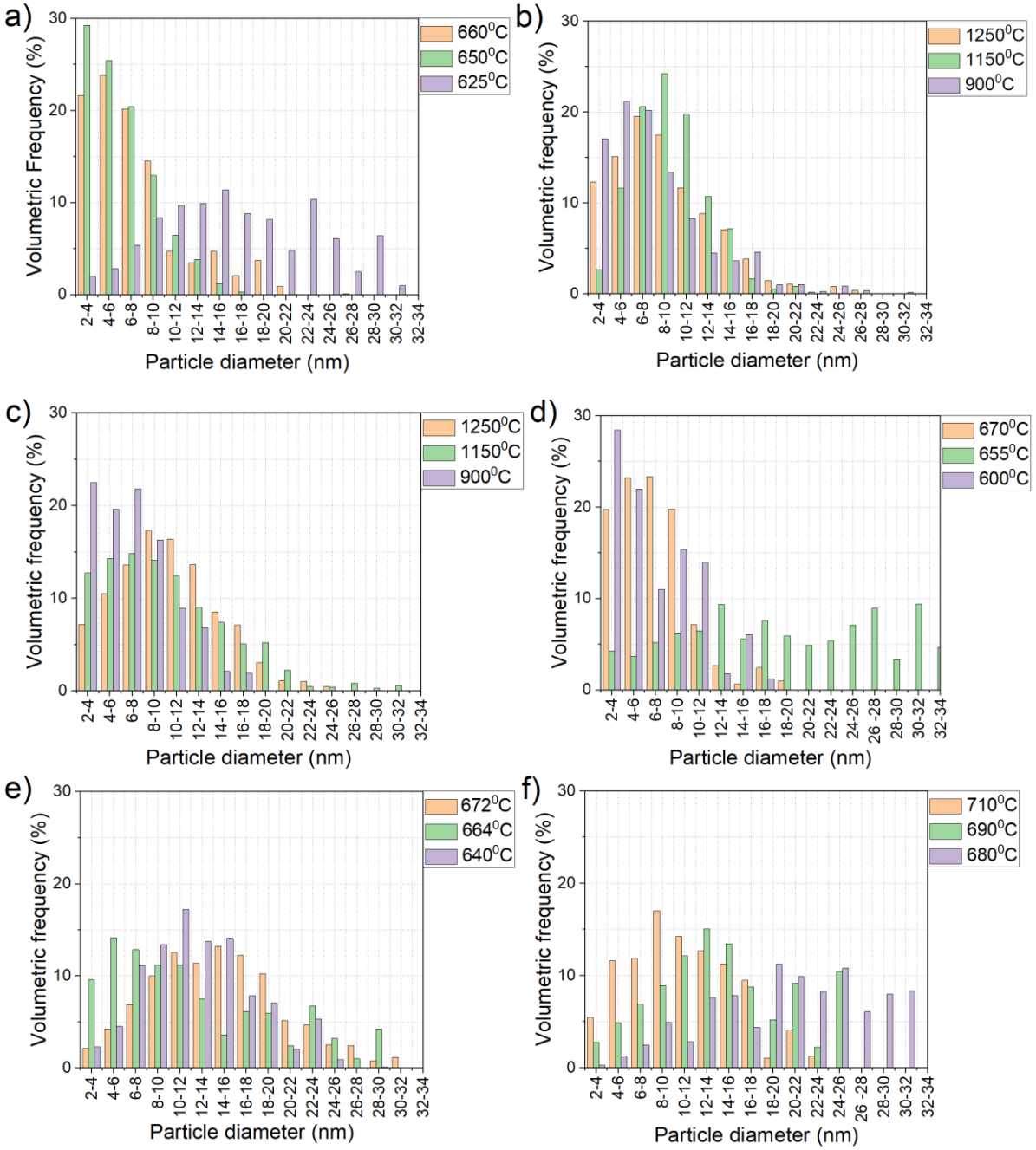

Figure 116. Size distribution of the precipitates within the ferrite of steels a) Cr-V-Mo-0.0 austenitization over 1250^{0}C and different isothermal transformations b) V-Mo-0.4 different austenitization temperatures and all isothermally transformed at 650^{0}C, c) Cr-V-Mo-0.4 different austenitization temperatures and all isothermally transformed at 660^{0}C, d) V-Mo-0.2 austenitization below 1250^{0}C and different isothermal transformations, e) Cr-V-Mo-0.2 austenitization below 1250^{0}C and different isothermal transformations, and f) Cr-Nb-V-0.2 austenitization below 1250^{0}C and different isothermal transformations.

Fraction of particles [%]									
Alloy	**Cr-V-Mo-0.0**			**V-Mo-0.4**			**Cr-V-Mo-0.4**		
Reaustenitization [^{0}C]	**<1200**	**<1200**	**<1200**	**900**	**1150**	**1245**	**900**	**1150**	**1245**
Isothermal Transformation [^{0}C]	**625**	**650**	**660**	**650**	**650**	**650**	**660**	**660**	**660**
2 to 4 [nm]	2.0	29.3	21.7	17.1	2.7	12.3	22.5	12.8	7.2
4 to 6 [nm]	2.9	25.4	23.9	21.2	11.6	15.1	19.6	14.3	10.5
6 to 8 [nm]	5.4	20.4	20.2	20.2	20.6	19.6	21.8	14.8	13.6
8 to 10 [nm]	8.3	13.0	14.5	13.4	24.2	17.5	16.3	14.1	17.3
10 to 12 [nm]	9.7	6.5	4.7	8.3	19.8	11.7	8.9	12.5	16.4
12 to 14 [nm]	9.9	3.8	3.5	4.5	10.7	8.8	6.8	9.0	13.6
14 to 16 [nm]	11.4	1.2	4.7	3.7	7.2	7.1	2.1	7.4	8.5
16 to 18 [nm]	8.8	0.3	2.1	4.6	1.7	3.9	1.9	5.1	7.1
18 to 20 [nm]	8.2	0	3.8	1.0	0.6	1.5	0	5.2	3.1
20 to 22 [nm]	4.8	0.1	0.9	1.0	0.8	1.1	0	2.3	1.1
22 to 24 [nm]	10.4	0	0	0.3	0	0.2	0	0.5	1.1
24 to 26 [nm]	6.1	0	0	0.9	0	0.8	0	0.4	0.5
26 to 28 [nm]	2.5	0	0.1	0.4	0	0.4	0	0.8	0
28 to 30 [nm]	6.4	0	0	0	0	0	0	0.3	0.03
30 to 32 [nm]	1.0	0	0	0.2	0	0	0	0.6	0

Fraction of particles [%]									
Alloy	**V-Mo-0.2**			**Cr-V-Mo-0.2**			**Cr-Nb-V-0.2**		
Reaustenitization [^{0}C]	**1250**	**1250**	**1250**	**1250**	**1250**	**1250**	**1150**	**1150**	**1150**
Isothermal Transformation [^{0}C]	**600**	**655**	**670**	**640**	**664**	**672**	**680**	**690**	**710**
2 to 4 [nm]	28.4	4.3	19.7	2.3	9.6	2.2	0.3	2.8	5.4
4 to 6 [nm]	22.0	3.7	23.2	4.5	14.2	4.3	1.3	4.9	11.6
6 to 8 [nm]	11.0	5.2	23.4	11.2	12.9	6.9	2.5	6.9	11.9
8 to 10 [nm]	15.4	6.2	19.8	13.5	11.2	10.0	4.9	8.9	17.0
10 to 12 [nm]	14.0	6.5	7.2	17.3	11.2	12.6	2.8	12.2	14.2
12 to 14 [nm]	1.8	9.4	2.6	13.8	7.5	11.4	7.6	15.1	12.7
14 to 16 [nm]	6.1	5.6	0.6	14.1	3.6	13.2	7.8	13.5	11.3
16 to 18 [nm]	1.3	7.6	2.5	7.9	6.2	12.3	4.4	8.8	9.5
18 to 20 [nm]	0	5.9	1.0	7.1	6.0	10.3	11.3	5.2	1.1
20 to 22 [nm]	0	4.9	0	2.0	2.4	5.2	9.9	9.2	4.1
22 to 24 [nm]	0	5.4	0	5.3	9.7	4.7	8.2	2.2	1.2
24 to 26 [nm]	0	7.1	0	1.0	3.2	2.6	10.8	10.5	0
26 to 28 [nm]	0	8.9	0	0	1.0	2.5	6.1	0	0
28 to 30 [nm]	0	3.4	0	0.1	4.3	0.8	8.0	0	0
30 to 32 [nm]	0	9.4	0	0	0	1.2	8.4	0	0

Table 41. Data of the size distribution of the interphase precipitates in the studied microalloyed steels.

4.7. PRECIPITATE MORPHOLOGY AND CHEMISTRY

The thin foil TEM images shown in Figure 117 and Figure 118 confirmed that planar interphase precipitation forms at low isothermal transformation temperatures. As the isothermal transformation temperature increases, the higher energy $\gamma \rightarrow \alpha$ interphases which migrate without the step propagation, leading to an increase in the inter-rows and intercarbide spacing in the planar interphase precipitation[172]. Thus, curved interphase precipitations are expected to form at high isothermal transformation temperatures. The high interface growth rate deters the formation of sheeted carbides[18]. At higher isothermal transformation temperatures, a disorderly pinning process occurs, resulting in variable spacing and random distribution of precipitates.

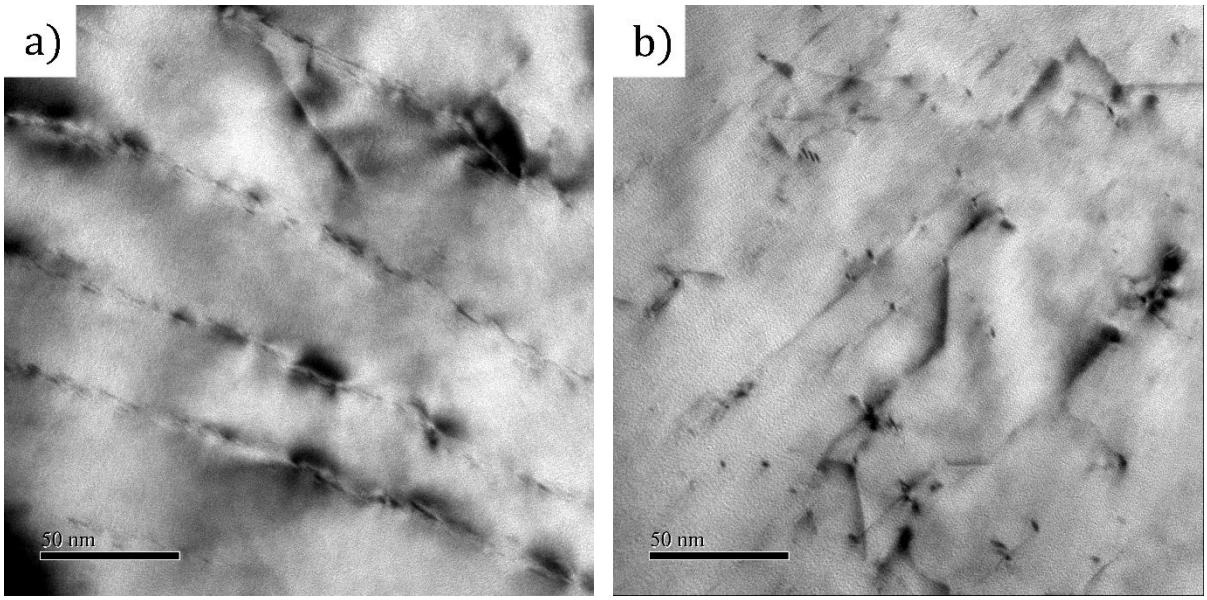

Figure 117. TEM thin foil micrographs of steel V-Mo-0.2 reaustenitized at 1250^{0}C and isothermally transformed for 90 min at 635^{0}C.

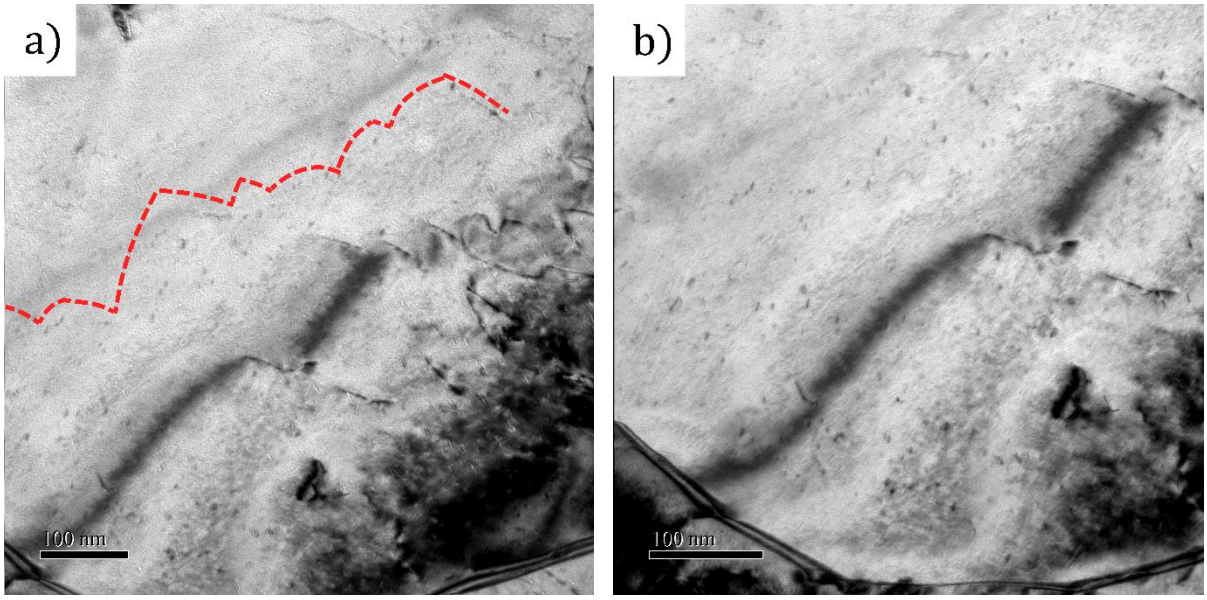

Figure 118. TEM thin foil micrographs of steel Cr-V-Mo-0.0 reaustenitized at <1250^{0}C and isothermally transformed for 90 min at 660^{0}C.

The precipitates morphology and size changes from steel to steel as a function of the transformation temperature. Previous research at the University of Sheffield found that the precipitate size distribution is the same for thin foil samples and extraction replicas within experimental error[26]. Also, less than 7 nm thick carbon extraction replicas revealed good quality images of the precipitate shape and distribution. In Figure 119 a) it is observed that along the grain boundaries the precipitation is much larger than the interphase precipitation within the ferrite. Carbon extraction replicas also extract big precipitates present in martensite which generally are much bigger than the interphase precipitations within the ferrite (Figure 119 b)).

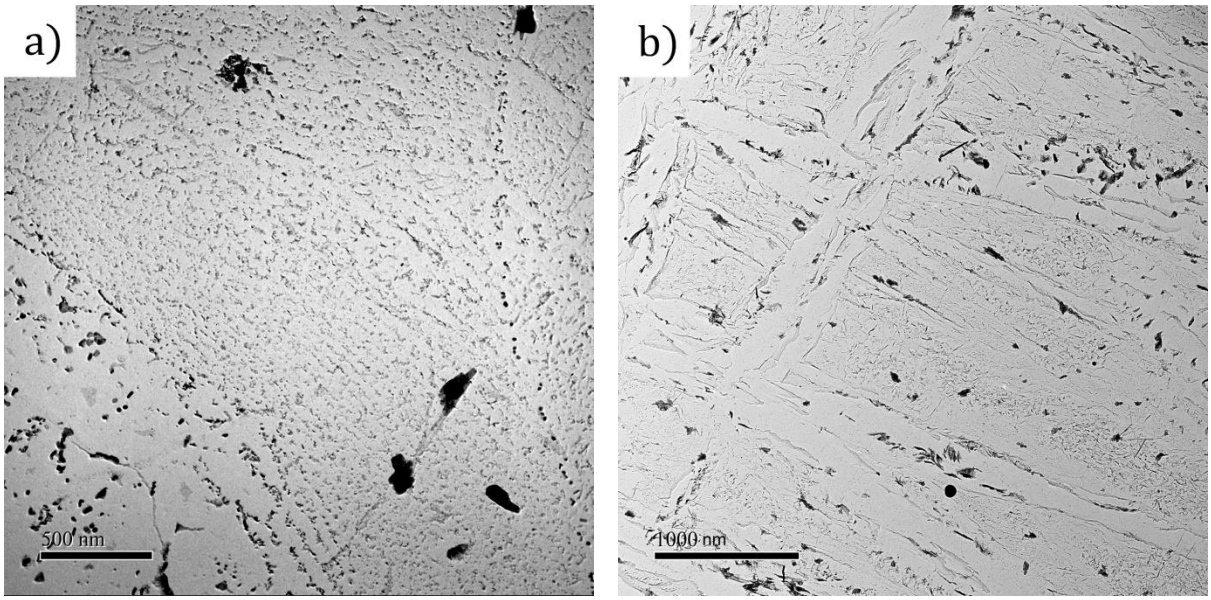

Figure 119. TEM micrographs taken from carbon extraction replicas of: a) interphase precipitation in the ferrite of steel Cr-V-Mo-0.4 reaustenitized at 900^{0}C and isothermally transformed at 660^{0}C, b) martensite laths of steel V-Mo-0.2 reaustenitized at 1250^{0}C and isothermally transformed at 655^{0}C.

Figure 120 shows precipitates in samples with no Cr additions adopt a quasi-spherical or ellipsoidal shape. In steels with the addition of Cr the majority of precipitates were found to have rod shapes with the presence of some cuboid precipitates as shown in Figure 121 and Figure 122. In the steel with Cr+Nb addition (Figure 123), the magnitude order of the precipitate size is different than the other steels and also the shape of them is more likely to have cuboid, parallelepiped and some kind of icosahedron (projection of a hexagon) shapes. The rod shape precipitates tend to be larger than precipitates with other shapes and therefore their strengthening contribution is less than the rest of precipitates (Figure 124).

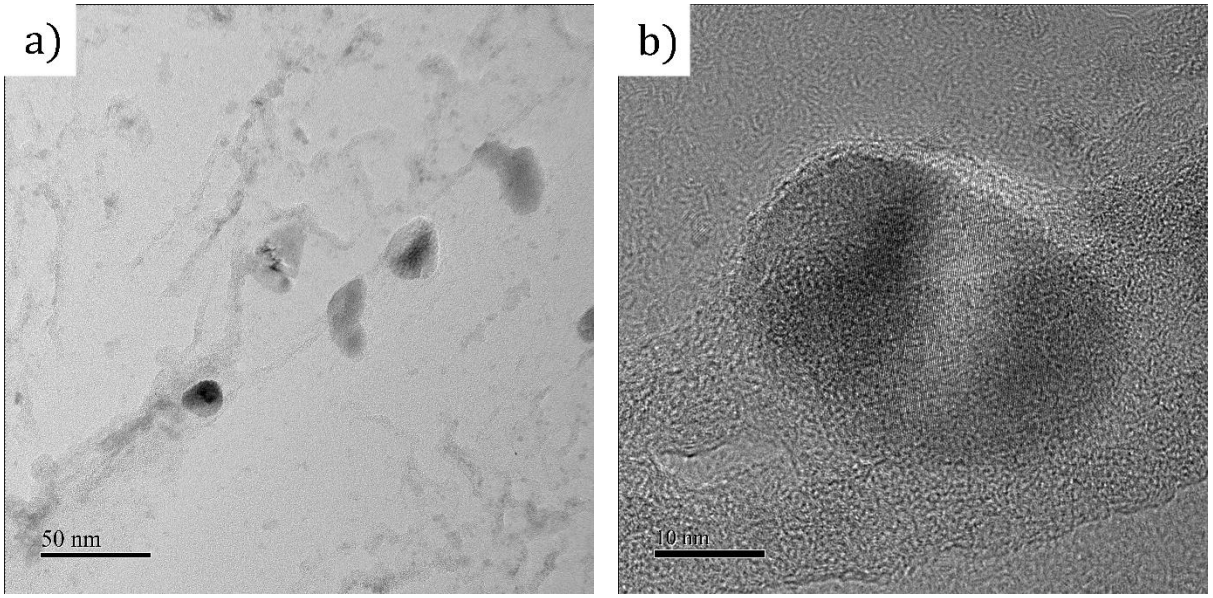

Figure 120. TEM micrographs taken from carbon extraction replicas of the steel V-Mo-0.4 at different magnifications reaustenitized at 1250^{0}C and isothermally transformed at 650^{0}C.

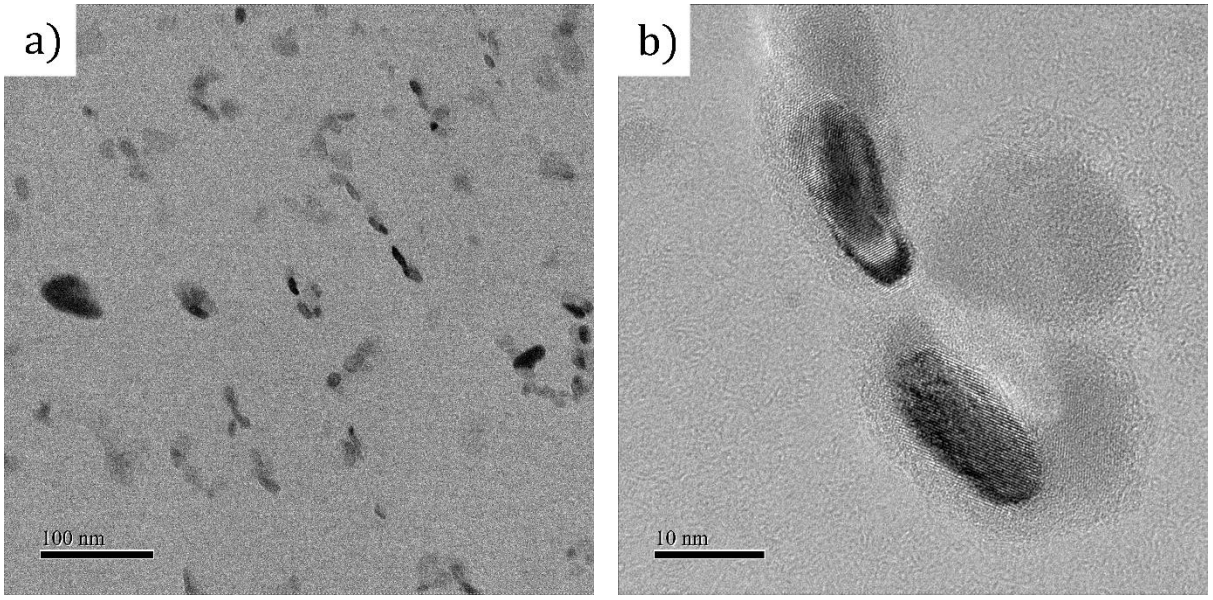

Figure 121. TEM micrographs taken from carbon extraction replicas of the steel Cr-V-Mo-0.4 at different magnifications reaustenitized at 900^{0}C and isothermally transformed at 660^{0}C.

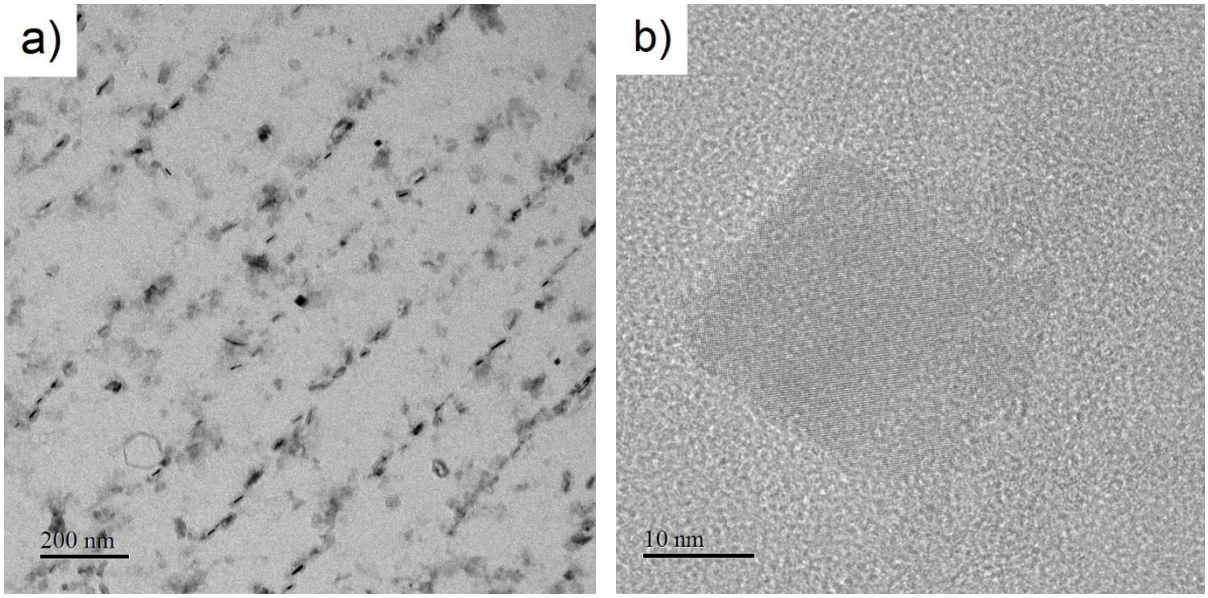

Figure 122. TEM micrographs taken from carbon extraction replicas of the steel Cr-V-Mo-0.4 at different magnifications reaustenitized at 1250^{0}C and isothermally transformed at 660^{0}C.

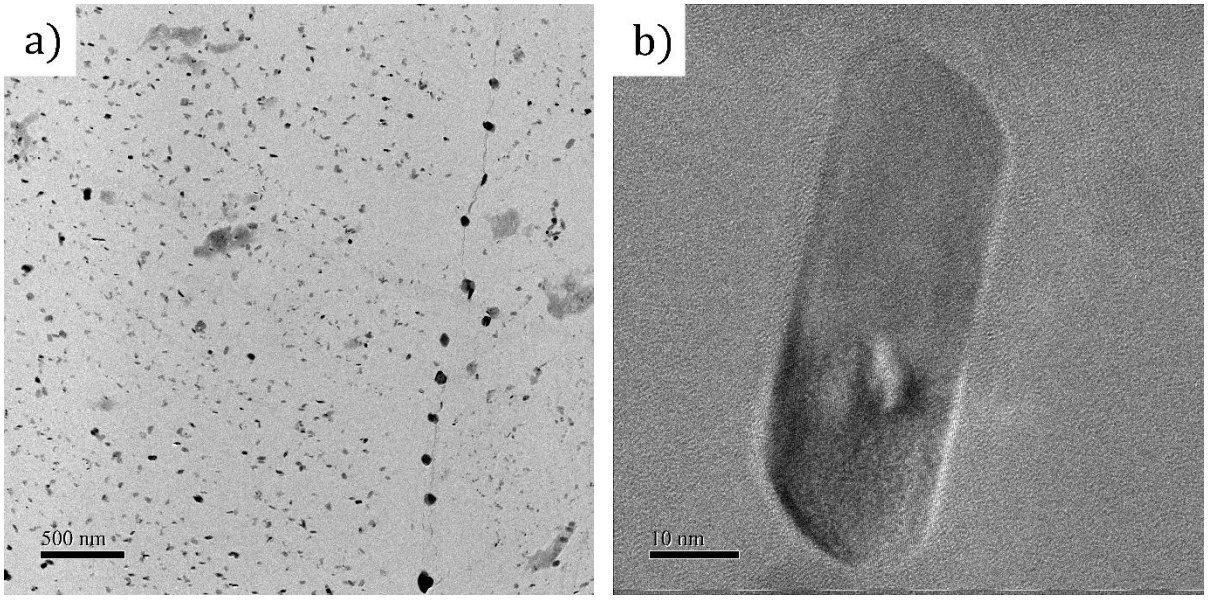

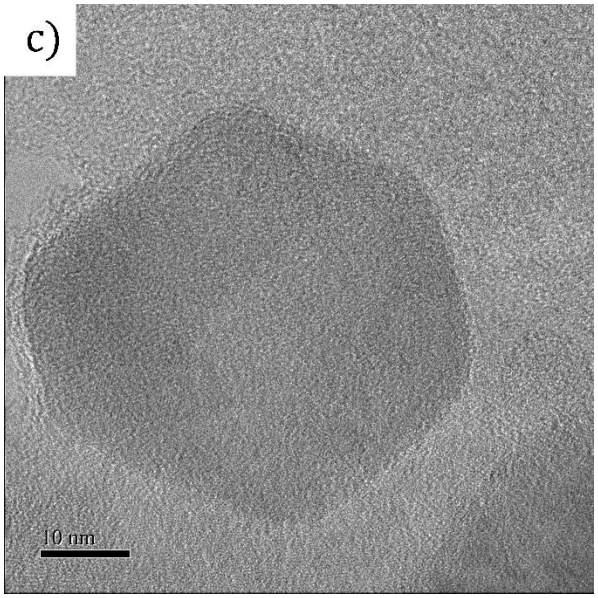

Figure 123. TEM micrographs taken from carbon extraction replicas of the steel Cr-Nb-V-0.2 at different magnifications reaustenitized at 1150^{0}C and isothermally transformed at 710^{0}C.

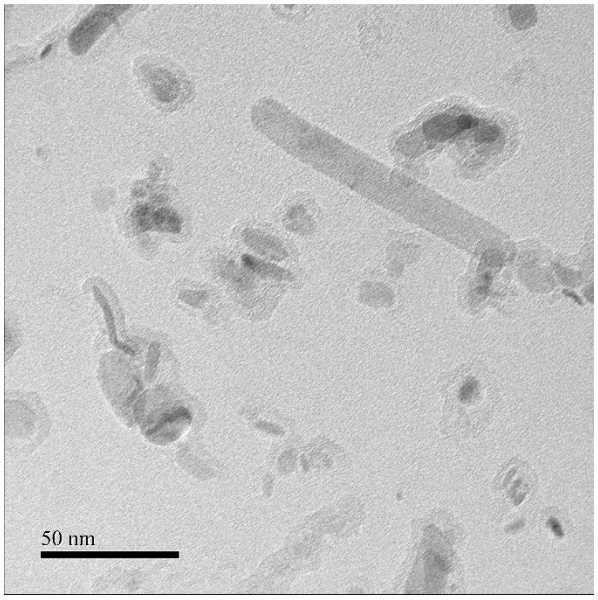

Figure 124. TEM micrograph taken from a carbon extraction replica of the steel Cr-V-Mo-0.2 reaustenitized at 1250^{0}C and isothermally transformed for 90 min at 670^{0}C.

To analyze the diffraction patterns of the particles found, it is much more accurate to obtain them from thin foil samples. Interphase precipitates should be imaged along <001> ferrite as a consistent condition to observe them[26].

Several diffraction patterns from the interphase precipitations had been taken to contrast them to others in literature and identify what they are. Figure 125 and Figure 126 show that in both steels, Cr-free and with Cr additions, the precipitation of VC is present just as observed by Pan and Umemoto[248]. Also, in steel Cr-V-Mo-0.2 steel isothermally transformed at 665^{0}C (Figure 127) (V, Mo)C and (V, Mo)$_4$C$_3$ were observed with the same lattice parameter and orientation as observed by in other studies and

formed through curved interphase precipitation[26,249]. (V, Mo)C grew close to $(1\ 0\ 0)_\alpha$ and $(V, Mo)_4C_3$ grew along $(0\ 1\ 1)_\alpha$.

One of the diffraction patterns of steel Cr-Nb-V-0.2, Figure 128, reveals the presence of $M_{23}C_6$ carbide in accordance with An et al.[250]. This precipitation has a lattice parameter of ≈0.99 nm which is smaller than the VC precipitates, resulting in a volume misfit. This misfit produces compressive stress which probably act as the driving force for the Cr atoms to be substituted by V atoms and increasing the nucleation rate of $M_{23}C_6$[251,252]. Following the V atoms diffusion into $M_{23}C_6$, a V-rich zone forms, promoting the precipitation of VC adjacent to the $M_{23}C_6$[250]. Also, the diffraction pattern shown in Figure 129 was taken in the same sample, over the coarsely spaced interphase precipitations. This is NbC formed in the austenite. Extra diffraction spots are related to the samples' surface oxidation and double diffraction from ferrite and oxide[253].

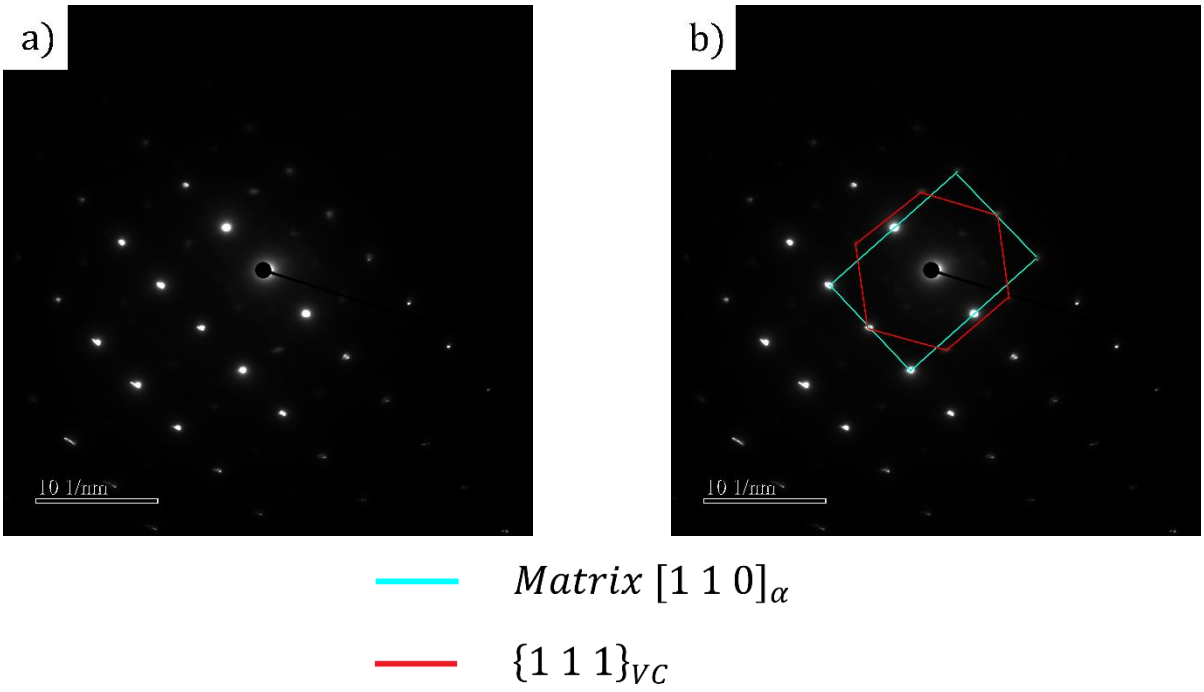

Figure 125. TEM images of the interphase carbides in steel V-Mo-0.2 reaustenitized at 1250^{0}C and isothermally transformed at 655^{0}C. a) the diffraction pattern as taken by the microscope, b) the corresponding selected area for each of the components observed.

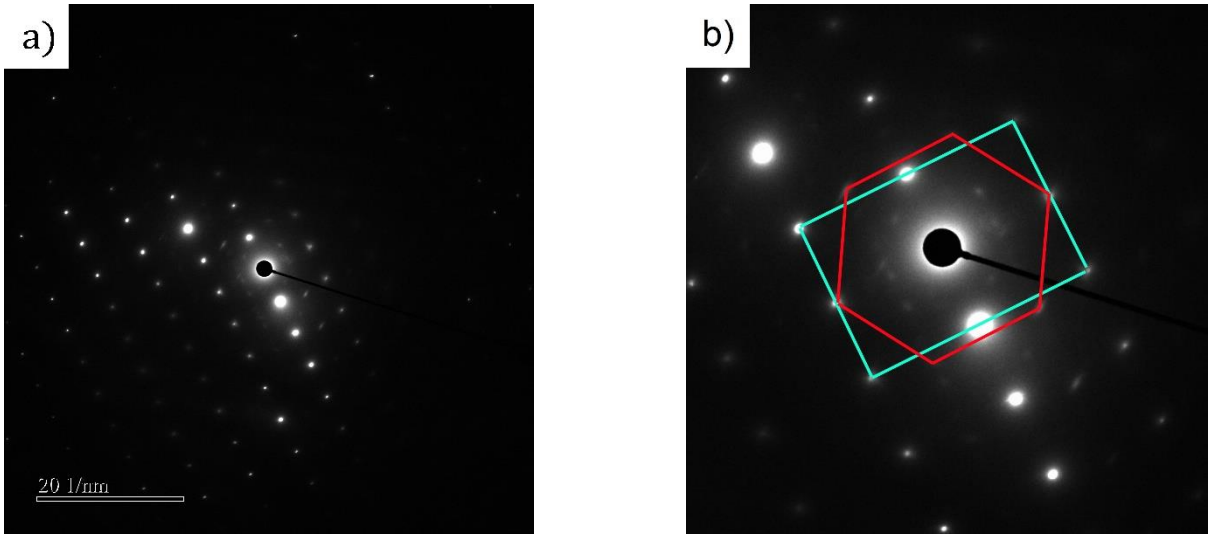

Figure 126. TEM images of the interphase carbides in steel Cr-V-Mo-0.2 reaustenitized at 1250^{0}C and isothermally transformed at 665^{0}C. a) the diffraction pattern as taken by the microscope, b) the corresponding selected area for each of the components observed.

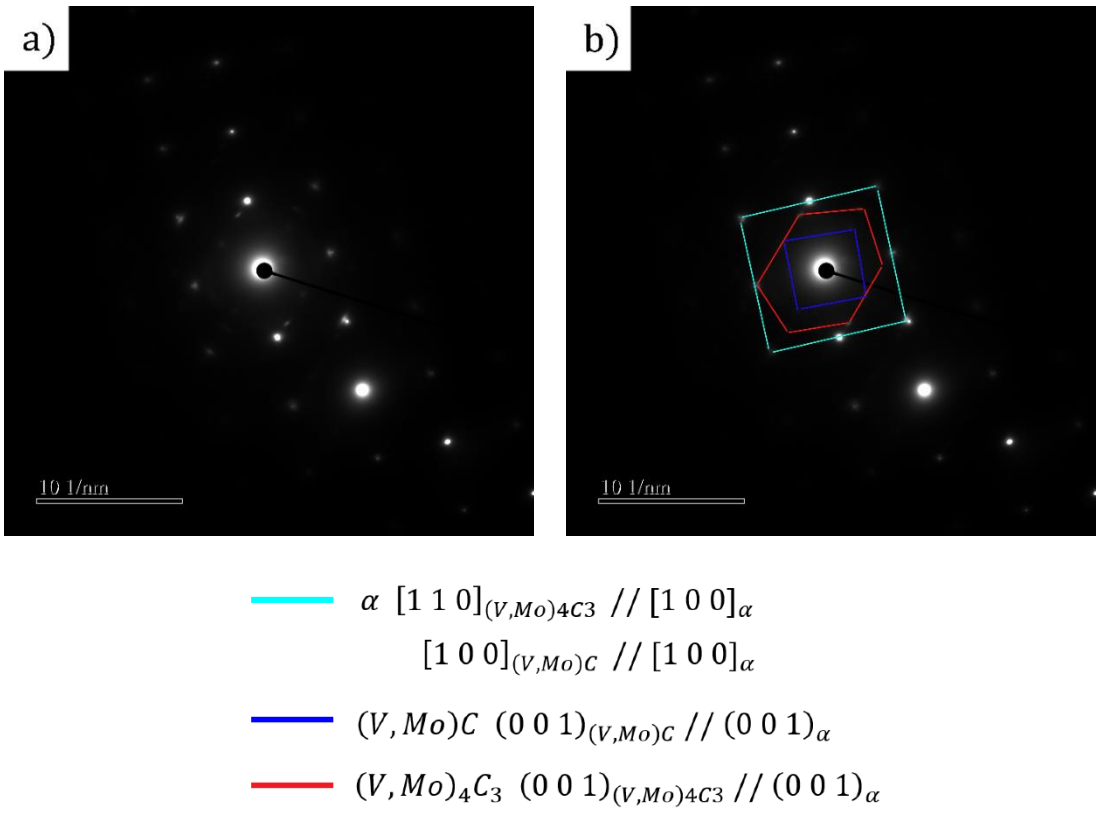

Figure 127. TEM images of the interphase carbides in steel Cr-V-Mo-0.2 reaustenitized at 1250^{0}C and isothermally transformed at 665^{0}C. a) the diffraction pattern as taken by the microscope, b) the corresponding selected area for each of the components observed.

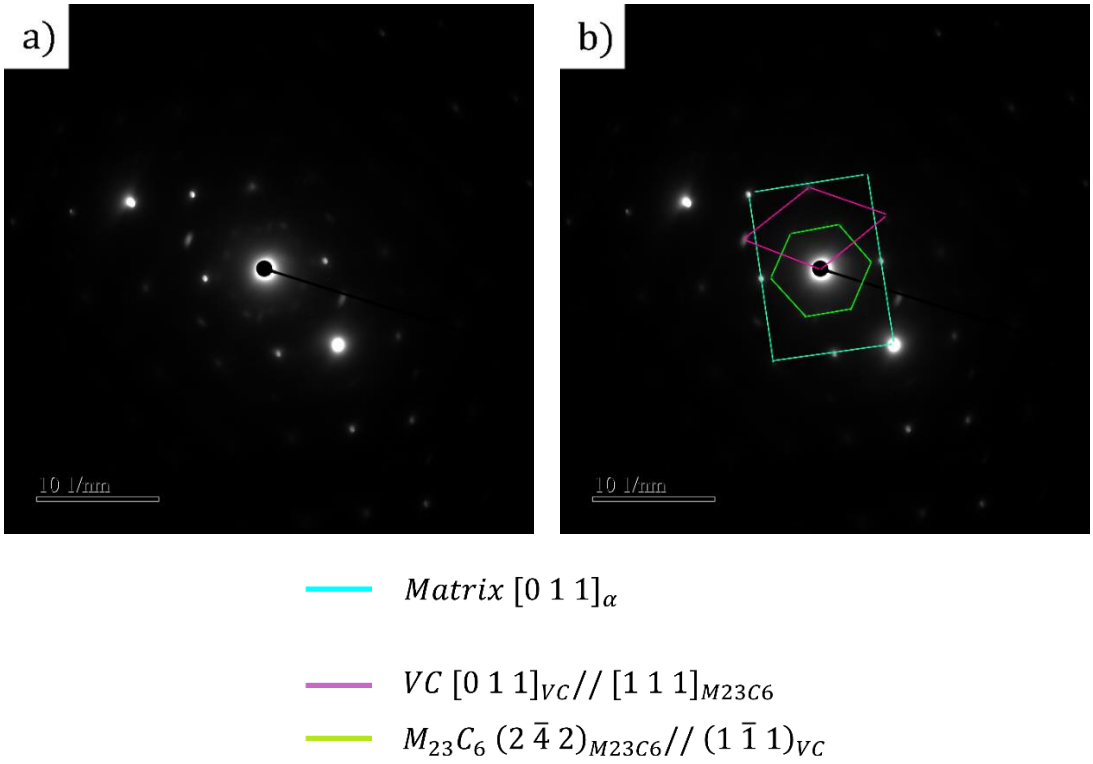

Figure 128. TEM images of the interphase carbides in steel Cr-Nb-V-0.2 reaustenitized at 1150^{0}C and isothermally transformed at 690^{0}C. a) the diffraction pattern as taken by the microscope, b) the corresponding selected area for each of the components observed.

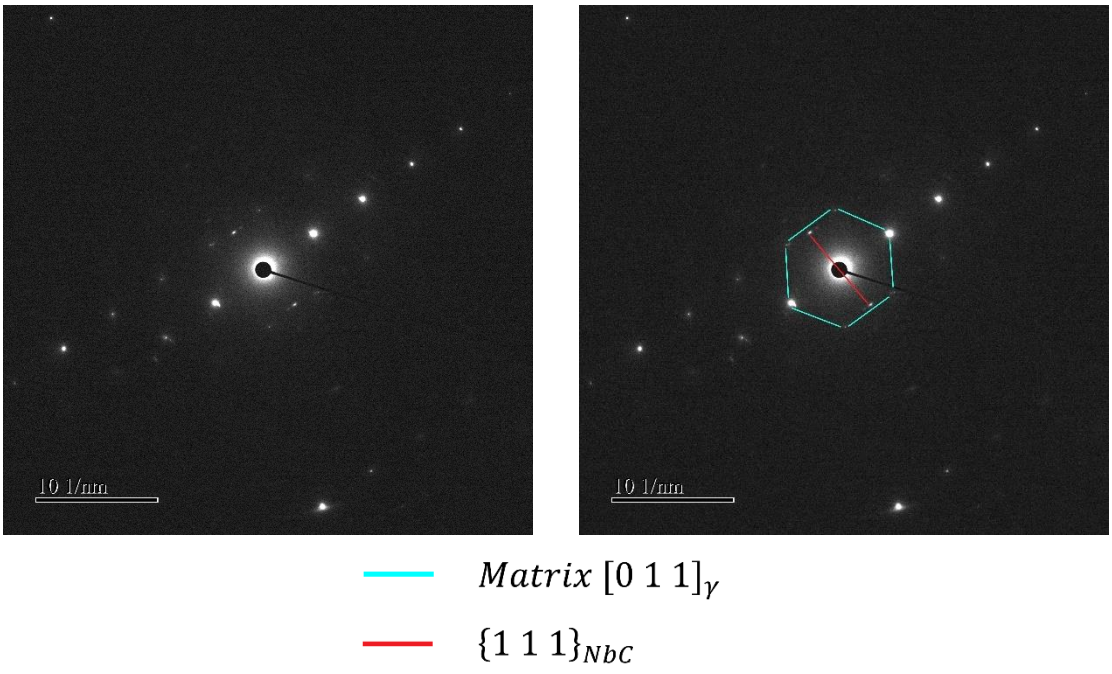

Figure 129 . TEM images of the interphase carbides in steel Cr-Nb-V-0.2 reaustenitized at 1150^{0}C and isothermally transformed at 690^{0}C. a) the diffraction pattern as taken by the microscope, b) the corresponding selected area for each of the components observed.

CHAPTER 5: DISCUSSION

5.1. PRIOR AUSTENITE GRAIN SIZE

As is well known, necklaces of recovered grains form around the prior-austenite grains, which are the most favourable sites for nucleation of static recrystallization[254]. Below 950^{0}C, undissolved carbonitrides that form on grain boundaries prevent austenite grain growth by a pinning effect in the reheating process. Fully recovered grains are shown at 1000^{0}C, and the austenite grain size of all alloys exhibit uniform growth until ≈1100^{0}C. For all steels except the Cr-Nb-V-0.2, grain growth was minimal between 1100^{0}C and 1250^{0}C. The Cr-Nb-V-0.2 steel behaved differently to the other steels, with abnormal grain growth of the austenite starting at 1200^{0}C, which then accelerated above 1250^{0}C. The NbC formed at the austenite grain boundaries starts its liquation and dissolution at temperatures around 1200^{0}C. The process does not occur immediately upon reaching the temperature. Instead, smaller precipitates dissolve first, and some particles may remain undissolved when the temperature is rapidly increased[255,256].

The strain rate while rolling does not affect the final ferrite grain size. The prior-austenite grain size of steels with a strain of 0.4 in each pass is considerably larger than steels with a lower deformation per pass. The rolling at ≈1050^{0}C corresponds to the austenite recrystallization region and the recrystallization process takes place while rolling, effectively reducing the prior-austenite grain size. Rolling above the non-recrystallization temperature (T_{nr}) allows the growth of recrystallised prior-austenite grains, reducing the nucleation sites for $\gamma \rightarrow \alpha$ transformation during the isothermal transformation, resulting in relative large ferrite grains[193,257,258]. It is noted that the alloys with the same rolling conditions presented almost identical grain sizes of ferrite. A big difference in the final ferrite grain size is only noticed in steel Cr-V-Mo-0.0 which was the one that exhibited abnormal austenite grain growth during the dilatometry test (Figure 130). Also, correlating the results in Figure 132 and Figure 133, the main effect of the strain per pass is on the volume fraction of IP within the ferrite and the volume fraction of ferrite by the improvement of dislocation density in the austenite which serve as nucleation points for precipitates and also for further ferrite nucleation.

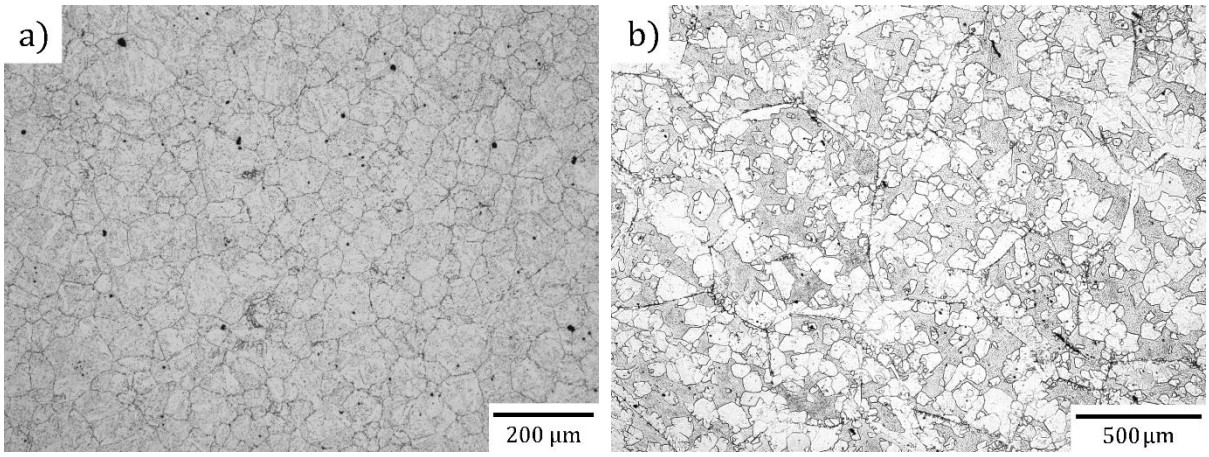

Figure 130. Prio-austenite grain size of steel Cr-V-Mo-0.0 a) before the dilatometry, b) after the dilatometry process.

5.2. TENSILE CONTRIBUTION OF THE IP

The tensile properties of the steels V-Mo-0.0 and Cr-V-Mo-0.0 were obtained from samples with the relationship $L_0/\sqrt{A_0} = 4.56$, whereas the other steels were evaluated with samples with the relationship $L_0/\sqrt{A_0} = 5.16$. This is the reason that the total elongation for steels V-Mo-0.0 and Cr-V-Mo-0.0 show a greater plastic zone and hence a greater elongation than the rest of the samples. No changes in the yield and ultimate strengths are expected. Thus, the elongation values obtained from steels V-Mo-0.4, Cr-V-Mo-0.4, V-Mo-0.2, Cr-V-Mo-0.2 and Cr-Nb-V-0.2 are less than samples that meet the ASTM standard. The difference in tensile sample dimensions was unavoidable because of the amount of material available.

The steels with Cr additions exhibited the higher concentration of interface precipitates of all steels, especially the steel with Cr that was rolled with a higher strain per pass. This difference is much more marked for the finer precipitates (<20 nm). The difference brought about by a Cr addition is irrespective of the transformation temperature. As Honeycombe reported [1], the additions of Cr+Al raises the TTT curve, leading to shorter transformation times. In the case of the steel with additions of Cr+Nb+Al, the TTT curve is raised much more than the others, but in contrast, the transformation times are much longer as a result of the addition of Nb which retards both the nucleation and growth kinetics[2]. Gong et al.[33] reported that higher volume fractions of precipitates were achieved in microalloyed steels with reduced transformation kinetics.

Table 42 shows that the average interphase precipitations diameter in V-MA steels decreases while the isothermal transformation temperature increases. The additions of Cr+Nb+V together have the same effect, but the addition of Cr without Nb produces the opposite effect. The increase in precipitate diameter with Cr addition is compensated by the greater ferrite and IP volume fraction produced by the additions of Cr. This result is consistent with the tensile test values. The combined addition of Cr+Nb+V produces a greater reduction of the ferrite grain size in steels with the same process conditions, but results in less ferrite and a smaller IP volume fraction with larger precipitates than V-MA steels or MA steels with additions of Cr. Interestingly, there was not a significant difference in ferrite grain size between steels with different isothermal transformation temperatures, or even with different microalloyed additions except Nb. The only steel which showed a relatively significant reduction in ferrite grain size was the one with Cr+Nb+V additions. However, further studies are required to investigate the effect of intermediate isothermal transformations between 680 and 710^{0}C to evaluate if a higher volume fraction of ferrite can be achieved.

The contribution of fine-particle distribution is usually obtained using the Orowan-Ashby model[259], expressing the strength contribution as a function of the precipitates volume fraction and the average particle spacing. This last parameter is an average in a given slip plane, which is difficult to define for IP because of the spacing between particles of adjacent sheets. To estimate the precipitate strengthening of HSLA steels another form of the Ashby-Orowan model has been widely adopted as given in Equation 21[260]. This equation assumes that all the carbon content of the steel is consumed by precipitations which contribute to strengthening.

$$\Delta\delta = \frac{K}{d} f^{1/2} ln \frac{d}{b} \qquad \textit{Equation 21}$$

f is the volume fraction of the nano-sized carbides, *d* is the average diameter of the precipitate, b the Burger's vector (estimated as 0.246nm), and *K* is a constant (5.9N/m). Some studies affirm that the use of the Ashby-Orowan equation is limited by precipitates >5nm which avoids shearing by dislocations[7,261]. For this investigation this relationship is not applicable because it does not consider the volume fraction of ferrite. Therefore, a structure-based strength model is required[156,209]. In this model, the total yield strength is a function of the solid solute strengthening ($\Delta\sigma_{SS}$), the grain boundary strengthening ($\Delta\sigma_{GB}$), the dislocation strengthening ($\Delta\sigma_S$), the precipitation strengthening ($\Delta\sigma_P$) and the friction stress of the ferritic matrix ($\Delta\sigma_0$) which is around 48 MPa for microalloyed steels[262]. This formula is written in Equation 22:

$$\Delta\sigma_{total} = \Delta\sigma_{SS} + \Delta\sigma_{GB} + \Delta\sigma_S + \Delta\sigma_P + \Delta\sigma_0 \quad \textit{Equation 22}$$

Yong calculated the solution hardening stress ($\Delta\sigma_{SS}$) as written in Equation 23, where [X] is the wt% of the element X in solution.

$$\Delta\sigma_{SS} = 4570[C] + 4570[N] + 37[Mn] + 83[Si] + 470[P] + 38[Cu] + 80[Ti] + 0[Ni] - 30[Cr] \quad \textit{Equation 23}$$

The grain refinement strengthening ($\Delta\sigma_{GB}$) is given using the Hall-Petch relationship:

$$\Delta\sigma_{GB} = K_y d_F^{-0.5} \quad \textit{Equation 24}$$

K_y is the constant (0.55 MPa $m^{0.5}$ for HSLA steel[7]) and d_F is the average grain size measured in m.

The Ashby-Orowan model as written in Equation 25, is widely used to calculate the precipitation hardening effect[11,209,263]. V_{IP} is the volume fraction of the interphase precipitation, and d_p is the average diameter of precipitation in nanometers. The calculations have been done with the values obtained from precipitates with diameter below 20 nm which is the maximum size at which precipitates are believed to contribute.

This formula does not allow the differentiation between the individual contribution from the interphase precipitate types.

$$\Delta\sigma_P = 8995 * \frac{{V_{IP}}^{1/2}}{d_p} ln(2.417 d_p) \quad \textit{Equation 25}$$

The contribution to the yield strength from the increased dislocation density was estimated with the Equation 26. α is a constant (0.435), *M* is the Taylor factor which for ferrite equals 2.75, *G* is the shear modulus calculated from the tensile charts of each sample and shown in Table 42, *b* is the Burgers vector (0.248 nm), and ρ is the dislocation density which in the ferrite matrix during isothermal transformation is estimated to be $5 \times 10^{13} \mathrm{m}^{-2}$. Gong et al.[26] reported the Equation 27 in which the $\Delta\sigma_{base}$ equals the sum of the solid solution hardening strengthening, the grain refinement strengthening, and the friction stress of single crystal pure iron. Furthermore, that product is function of the composition of the steel [%wt. of the element], the ferrite grain diameter (GS_f), the volume fraction of ferrite (*Vf*), and the martensite interlamellar spacing (s). This last one was not calculated in this thesis, but obtained from the Equation 22, knowing the yield stress from the tensile tests. Results are presented in Table 42 and plotted in Figure 131.

$$\Delta\sigma_S = \alpha M G b \sqrt{\rho}$$ *Equation 26*

$$\Delta\sigma_{base} = \Delta\sigma_0 + \Delta\sigma_{SS} + \Delta\sigma_{GB} = V_f^{\frac{1}{3}}35 + 58[Mn] + 17.4GS_f^{-\frac{1}{2}} + \left(1 - V_f^{\frac{1}{3}}\right)\left(178 + 3.8s^{-\frac{1}{2}}\right) + 63[Si] + 426[N]^{\frac{1}{2}}$$ *Equation 27*

In steels where the reaustenitization during the dilatometry was evaluated (V-Mo-0.4 and Cr-V-Mo-0.4), it is clear that the maximum yield stress is reached with a reaustenitization temperature of 1150^{0}C for both steels, with and without Cr additions. At a reaustenitization temperature of 900^{0}C, the maximum contribution is given by the grain refinement strengthening, but it reduces while the austenitization temperature increases. Also, contrasting the results from steel V-Mo-0.4 with Cr-V-Mo-0.4 in Figure 131, it is observed that the Cr additions produces a more constant solid solution contribution hardening at low and high austenitization temperatures, while steels with no Cr additions shown a significant reduction of the solid solution contribution at low austenitization temperatures. Comparing the same samples but with different reduction per pass a higher strain per rolling pass magnifies not only the grain refinement strengthening, but also the interphase precipitation contribution and the solid solution strengthening. According to Yong[264], that directly reflects the reduction of certain alloying elements concentration such as C, N, Mn, Si, and Ni in the solid solution at low isothermal transformation temperatures in steels with no additions of Cr.

Steels with a higher strain per pass during rolling and the steel with the addition of Nb showed a finer ferrite grain size and thus the greatest grain refinement hardening stress. In the steels with less strain per pass, the interphase precipitation contribution and the contribution from the increased dislocation density were increased at the isothermal transformation temperatures at which the maximum volume fraction of ferrite was obtained for each steel.

The previous analysis does not include the interaction with martensite specially because of the lack of research in high-volume fraction of martensite dual-phase steels, where martensite contents above25% rapidly degrades the ductility and impact toughness of dual-phase steels[265]. Intermediate-quenching steels usually have a banded microstructure, while step-quenching have a more homogeneous microstructure. It has been reported that intermediate-quenching steels the tensile strength increases with the volume fraction of martensite peaking at around 55% and then gradually decreasing with increase in the martensite volume fraction[266]. Ductility decreases substantially with increment in the martensite volume fraction. Dual-phase steels with banded martensitic structures have inferior ductility than finely dispersed martensite[266].

This study does not match models which include parameters such as the shape of martensite. The morphology and size of martensitic regions depend on the formation of ferrite while the isothermal transformation. Most of ferrite regions nucleates at austenite grain boundaries and some others inside the austenite grains, growing inside the austenite matrix, producing plate and lath martenisitic morphologies.

The tensile strength of dual-phase steels has been empirically modelled as a function of a mixture of phases strength (Equation 28)[1,267,268]. V_m is the volume fraction of the martensite σ_{tf} and σ_{tm} are the tensile strengths of the ferrite and the martensite respectively. Other models have been developed, including parameters and assumptions which restrict the applicability of the models to certain percentage of martensite volume fraction[269–271]. The experimental results in this work do not agree

with the suggested expressions because there is no model in bibliography that matches the range of transformation discussed in this research, and also, because results show that the strength of the studied steels go in opposite direction to these models, showing the highest yield and ultimate strength in steels with the highest fraction of ferrite strengthened with interphase precipitates.

$$\sigma_t = \sigma_{tf}(1 - V_m) + \sigma_{tm}V_m \qquad \textit{Equation 28}$$

Another representation to better observe the effect of key parameters on properties are radar charts. Figure 132 presents a radar chart correlating tensile properties with the ferrite volume fraction of the steels with constant reaustenitization temperature. Figure 133 shows the radar chart for steels with different reaustenitization temperature and constant isothermal transformation temperature. These show the effect of the different strain per pass during the rolling. In steels with the same isothermal temperature transformation, the total elongation increases with the ferrite volume fraction in all steels. The elongation of Cr-V-Mo-0.0 shows is larger because the samples manufactured matched the ASTM standard, contrary to the rest of the tensile samples which matched British standard with $5 = l_0/\sqrt{A_0}$.

The yield and ultimate strength reduce significantly on steels with no Cr. All steels with an increase in the isothermal transformation temperature expands on the diagram until the temperature at which maximum ferrite volume fraction is reached, then the charts compress again with isothermal transformation temperature rise. In all cases, the change in the volume fraction of ferrite is the parameter with the strongest effect. Interestingly, steels with a higher volume fraction of ferrite have a higher volume fraction of precipitates $\emptyset$ <20nm. This is a direct reflection of the increased defect density in the austenite produced by strain during rolling and by replacement of Cr in complex precipitates ($M_{23}C_6$ carbide). That precipitates produce compressive stress by volume misfit, which act as driving force for the Cr atoms to be substituted by V atoms, improving the nucleation rate of $M_{23}C_6$[251,252], producing a chain reaction and larger fine interphase precipitation. The Cr-Nb-V-0.2 steel shows the highest ultimate tensile stress is the one with the lowest elongation, but at the same time the one with the highest volume fraction of precipitates.

Alloy	Reaustenitisation [^{0}C]	Isothermal Transformation [^{0}C]	$V_{IP\text{-}total}$ [%]	$V_{IP\text{-}<20nm}$ [%]	d_p [nm]	S.D.	V_f [%]	GS_f [μm]	G [GPa]	$\Delta\sigma_{GB}$ [MPa]	$\Delta\sigma_P$ [MPa]	$\Delta\sigma_S$ [MPa]	$\Delta\sigma_{SS}$ [MPa]
Cr-V-Mo-0.0	>1200^{0}C	625	5.19	3.45	7.47	5.2	72.9	16.7	59.6	134.6	120.2	125.0	192.7
	>1200^{0}C	650	4.84	4.8	5	2.7	70	18.4	65.4	128.2	215.2	137.2	191.2
	>1200^{0}C	660	5.59	5.59	6.5	2.8	76.9	16.5	67.4	135.4	213.1	141.3	211.8
V-Mo-0.4	900^{0}C	650	4.52	4.25	4.25	3.1	81.7	4.4	54.2	262.2	209.4	113.6	101.8
	1150^{0}C	650	8.04	7.97	8.1	4.1	86.2	5.3	88.1	238.9	263.3	184.8	310.8
	1245^{0}C	650	6.56	6.4	6.13	3.6	88.5	7.6	79.1	199.5	253.2	165.8	264.5
Cr-V-Mo-0.4	900^{0}C	660	6.05	6.05	5.24	2.9	82	5.6	69.8	232.4	263.7	146.5	256.0
	1150^{0}C	660	6.71	6.38	5.68	3.6	85.6	7.9	87.4	195.6	264.8	183.3	259.2
	1245^{0}C	660	10.35	10.08	6.94	4.2	90.8	9.7	83.9	176.6	368.4	175.9	303.9
V-Mo-0.2	1245^{0}C	600	3.25	3.24	3.62	2.1	64	9	45.9	183.3	174.6	96.2	40.0
	1245^{0}C	655	9.18	4.98	6.38	4.5	69.6	7.2	74.9	204.9	192.0	157.1	52.9
	1245^{0}C	670	4.29	4.29	5.4	2.9	61.3	6.4	49.7	217.4	183.7	104.3	45.9
Cr-V-Mo-0.2	1245^{0}C	640	3.16	2.89	5.2	4.4	64.5	8.4	51.6	189.8	126.6	108.2	72.3
	1245^{0}C	664	5.57	4.58	5.4	3.4	86.9	8.2	64.7	192.1	196.2	135.7	78.6
	1245^{0}C	672	7.51	6.24	8.04	5.1	77.5	8.6	50.9	187.6	207.1	106.7	90.12
Cr-Nb-V-0.2	1190^{0}C	680	10.65	4.56	11.15	4.7	36.5	6.6	46.6	214.1	121.2	97.7	113.3
	1190^{0}C	690	4.82	3.76	8.5	4.9	55.6	6.5	56.3	215.7	120.3	118.0	43.7
	1190^{0}C	710	3.95	3.73	6.17	4.3	50.4	6.7	53.1	212.5	146.9	111.4	53.4

Table 42. Table of the measured interphase precipitation in the studied steels.

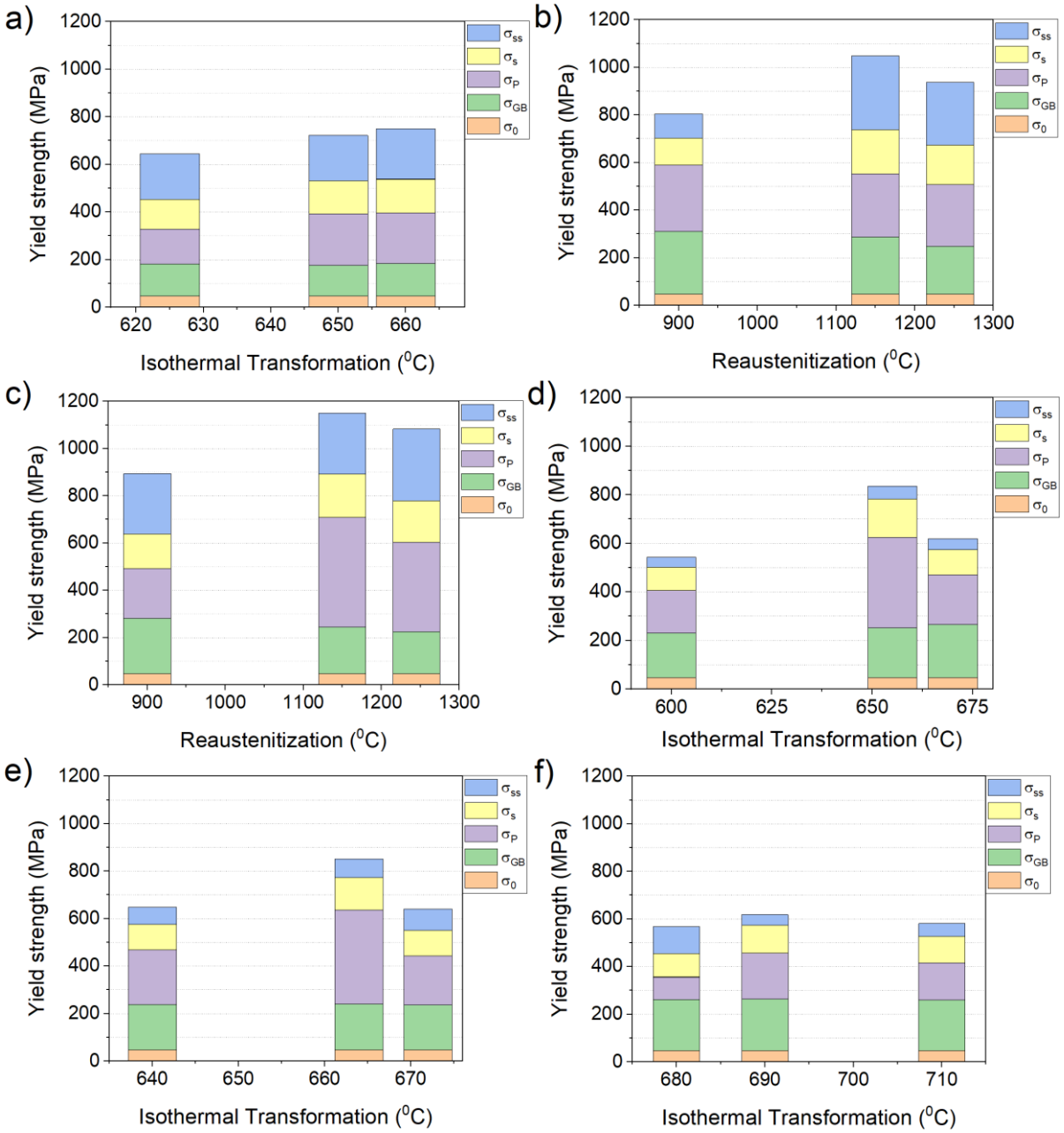

Figure 131. Different contributions to the yield strength of steels a) Cr-V-Mo-0.0 austenitization over 1250°C and different isothermal transformations b) V-Mo-0.4 different austenitization temperatures and all isothermally transformed at 650°C, c) Cr-V-Mo-0.4 different austenitization temperatures and all isothermally transformed at 660°C, d) V-Mo-0.2 austenitization below 1250°C and different isothermal transformations, e) Cr-V-Mo-0.2 austenitization below 1250°C and different isothermal transformations, and f) Cr-Nb-V-0.2 austenitization below 1250°C and different isothermal transformations.

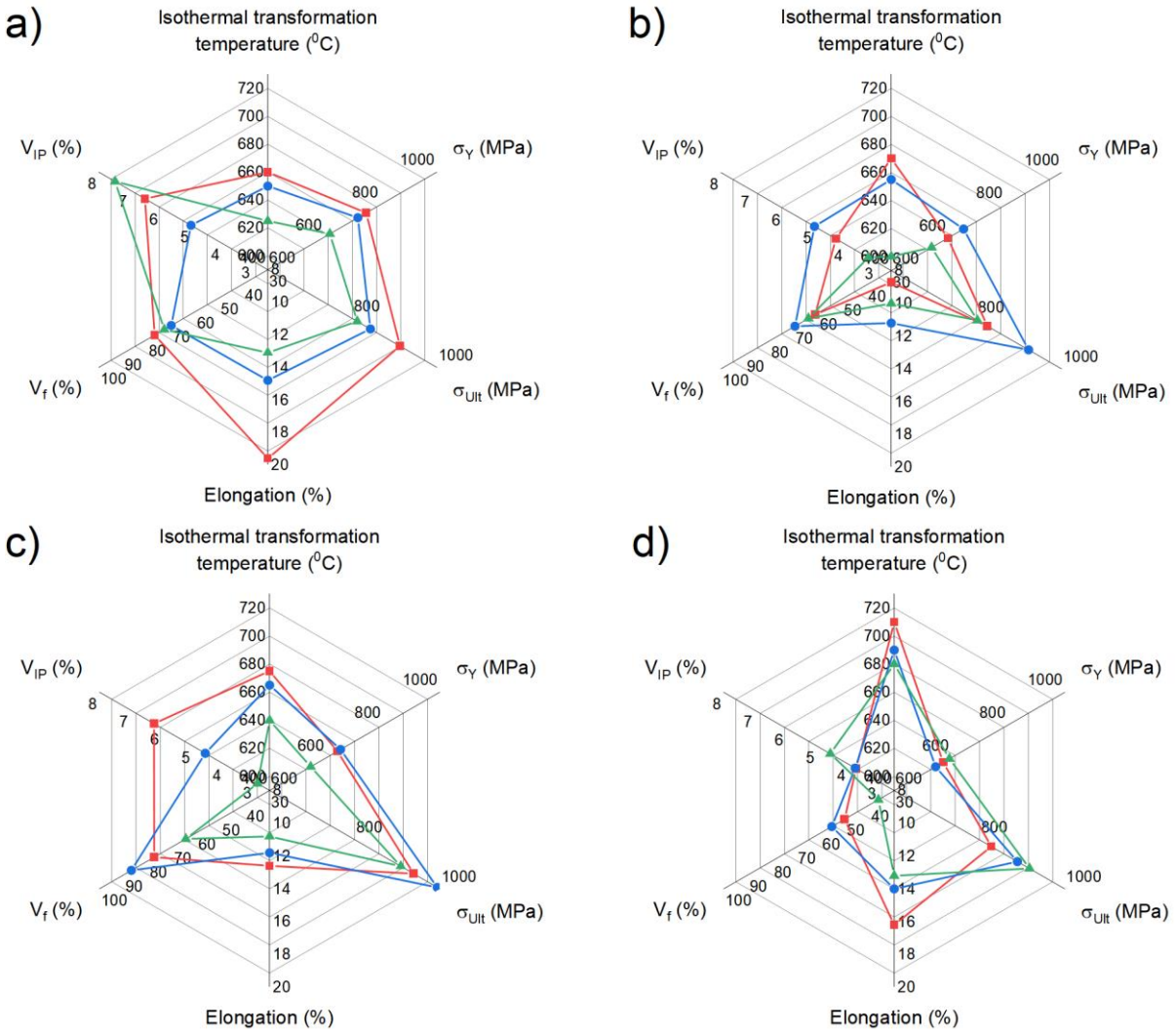

Figure 132. Radar charts correlating isothermal transformation temperature, yield strength, ultimate tensile strength, total elongation, ferrite volume fraction and the <20nm interphase precipitation volume fraction of microalloyed steels: a) Cr-V-Mo-0.0, b) V-Mo-0.2, c) Cr-V-Mo-0.2, and d) Cr-Nb-V-0.2.

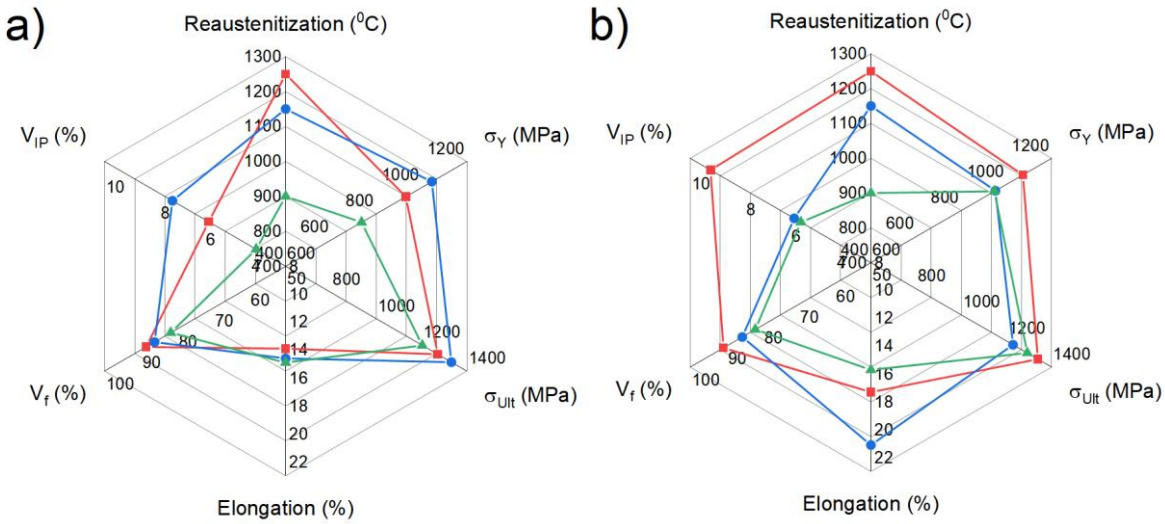

Figure 133. Radar charts correlating reaustenitization temperature, yield strength, ultimate tensile strength, total elongation, ferrite volume fraction and the <20nm interphase precipitation volume fraction of microalloyed steels V-Mo-0.4 and Cr-V-Mo-0.4.

CHAPTER 6: CONCLUSIONS

The research developed in this thesis was focused on maximizing the mechanical properties of microalloyed steels for the car industry while an evaluation of the effect of Cr additions on the interphase precipitation was undertaken. The conclusions found during the investigation and analysis of results are:

1. In both Cr-V-Mo and V-Mo-added steels, isothermal transformation at temperatures between 650 and 670^0C for 90 min led to a dual-phase microstructure with a high ferrite volume fraction and a high fraction of fine-sized interphase precipitation. Steels with a Cr addition exhibited larger average precipitate size, but also a higher volume fraction of precipitates, which overall provided an increase in precipitation strengthening.

2. Optimum processing of the Cr-V-Mo dual-phase steel achieved an excellent combination of mechanical properties (yield strength of 1000 MPa, ultimate tensile strength of around 1300 MPa, and elongation of 17%). These properties are attributed to the increase in strengthening from interphase-precipitated nanometer-sized carbides in ferrite. Isothermal transformation experiments coupled with optical microscopy and transmission electron microscopy have been conducted to investigate Cr-V-Mo and V-Mo dual-phase steels. It was found that a much higher density of nanometer-sized interphase-precipitated carbides in ferrite in Cr-V-Mo dual-phase steel can be produced, as compared with Cr-free microalloyed dual-phase steel.

3. Contrasting results from samples with similar TMCP, it can be concluded that the addition of Cr produces a strong effect of isothermal transformation temperature on the volume fraction of the ferrite and interphase precipitation. In general, a higher fraction of small interphase precipitates was observed in Cr-added steels, increasing the precipitate hardening. However, a big difference in the total elongation is noticed, especially observing the radar chart of steel Cr-V-Mo-0.4, which shows that the total elongation is a function not only of the volume fraction of the interphase precipitations but also how homogeneous the distribution of precipitates is (not a big difference between the fraction of particles Ø<10nm).

4. Comparing steels with the same chemical composition, a higher strain per pass during the hot-rolling increases all of the grain refinement strengthening, the interphase precipitation contribution, the dislocation hardening stress and the solid solution strengthening.

5. The optimum combination of grain refinement, solid solution strengthening, high dislocation density, and precipitation hardening produced by the higher strain per pass during the hot-rolling process resulted in high strength for the V-Mo-0.4 and Cr-V-Mo-0.4 steels. By comparing steels with the maximum strength produced by different heat treatments, the main reason for the increment in strength is because of the maximising the contribution from precipitation hardening.

6. The precipitation hardening is a reflection of the volume fraction of precipitates and of the average diameter of precipitate as well. Samples which show large volume fraction of precipitates at high isothermal transformation temperatures exhibit relative short precipitation contribution because of the precipitate coarsening.

7. Samples which exhibited abnormal austenite grain growth (V-Mo-0.0 and Cr-V-Mo-0.0) showed three main effects: 1) reduction of the volume fraction of ferrite after the isothermal transformation 2) increase of the main ferrite grain size, 3) the volumetric fraction of interphase precipitation within the ferrite reduces, reducing the contributions to the final yield strength.

8. The TEM analysis results show that the distribution of the interphase precipitation changes with the isothermal transformation temperature, and also with the addition of Cr. In general, the Cr addition accelerates the transformation kinetics of microalloyed steels. Also, it is clear that an increase in the strain per pass during the hot-working reduces the transformation kinetics, producing a higher volume fraction of ferrite with an improved percentage of interphase precipitations (mainly vanadium carbides) within it.

CHAPTER 7: FUTURE WORK

This research pointed to the improvement of the mechanical properties of microalloyed steels for the car industry, which was a result of adopting several development axes. The analysis of the results pointed to many other factors that would be of interest to continue with the development of the principal objective.

1) ***Evaluation of the strain-per-pass during the hot-rolling of microalloyed steels:***
   It was shown that the increase in the strain per pass during the hot-rolling the microalloyed steels led to an important increase in the tensile properties. Furthermore, that process involves other parameters which would be interesting to test and analyse, such as:
   - the maximum strain per pass permitted before the steel suffers damage and how the interphase precipitation develops along that range of hot-rolling schedules.
   - The temperature at which the plate is heated before the hot working. The interphase precipitation seems to be affected by different coiling temperatures, but the evolution of the interphase precipitation with changes in the rolling temperature for specific compositions was not analyzed until now in most of the cases.

2) ***Establishment of the relationship between reaustenitization and isothermal transformation temperatures:***
   The results of this research revealed how important the reaustenitization during the dilatometry really is. This temperature was established in the constant range of prior-austenite grain sizes. Further, samples where the temperature was on the limit of that range did not produce the maximum fraction of precipitates. The reason for this requires a detailed analysis on that region would be of great scientific and industrial interest.

3) ***Other compositions:***
   There are other microalloying additions which can be of interest to be studied. Focused in the compositions used for this thesis, it would be interesting to investigate new alloys with the same thermomechanical processing parameters but with small changes in the alloy additions which are known to directly influence the interphase formation:
   - V addition between 0.2 - 0.3 wt.%.
   - Mo addition between 0.45 – 0.6 wt.%.
   - Cr between 0.5 – 0.6 wt.%.

4) ***Transition from dual-phase ferrite/martensite to ferrite/upper bainite:***
   In the tensile curves of Cr-Nb-V steel, Figure 100, one condition shows a very high yield and ultimate stress, Table 36. Samples isothermally transformed between 650 and 675^{0}C show a remarkable combination of yield and ultimate stress of around 1 GPa and 1.3 GPa respectively with a total elongation of 13-16 %. The structure of these samples was a mixture of bainite and ferrite. This opens a new interesting option to evaluate the transition from martensite-ferrite to ferrite-bainite dual phase microalloyed steels isothermally transformed at low temperatures and search what are the mechanisms of transformation and interphase precipitation in them. These steels can be considered as an alternative to enhance the mechanical properties of DP steels, but more research is needed about not only the properties of these steels, but also about the technology, furnaces and heating systems required to their adaptation in industrial production.

ATTACHMENTS

Publication: A new approach to etching low-carbon microalloyed steels to reveal prior austenite grain boundaries and the dual-phase microstructure[272]

Karol F. Rodriguez-Galeano, Luis F. Romano-Acosta, Eric J. Palmiere, W. Mark Rainforth

Department of Materials Science and Engineering, The University of Sheffield, Sir Robert Hadfield Building, Mappin Street, Sheffield S1 3JD, UK

Corresponding authors.

E-mail addresses: kfrodriguezg@unal.edu.co (K. F. Rodriguez-Galeano), m.rainforth@sheffield.ac.uk (W. M. Rainforth)

Abstract

A modification to picric acid solutions has been undertaken to reveal the prior-austenite grain boundaries in microalloyed steels as a result of elemental segregation. It has been found the maximum addition of sodium dodecyl sulphate plus hydrochloric acid to fully reveal both the prior austenite grain boundaries and the final post-processed structures in these steels.

Keywords: Microalloyed steels; prior austenite grain boundaries; post-processed structures; sodium dodecyl sulphate.

1. Introduction

Determination of the prior-austenite grain size is of great importance in steel due to its strong influence on final microstructure, mechanical properties, and more[273–275]. The process of revealing the prior-austenite grain size depends on several factors, such as the steel chemical composition, the heat treatments, and other variables that until now have not been well-identified[222]. Low-carbon alloy steels have been reported as very difficult to etch, and some as ‘‘impossible to etch’’ with picric acid solutions, so that several different reagents have been studied for this purpose[225]. In this regard, several different approaches have been taken to identify the prior-austenite grain boundaries in microalloyed steels[225,276].

Multiple studies have shown that prior-austenite grain boundaries in quenched steels can be revealed using picric acid solutions plus wetting agents [277–280]. This is because during austenitization and tempering phosphorus and other trace solute atoms segregate to the grain boundaries [281,282]. Wetting agents or surface-active agents (surfactants) are added to etchants to improve grain boundary delineation in steels acting on the etching speed or selectivity modification[277]. Sodium dodecyl sulfate (SDS) has been used as a wetting agent in previous studies, showing good results with low and medium carbon steels[283]. Other authors also reported that the addition of HCl increases the attack on the phosphorus-rich regions, better outlining the prior-austenite grain boundaries in steels [224,226,284].

In this research, chemical etching based on picric acid with additions of sodium dodecyl sulphate and some drops of hydrochloric acid (HCl) was investigated to reveal the prior-austenite grain boundaries

in microalloyed steels at different normalization temperatures after hot-rolling. Also, the same solution was used to reveal and contrast the bainitic and martensitic grain boundaries of the post-treated steels. Results indicate a high-quality delineation on microalloyed steels and the possibility for future research on other alloys.

2. Experimental Procedure

Table 1 lists the chemical composition of three microalloyed steels with different chromium and niobium content. They were vacuum-induction melted in ingots of 80 mm × 80 mm × 100 mm at the University of Sheffield. The ingots were cut to 40mm thick and homogenized at 1300^0C for 2h, then hot worked in several passes to 7.6mm thick plates. Specimens of 12 mm × 12 mm × 7.6 mm were cut from the plate's mid-section and then heated in an argon atmosphere from 950^0C to 1300^0C. The samples were then cut in half, mounted in bakelite and prepared for metallographic analysis to observe the microstructure in the plane of the rolling direction/normal direction.

For the post-treated results, samples of 150mm long × 15mm wide × 7.6mm thick were machined from the plates for dilatometry along the rolling direction. These specimens were solution annealed at the temperatures listed in table 2. The heat treatments were performed in a Dilatronic dilatometer at the University of Sheffield was used to conduct the heat treatment shown in Fig. 1. Specimens were heated at a heating rate of 10^0C/s to the austenitization temperature ($T\gamma$), which is the same as the solution annealing temperature, for 3 min. After that, the samples were cooled at a cooling rate of 10^0C/s to the temperature of isothermal transformation, T_{ISO}, during 90 min followed by a water quench to room temperature.

Steel	C	Mn	Si	Al	V	Mo	Cr	N	Nb
V	0.12	1.11	0.23	<0.01	0.2	0.47	-	-	-
CrV	0.13	1.56	0.19	<0.005	0.21	0.5	0.51	-	-
CrNbV	0.13	1.42	0.25	0.016	0.21	0.51	0.48	-	0.03
AlCrNb	0.25	1.90	0.20	0.04	0.2	0.5	0.25	-	0.06

Table 1. Chemical composition (wt.%).

Alloy	Austenitization temperature
V	1245^0C
CrV	1200^0C
CrNbV	1245^0C
AlCrNb	1200^0C

Table 2. Austenitization temperature of the post-processed steels (wt.%).

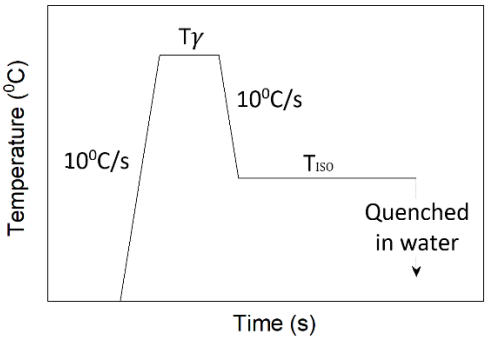

Figure 1. Heat treatment.

2.2. Metallographic Preparation

All the samples were polished using standard metallographic techniques. Table 3 lists the two reagents used to reveal the prior-austenite grain boundaries. Optical microscopy was carried out on a Nikon ECLIPSE LV150 microscope.

Chemical Etchant	Description
E1	150 ml of distilled H_2O + 4.5gr of picric acid ($C_6H_3N_3O_7$) + 20 ml of sodium alkylsulfonate ("Teepol") + drops of HCl
E2	150 ml of distilled H_2O + 4.5gr of picric acid ($C_6H_3N_3O_7$) + between 0.85 and 1.15 gr of sodium dodecyl sulphate ($C_{12}H_{25}NaO_4S$) as wetting agent + between 4 and 12 drops of HCl

Table 3. Chemical etchants

2.3. Preparation of the Reagent E2

After several trial-and-error experiments, adequate preparation of the reagent E2 was established. Firstly, the acid and the wetting agent were added to the distilled water. Then, the solution was heated between 75 and 90^{0}C. During this process, the solid particles dissolve, which changed the colour from a) to b) in fig. 2. When the solution reached the desired temperature, drops of HCl were added, followed by the addition of several dummy samples to reduce the solution's strength, and change the colour to match fig. 2 c) (around 5 dummy samples submerged in the solution for 5 min each). While the specimens etch, the colour of the etch becomes darker as shown in fig. 2 d). The solution was found to work until crystals start to appear on the surface of the solution. After the etching process, the samples required a rapid deep clean with water + teepol and then submerge them in isopropanol to protect them from oxidation.

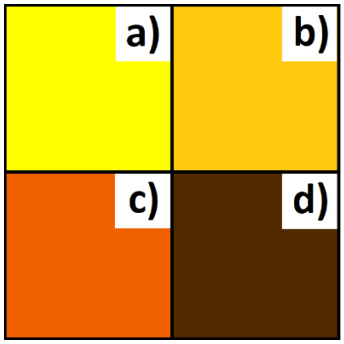

Figure 2. Colour evolution of the etching E2.

3. Results and discussion

3.1. Prior austenite grain boundaries revelation

Fig. 3 a) shows prior-austenite grain size of V steel revealed with reagent E1. This solution showed poor results on all steels evaluated in this research.

Reagent E2 showed better results, but small variations in the quantity of each component of the etch show big differences in how well the prior-austenite grain boundaries are revealed. Excess of wetting agent, in this case sodium dodecyl sulphate, results in an inability for the picric acid to reveal the prior-austenite grain boundaries as reported by Nelson[285]. This results in etch pits at the prior austenite grain boundaries (fig. 3 b)). This problem cannot be solved by the addition of more HCl, as shown in fig. 3 c), which only increases the size of the etch pits but does not improve the delineation. Reagent E2 with 1.15 gr of sodium dodecyl sulphate works for steels V, VCr, VNbCr with different alloying additions but with the same carbon content.

Fig. 4 a) shows the V Steel heat treated at 1200^{0}C and etched with solution E2 with 9 drops of HCl for 10s. The etch is light, with only some of the prior austenite boundaries revealed. In this case no dummy samples had been etched, so the etchant was at full strength. The colour shown at the right corner of the micrograph corresponds to the colour of the solution when the etch had been completed. Fig. 4 b) shows the effect of swabbing with a piece of cotton produces over the same sample, with the same solution as Fig. 4 a). The swabbing constantly removes the etch over the smoother intragranular region, but the etch concentrates in the etched grain boundary recesses resulting in better delineation of the grain boundaries compared to the standard immersion approach. If the prior-austenite grain boundaries are not fully revealed as Fig. 4 c), adding more HCl drops and then reducing the strength of the acid by etching more dummy samples results in all of the grain boundaries being revealed as shown in Fig. 4 d). An excess of HCl will causes very dark lines over the grain boundaries, making them very difficult to measure (Fig. 4 e)).

For steels with 0.1C, the reagent E2 shows very good results at 80^{0}C. At higher temperatures, the delineation of the prior-austenite grain boundaries increases, especially for steels with relative big grains, but the pitting effect appears in form of dark lines along the micrography as shown in Fig. 5 a) and b). Fig. 5 c) shows how the etch E2 delimitates all the prior-austenite grain boundaries at ~95^{0}C, but the pitting stains are much bigger than the ones left by the same solution at lower temperature.

The reagent E2 with 8 drops of HCl at 80^{0}C successfully reveals the prior-austenite grain size of steels with 0.1C at all solution annealing temperatures, even with massive grain growth. Fig. 6 and Fig. 7

gives evidence of the success of this solution to reveal the prior austenite-grain boundaries in steels V, CrV and CrNbV.

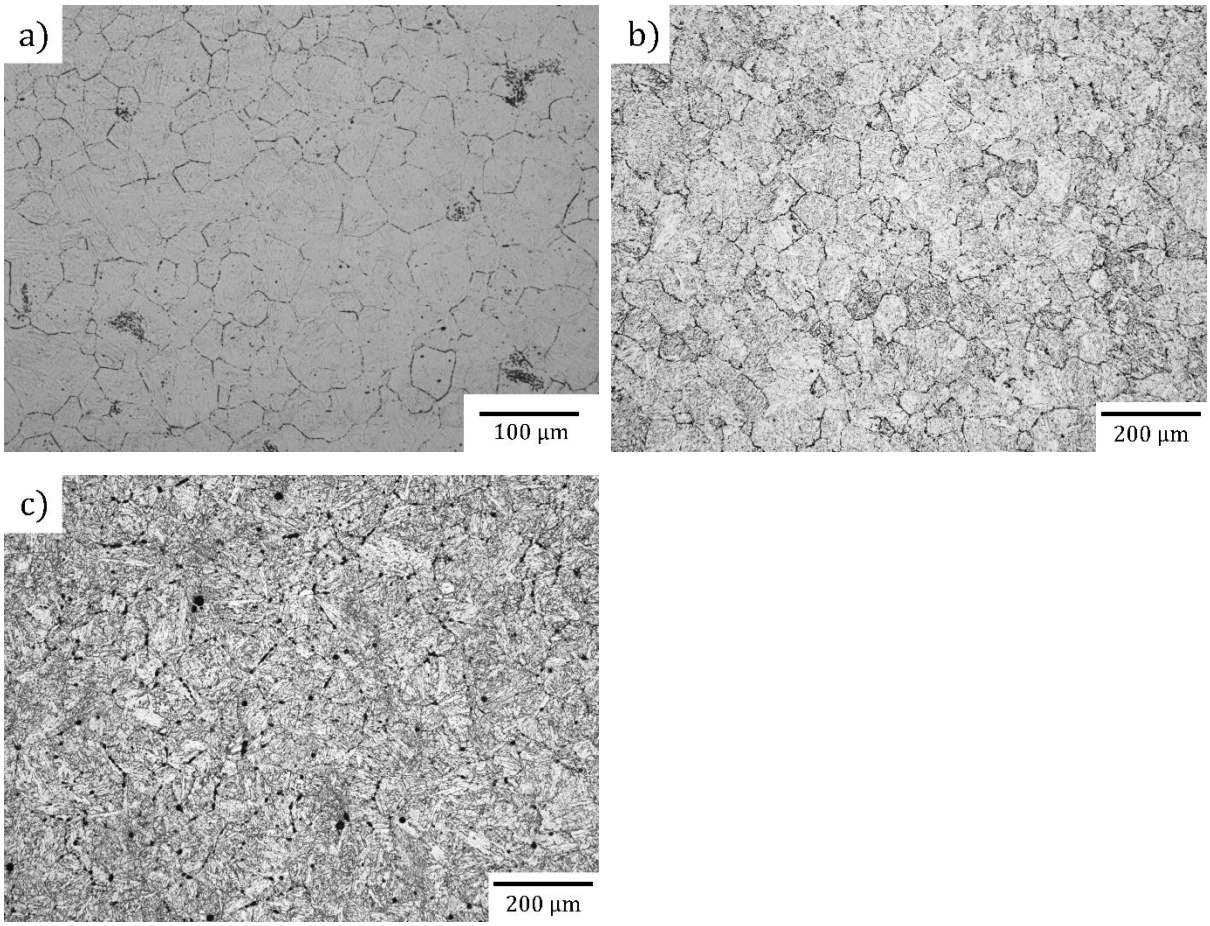

Figure 3. V Steel a) 1000^{0}C Tγ, etched with solution E1, b) 1250^{0}C Tγ etched with solution E2, 1.22 gr sodium dodecyl sulphate + 8 drops of HCl. c) 1250^{0}C Tγ etched with solution E2, 1.22 gr sodium dodecyl sulphate + 12 drops of HCl.

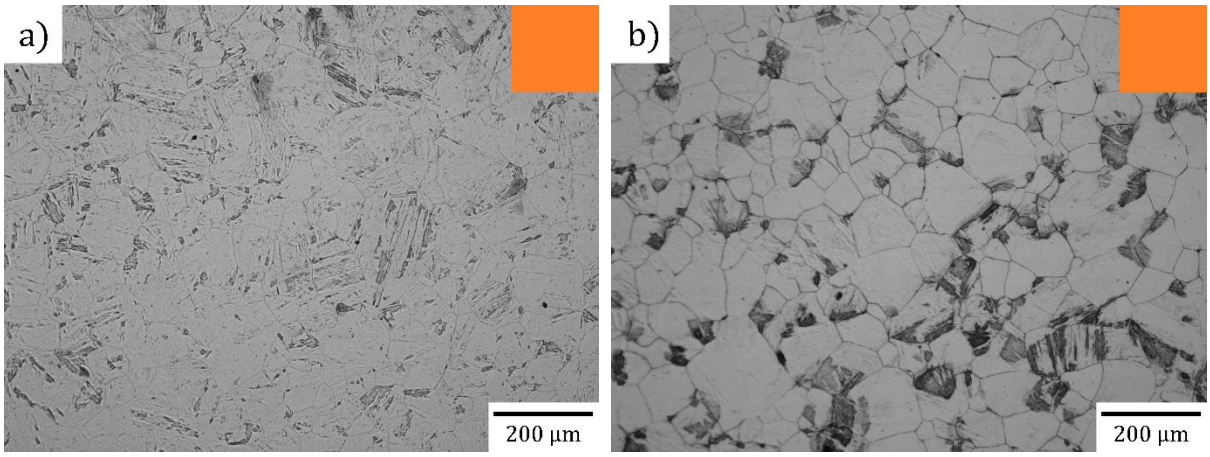

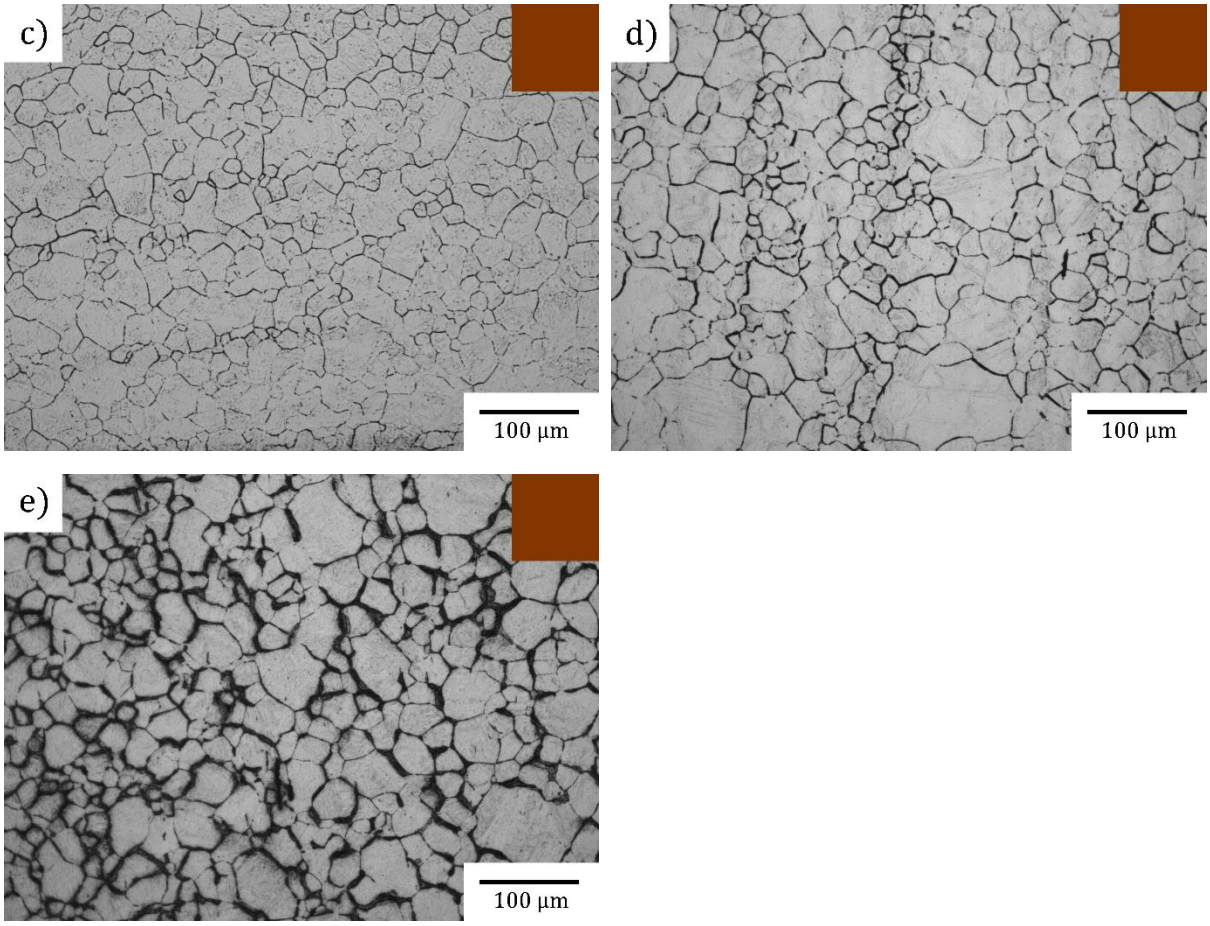

Figure 4. V Steel a) 1200^{0}C Tγ, etched with solution E2– 9 drops of HCl, submerging the sample for 10s. b) 1200^{0}C Tγ etched with solution E2 – 9 drops of HCl and swabbing with cotton for around 60s. c) 1000^{0}C Tγ etched with solution E2 – 6 drops of HCl and swabbing with cotton for around 60s. d) 1050^{0}C Tγ etched with solution E2 – 9 drops of HCl and swabbing with cotton for around 60s. e) 1050^{0}C Tγ etched with solution E2 – 12 drops of HCl and swabbing with cotton for around 60s.

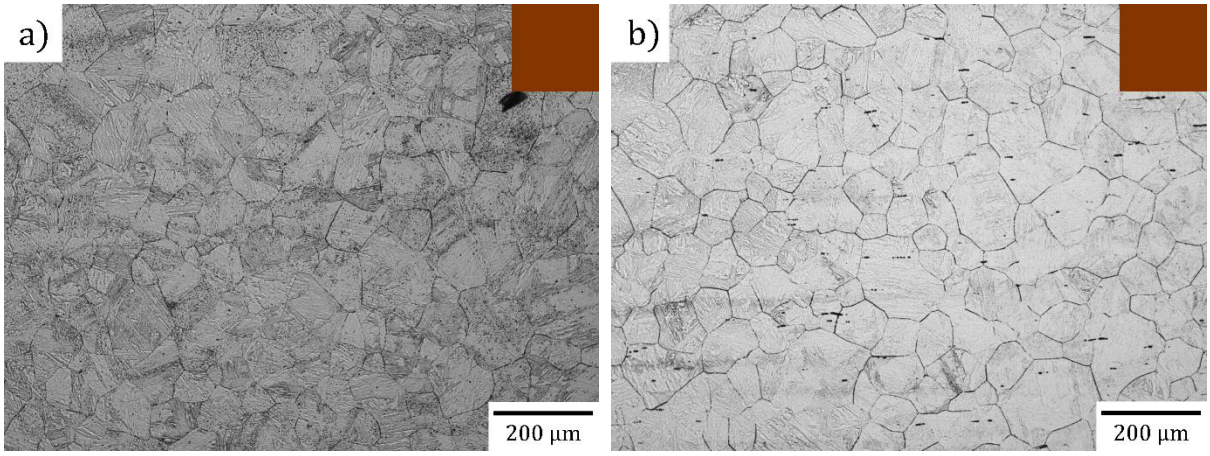

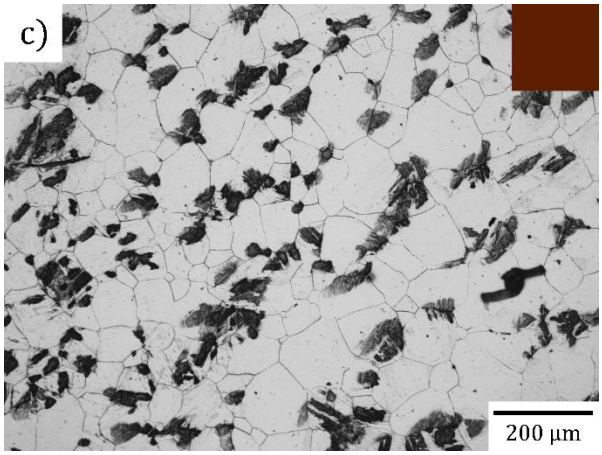

Figure 5. Effect of the temperature of the etch E2 over V steel samples treated at 1250 ^{0}C Tγ, a) at 70^{0}C, b) at 80^{0}C, c) at 90^{0}C.

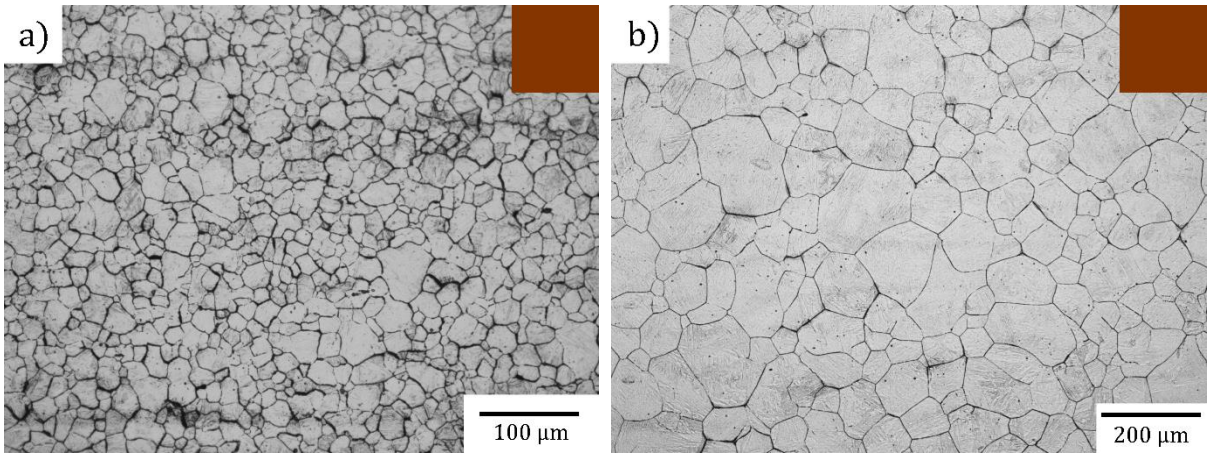

Figure 6. Steel CrV etched with solution E2 austenitized at: a) 1000^{0}C Tγ, b) 1300^{0}C Tγ.

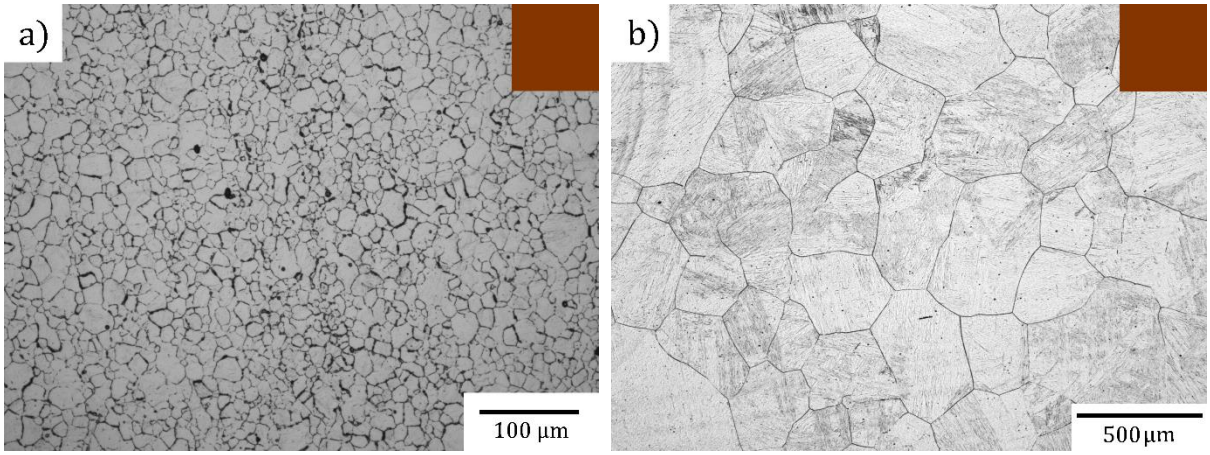

Figure 7. Steel CrNbV etched with solution E2 austenitized at: a) 1000^{0}C Tγ, b) 1300^{0}C Tγ.

3.2. Revealing bainite and martensite in the post-processed steels

Fig. 8 shows the etching of the V steel heat treated at 1245^{0}C Tγ followed by isothermal transformation at 610^{0}C T_{ISO} comparing the E2 reagent and Nital. Fig. 8 a) shows how etching with E2 with 9 drops of HCl at 80^{0}C, applied by swabbing energetically with cotton, produces a well-defined delineation of the grain boundaries of heat-treated steels. Not only the allotriomorphic ferrite which boundaries the prior-austenite grains is revealed with this reagent, but also the martensitic and bainitic regions at grain boundaries. It represents a good improvement from the Nital 2% etch, which with the cotton swabbing delineates the ferrite, and produces a high contrast with other phases (Fig. 8 b)).

The 2% Nital etch does not gives much information about phases such as martensite or bainite, so without the E2 etch, evaluation of the microstructure would require much more expensive techniques such as scanning electron microscopy (SEM) or Electron Backscatter Diffraction (EBSD). The Nital etch gives a well-defined ferrite grain boundaries in steels with much higher ferrite volume fraction, e.g. Fig. 9, or in steels with fine grains and very low ferrite transformation (Fig. 10). In Fig. 11 it is clear how a slight repolish (which does not remove all the previous etch) after etching with this reagent partially removes the grain area etching, but the intragranular detail remains, revealing the prior-austenite grain boundaries in steels with high percentage of transformation.

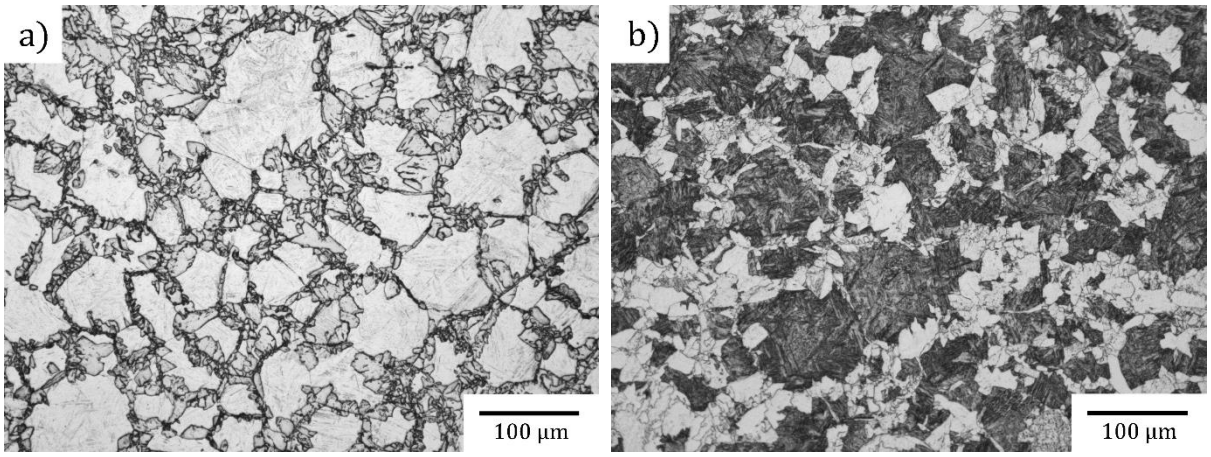

Figure 8. Steel V heat treated at 1245^{0}C Tγ and 610^{0}C T_{ISO} etched with: a) E2 reagent, b) Nital 2%.

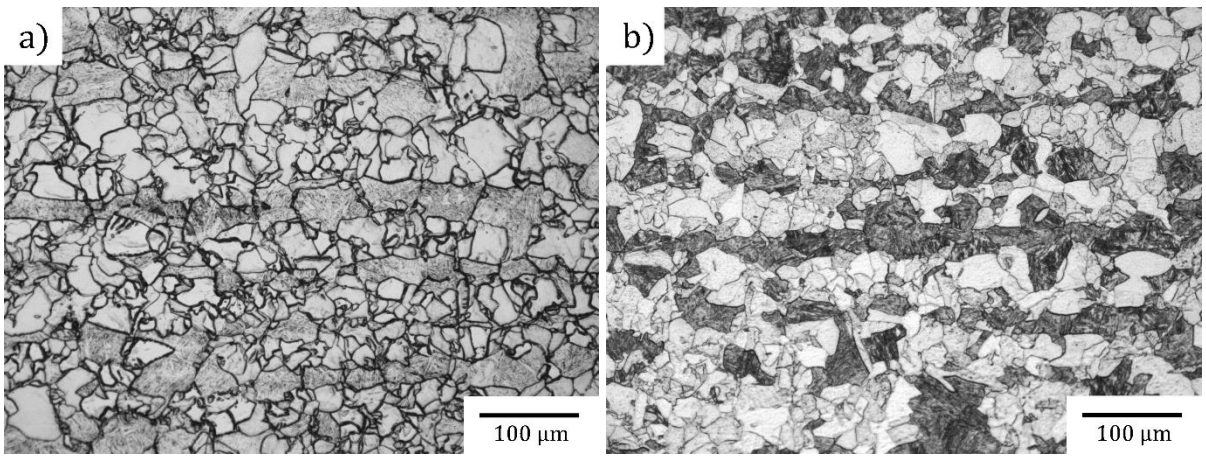

Figure 9. Steel CrV heat treated at 1100^{0}C Tγ and 600^{0}C T_{ISO} etched with: a) E2 reagent, b) Nital 2%.

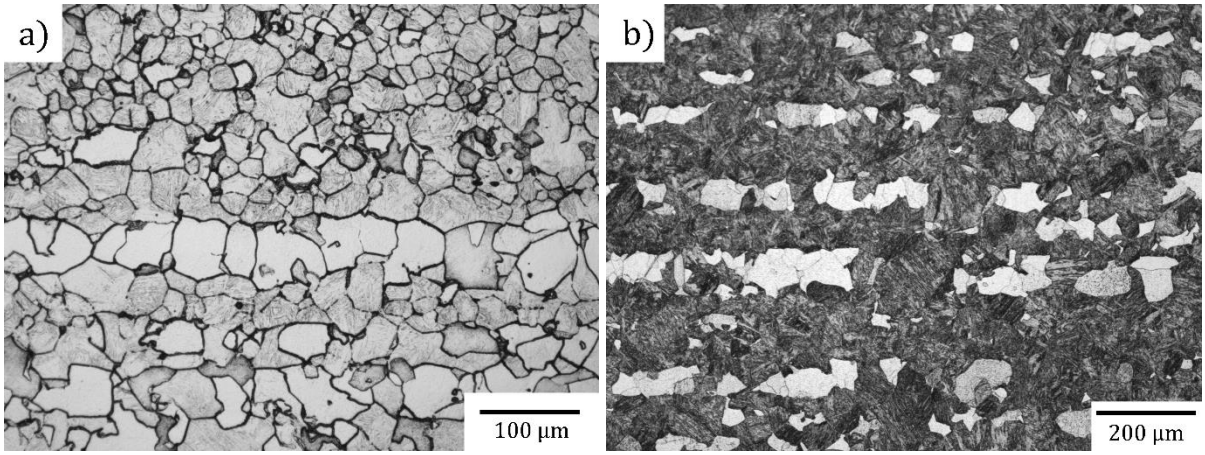

Figure 10. Steel CrNbV heat treated at 1245^{0}C Tγ and 610^{0}C T_{ISO} etched with: a) E2 reagent, b) Nital 2%.

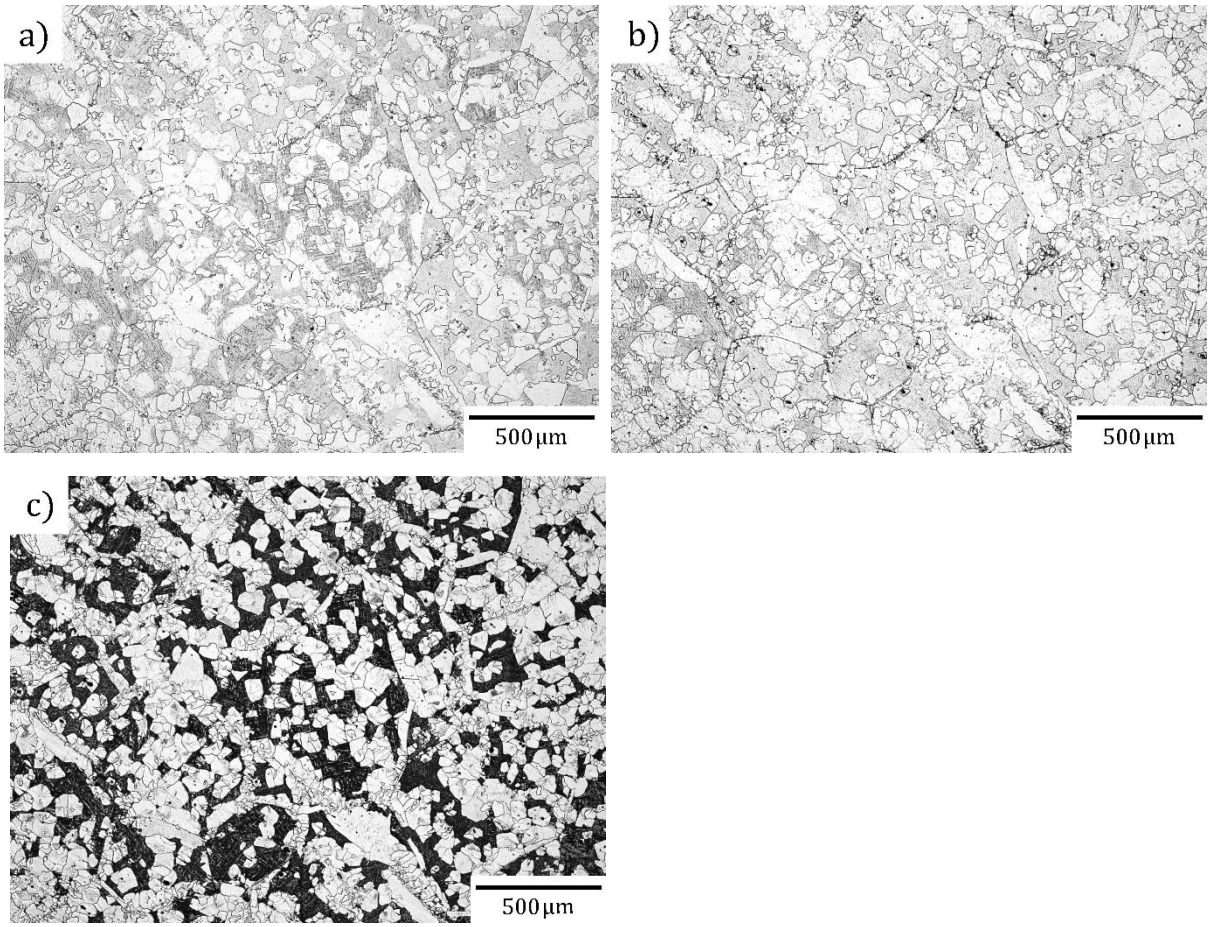

Figure 11. CrV Steel heat treated at 1300^{0}C Tγ and 625^{0}C T_{ISO} etched with: a) E2 reagent, b) Back polished from the first etchant and then re-etched with the same solution, c) Etched in 2% Nital. (all the images had been taken in the same region of the sample).

Samples of a steel with relative similar addition of carbide-former elements with a similar heat treatment but more than the double carbon addition [286] were used to observe the effectiveness of the

solution E2 on higher carbon steels. By contrasting the images with the results of etching E2 on V, CrV and CrNbV steels, it was determined a reduction in the amount of HCl was required in solution E2 to obtain good micrographs. It is known that the amount of HCl required is inversely proportional to the carbon content in the alloy[279]. Fig 12 presents the images obtained from etching the steel with a modification of the etching E2: 1 gr sodium dodecyl sulphate + 5 drops of HCl, showing that not only a reduction in the HCl but also in the wetting agent.

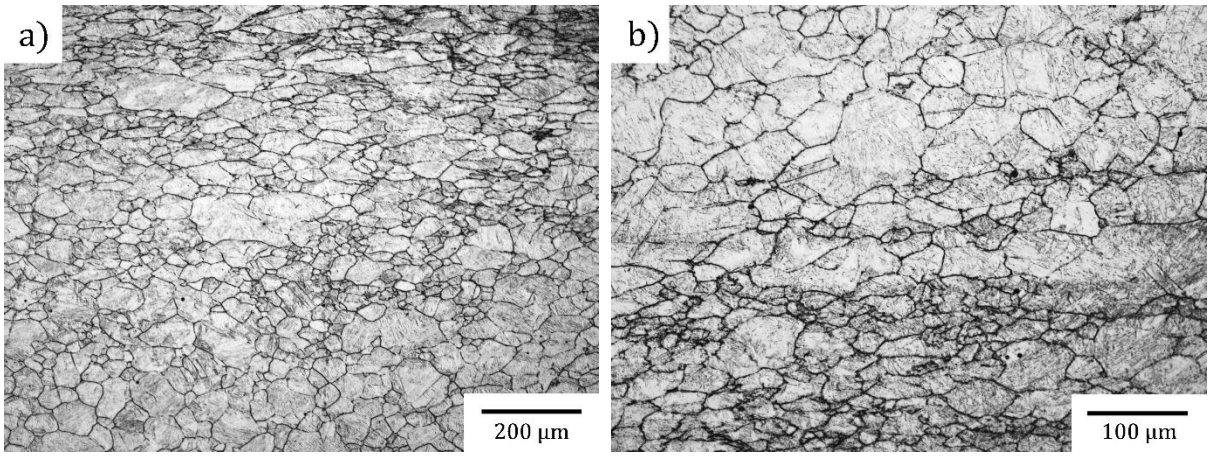

Figure 12. AlCrNb Steel etched with a modification of solution E2– 1 gr sodium dodecyl sulphate + 5 drops of HCl.

4. Conclusions

1. A methodical approach allowed the optimisation of the etching of low carbon steel to provide a comprehensive view of the microstructure that was not possible with standard etches. The new etching procedure reveals at once the different features of the microstructure in steel with a wide range of prior heat treatments.
2. 1.15 gr is the maximum possible addition of sodium dodecyl sulphate to reveal the prior-austenite grain boundaries of microalloyed steels with 0.1%C content.
3. With higher carbon content in the alloy, the wetting agent impedes the acid to etch all the high segregation areas, affecting the selectivity of the reagents and then the prior-austenite grain boundary delineation. For this reason, wetting agents which work on low carbon steels need to be reduced and studied to analyse their capability to produce clean etching of the microstructure and grain boundaries.

5. Data availability

This manuscript presents raw data; all the included pictures are as recorded from apparatus.

REFERENCES

1. Davies RG. Influence of martensite composition and content on the properties of dual phase steels. *Metall Trans A*. 1978;9(5):671-679. doi:10.1007/BF02659924

2. Speich GR, Demarest VA, Miller RL. Formation of Austenite During Intercritical Annealing of Dual-Phase Steels. *Metall Trans A, Phys Metall Mater Sci*. 1981;12 A(8):1419-1428. doi:10.1007/bf02643686

3. Misra RDK, Nathani H, Hartmann JE, Siciliano F. Microstructural evolution in a new 770 MPa hot rolled Nb-Ti microalloyed steel. *Mater Sci Eng A*. 2005;394(1-2):339-352. doi:10.1016/j.msea.2004.11.041

4. Hu J, Du LX, Ma YN, Sun GS, Xie H, Misra RDK. Effect of microalloying with molybdenum and boron on the microstructure and mechanical properties of ultra-low-C Ti bearing steel. *Mater Sci Eng A*. 2015;640:259-266. doi:10.1016/j.msea.2015.05.087

5. Chen MY, Yen HW, Yang JR. The transition from interphase-precipitated carbides to fibrous carbides in a vanadium-containing medium-carbon steel. *Scr Mater*. 2013;68(11):829-832. doi:10.1016/j.scriptamat.2013.01.020

6. Yang G, Sun X, Yong Q, Li Z, Li X. Austenite grain refinement and isothermal growth behavior in a low carbon vanadium microalloyed steel. *J Iron Steel Res Int*. 2014;21(8):757-764. doi:10.1016/S1006-706X(14)60138-2

7. Funakawa Y, Shiozaki T, Tomita K, Yamamoto T, Maeda E. Development of High Strength Hot-rolled Sheet Steel Consisting of Ferrite and Nanometer-sized Carbides. *ISIJ Int*. 2004;44(11):1945-1951. doi:10.2355/isijinternational.44.1945

8. Bu FZ, Wang XM, Yang SW, Shang CJ, Misra RDK. Contribution of interphase precipitation on yield strength in thermomechanically simulated Ti-Nb and Ti-Nb-Mo microalloyed steels. *Mater Sci Eng A*. 2015;620:22-29. doi:10.1016/j.msea.2014.09.111

9. Okamoto R, Borgenstam A, Ågren J. Interphase precipitation in niobium-microalloyed steels. *Acta Mater*. 2010;58(14):4783-4790. doi:10.1016/j.actamat.2010.05.014

10. Tamura I, Tanaka T, Sekine H. *Thermomechanical Processing of High-Strength Low-Alloy Steels.* London: Butterworth-Heinemann; 1988.

11. Kestenbach HJ, Campos SS, Morales E V. Role of interphase precipitation in microalloyed hot strip steels. *Mater Sci Technol*. 2006;22(6):615-626. doi:10.1179/026708306X81487

12. DeArdo AJ, Hua MJ, Cho KG, Garcia CI. On strength of microalloyed steels: An interpretive review. *Mater Sci Technol*. 2009;25(9):1074-1082. doi:10.1179/174328409X455233

13. Ouchi C. Development of steel plates by intensive use of TMCP and direct quenching processes. *ISIJ Int*. 2001;41(6):542-553. doi:10.2355/isijinternational.41.542

14. Vervynckt S, Verbeken K, Lopez B, Jonas JJ. Modern HSLA steels and role of non-recrystallisation temperature. *Int Mater Rev*. 2012;57(4):187-207. doi:10.1179/1743280411Y.0000000013

15. Hanlon DN, Sietsma J, Van Der Zwaag S. The effect of plastic deformation of austenite on the kinetics of subsequent ferrite formation. *ISIJ Int*. 2001;41(9):1028-1036. doi:10.2355/isijinternational.41.1028

16. Calvo J, Jung IH, Elwazri AM, Bai D, Yue S. Influence of the chemical composition on transformation behaviour of low carbon microalloyed steels. *Mater Sci Eng A*. 2009;520(1-2):90-96. doi:10.1016/j.msea.2009.05.027

17. Lanzagorta JL, Jorge-Badiola D, Gutiérrez I. Effect of the strain reversal on austenite-ferrite phase transformation in a Nb-microalloyed steel. *Mater Sci Eng A*. 2010;527(4-5):934-940. doi:10.1016/j.msea.2009.09.007

18. Yen HW, Chen PY, Huang CY, Yang JR. Interphase precipitation of nanometer-sized carbides in a titanium-molybdenum-bearing low-carbon steel. *Acta Mater*. 2011;59(16):6264-6274. doi:10.1016/j.actamat.2011.06.037

19. Jang JH, Heo YU, Lee CH, Bhadeshia HKDH, Suh DW. Interphase precipitation in Ti-Nb and Ti-Nb-Mo bearing steel. *Mater Sci Technol (United Kingdom)*. 2013;29(3):309-313. doi:10.1179/1743284712Y.0000000131

20. Zhang YQ, Zhang HQ, Liu WM, Hou H. Effects of Nb on microstructure and continuous cooling transformation of coarse grain heat-affected zone in 610 MPa class high-strength low-alloy structural steels. *Mater Sci Eng A*. 2009;499(1-2):182-186. doi:10.1016/j.msea.2007.10.118

21. Freeman S, Honeycombe RWK. Strengthening of titanium steels by carbide precipitation. *Met Sci*. 1977;11(2):59-64. doi:10.1179/msc.1977.11.2.59

22. Balliger NK, Honeycombe RWK. Coarsening of vanadium carbide, carbonitride, and nitride in low-alloy steels. *Met Sci*. 1980;14(4):121-133. doi:10.1179/030634580790426337

23. Tsai SP, Su TC, Yang JR, Chen CY, Wang YT, Huang CY. Effect of Cr and Al additions on the development of interphase-precipitated carbides strengthened dual-phase Ti-bearing steels. *Mater Des*. 2017;119:319-325. doi:10.1016/j.matdes.2017.01.071

24. Campbell K, Honeycombe RWK. The Isothermal Decomposition of Austenite in Simple Chromium Steels. *Met Sci*. 1974;8(1):197-203. doi:10.1080/03063453.1974.11910766

25. Westgren AF. Complex Chromium and Iron Carbides. *Nature*. 1933;132:480.

26. Gong P, Liu XG, Rijkenberg A, Rainforth WM. The effect of molybdenum on interphase precipitation and microstructures in microalloyed steels containing titanium and vanadium. *Acta Mater*. 2018;161:374-387. doi:10.1016/j.actamat.2018.09.008

27. Gong P, Palmiere EJ, Rainforth WM. Thermomechanical processing route to achieve ultrafine grains in low carbon microalloyed steels. *Acta Mater*. 2016;119:43-54. doi:10.1016/j.actamat.2016.08.010

28. San Martín D, Rivera-Díaz-del-Castillo PEJ, García-de-Andrés C. In situ study of austenite formation by dilatometry in a low carbon microalloyed steel. *Scr Mater*. 2008;58(10):926-929. doi:10.1016/j.scriptamat.2008.01.019

29. García C, Alvarez LF, Carsí M. Interest of dilatometric analysis in the study of structural transformations of martensitic stainless steels. *Proc Int Conf MatTech*. 1990;90.

30. García De Andrés C, Caballero FG, Capdevila C, Álvarez LF. Application of dilatometric analysis to the study of solid-solid phase transformations in steels. *Mater Charact*. 2002;48(1):101-111. doi:10.1016/S1044-5803(02)00259-0

31. Kleiner M, Geiger M, Klaus A. Manufacturing of lightweight components by metal forming. *CIRP Ann - Manuf Technol*. 2003;52(2):521-542. doi:10.1016/S0007-8506(07)60202-9

32. Singh M. Application of Steel in Automotive Industry. *Int J Emerg Technol Adv Eng*.

2016;6(7):246-253. www.ijetae.com.

33. Jeswiet J, Geiger M, Engel U, et al. Metal forming progress since 2000. *CIRP J Manuf Sci Technol*. 2008;1(1):2-17. doi:10.1016/j.cirpj.2008.06.005

34. Wallentowitz H, Adam H. Predicting the crashworthiness of vehicle structures made by lightweight design materials and innovative joining methods. *Int J Crashworthiness*. 1996;1(2):163-180. doi:10.1533/cras.1996.0012

35. Nehuis F, Kleemann S, Egede P, Vietor T, Herrmann C. Future Trends in the Development of Vehicles Bodies Regarding Lightweight and Cost. In: *Innovative Design, Analysis and Development Practices in Aerospace and Automotive Engineering*. New Delhi: Springer; 2014:13-21. doi:10.1007/978-81-322-1871-5

36. Paules JR. Developments in HSLA steel products. *JOM J Miner Met Mater Soc*. 1991;43(1):41-44. doi:10.1007/BF03220117

37. De Souza Paraiso Filho O, R. DE FUCCIO J. No Title. In: Stuart H, ed. *Niobium*. Warrendale, PA, TMS.; 1984:113-132.

38. Deardo AJ. Niobium in modern steels. *Int Mater Rev*. 2003;48(6):371-402. doi:10.1179/095066003225008833

39. Williams FH. Influence of Copper in Retarding Corrosion of Soft Steel and Wrought Iron. *Proc Eng Soc West Pennsylvania*. 1900;16:231-233.

40. Cone EF. Low-Alloy High Tensile Steels. *Steel*. 1934;September2:41-44.

41. Porter LF, Repas PE. The Evolution of HSLA Steels. *JOM J Miner Met Mater Soc*. 1982;34(4):14-21. doi:10.1007/BF03337994

42. Billur E, Altan T. Three greerations of advanced high strength steels for automotive applications, Part I. *Stamp J*. 2014;(December 2013).

43. Zhang MD, Hu J, Cao WQ, Dong H. Microstructure and mechanical properties of high strength and high toughness micro-laminated dual phase steels. *Mater Sci Eng A*. 2014;618:168-175. doi:10.1016/j.msea.2014.08.073

44. Bhadeshia H, Honeycombe R. *Steels: Microstructure and Properties*.; 2006. doi:10.1016/B978-0-7506-8084-4.X5000-6

45. Mallick PK. *Materials, Design and Manufacturing for Lightweight Vehicles*.; 2010. doi:10.1533/9781845697822

46. Bhattacharya D. Microalloyed Steels for the Automotive Industry. *Tecnol em Metal Mater e Mineração*. 2014;11(4):371-383. doi:10.4322/tmm.2014.052

47. Chen CY, Yen HW, Kao FH, et al. Precipitation hardening of high-strength low-alloy steels by nanometer-sized carbides. *Mater Sci Eng A*. 2009;499(1-2):162-166. doi:10.1016/j.msea.2007.11.110

48. Nanda T, Singh V, Singh V, Chakraborty A, Sharma S. Third generation of advanced high-strength steels: Processing routes and properties. *Proc Inst Mech Eng Part L J Mater Des Appl*. 2019;233(2):209-238. doi:10.1177/1464420716664198

49. Karelova A, Hairer F, Krempaszky C, Werner E, Hebesberger T, Pichler A. Influence of the Overaging Temperature on Microstructure and Mechanical Properties of Complex-Phase Bainitic Steel. *J Mater Sci Technol*. 2009;2:129-135.

50. Berglund G. PRESS-HARDENING-THE INFLUENCE OF SHEET-METAL AND TOOL DESIGN ON THE PRODUCTION-RATE. 1980.

51. Seo EJ, Cho L, De Cooman BC. Application of quenching and partitioning (Q&P) processing to press hardening steel. *Metall Mater Trans A Phys Metall Mater Sci*. 2014;45(9):4022-4037. doi:10.1007/s11661-014-2316-z

52. Altan T. Hot-stamping boron-alloyed steels for automotive parts Part II: Microstructure, material strength changes during hot stamping. *Stamp J*. 2007;19(1):14-15.

53. Dong W. Fan, Han S. Kim and BCDC. A Review of the Physical Metallurgy related to the Hot Press Forming of Advanced High Strength Steel. *Steel Res Int*. 2009;80(3):218-222. doi:10.2374/SRI08SP131

54. Cooman BD, Speer JG, Pyshmintsev IY, Yoshinaga NY. *Materials Design: The Key to Modern Steel Product. GRIPS Media GmbH.* GRIPS media; 2007.

55. Åkerström P. Modelling and Simulation of Hot Stamping. 2006.

56. Burgold A, Kuna M, Prüger S. Material Forces in Consideration of Phase Transformation in TRIP-steel. *Procedia Mater Sci*. 2014;3:461-466. doi:10.1016/j.mspro.2014.06.077

57. Skálová L, Divišová R, Jandová D. Thermo-mechanical processing of low-alloy TRIP-steel. *J Mater Process Technol*. 2006;175(1-3):387-392. doi:10.1016/j.jmatprotec.2005.04.067

58. Matlock DK, Speer JG. Processing opportunities for new advanced high-strength sheet steels. *Mater Manuf Process*. 2010;25(1-3):7-13. doi:10.1080/10426910903158272

59. Imandoust A, Zarei-Hanzaki A, Heshmati-Manesh S, Moemeni S, Changizian P. Effects of ferrite volume fraction on the tensile deformation characteristics of dual phase twinning induced plasticity steel. *Mater Des*. 2014;53:99-105. doi:10.1016/j.matdes.2013.06.033

60. Grässel O, Krüger L, Frommeyer G, Meyer LW. High strength Fe ± Mn ± (Al , Si) TRIP / TWIP steels development Đ properties Đ application. *Int J Plast*. 2000;16:1391-1409. doi:10.1016/j.tsf.2004.06.175

61. Chen L, Zhao Y, Qin X. Some aspects of high manganese twinning-induced plasticity (TWIP) steel, a review. *Acta Metall Sin (English Lett*. 2013;26(1):1-15. doi:10.1007/s40195-012-0501-x

62. GRAJCAR A, BOREK W. Thermo-mechanical processing of high-manganese austenitic TWIP-type steels. *Arch Civ Mech Eng*. 2012;8(4):29-38. doi:10.1016/s1644-9665(12)60119-8

63. De Cooman BC, Kwon O, Chin K-G. State-of-the-knowledge on TWIP steel. *Mater Sci Technol*. 2011;28(5):513-527. doi:10.1179/1743284711y.0000000095

64. Pickering F. *Physical Metallurgy and the Design of Steels.* London: Applied Science Publishers Ltd; 1978.

65. Ashby MF. Strengthening methods in crystals. *Elsevier, Amsterdam*. 1971:137.

66. Keh AS, Weissman S. Deformation substructure in body-centred cubic metals. *Electron Microsc strength crystals*. 1963:231-300.

67. B. E. O. Hall. The Deformation and Ageing of Mild Steel: III Discussion of Results. *Proc Phys Soc Sect B*. 1951;64:747.

68. Petch NJ. The cleavage strength of polycrystals. *J Iron Steel Inst*. 1953;174:25-28.

69. Cottrell AH. *Dislocations and Plastic Flow in Crystals.* Oxford: Clarendon Press; 1953.

70. Misra RDK, Tenneti KK, Weatherly GC, Tither G. Microstructure and texture of hot-rolled Cb-Ti and V-Cb microalloyed steels with differences in formability and toughness. *Metall Mater Trans A Phys Metall Mater Sci*. 2003;34 A(10):2341-2351. doi:10.1007/s11661-003-0297-4

71. Misra RDK, Thompson SW, Hylton TA, Boucek AJ. Microstructures of hot-rolled high-strength steels with significant differences in edge formability. *Metall Mater Trans A Phys Metall Mater Sci*. 2001;32(13):745-760. doi:10.1007/s11661-001-1009-6

72. Gray JM, Siciliano F. High Strength Microalloyed Linepipe: Half a Century of Evolution. *Proc an Int Symp high-strength, low-alloy steels*. 1959:1-26.

73. Sellars CM, Tegart WJMG. Relation between strength and structure in deformation at elevated temperatures. *Mem Sci LA Rev Metall*. 1966;63:731.

74. Jonas JJ, Sellars CM, Tegart WJMG. Strength and structure under hot-working conditions. *Metall Rev*. 1969;14(1):1-24. doi:10.1179/mtlr.1969.14.1.1

75. Dhua SK, Sen SK. Effect of direct quenching on the microstructure and mechanical properties of the lean-chemistry HSLA-100 steel plates. *Mater Sci Eng A*. 2011;528(21):6356-6365. doi:10.1016/j.msea.2011.04.084

76. Deardo AJ. Proceedings of the Third International Conference on HSLA STEELS. In: *China Science and Technology Press*. Beijing; 1995:99.

77. Zrník J, Kvackaj T, Pongpaybul A, Sricharoenchai P, Vilk J, Vrchovinsky V. Effect of thermomechanical processing on the microstructure and mechanical properties of Nb-Ti microalloyed steel. *Mater Sci Eng A*. 2001;319-321:321-325. doi:10.1016/S0921-5093(01)01033-4

78. Webster D, Woodhead JH. Effect of 0.03 percent niobium on ferrite grain size of mild steel. *J Iron Steel Inst*. 1964;202:987-994.

79. Verhoeven JD. *Steel Metallurgy for the Non-Metallurgist.* ASM International; 2007. doi:10.1361/smnm2007p001

80. Virasak LN. *Manufacturing Processes 4-5*. Open Oregon Educational Resources; 2017. https://books.google.co.uk/books?id=77P-uQEACAAJ.

81. Zener C. quoted by Smith C.S. Introduction to grains, phases, and interfaces — an interpretation of microstructure. *Trans Metall Soc AIME*. 1948;175:15-51.

82. Gladman T. The physical metallurgy of microalloyed steels. *Maney Pub*. 1997;615:176-784.

83. Gladman T. On the theory of the effect of precipitate particles on grain growth in metals. *Proc R Soc London Ser A Math Phys Sci*. 1966;294(1438):298-309. doi:10.1098/rspa.1966.0208

84. Dunn CG, Walter JL. Secondary Recrystallization, Recrystallization, Grain Growth and Textures. *Am Soc Met*. 1965:461-521.

85. Tweed CJ, Ralph B, Hansen N. The pinning by particles of low and high angle grain boundaries during grain growth. *Acta Metall*. 1984;32(9):1407-1414. doi:10.1016/0001-6160(84)90086-5

86. Wilson FG, Gladman T. Aluminium nitride in steel. *Int Mater Rev*. 1988;33(1):221-286. doi:10.1179/imr.1988.33.1.221

87. G.F. Melloy. Austenite Grain Size—Its Control and Effects. *Met Eng Institute, Am Soc Met*. 1968.

88. Gladman T. The Effect of Aluminum Nitride on the Grain Coarsening Behavior of Austenite, Metallurgical Developments in Carbon Steels, Special Report 81. *Iron Steel Institute, London*. 1963:68–70.

89. Turkdogan ET. Causes and Effects of Nitride and Carbonitride Precipitation during Continuous Casting. *Iron Steelmak*. 1989;16:61–75.

90. Repas PE. Metallurgical Fundamentals for HSLA Steels, Microalloyed HSLA Steels. *ASM Int*. 1988:3–14.

91. Baker TN. *Titanium Technology in Microalloyed Steels*. Vol 662.; 1997.

92. Cuddy LJ, Raley JC. Austenite grain coarsening in microalloyed steels. *Metall Trans A*. 1983;14(10):1989-1995. doi:10.1007/BF02662366

93. Kozasu I, Shimizu T, Kubota H. Recrystallization of Austenite of Si- Mn Steels with Minor Alloying Elements after Hot Rolling. *Trans ISIJ*. 1971;11:364-375.

94. Thillou V, Hua M, Garcia CI, Perdrix C, DeArdo AJ. Precipitation of NbC and Effect of Mn on the Strength Properties of Hot Strip HSLA Low Carbon Steel. *Mater Sci Forum*. 2009;284-286:311-318. doi:10.4028/www.scientific.net/msf.284-286.311

95. Speich GR, Cuddy LJ, Gordon CR, DeArdo AJ. Formation of ferrite from control-rolled austenite. *Phase Transform Ferr Alloy*. 1983:341-389.

96. Speich GR, Cuddy LJ, Gordon CR, DeArdo AJ. Formation of Ferrite from Control-Rolled Austenite, Phase Transformations in Ferrous Alloys. *AR Marder JI Goldstein, Ed, TMS-AIME, Warrendale, PA*. 1984:341–389.

97. Xie H, Du LX, Hu J, Misra RDK. Microstructure and mechanical properties of a novel 1000MPa grade TMCP low carbon microalloyed steel with combination of high strength and excellent toughness. *Mater Sci Eng A*. 2014;612:123-130. doi:10.1016/j.msea.2014.06.033

98. Krauss G. *Steels: Processing, Structure, and Performance*.; 2015. doi:10.1007/s007690000247

99. Deardo AJ. Accelerated cooling: A physical metallurgy perspective. *Can Metall Q*. 1988;27(2):141-154. doi:10.1179/cmq.1988.27.2.141

100. Krauss G. Principles of heat treatment of steel. *Am Soc Met*. 1980:291.

101. Maji BC, Krishnan M. The effect of microstructure on the shape recovery of a Fe-Mn-Si-Cr-Ni stainless steel shape memory alloy. *Scr Mater*. 2003;48(1):71-77. doi:10.1016/S1359-6462(02)00348-2

102. Zaefferer S, Ohlert J, Bleck W. A study of microstructure, transformation mechanisms and correlation between microstructure and mechanical properties of a low alloyed TRIP steel. *Acta Mater*. 2004;52(9):2765-2778. doi:10.1016/j.actamat.2004.02.044

103. Cao Y, Ni S, Liao X, Song M, Zhu Y. Materials Science & Engineering R Structural evolutions of metallic materials processed by severe plastic deformation. *Mater Sci Eng R*. 2018;133(May):1-59. doi:10.1016/j.mser.2018.06.001

104. Doong SH, Socie DF, Robertson IM. Dislocation substructures and nonproportional hardening. *J Eng Mater Technol Trans ASME*. 1990;112(4):456-464. doi:10.1115/1.2903357

105. Mittemeijer EJ. *Fundamentals of Materials Science. Vol. 8.* Berlin: Springer; 2010.

106. Yoshie A, Morikawa H, Yasumitsu O, Itoh Kametaro. Formulation of static recrystallization of austenite in hot rolling process of steel plate. *Trans Iron Steel Inst Japan*. 1987;27(6):425-431.

107. Ralph B. Grain growth. *Mater Sci Technol (United Kingdom)*. 1990;6(11):1136-1144. doi:10.1179/mst.1990.6.11.1136

108. Komura S, Horita Z, Nemoto M, Langdon TG. Influence of stacking fault energy on microstructural development in equal-channel angular pressing. *J Mater Res*. 1999;14(10):4044-4050. doi:10.1557/JMR.1999.0546

109. Orsetti PL, Sellars CM. Quantitative metallography of recrystallization. *Acta Mater*. 1997;45(1):137-148.

110. Tsukatani I. Effect of hot band microstructural factors on recrystallization texture in Ti-added ultra-low carbon cold-rolled sheet steels. *ISIJ Int*. 1998;38(6):625-632.

111. Ye W, Le Gall R, Saindrenan G. A study of the recrystallization of an IF steel by kinetics models. *Mater Sci Eng A*. 2002;332(1-2):41-46.

112. Drury MR, Urai JL. Deformation-related recrystallization processes. *Tectonophysics*. 1990;172(3-4):235-253. doi:10.1109/IMFEDK.2013.6602261

113. Rios PR, Siciliano F, Sandim HRZ, Plaut RL, Padilha AF. Nucleation and growth during recrystallization. *Mater Res*. 2005;8(3):225-238. doi:10.1590/S1516-14392005000300002

114. Koch E. Non-isothermal reaction analysis. *Acad Press*. 1977.

115. Aloi NE. Hot deformation, microstructure, and property analysis of ferritic/pearlitic and bainitic microalloyed forging steels. 1994. https://mountainscholar.org/bitstream/handle/11124/170340/T4617.pdf?sequence=1.

116. Weiss I, Jonas JJ. Interaction between recrystallization and precipitation during the high temperature deformation of HSLA steels. *Metall Trans A*. 1979;10(7):831-840. doi:10.1007/BF02658301

117. Sellars CM. Modelling microstructural development during hot rolling. *Mater Sci Technol (United Kingdom)*. 1990;6(11):1072-1081. doi:10.1179/mst.1990.6.11.1072

118. Hansen SS, Vander Sande JB, Cohen M. Niobium carbonitride precipitation and austenite recrystallization in hot-rolled microalloyed steels. *Metall Trans A*. 1980;11(3):387-402.

119. Cuddy LJ. The effect of microalloy concentration on the recrystallization of austenite during hot deformation. *Metall Soc*. 1982:129-140.

120. Zener C. quoted by Smith C.S. Grains, phases, and interfaces-an interpretation of microstructure. *Metall Mater Trans A Phys Metall Mater Sci*. 1948;175:47.

121. Irvine KJ, Pickering FB, Gladman T. Grain-refined C-Mn steels. *J Iron Steel Inst*. 1967;205(2):161-182.

122. Rhines FN, Craig KR, DeHoff RT. Mechanism of steady-state grain growth in aluminum. *Metall Trans*. 1974;5(2):413-425. doi:10.1007/BF02644109

123. Sellars CM, Whiteman JA. Recrystallization and grain growth in hot rolling. *Met Sci*. 1979;13((3-4)):187-194. doi:10.1179/msc.1979.13.3-4.187

124. Hillert M. On the theory of normal and abnormal grain growth. *Acta Metall*. 1965;13(3):227-238. doi:10.1016/0001-6160(65)90200-2

125. Gladman T, Pickering FB. Grain-coarsening of austenite. *J Iron Steel Inst*. 1967;205:653-664.

126. Humphreys FJ, Hatherly M. *Recrystallization and Related Annealing Phenomena.* Elsevier;

2012.

127. Manohar PA, Dunne DP, Chandra T, Killmore CR. Grain growth predictions in microalloyed steels. *ISIJ Int*. 1996;36(2):194-200. doi:10.2355/isijinternational.36.194

128. Khaki DM, Otaaghvar VA, Khaki MM. Determination of austenite grain coarsening temperature of a Nb-microalloyed steel sheet. *Adv Mater Res*. 2011;213:600-603. doi:10.4028/www.scientific.net/AMR.213.600

129. Gladman T. The theory and inhibition of abnormal grain growth in steels. *J Miner Met Mater Soc*. 1992;44(9):21-24. doi:10.1007/BF03222321

130. Chamisa A. PhD thesis: Development of Ultra High Strength Steels for Reduced Carbon Emission in Automotive Vehicles. 2014;(February).

131. Gomez M, Rancel L, Escudero E, Medina SF. Phase Transformation under Continuous Cooling Conditions in Medium Carbon Microalloyed Steels. *J Mater Sci Technol*. 2014;30(5):511-516. doi:10.1016/j.jmst.2014.03.015

132. Kral M V. Proeutectoid ferrite and cementite transformations in steels. In: *Phase Transformations in Steels*. Vol 1. Woodhead Publishing Limited; 2012:225-275. doi:10.1533/9780857096104.2.225

133. Kestenbach HJ. Dispersion hardening by niobium carbonitride precipitation in ferrite. *Mater Sci Technol*. 1997;13(9):731-739. doi:10.1179/mst.1997.13.9.731

134. Bhadeshia HKDH. Bainite : Overall transformation kinetics. *Le J Phys Colloq*. 1982;43(C4):C4-448. https://hal.archives-ouvertes.fr/jpa-00222187%0D.

135. Aaronson HI. Proeutectoid ferrite and cementite reactions. In: Zackay VF, Aaronson HI, eds. *The Decomposition of Austenite by Diffusional Processes*. New York: Interscience; 1962:387-546.

136. Dube CA, Aaronson HI, Mehl RF. La formation de la ferrite proeutectoïde dans les aciers au carbone.. *Rev Metall*. 1958;55(3):201-210.

137. Kral M V., Spanos G. Three-dimensional analysis and classification of grain-boundary-nucleated proeutectoid ferrite precipitates. *Metall Mater Trans A Phys Metall Mater Sci*. 2005;36(5):1199-1207. doi:10.1007/s11661-005-0212-2

138. Gladman T, B. H, McIvor ID. *Effect of Second-Phase Particles on the Mechanical Properties of Steel.* London: Iron and Steel Institute; 1971.

139. Wilyman PR, Honeycombe RWK. Relation between austenite-ferrite transformation kinetics and mechanical properties of vanadium steels. *Met Sci*. 1982;16(June):295-303. doi:10.1179/030634582790427398

140. Meyers M, Chawla KK. *Mechanical Behavior of Materials*. Cambridge University Press; 2008.

141. Dunne DP. Review: Interaction of precipitation with recrystallisation and phase transformation in low alloy steels. *Mater Sci Technol*. 2010;26(4):410-420. doi:10.1179/026708309X12526555493350

142. Cahn JW. Nucleation on dislocations. *Acta Metall*. 1957;5(3):169-172. doi:10.1016/0001-6160(57)90021-4

143. Gómez-Ramírez R, Pound GM. Nucleation of a second solid phase along dislocations. *Metall Trans*. 1973;4(6):1563-1570. doi:10.1007/BF02668009

144. Wilson D V., Russell B. The contribution of precipitation to strain ageing in low carbon steels. *Acta Metall*. 1960;8(7):468-479.

145. K.C. Russell. Nucleation in solids: The induction and steady state effects. *Adv Colloid Interface Sci*. 1980;13(3–4):205-318. doi:10.1016/0001-8686(80)80003-0

146. Kelly A, Nicholson RB. Precipitation Hardening, Progress in Materials Scince Vol. 10. In: ; 1963:149.

147. Gao N, Baker TN. Influence of AlN Precipitation on Thermodynamic Parameters in C-Al-V-N Microalloyed Steels. *ISIJ Int*. 1997;37(6):596-604.

148. Houghton DC, Weatherly GC, Embury JD. Characterization of carbonitrides in titanium-bearing HSLA steels. *Thermomechanical Process microalloyed austenite*. 1981:267-292.

149. Gray JM, Webster D, Woodhead JH. Precipitation in mild steels containing small additions of niobium. *J Iron Steel Inst*. 1965;203(8):812-818.

150. Halley JW. Grain-growth inhibitors in steel. Trans. AIME. *Trans Metall Soc AIME*. 1946;167:224-234.

151. Rainforth WM, Black MP, Higginson RL, et al. Precipitation of NbC in a model austenitic steel. *Acta Mater*. 2002;50:735-747. www.elsevier.com/locate/actamat.

152. Wang Z, Mao X, Yang Z, et al. Strain-induced precipitation in a Ti micro-alloyed HSLA steel. *Mater Sci Eng A*. 2011;529(1):459-467. doi:10.1016/j.msea.2011.09.062

153. Davenport AT, Berry FG, Honeycombe RWK, Berry FG, Honeycombe RWK. Interphase Precipitation in Iron Alloys Interphase Precipitation in Iron Alloys. *Met Sci J*. 1968;2:1(1968):104-106. doi:10.1179/030634568790443341

154. Baker BG, Nutting J. *Precipitation Processes in Steels.* London; 1959.

155. Davenport AT, Brossard LC, Miner RE. Precipitation in Microalloyed High-Strength Low-Alloy Steels. *J Miner Met Mater Soc*. 1975;27(6):21-27. doi:10.1007/BF03355951

156. Kamikawa N, Abe Y, Miyamoto G, Funakawa Y, Furuhara T. Tensile behavior of Ti, Mo-added low carbon steels with interphase precipitation. *ISIJ Int*. 2014;54(1):212-221. doi:10.2355/isijinternational.54.474

157. Wilson R. *Metallurgy and Heat Treatment of Tool Steels*. London, United Kingdom: McGraw-Hill Companies; 1975.

158. Honeycombe RWK. Transformation From Austenite in Alloy Steels. *Met Trans A*. 1976;7(7):915-936. doi:10.1007/BF02644057

159. Berns H, Theisen W. *Ferrous Materials: Steel and Cast Iron.* Springer Science & Business Media; 2008.

160. Gray JM, Yeo RBG. columbium carbonitride precipitation in Low-Alloy steels with particular emphasis on “precipitate-Row” Formation. *Am Soc Met Trans Q*. 1968;61:255-269.

161. Batte, A. D., & Honeycombe RWK. Precipitaion of vanadium carbide in ferrite. *J Iron Steel Inst*. 1973;211 (4):284-289.

162. Morrison WB. Influence of silver on structure and properties of low-carbon steel. *Mater Sci Technol (United Kingdom)*. 1985;1(11):954-960. doi:10.1179/mst.1985.1.11.954

163. Davenport AT, Honeycombe RWK. Precipitation of Carbides at γ -α Boundaries in Alloy Steels.

Proc R Soc Lond A Math Phys Sci. 1971;322(1549):191-205.

164. Honeycombe RWK. Fundamental aspects of precipitation in microalloyed steels. In: *HSLA Steels: Metallurgy and Applications*. ; 1985:243-250.

165. Riva R, Mapelli C, Venturini R. Effect of Coiling Temperature on Formability and Mechanical Properties of Mild Low Carbon and HSLA Steels Processed by Thin Slab Casting and Direct Rolling. *ISIJ Int*. 2007;47(8):1204-1213. doi:10.2355/isijinternational.47.1204

166. Lee WB, Hong SG, Park CG, Park SH. Carbide precipitation and high-temperature strength of hot-rolled high-strength, low-alloy steels containing Nb and Mo. *Metall Mater Trans A Phys Metall Mater Sci*. 2002;33(6):1689-1698. doi:10.1007/s11661-002-0178-2

167. Bee J V., Howell PR, Honeycombe RWK. Isothermal transformations in iron-chromium-carbon alloys. *Metall Trans A*. 1979;10(9):1207-1212. doi:10.1007/BF02811975

168. Howell PR, Ricks RA, Bee J V., Honeycombe RWK. Precipitate orientations in isothermally transformed iron-base alloys. *Philos Mag A Phys Condens Matter, Struct Defects Mech Prop*. 1980;41(2):165-175. doi:10.1080/01418618008236132

169. Johnson WC, White CL, Marth PE, Ruf PK, Tuominen SM. KD Wade, KC Russell and HI Aaronson. *Met Trans A*. 1975;6:911.

170. Lee JK, Aaronson HI. Influence of faceting upon the equilibrium shape of nuclei at grain boundaries-II. Three-dimensions. *Acta Metall*. 1975;23(7):809-820. doi:10.1016/0001-6160(75)90197-2

171. Ricks RA, Howell PR. Formation of Discrete Precipi. on Modile Interphase Boundary.Pdf. 1983;31(6):853-861.

172. Ricks RA, Howell PR. Bowing mechanism for interphase boundary migration in alloy steels. *Met Sci*. 1982;16(6):317-322. doi:10.1179/030634582790427389

173. Freeman S, Honeycombe RWK. Strengthening of titanium steels by carbide precipitation. *Met Sci*. 1977;11(2):59-64. doi:10.1179/msc.1977.11.2.59

174. Sakuma T, Honeycombe RWK. Microstructures of isothermally transformed Fe-Nb-C alloys. *Met Sci*. 1984;18(9):449-454. doi:10.1179/030634584790419791

175. Nordberg H, Aronsson B. Solubility of niobium carbide in austenite. *J Iron Steel Inst*. 1968;206(12):1263-1266.

176. Pickering FB, Garbarz B. Strengthening in pearlite formed from thermomechanically processed austenite in vanadium steels and implications for toughness. *Mater Sci Technol (United Kingdom)*. 1989;5(3):227-237. doi:10.1179/mst.1989.5.3.227

177. Yong QL. Secondary phases in steels. *Press Metall Ind Beijing, China*. 2006.

178. Liu Y, Sun Y hui, Wu H tian. Effects of chromium on the microstructure and hot ductility of Nb-microalloyed steel. *Int J Miner Metall Mater*. 2021;28(6):1011-1021. doi:10.1007/s12613-020-2092-2

179. Yokota T, Kobayashi A, Seto K, et al. High strength steel excellent in uniform elongation properties and method of manufacturing the same." U.S. Patent 8,815,025. 2014;2(August 26).

180. Lee WB, Hong SG, Park CG, Kim KH, Park SH. Influence of Mo on precipitation hardening in hot rolled HSLA steels containing Nb. *Scr Mater*. 2000;43(4):319-324. doi:10.1016/S1359-

6462(00)00411-5

181. Zhang K, Li ZD, Sun XJ, et al. Development of Ti-V-Mo complex microalloyed hot-rolled 900-MPa-grade high-strength steel. *Acta Metall Sin (English Lett*. 2015;28(5):641-648. doi:10.1007/s40195-015-0243-7

182. Berry FG, Honeycombe RWK. The isothermal decomposition of austenite in Fe-Mo-C alloys. *Metall Trans*. 1970;1(12):3279-3286. doi:10.1007/BF03037854

183. Kinsman KR, Aaronson HI. Influence of Al, Co, and Si upon the kinetics of the proeutectoid ferrite reaction. *Metall Trans*. 1973;4(4):959-967. doi:10.1007/BF02645596

184. López-Chipres E, Mejía I, Maldonado C, Bedolla-Jacuinde A, Cabrera JM. Hot ductility behavior of boron microalloyed steels. *Mater Sci Eng A*. 2007;460-461:464-470. doi:10.1016/j.msea.2007.01.098

185. Zarandi F, Yue S. The effect of boron on hot ductility of Nb-microalloyed steels. *ISIJ Int*. 2006;46(4):591-598. doi:10.2355/isijinternational.46.591

186. Peng Z, Li L, Gao J, Huo X. Precipitation strengthening of titanium microalloyed high-strength steel plates with isothermal treatment. *Mater Sci Eng A*. 2016;657:413-421. doi:10.1016/j.msea.2016.01.064

187. Iza-Mendia A, Altuna MA, Pereda B, Gutiérrez I. Precipitation of Nb in ferrite after austenite conditioning. Part I: Microstructural characterization. *Metall Mater Trans A Phys Metall Mater Sci*. 2012;43(12):4553-4570. doi:10.1007/s11661-012-1395-y

188. Chong X, Jiang Y, Zhou R, Feng J. Electronic structures mechanical and thermal properties of V–C binary compounds. *RSC Adv*. 2014;4(85):44959-44971.

189. Miyamoto G, Hori R, Poorganji B, Furuhara T. Interphase precipitation of VC and resultant hardening in V-added medium carbon steels. *ISIJ Int*. 2011;51(10):1733-1739. doi:10.2355/isijinternational.51.1733

190. Baker TN. Processes, microstructure and properties of vanadium microalloyed steels. *Mater Sci Technol*. 2009;25(9):1083-1107. doi:10.1179/174328409X453253

191. Nartowski AM, Parkin IP, MacKenzie M, Craven AJ, MacLeod I. Solid state metathesis routes to transition metal carbides. *J Mater Chem*. 1999;9(6):1275-1281. doi:10.1039/a808642g

192. Brito RM, Kestenbach HJ. On the dispersion hardening potential of interphase precipitation in micro-alloyed niobium steel. *J Mater Sci*. 1981;16(5):1257-1263. doi:10.1007/BF01033840

193. Kim YW, Song SW, Seo SJ, Hong SG, Lee CS. Development of Ti and Mo micro-alloyed hot-rolled high strength sheet steel by controlling thermomechanical controlled processing schedule. *Mater Sci Eng A*. 2013;565:430-438. doi:10.1016/j.msea.2012.12.055

194. Baker RG. The tempering of 2.25 Cr%-1% Mo steel after quenching and normalizing. *J Iron Steel Inst*. 1959;192(3):257-268.

195. Ridal KA, Quarrell AG. Effect of Creep Deformation Upon Carbide Transformations in Ferritic Alloy Steels. *J Iron Steel Inst*. 1962;200(5):366.

196. Andrews KW, Hughes H, Dyson DJ. Constitution diagrams for Cr-Mo-V steels. *J Iron Steel Inst*. 1972;210(5):337-350.

197. Pigrova GD. Carbide diagrams and precipitation of alloying elements during aging of low-alloy steels. *Metall Mater Trans A Phys Metall Mater Sci*. 1996;27(2):498-502.

doi:10.1007/BF02648434

198. Shaw SWK. The Formation of Carbide in Low-Carbon, Chromium-Vanadium Steels at 700℃. *J Iron Steel Inst*. 1957;185:10-22.

199. Senior BA. A Critical Review of Precipitation Behaviour in lCr-Mo-V Rotor Steels tempering results in some coarsening and spner oidization of M , C [7], and a feathery lath-like a. *Mater Sci Eng A*. 1988;103:263-271.

200. Smith R. Fe-Cr-Mo-V constitution diagrams. " *Precip Process Steels, Spec Rep*. 1959;64:307-311.

201. Janovec J, Svoboda M, Výrostková A, Kroupa A. Time-temperature-precipitation diagrams of carbide evolution in low alloy steels. *Mater Sci Eng A*. 2005;402(1-2):288-293. doi:10.1016/j.msea.2005.04.048

202. Zhou LY, Liu YZ, Yuan F, Huang QW, Song RB. Effect of Cr on transformation of ferrite and bainite dual phase steels. *J Iron Steel Res Int*. 2009;21:37-41.

203. Kostryzhev A, Singh N, Chen L, Killmore C, Pereloma E. Comparative effect of Mo and Cr on microstructure and mechanical properties in NbV-microalloyed bainitic steels. *Metals (Basel)*. 2018;8(2):134. doi:10.3390/met8020134

204. Tian J, Xu G, Zhou M, Hu H, Wan X. The effects of Cr and Al addition on transformation and properties in low-carbon bainitic steels. *Metals (Basel)*. 2017;7(2):12-17. doi:10.3390/met7020040

205. Wei Y, Wei-hong X, Ya-xiu L, Bing-zhe B, Hong-sheng F. Effect of Chromium on CCT Diagrams of Novel Air-Cooled Bainite Steels Analyzed by Neural Network. *J Iron Steel Res Int*. 2007;14(4):39-42. doi:10.1016/S1006-706X(07)60055-7

206. Chance J, Ridley N. Chromium Partitioning During Isothermal Transformation of a Eutectoid Steel. *Metall Trans A, Phys Metall Mater Sci*. 1981;12 A(7):1205-1213. doi:10.1007/BF02642334

207. Kestenbach HJ, Gallego J. On dispersion hardening of microalloyed hot strip steels by carbonitride precipitation in austenite. *Scr Mater*. 2001;44(5):791-796. doi:10.1016/S1359-6462(00)00660-6

208. Morrison WB, Woodhead JH. Influence of small niobium additions on mechanical properties of commercial mild steels. *J Iron Steel Inst*. 1963;201(1):43.

209. Chen MY, Gouné M, Verdier M, Bréchet Y, Yang JR. Interphase precipitation in vanadium-alloyed steels: Strengthening contribution and morphological variability with austenite to ferrite transformation. *Acta Mater*. 2014;64:78-92. doi:10.1016/j.actamat.2013.11.025

210. Miyamoto G, Hori R, Poorganji B, Furuhara T. Crystallographic analysis of proeutectoid ferrite/austenite interface and interphase precipitation of vanadium carbide in medium-carbon steel. *Metall Mater Trans A Phys Metall Mater Sci*. 2013;44(8):3436-3443. doi:10.1007/s11661-013-1702-2

211. Gorokhova NA, Sarrak VI, Suvorava SO. Solubility of titanium and niobium carbides in high-chromium ferrite. *Met Sci Heat Treat Met(Engl Transl);(United States)*. 1986;28(4).

212. Ray A. Niobium microalloying in rail steels. *Mater Sci Technol (United Kingdom)*. 2017;33(14):1584-1600. doi:10.1080/02670836.2017.1309111

213. Koyama S, Ishii T, Narita K. EFFECTS OF Mn, Si, Cr, AND Ni ON THE SOLUTION AND

PRECIPITATION OF NIOBIUM CARBIDE IN IRON AUSTENITE. *Kobe Steel Ltd, Japan*. 1971.

214. Kostryzhev A, Killmore C, Pereloma E. Effect of processing parameters on interphase precipitation and mechanical properties in novel CrVNb microalloyed steel. *Metals (Basel)*. 2021;11(1):1-14. doi:10.3390/met11010107

215. Pandit A, Murugaiyan A, Podder AS, et al. Strain induced precipitation of complex carbonitrides in Nb-V and Ti-V microalloyed steels. *Scr Mater*. 2005;53(11):1309-1314. doi:10.1016/j.scriptamat.2005.07.003

216. Lienert T, Siewert T, Babu S, Acoff V. Solid-State Transformations in Weldments, Welding, Brazing, and Soldering. In: *ASM Handbook, Vol. 6A - Welding Fundamentals and Processes*. ; 2011:122-145. doi:10.31399/asm.hb.v06a.a0005613

217. Bolton W. *Control Systems. Newnes.*; 2002.

218. Kostryzhev AG, Al Shahrani A, Zhu C, et al. Effect of niobium clustering and precipitation on strength of an NbTi-microalloyed ferritic steel. *Mater Sci Eng A*. 2014;607:226-235. doi:10.1016/j.msea.2014.03.140

219. Pereloma E V., Kostryzhev AG, Alshahrani A, et al. Effect of austenite deformation temperature on Nb clustering and precipitation in microalloyed steel. *Scr Mater*. 2014;75:74-77. doi:10.1016/j.scriptamat.2013.11.026

220. Davies J. Conduction and induction heating. *IEE POWER Eng Ser 11*. 1990.

221. Chun-Kan Hou. The effects of grain size on the magnetic properties of fully processed, continuous-annealed low-carbon electrical steels. *IEEE Trans Magn*. 1996;32(2):471-477. doi:10.1109/20.486534

222. García De Andrés C, Bartolomé MJ, Capdevila C, San Martín D, Caballero FG, López V. Metallographic techniques for the determination of the austenite grain size in medium-carbon microalloyed steels. *Mater Charact*. 2001;46(5):389-398. doi:10.1016/S1044-5803(01)00142-5

223. Béchet S, Beaujard L. Nouveau réactif pour la mise en évidence micrographique du grain austénitique des aciers trempés ou trempés-revenus. *Rev Metall*. 1955;52(10):830-836.

224. Bodnar RL, McGraw VE, Brandemarte A V. Technique for Revealing Prior Austenite Grain Boundaries in CrMoV Turbine Rotor Steel. *Metallography*. 1984;17(1):109-114.

225. Zhang L, Guo DC. A General Etchant for Revealing Prior-Austenite Grain Boundaries in Steels. *Mater Charact*. 1993;30(4):299-302.

226. Brownrigg A, Curcio P, Boelen R. Etching of prior austenite grain boundaries in martensite. *Metallography*. 1975;8(6):529-533.

227. Standard ASTM. E8/E8M 16a Standard Test Methods for Tension Testing of Metallic Materials 1. 2018:1-30.

228. Gao J, Huang Y, Guan D, et al. Deformation mechanisms in a metastable beta titanium twinning induced plasticity alloy with high yield strength and high strain hardening rate. *Acta Mater*. 2018;152:301-314. doi:10.1016/j.actamat.2018.04.035

229. Williams DB, Carter CB. *Transmission Electron Microscopy A Textbook for Materials Science*. Second. New York: Springer Science & Business Media; 2009. doi:10.1007/978-1-4757-2519-3_1

230. Higginson RL, Sellars CM. *Worked Examples in Quantitative Metallography*. Vol. 788. London, United Kingdom: Maney Publishing; 2003.

231. Zackay VF, Aaronson HI. Decomposition of austenite by diffusional processes. In: *Proceedings of a Symposium Held in Philadelphia, Pennsylvania, October 19, 1960 under the Sponsorship of the Ferrous Metallurgy Committee of the Institute of Metals Division, the Metallurgical Society, American Institute of Mining, Metallurgical, and Petr*. Vol. 2 Interscience Publishers; 1962.

232. Cahn JW. The kinetics of grain boundary nucleated reactions. *Acta Metall*. 1956;4(5):449-459. doi:10.1016/0001-6160(56)90041-4

233. Krahe PR, Kinsman KR, Aaronson HI. Influence of austenite grain sile upon the widmanstatten-start (Ws) temperature for the proeutectoid ferrite reaction. *Acta Metall*. 1972;20(9):1109-1121.

234. Aaronson HI, Spanos G, Masamura RA, et al. Sympathetic nucleation: an overview. *Mater Sci Eng B*. 1995;32(3):107-123. doi:10.1016/0921-5107(95)80022-0

235. Spanos G, Hall MG. The formation mechanism(s), morphology, and crystallography of ferrite sideplates. *Metall Mater Trans A Phys Metall Mater Sci*. 1996;27(6):1519-1534. doi:10.1007/BF02649812

236. Yokomizo T, Enomoto M, Umezawa O, Spanos G, Rosenberg RO. Three-dimensional distribution, morphology, and nucleation site of intragranular ferrite formed in association with inclusions. *Mater Sci Eng A*. 2003;344(1-2):261-267. doi:10.1016/S0921-5093(02)00411-2

237. Samuels LE. Optical microscopy of carbon steels. 1980.

238. Jatczak CF, Girardi DJ, Rowland ES. On banding in steel. *Trans ASM*. 1956;48:279-305.

239. Bastien PG. The mechanism of formation of banded structures. *J Iron Steel Res Int*. 1957;187:281-291.

240. Ward RG". EFFECT OF ANNEALING ON DENDRITIC SEGREGATION OF MANGANESE IN STEEL. *J Iron Steel Inst*. 1965;203:930.

241. Grange RA. Effect of microstructural banding in steel. *Metall Trans*. 1971;2(2):417-426. doi:10.1007/BF02663328

242. Fisher RM, Speich GR, Cuddy LJ, Hu H. Phase transformations during steel production. *Phys Chem Metall U S Steel Res Lab, Monroeville, Pa*. 1976:463-488.

243. Kattamis TZ, Flemings MC. Dendrite morphology, microsegregation, and homogenization of low-alloy steel. *Trans Metall Soc AIME*. 1965;233(2):992-999.

244. Bor AS. Effect of pearlite banding on mechanical properties of hot-rolled steel plates. " *ISIJ Int*. 1991;31(12):1445-1446.

245. Ghaemifar S, Mirzadeh H. Refinement of Banded Structure via Thermal Cycling and Its Effects on Mechanical Properties of Dual Phase Steel. *Steel Res Int*. 2018;89(6):1-6. doi:10.1002/srin.201700531

246. Thompson SW, Howell PR. Factors influencing ferrite/pearlite banding and origin of large pearlite nodules in a hypoeutectoid plate steel. *Mater Sci Technol (United Kingdom)*. 1992;8(9):777-784. doi:10.1179/mst.1992.8.9.777

247. Chen CY, Chen CC, Yang JR. Synergistic effect of austenitizing temperature and hot plastic deformation strain on the precipitation behavior in novel HSLA steel. *Mater Sci Eng A*. 2015;639:145-154. doi:10.1016/j.msea.2015.05.014

248. Pan XL, Umemoto M. Precipitation Characteristics and Mechanism of Vanadium Carbides in a V-Microalloyed Medium-Carbon Steel. *Acta Metall Sin (English Lett*. 2018;31(11):1197-1206. doi:10.1007/s40195-018-0775-8

249. Smith RM, Dunne DP. Structural aspects of alloy carbonitride precipitation in microalloyed steels. *Mater forum (Rushcutters Bay)*. 1988;11:166-181.

250. An FC, Zhang Y, Wang JJ, Zhao SX, Yuan G, Liu CM. Precipitation process of vanadium carbide in M23C6 by atomic-scale configuration analysis. *J Mater Sci*. 2020;55(2):762-773. doi:10.1007/s10853-019-03965-z

251. Beckitt FR, Clark BR. The shape and mechanism of formation of M23C6 carbide in austenite. *Acta Metall*. 1967;15(1):113-129.

252. Xu Y, Zhang X, Tian Y, et al. Study on the nucleation and growth of M23C6 carbides in a 10% Cr martensite ferritic steel after long-term aging. *Mater Charact*. 2016;111:122-127. doi:10.1016/j.matchar.2015.11.023

253. Yen HW, Huang CY, Yang JR. Characterization of interphase-precipitated nanometer-sized carbides in a Ti-Mo-bearing steel. *Scr Mater*. 2009;61(6):616-619. doi:10.1016/j.scriptamat.2009.05.036

254. Shewmon PG. *Transformations in Metals.* New York: McGraw-Hill.; 1969.

255. Li L, Messler RW. Dissolution kinetics of NbC particles in the heat-affected zone of type 347 austenitic stainless steel. *Metall Mater Trans A Phys Metall Mater Sci*. 2002;33(7):2031-2042. doi:10.1007/s11661-002-0035-3

256. Eom HJ, Shin JH, Kong BS, et al. Dissolution of nanosized NbC precipitates in austenite matrix during elastic deformation - Deleterious effect of high number density. *Mater Sci Eng A*. 2022;833(December 2021):142506. doi:10.1016/j.msea.2021.142506

257. Bengochea R, López B, Gutierrez I. Influence of the prior austenite microstructure on the transformation products obtained for C-Mn-Nb steels after continuous cooling. *ISIJ Int*. 1999;39(6):583-591. doi:10.2355/isijinternational.39.583

258. Xu YB, Yu YM, Xiao BL, Liu ZY, Wang GD. Microstructural evolution in an ultralow-C and high-Nb bearing steel during continuous cooling. *J Mater Sci*. 2009;44(15):3928-3935. doi:10.1007/s10853-009-3526-4

259. Ashby MF. Results and consequences of a recalculation of the frank-read and the orowan stress. *Acta Metall*. 1966;14(5):679-681. doi:10.1016/0001-6160(66)90074-5

260. Charleux M, Poole WJ, Militzer M, Deschamps A. Precipitation behavior and its effect on strengthening of an HSLA-Nb/Ti steel. *Metall Mater Trans A Phys Metall Mater Sci*. 2001;32(7):1635-1647. doi:10.1007/s11661-001-0142-6

261. Tang S, Liu ZY, Wang GD, Misra RDK. Microstructural evolution and mechanical properties of high strength microalloyed steels: Ultra Fast Cooling (UFC) versus Accelerated Cooling (ACC). *Mater Sci Eng A*. 2013;580:257-265. doi:10.1016/j.msea.2013.05.016

262. Mao X, Huo X, Sun X, Chai Y. Strengthening mechanisms of a new 700 MPa hot rolled Ti-microalloyed steel produced by compact strip production. *J Mater Process Technol*. 2010;210(12):1660-1666. doi:10.1016/j.jmatprotec.2010.05.018

263. Krishna SC, Gangwar NK, Jha AK, Pant B. On the Prediction of Strength from Hardness for Copper Alloys. *J Mater*. 2013;2013:1-6. doi:10.1155/2013/352578

264. Yong QL, Ma MT, Wu BR. Microalloyed steel-physical and mechanical metallurgy. 1989.

265. Kang SM, Kwon H. Fracture behavior of intercritically treated complex structure in medium-Carbon 6Ni steel. *Metall Trans A*. 1987;18(9):1587-1592. doi:10.1016/0956-716X(91)90176-2

266. Bag A, Ray KK, Dwarakadasa ES. Influence of martensite content and morphology on tensile and impact properties of high-martensite dual-phase steels. *Metall Mater Trans A Phys Metall Mater Sci*. 1999;30(5):1193-1202. doi:10.1007/s11661-999-0269-4

267. Marder AR. Deformation Characteristics of Dual-Phase Steels. *Metall Trans A, Phys Metall Mater Sci*. 1982;13 A(1):85-92. doi:10.1007/BF02642418

268. Byun TS, Kim IS. Tensile properties and inhomogeneous deformation of ferrite-martensite dual-phase steels. *J Mater Sci*. 1993;28(11):2923-2932. doi:10.1007/BF00354695

269. Peng-Heng C, Preban AG. The effect of ferrite grain size and martensite volume fraction on the tensile properties of dual phase steel. *Acta Metall*. 1985;33(5):897-903. doi:10.1016/0001-6160(85)90114-2

270. Bhattacharyya A, Sakaki T, Weng GJ. The influence of martensite shape, concentration, and phase transformation strain on the deformation behavior of stable dual-phase steels. *Metall Trans A*. 1993;24(2):301-314. doi:10.1007/BF02657317

271. Kim C. Modeling tensile deformation of dual-phase steel. *Metall Trans A*. 1988;19(5):1263-1268. doi:10.1007/BF02662587

272. Rodriguez-galeano KF, Rainforth WM, Romano-acosta LF, Palmiere EJ. A new approach to etching low-carbon microalloyed steels to reveal prior austenite grain boundaries and the dual-phase microstructure. *J Microsc*. 2023;289(2):73-79. doi:10.1111/jmi.13153

273. Grange RA. Strengthening steel by austenite grain refinement. *ASM Trans Quart*. 1966;59(1):26-48.

274. Morito S, Saito H, Maki T, Furuhara T. Effect of PAGS on crystallography and morphology of lath martensite in low carbon steels. *ISIJ Int*. 2004;45(1):91-94. http://dx.doi.org/10.1016/j.ijplas.2014.06.004%0Ahttp://dx.doi.org/10.1016/j.matlet.2009.06.020%0Ahttps://doi.org/10.1016/j.actamat.2018.03.030%0Ahttp://dx.doi.org/10.1016/j.actamat.2014.01.058%0Ahttps://doi.org/10.1016/j.matchar.2017.11.039%0Ahttp://dx.d.

275. Hanamura T, Yin F, Nagai K. Ductile-brittle transition temperature of ultrafine ferrite/cementite microstructure in a low carbon steel controlled by effective grain size. *ISIJ Int*. 2004;44(3):610-617. doi:10.2355/isijinternational.44.610

276. Baldinger P, Posch G, Kneissl A. Revealing austenitic grains in micro-alloyed steels by picric acid etching. *Prakt Met*. 1994;31:252-261.

277. Voort GFV. Wetting agents in metallography. *Mater Charact*. 1995;35(2):135-137. doi:10.1016/1044-5803(95)80111-1

278. Dreyer GA, Austin DE, Smith WD. New etchant brings out grain boundaries in martensitic steels. *Met Prog*. 1964;86(1):116-117.

279. Brewer AW, Erven KA, Krauss G. Etching and image analysis of prior austenite grain boundaries in hardened steels. *Mater Charact*. 1991;27(1):53-56. doi:10.1016/1044-5803(91)90079-J

280. Wiedermann J, Wojtas J, Stepień J. Etchant for Revealing Prior Austenite Grain in Alloy Steel/Ätzmittel für die Entwicklung des Primäraustenitkorns in legierten Stählen. *Pract Metallogr*. 1988;25(9):449-455.

281. Vander Voort GF. No Title. In: *Metallography, Principles and Practice.* ; 1999:218.

282. Papworth AJ, Williams DB. Segregation to prior austenite grain boundaries in low-alloy steels. *Scr Mater*. 2000;42(11):1107-1112.

283. Thackray R, Palmiere EJ, Khalid O. Novel etching technique for delineation of prior-austenite grain boundaries in low, medium and high carbon steels. *Materials (Basel)*. 2020;13(15). doi:10.3390/MA13153296

284. Vander Voort GF. No Title. In: *Metallography, Principles and Practice.* ; 1999:7.

285. Nelson JA. The use of wetting agents in metallographic etchants. *Pract Metallogr*. 1967;4(4):192-198.

286. Romano-Acosta LF, García-Rincon O, Pedraza JP, Palmiere EJ. Influence of thermomechanical processing parameters on critical temperatures to develop an Advanced High-Strength Steel microstructure. *J Mater Sci*. 2021;56(33):18710-18721. doi:10.1007/s10853-021-06444-6